THÈSE

En vue de l'obtention du

DOCTORAT DE L'UNIVERSITÉ DE TOULOUSE

Délivré par : *l'Institut National Polytechnique de Toulouse (INP Toulouse)*
Cotutelle internationale : *Université de Sherbrooke*

Présentée et soutenue le *06/07/2017* **par :**
MAJD DAROUKH

Effets de la distorsion sur le bruit tonal d'un turboréacteur moderne

Effects of distortion on modern turbofan tonal noise

CONFIDENTIEL INDUSTRIE

JURY

M. ROGER	Ecole Centrale Lyon	Rapporteur
S. GRACE	Boston University	Rapporteur
S. PONCET	Université de Sherbrooke	Rapporteur
C. POLACSEK	ONERA Châtillon	Examinateur
J.-F. BOUSSUGE	CERFACS	Examinateur
N. GOURDAIN	ISAE	Directeur
S. MOREAU	Université de Sherbrooke	Co-directeur
C. SENSIAU	Safran Aircraft Engines	Invité

École doctorale et spécialité :
MEGEP : Dynamique des fluides
Unité de Recherche :
CERFACS (UMR 5318)

Remerciements

Quel plaisir d'écrire ces quelques lignes ! Beaucoup de personnes ont contribué au bon déroulement de ces trois dernières années et le moment est venu de les remercier. Je souhaite commencer par tous les membres du jury, et en particulier les rapporteurs Michel Roger et Sheryl Grace, pour avoir accepté d'évaluer ce travail et pour leurs remarques constructives qui ont contribué à l'améliorer.

Merci également à Safran Aircraft Engines qui a financé ce projet (remerciements particuliers à Cédric Morel et à Matthieu Fiack) et au CERFACS qui m'a accueilli pendant la quasi-totalité de la thèse (merci Thierry Poinsot et Jean-François Boussuge). Je souhaite remercier tout particulièrement mes différents encadrants, Stéphane Moreau, Nicolas Gourdain, Jean-François Boussuge et Claude Sensiau, pour votre présence et votre aide tout au long de la thèse. Vous m'avez tous apporté quelque chose en plus d'un suivi régulier et je vous en suis très reconnaissant : merci Stéphane pour ta grande réactivité et ton aide lors de l'écriture des différents papiers, merci Nicolas pour tes précieux conseils lors de la rédaction, merci Jeff pour avoir transformé mes présentations (en bien, bien sûr !) et merci Claude pour ton souci de synthèse qui m'a toujours permis de raccrocher ce que je faisais au besoin industriel. Je tiens aussi à remercier Frédéric Sicot, pour m'avoir formé aux différents outils du CERFACS en début de thèse, et Marlène Sanjosé pour (entre autres) tout le support sur Optibrui.

La majeure partie de la thèse a été faite au CERFACS où j'ai passé trois très belles années et la liste des personnes à remercier est donc très longue ! Merci à tous les séniors, et en particulier merci (beaucoup beaucoup beaucoup) à Marc Montagnac pour toute l'aide que tu m'as apportée (et pas que !). Merci à toute l'administration et en particulier à Chantal (qui a tenu sa promesse pour le maillot !), Michèle, Marie, Nicole et Lydia pour votre bonne humeur que vous nous transmettez tous les jours ! Merci également à toute l'équipe CSG pour le support tout au long de la thèse, avec une attention particulière à Fred et Gérard pour l'organisation de la soutenance. Un grand merci aussi à tous les thésards qui ont illuminé mes journées au CERFACS (et en dehors aussi). Merci Biolchi pour les victoires faciles à FIFA, Nico pour avoir converti mes passes clés, Dario pour tes cheveux rigolos, Mélissa aussi pour tes cheveux rigolos et Césario pour tous ces bons Japoyaki. Merci Douds pour ta contribution à l'EAC, Kelu pour tes incroyables histoires, Pedro pour le pierre-feuille-ciseaux géant et Grosnick pour avoir supporté mon attaque de tasse de café. Je pense aussi à señor Cassou, à Catchi et aux duos Franchinou & Aïchou et Luis & Francis. Je n'oublie pas les plus jeunes : Maxou, l'homme le plus gentil au monde, Tastoul le grimpeur fou, Gagarin et Quegui les éternels stagiaires, Valou le bouffeur de cajou, Fél le bouffeur de pailles et Lulu le bouffeur de tibias. Je n'oublie pas non plus les mi-jeunes mi-vieux (post-docs et jeunes séniors) : Guillaume double-pédale, Micha, Lucas, Misda, la Pech et Nico le Grenoblois. Ni ceux qui ont déjà quitté le CERFACS : Carlitos le co-bureau de folie et reporter officiel de l'EAC, Lolo la joueuse d'accordéon (incroyable !), Gaëllou, Sophie, Laure, Moff, Jarjar, Abdullah, Greg, Yannis, David, Julio, Thibault et Jéjé.

Enfin, je termine la page CERFACS par une grande pensée à tous les joueurs de mon club de coeur de toujours : l'EAC (forcément !).

J'ai également eu la chance de passer quelques mois à Sherbrooke pendant cette thèse et je voulais remercier toute l'équipe d'aéroacoustique avec qui j'ai passé de très bons moments. Merci à Marlène et à Thomas (ou Léonard ?) pour m'avoir prêté votre canapé et avoir supporté mes questions pour la DPR. Un grand merci à Vianney pour nos incroyables discussions et nos matchs de ping-pong de légende ! Merci aussi au poète Aurélien, à Dark Chaofan, Hao, Prateek, Micha, Albane et Alexis. J'ai vraiment apprécié tous les moments passés avec vous !

Je souhaite aussi remercier toute l'équipe acoustique de Safran Aircraft Engines qui m'a toujours bien accueilli à chacun de mes passages. Je pense notamment à tous ceux qui avec qui j'ai interagi pendant la thèse (Claude Sensiau, Matthieu Fiack, Cédric Morel, François Julienne, Jacky Mardjono, Anthony Laffite, Mathieu Gruber, Rasika Fernando, Johan Thisse), aux footeux (Norman Jodet et Jérémy González) et à tous les autres pour les bons moments partagés autour d'un café !

Enfin, je termine par une pensée pour mes amis parisiens que je n'ai pas beaucoup vus pendant ces trois années (big up Nono, Paul, Charles, Julien, Chami, Fabio et Farah) mais qui m'ont inspiré à chaque repas partagé. Merci à Agathe pour cette dernière année passée à mes côtés et un très grand merci à toute ma famille à qui je dois beaucoup et qui m'a toujours soutenu pendant cette thèse.

Abstract

Fuel consumption and noise reduction trigger the evolution of aircraft engines towards Ultra High Bypass Ratio (UHBR) architectures. Their short air inlet design and the reduction of their interstage length lead to an increased circumferential inhomogeneity of the flow close to the fan. This inhomogeneity, called distortion, may have an impact on the tonal noise radiated from the fan module. Usually, such a noise source is supposed to be dominated by the interaction of fan-blade wakes with Outlet Guide Vanes (OGVs). At transonic tip speeds, the noise generated by the shocks and the steady loading on the blades also appears to be significant. The increased distortion may be responsible for new acoustic sources while interacting with the fan blades and the present work aims at evaluating their contribution. The effects of distortion on the other noise mechanisms are also investigated. The work is based on full-annulus simulations of the Unsteady Reynolds-Averaged Navier-Stokes (URANS) equations. A whole fan module including the inlet duct, the fan and the Inlet and Outlet Guide Vanes (IGVs/OGVs) is studied. The OGV row is typical of current engine architecture with an integrated pylon and two different air inlet ducts are compared in order to isolate the effects of inlet distortion. The first one is axisymmetric and does not produce any distortion while the other one is asymmetric and produces a level of distortion typical of the ones expected in UHBR engines. A description and a quantification of the distortion that is caused by both the potential effect of the OGVs and the inlet asymmetry are proposed. The effects of the distortion on aerodynamics are highlighted with significant modifications of the fan-blade wakes, the shocks and the unsteady loading on the blades and on the vanes. Both direct and hybrid acoustic predictions are provided and highlight the contribution of the fan-blade sources to the upstream noise. The downstream noise is still dominated by the OGV sources but it is shown to be significantly impacted by the inlet distortion via the modification of the impinging wakes.

Résumé

Les objectifs en termes de réduction de la consommation et du bruit émis par les moteurs d'avions ont progressivement mené aux architectures à très grand taux de dilution (UHBR). Leur géométrie est caractérisée par une entrée d'air courte et par une réduction de l'espace entre la soufflante et les aubes du redresseur du flux secondaire (OGVs), entraînant alors une augmentation de l'inhomogénéité azimutale de l'écoulement au niveau de la soufflante. Cette inhomogénéité, appelée distorsion, pourrait impacter le bruit tonal généré par le module de la soufflante. Ce bruit est généralement supposé être dominé par le mécanisme d'interaction des sillages des pales de la soufflante avec les OGVs. En régime transsonique, le bruit de choc et le bruit de charge stationnaire deviennent également prépondérants. L'augmentation de la distorsion pourrait être à l'origine de nouvelles sources de bruit en interagissant avec les pales de la soufflante et l'objectif de cette thèse est d'évaluer leur contribution. Les effets de la distorsion sur les mécanismes de bruit déjà existants sont également analysés. Cette étude est réalisée à l'aide de simulations numériques des équations instationnaires de Navier-Stokes moyennées (URANS). Un module complet de fan est considéré sur 360 degrés et se compose d'un conduit d'entrée d'air, de la soufflante et des redresseurs des flux primaire et secondaire (IGVs/OGVs). Le redresseur du flux secondaire est typique des moteurs actuels avec un pylône intégré et deux entrées d'air différentes sont étudiées de manière à isoler les effets de la distorsion d'entrée d'air. La première est axisymétrique et ne produit donc pas de distorsion alors que la deuxième ne l'est pas et produit un niveau de distorsion typique de ceux attendus dans les moteurs UHBR. Une description et une quantification de la distorsion due à l'effet potentiel des OGVs et de celle due à l'asymétrie de l'entrée d'air sont proposées. Les effets de la distorsion sur l'aérodynamique sont mis en évidence avec notamment une modification importante des sillages des pales de la soufflante, des chocs et de la charge instationnaire exercée sur les différentes pales et aubes. Des prévisions acoustiques basées sur les approches directe et hybride sont réalisées et soulignent la contribution importante des sources localisées sur les pales de la soufflante sur le bruit amont. Le bruit aval reste dominé par les sources sur les OGVs mais est tout de même impacté par la distorsion d'entrée d'air via la modification des sillages.

Contents

List of symbols

Latin characters

a_0	Speed of sound of the uniform flow
A_{mn}	Weight of $J_m(\alpha_{mn}r)$
b	Half-chord
B	Number of rotor blades
B_{mn}	Weight of $Y_m(\alpha_{mn}r)$
D	Acoustic energy dissipation or fan diameter depending on the context
E	Acoustic energy density
f_i	Components of pressure force vector
g	Amiet's transfer function
G	Green's function
h	Position height
H	Total vane height
I_x	Acoustic energy flux along the x-axis
$\boldsymbol{I}$	Acoustic energy flux
J_m	Bessel function of the first kind of order m
k_0	Wavenumber of the uniform flow
k_{mn}	Defined by $k_{mn}^2 = k_0^2 - \beta_0^2\alpha_{mn}^2$
k_x	Spatial wavenumber along the x-direction
k_y	Spatial wavenumber along the y-direction
L	Distance to the fan L
m	Azimuthal order
M_0	Axial Mach number of the uniform flow
n	Radial order
$\boldsymbol{n}$	Normal vector to the wall
p_{mn}	Pressure of the mode (m, n)
P_s	Acoustic power carried by the s^{th} harmonic
R_h	Hub radius
R_t	Tip radius
S	Source surface
S_{mn}	Source term of the mode (m, n)
t	Receiving time
$\boldsymbol{T}$	Lighthill's tensor, also written (T_{ij})

u_{mn}	Axial velocity of the mode (m, n)
U_0	Axial velocity of the uniform flow
V	Number of stator vanes
w	Upwash
X	Slowly varying observer axial coordinate
$\boldsymbol{x}$	Observer position, also written (x_i) or (x, r, θ)
Y	Slowly varying source axial coordinate
Y_m	Bessel function of the second kind of order m
$\boldsymbol{y}$	Source position, also written (y_i) or (y, r_y, θ_y)

Greek characters

α_{mn}	Radial eigenvalue of the mode (m, n)
β_0	Defined by $\beta_0^2 = 1 - M_0^2$
γ_{mn}	Axial wavenumber related to the mode (m, n)
Γ_{mn}	Norm of the duct eigenfunction Ψ_{mn}
δ	Dirac's distribution
ΔP	Pressure jump over the airfoil
ρ_0	Mean density
ρ_{mn}	Density of the mode (m, n)
τ	Emission time
Ψ_{mn}	Duct eigenfunction of the mode (m, n)
ω	Pulsation
Ω	Engine rotational speed

Indices and superscripts

m	Azimuthal mode order
n	Radial mode order
s	Harmonic order
0	Mean flow values
$'$	Fluctuating values
$+$	Upstream value
$-$	Downstream value

Acronyms

BPF	Blade Passing Frequency
BPR	ByPass Ratio
CAA	Computational AeroAcoustics
CDC	Circumferential Distortion Coefficient
CFD	Computational Fluid Dynamics
DNS	Direct Numerical Simulation
DRI	Distortion-Rotor Interaction
DTS	Dual Time Step
ICAO	International Civil Aviation Organization

IGV	Inlet Guide Vane
LEE	Linearized Euler Equations
LES	Large Eddy Simulations
OGV	Outlet Guide Vane
RANS	Reynolds-Averaged Navier-Stokes
RF	Rotational Frequency
UHBR	Ultra High Bypass Ratio
URANS	Unsteady Reynolds-Averaged Navier-Stokes
WSI	Wakes-Stator Interaction

Introduction

General context

The environmental impacts from aviation are multiple and could lead to a critical constraint on capacity growth. Aircraft engine emissions contribute to the air quality and the climate change [1] and aircraft engine noise causes health hazards to the exposed population, especially with the expansion of urban areas around airports. Standards are therefore defined by the International Civil Aviation Organization (ICAO) in support of an environmentally responsible civil aviation sector [2].

In its strand dedicated to aircraft noise, the ICAO has defined the maximum noise levels acceptable for civil aircrafts. These levels are expressed in EPNdB, a unit representative of the nuisance to airport communities. They are established from three certification points, illustrated in Fig. 1:

- one lateral point measured 450 m from the runaway at full power (sideline);
- one point at 6.5 km on the extended centre line of the runaway after the reduction of thrust (cutback);
- and one point at 2 km on the extended centre line of the runaway at low speed (approach).

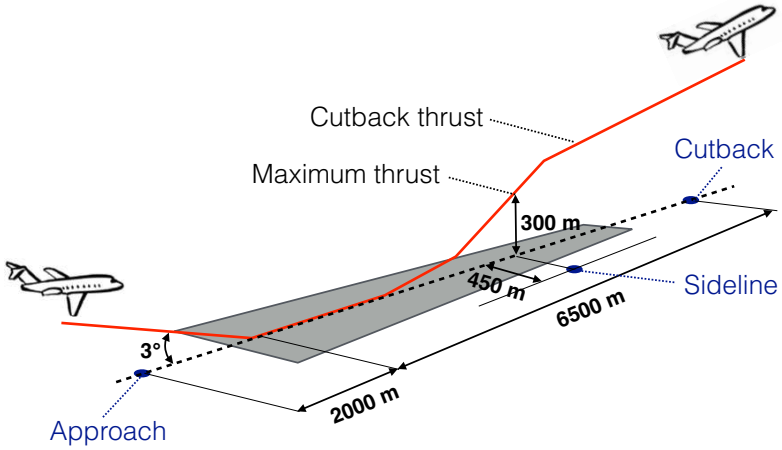

Figure 1: **Acoustic certification points (reproduced from [3])**

The standards imposed by the ICAO become more restrictive to mitigate the constantly increasing air traffic. They are driven by the chapter evolution of the volume I of the ICAO report. Current standards are described in chapter 4 but the ones of chapter 14, which impose a reduction of 7 EPNdB, are being applied or will be applied by 2020 depending on the type of aircraft [2].

In addition to these certifications, Europe, via the Advisory Council for Aeronautics Research in Europe (ACARE) has established in 2001 even more challenging goals. Thus, the subjective perception of the noise radiated by an aircraft should be reduced by 50 % in 2020 and by 65 % in 2050, relative to year 2000 average levels. This corresponds to a reduction of 30 EPNdB (10 EPNdB per certification point) and 39 EPNdB (13 EPNdB per certification point) respectively [4].

Two main contributions are identified at the three certification points: the engine noise and the airframe noise. First experimental studies have shown a domination of engine noise at high speed (cutback and sideline points), when the landing gear and the high-lift devices are not (entirely) deployed. At low speed (approach point), both the landing gear and the high-lift devices are released and are responsible for an important noise thus making the airframe and the engine noise comparable [5]. A better understanding of both sources becomes a necessity to respect the future more stringent standards. The present study focuses on the noise radiated from the engine.

Noise from an aircraft engine

The noise from an aircraft engine naturally depends on the architecture of the engine. The study is limited to turbofan engines which propel most commercial aircrafts because of their high efficiency. Counter Rotating Open Rotors (CRORs) are expected to present higher propulsive efficiency but technical challenges in terms of installation, noise and certification remain [6].

In a turbofan engine, the thrust is not only resulting from the burnt gases. As illustrated in Fig. 2, air is ingested (and compressed) by the fan and is split into two streams. The air of the primary stream follows the Brayton thermodynamic cycle. It is straightened by the Inlet Guide Vanes (IGV), compressed through the stages of the compressor, mixed with the fuel, burnt in the combustion chamber, expanded through the stages of the turbine and accelerated in the nozzle. The energy collected by the turbine is used to rotate the fan and the compressor. As for the air of the secondary stream, it is directly straightened by the Outlet Guide Vanes (OGV) and accelerated through the nozzle.

Both streams contribute to provide thrust: the primary stream by accelerating the flow and the secondary stream by ingesting an air mass-flow rate. The ratio between the mass-flow rate of air in the secondary stream and the one in the primary stream is called the ByPass Ratio (BPR). The higher the BPR, the lower the fuel consumption is (for a given thrust). However, the higher the BPR, the larger

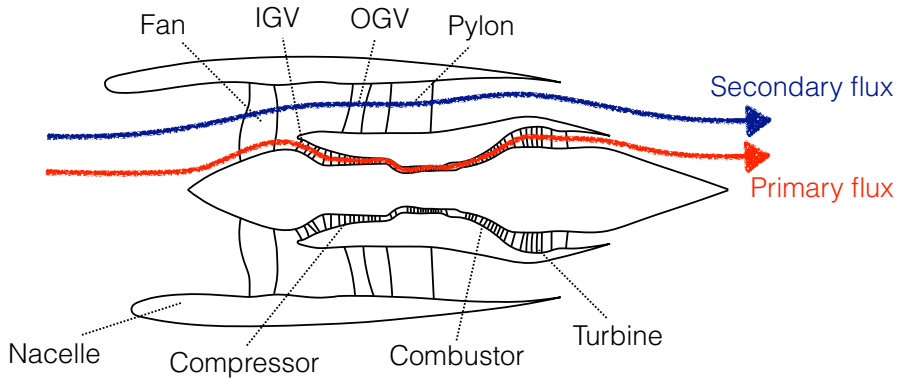

Figure 2: **Turbofan engine architecture (reproduced from [7])**

the engine is, and consequently, the higher the weight and drag are. A trade-off between engine efficiency and engine size must be done. Current classical engines are characterized by a BPR of about 5-7. The newer ones, such as the LEAP which propels the A320neo, are characterized by a BPR of about 10. They are referred to as High Bypass Ratio (HBR) engines. An optimization of this trade-off will be achieved in future engines by reducing the length of their nacelle by:

- shortening the air inlet duct;
- including the structural pylon into the OGV row;
- and moving closer to the fan the OGV and the pylon.

These evolutions are schematically represented in Fig. 3. These new engines will have a BPR around 15 and are called Ultra High Bypass Ratio (UHBR) engines. They are likely the last evolution of turbofan engines before a technological breakthrough.

Almost all the components of a turbofan engine create some noise. Studies that have been conducted so far allows identifying three main sources of engine noise:

- the fan, compressor and turbine noise, due to the rotation of physical elements;
- the jet noise, caused by the turbulent shear layer between the jet and the ambiant air;
- and the combustion noise, essentially due to flame unsteadiness in the combustor and acceleration of entropy spots.

Jet noise has been the dominant source of an engine for a long time but the evolution towards higher BPR is modifying the breakdown. This is shown in Fig. 4 which shows the contribution of the main sources at the three certification points for typical HBR and UHBR engines. When increasing the BPR, the exhaust velocities become lower and the importance of jet noise starts to decrease compared to fan noise. This trend is further accentuated by the short nacelle design in UHBR engines whichs reduces the surface available for acoustic treatments [6].

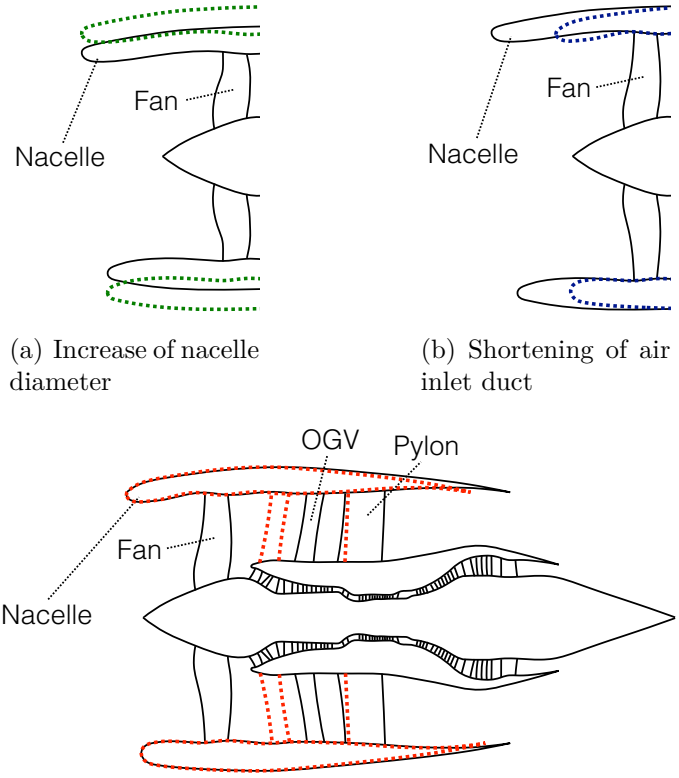

(a) Increase of nacelle diameter

(b) Shortening of air inlet duct

(c) Reduction of space between the fan and the OGV

Figure 3: **Evolution towards UHBR architectures**

Noise from a fan module

The study focuses on the noise radiated by the fan which becomes the main issue (in terms of acoustics) in UHBR engines because of its contribution at all certification points. Typical noise spectra of a fan operating at subsonic and supersonic conditions are given in Fig. 5. At both operating conditions, the noise is composed of a tonal contribution and a broadband one. At subsonic tip speeds, the broadband noise generated by the fan is expected to be larger than the tonal noise. Tones emerge at the Blade Passing Frequency (BPF) $f_{BPF} = B\Omega/2\pi$, where B is the number of fan blades and Ω is the shaft-rotational speed. Their levels are above the broadband noise level by a few tens of decibels. At supersonic tip speeds, the trend is generally reversed and the tonal noise dominates. A lot of additional tones, called Multiple Pure Tones (MPT) and linked to the Rotational Frequency (RF) $f_{RF} = \Omega/2\pi$, become significant.

Sources of fan tonal noise

The main mechanisms that are responsible for tonal noise are schematically represented in Fig. 6 and can be classified into three categories that are detailed below [6].

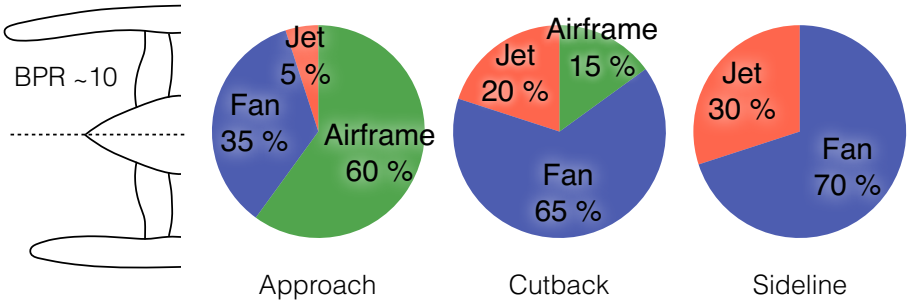

(a) HBR engine

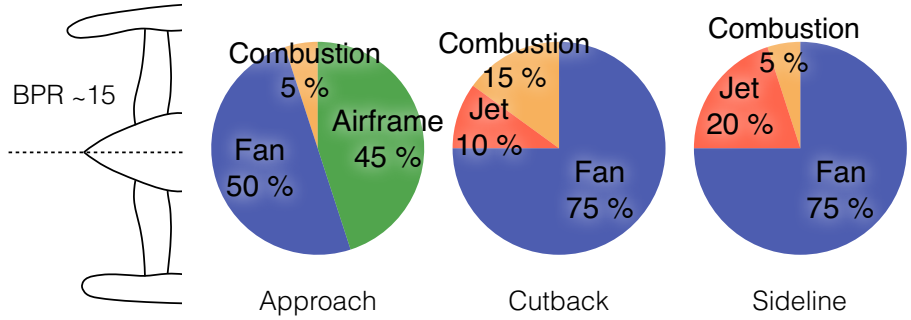

(b) UHBR engine

Figure 4: **Source breakdown at certification points for typical HBR and UHBR engines (Safran estimates)**

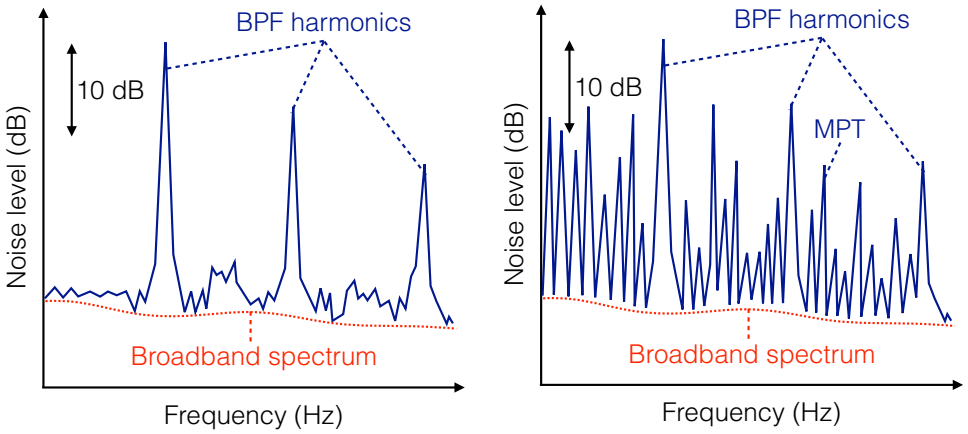

(a) Subsonic fan

(b) Supersonic fan

Figure 5: **Typical noise spectrum from a subsonic fan and a supersonic fan (reproduced from [7])**

Rotor self-noise

Rotor self-noise is the noise generated by the rotor itself, without interacting with its environment. One part of this noise is produced by the force and volume-displacement effects exerted by the rotating blades on the fluid. It is linked to the steady loading on fan blades which propagates because of the rotational motion.

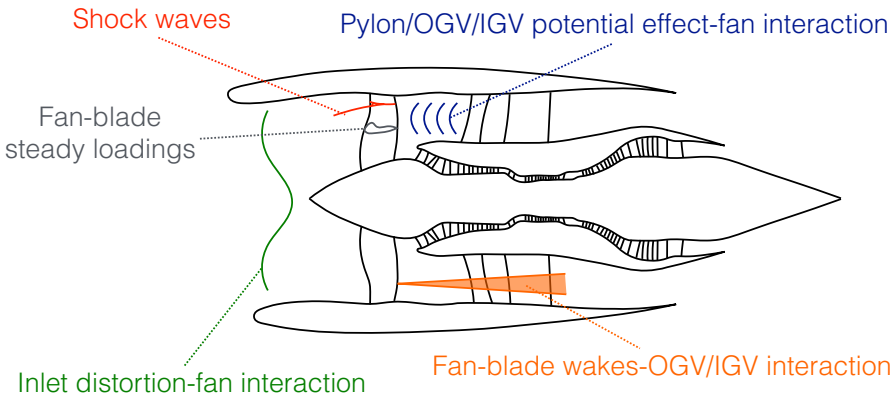

Figure 6: **Mechanisms generating fan tonal noise (reproduced from [7])**

A fan with B identical blades will produce noise at harmonics of the BPF. The resulting sound field can be decomposed into azimuthal Fourier harmonics of order equal to multiples of B (more details in Sec. 1.6.1). These modes cannot propagate through the duct at subsonic fan-tip speeds but are dominant as soon as the latter becomes supersonic (at takeoff conditions typically) [8].

In addition to this mechanism, shocks also start to develop at these supersonic tip speeds. These shocks rotate with the fan and should have the periodicity of the number of blades B. In reality, small blade-to-blade geometry variations exist because of the manufacturing and the assembly of the blades and are responsible for significant variations in shock strength. Therefore, the shocks combine together while propagating thus causing the loss of original periodicity. This results in a noise at harmonics of the RF which is often referred to as Buzz-Saw Noise (BSN). These shocks propagate only in the upstream direction and are generally responsible for an important increase of the total noise [9].

Rotor-stator interaction noise

Rotor-stator interaction noise is the noise caused by the impact of rotor-blade wakes on the stator vanes. The fan-blade wakes are steady in the rotor frame and lead to a rotating field with azimuthal orders that are multiples of the number of blades B in the stationary frame. They interact with the OGV located downstream and are responsible for unsteady lift variation. A noise is produced, again at BPF harmonics. Contrary to fan self-noise, a wide range of azimuthal orders is created. They correspond to the so-called Tyler & Sofrin modes $m = nB - kV$ where V is the number of vanes, n the order of the BPF harmonic and k any integer [10]. This formula is valid when the stator vanes are all identical and evenly spaced. In current engines, the OGV is heterogeneous and all azimuthal orders could be generated (replacement of V by 1 in Tyler & Sofrin formula) [11]. Fan-IGV interaction noise is generally neglected but fan-OGV interaction is considered to be the main source of fan tonal noise [6].

Distortion-rotor interaction noise

Distortion-rotor interaction noise is caused by the impact of a stationnary circumferential inhomogeneity of the flow (called distortion) with the rotating fan. When the air inlet is not axisymmetric or when the potential effect of the downstream pylon is significant, the flow contains components of low azimuthal order, typically from $m = -5$ to $m = 5$. These components will be unsteady in the rotating frame and will interact with the fan blades, creating unsteady lift variations. A noise is produced at harmonics of the BPF if all blades are identical and the resulting sound field can be decomposed into azimuthal orders going from $m = nB - 5$ to $m = nB + 5$. This noise mechanism is generally neglected for current engine architectures in which the inlet duct and the interstage are sufficiently long to attenuate both the inlet distortion and the potential effect of the pylon.

A noise can also be produced by the interaction of the fan with the potential effect of the stators (OGV and IGV). If the potential effect of these stators is important enough, the flow contains azimuthal harmonics of order equal to multiples of the number of vanes V. These components are unsteady in the rotor frame and are responsible for unsteady lift variations on the blades. The resulting sound field can be decomposed into azimuthal harmonics of order given by Tyler & Sofrin law $m = nB - kV$ where V is the number of vanes, n the order of the BPF harmonic and k any integer. These noise mechanisms are generally neglected because they are considered much less important than rotor-stator interaction [6].

Sources of fan broadband noise

Historically, fan broadband noise has been less studied than fan tonal noise. Experimental studies have allowed for the identification of the main sources, which are linked to turbulent phenomena [12]. They are schematically represented in Fig. 7. Again, they can be classified into three categories detailed below.

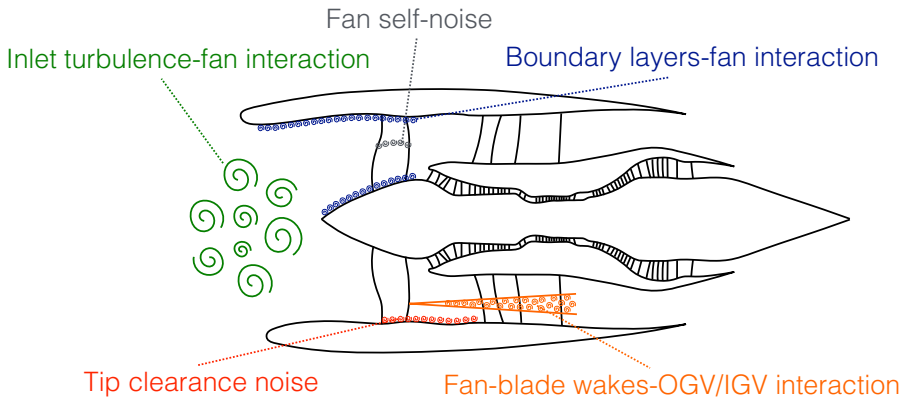

Figure 7: **Mechanisms generating fan broadband noise (reproduced from [7])**

Rotor self-noise

The fan itself produces noise even when it is isolated from its environment. This noise comes from the passage of the turbulent boundary layer over the trailing edge of each blade. The interaction between the turbulent and the trailing edge eddies amplifies the quadrupole noise associated with the fluid motion in a plane normal to the edge [13]. This source is a significant source of fan broadband noise [6].

Rotor-stator interaction noise

The interaction of fan-blade wakes with stator vanes has been shown to be the main contributor to fan tonal noise. These wakes possess a fully turbulent component and are also responsible for nonperiodic lift variations on the blades. This results in a broadband noise which clearly dominates other broadband noise sources [6].

Turbulence-rotor interaction noise

The interaction of a turbulent flow with the rotating fan is also responsible for broadband noise. The probably most important contribution to this noise is caused by the hub and shroud boundary layers which interact with the rotating flow in the fan region. Around the casing, this noise could be very important. Its prediction is difficult and numerical simulations and experiments show humps around multiples of BPF, which might indicate the presence of noise-generating structures with a range of length scales in the boundary layer [14, 15].

Another source comes from the interaction of the inlet turbulence with the fan. The vortices of atmospheric turbulence are stretched out while ingested by the fan. When the scale of the vortices becomes high compared with the fan-blade chord, the interaction mechanism becomes coherent. Therefore, it can be seen as a distorsion-rotor mechanism and the resulting noise is mainly tonal. However, the small-scale vortices are responsible for non-coherent lift variations on the blades and result in a broadband noise.

Finally, the tip clearance noise can also be seen as an interaction mechanism between a turbulent flow and the fan. The mechanism is actually one of the most complex one. The tip clearance flow interacts with the casing boundary layer and generates tip leakage vortices. The latter interact with the blades and create unsteady lift variations which result in a broadband noise. The effect of tip clearance on the noise is not completely understood but it seems to alter both the fan-self noise and the casing boundary layer-fan interaction noise mechanisms [12, 16].

A new source breakdown caused by distortion?

The study focuses on fan tonal noise. In regular flow conditions and current architectures, it is dominated by the fan-OGV interaction (called here WSI for Wakes-Stator Interaction) and by the fan-self noise at transonic regimes [6, 17]. The noise caused by distortion-fan interaction (called here DRI for Distortion-Rotor Interaction) is

generally neglected.

However, this breakdown might change in UHBR engines where the distortion is expected to increase because of the geometrical evolutions shown in Fig. 3. The most important distortion comes from the inlet which can be asymmetric for two different reasons. The first reason is that the engine intake is not perfectly aligned with the fan axis to account for the downward deflection of the flow by the wing in cruise conditions. The other one is due to ground-clearance requirements which leads to non-circular cross sections for large engines. Due to this asymmetry, a circumferential inhomogeneity of the flow is created at the entrance of the engine. This inhomogeneity is not sufficiently damped before reaching the fan because of the reduced length of the air inlet and will interact with it. In addition to this so-called "inlet" or "upstream distortion", the potential effect of the OGV and the pylon is increased because of the reduction of space between them and the fan. This potential effect, or "downstream distortion", is stationnary and also interacts with the rotating fan. For illustration purposes, typical axial velocity contours for a clean and a distorted inflow are given in Figs. 8(a) and 8(b) respectively.

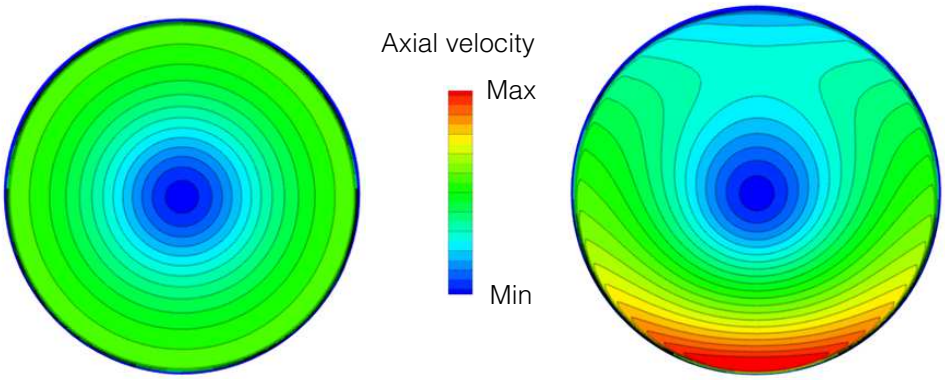

(a) Clean inflow (b) Distorted inflow

Figure 8: **Typical axial velocity contours for a clean and a distorted inflow**

The impact of distortion on fan noise started to be studied experimentally in the 1970s because significant differences in noise levels were measured between static and in-flight tests [18]. These differences were attributed to the ingestion of large-scale vortices by the fan which could be seen as a stationnary distortion. The studies have led to the use of a Turbulence Control Screen (TCS) in static tests to provide a clean inflow and remove the mentionned differences [19]. Since then, the studies about the impact of distortion on the noise have been put aside. They started again very recently, precisely because of the evolution of aircraft engine architectures. The complexity of the studies is increased step by step. Holewa *et al.* [20] studied the impact of the bifurcations (or pylon) on the fan tonal noise by means of a quasi-3D numerical simulation of a fan and an OGV with struts and bifurcations. They found that the noise generated by the DRI mechanism was negligible compared with the one generated by the WSI mechanism. However, they highlighted the influence of

the potential effects of the bifurcations on the latter. This last point was also studied by Bonneau *et al.* [21] and Roger & Caule [22] who explained the unexpected emergence of the first BPF harmonic by the invalidity of Tyler & Sofrin's rule [10] in the presence of an azimuthal heterogeneity. In contrast with the study of Holewa *et al.* [20], Oishi *et al.* [23] worked on a fan-OGV-bifurcation configuration in 3D and found that the DRI mechanism plays a major role on the fan tonal noise, but only for high subsonic and transonic regimes. The addition of an asymmetric air inlet was investigated by Sturm *et al.* [24] and Conte *et al.* [25] who evaluated the noise caused by an inflow distortion on low-speed fans thanks to analytical models and numerical simulations. In the fields of turbofan, Winkler *et al.* [26] and Doherty & Namgoong [27] used a numerical approach to predict the noise caused by an asymmetric air inlet. They were able to determine the far-field sound, but they could not draw any conclusion on its contribution to the fan tonal noise because the OGV was not included.

The objective of this PhD thesis is to evaluate the effects of the distortion in a modern turbofan engine including an heterogeneous OGV with struts and bifurcations and an inlet distortion typical of what will be encountered in UHBR engines. The contribution of the sources caused by the distortion will be evaluated and the influence of distortion on other noise source will be investigated.

Organization of the manuscript

The theoretical framework that is needed for this study is given in Chap. 1. The fan tonal noise is caused by the dynamics of the flow so its study lies in the field of aeroacoustics. The fundamental theories are presented and the distinction between the direct approach and the hybrid approach is made. In the direct approach, the generation and the propagation of the acoustic sources are dealt simultaneously, contrary to the hybrid approach where they are considered as two successive steps. Both approaches will be used in this thesis and some details on each method are given.

The numerical simulations that have been performed to study the effect of inlet distortion are then presented in Chap. 2. The choice of the engine model is driven by the necessity to account for all the sources of fan tonal noise: the ones classically accounted for and the ones linked to distortion that are generally neglected. The numerical setup is described and the convergence in terms of acoustics is evaluated. A basic flow analysis without inlet distortion is then realized to evaluate the main performances of the engine.

In Chap. 3, both the distortion caused by the potential effect of the pylon and the one linked to the air inlet asymmetry are studied. Its initial shape and its evolution along the engine duct is discussed. A quantification is also proposed to identify the regions of high distortion. The effects of the distortion on unsteady aerodynamics is then investigated, with a particular focus on the flow features that are at the origin of the different noise mechanisms.

The impact of the distortion on the acoustics is finally adressed in Chap. 4. The noise sources are first studied independently thanks to the use of hybrid methods. A classification based on this approach is proposed and the influence of inlet distortion on this breakdown is discussed. A direct noise analysis is also performed in order to provide a deeper understanding of the propagation of these sources.

Chapter 1

Methods for the prediction of fan tonal noise

Contents

1.1 Introduction

The methods for the prediction of fan tonal noise are presented in this chapter. Fundamental theories of aeroacoustics are first given in Sec. 1.2. The hybrid approach, in which the generation and the propagation of the sources are dealt separately, and the direct approach are distinguished. For each approach, the sound emitted by the

fan has to be quantified by an acoustic energy. Its formulation is defined in Sec. 1.3. Some details about direct noise predictions are then given in Sec. 1.4. The hybrid approach is finally introduced with the description of analytical models for source computation and for source propagation in Secs. 1.5 and 1.6 respectively.

1.2 Fundamentals of aeroacoustics

Aeroacoustics concerns the study of the sound generated by a flow and is therefore described by the equations of fluid dynamics which are first recalled. Some important theories of this field and the way they can be used for the prediction of fan tonal noise are then presented.

1.2.1 Equations in fluid dynamics

Under the continuum assumption, the fluid is described by the conservation equations. If t, ρ, $\boldsymbol{v}$, p, $\boldsymbol{\tau}$, $\boldsymbol{f}$, E and $\boldsymbol{q}$ stand respectively for the time, density, velocity vector, pressure, viscous stress tensor, body force vector, total energy and heat flux vector, they are written [28]

$$\frac{\partial \rho}{\partial t} + \boldsymbol{\nabla} \cdot (\rho \boldsymbol{v}) = 0, \tag{1.1a}$$

$$\frac{\partial (\rho \boldsymbol{v})}{\partial t} + \boldsymbol{\nabla} \cdot (\rho \boldsymbol{v} \otimes \boldsymbol{v} + p \boldsymbol{I} - \boldsymbol{\tau}) = \rho \boldsymbol{f}, \tag{1.1b}$$

$$\frac{\partial (\rho E)}{\partial t} + \boldsymbol{\nabla} \cdot (\rho E \boldsymbol{v} + p \boldsymbol{v} - \boldsymbol{\tau} \cdot \boldsymbol{v} + \boldsymbol{q}) = \rho \boldsymbol{f} \cdot \boldsymbol{v}, \tag{1.1c}$$

with $\boldsymbol{\nabla}$ the nabla operator, $\otimes$ the tensor product and $\boldsymbol{I}$ the identity tensor. Equations (1.1a), (1.1b) and (1.1c) are the mass, momentum and energy conservation equations respectively and are often referred to as Navier-Stokes equations. Source terms for mass production or heat addition are not included in this set of equations because they do not represent any physical phenomenon in the context of the study.

It might be useful for some applications to deal with the Navier-Stokes equations expressed in a different way. By defining the material derivative

$$\frac{D}{Dt} = \frac{\partial}{\partial t} + \boldsymbol{v} \cdot \boldsymbol{\nabla}, \tag{1.2}$$

the set of equations (1.1) reduce to

$$\frac{D\rho}{Dt} = -\rho \boldsymbol{\nabla} \cdot \boldsymbol{v}, \tag{1.3a}$$

$$\rho \frac{D\boldsymbol{v}}{Dt} = -\boldsymbol{\nabla} p + \boldsymbol{\nabla} \cdot \boldsymbol{\tau} + \rho \boldsymbol{f}, \tag{1.3b}$$

$$\rho T \frac{Ds}{Dt} = -\boldsymbol{\nabla} \cdot \boldsymbol{q} + \boldsymbol{\tau} : \boldsymbol{\nabla} \boldsymbol{v}. \tag{1.3c}$$

For a newtonian fluid and under the local thermodynamic equilibrium assumption, it is possible to write

$$d\rho = \frac{1}{a^2} dp + \left(\frac{\partial \rho}{\partial s}\right)_p ds, \tag{1.4}$$

where s is the entropy of the fluid and a^2 is defined by

$$a^2 = 1/\left(\frac{\partial \rho}{\partial p}\right)_s = \left(\frac{\partial p}{\partial \rho}\right)_s. \tag{1.5}$$

a^2 represents the square of the speed of sound. In some theories that are presented in this chapter, the flow is assumed to be isentropic ($ds = 0$) and the pressure and density fluctuations are therefore linked by

$$dp = a^2 d\rho. \tag{1.6}$$

If the gas is in addition an ideal gas, the relation

$$p/\rho^\gamma = \text{constant}, \tag{1.7}$$

is satisfied with γ the ratio of specific heats. The speed of sound can be shown to reduce to

$$a = \sqrt{\frac{\gamma p}{\rho}}. \tag{1.8}$$

Using the equation of state $p = \rho RT$ with R the specific gas constant yields

$$a = \sqrt{\gamma RT}. \tag{1.9}$$

The governing equations (1.1) or (1.3) dictate the behavior of the fluid and consequently the behavior of acoustic fluctuations. The most natural way to deal with aeroacoustics is therefore to solve them directly. This is the principle of direct methods which require the use of numerical simulations. This is referred to as Computational Fluid Dynamics (CFD) or Computational AeroAcoustics (CAA). Such simulations were not available and/or affordable in the past and alternative approaches emerged.

1.2.2 Lighthill's analogy

In order to face the complexity of Navier-Stokes equations (1.1), Lighthill proposed in 1952 an analogy which is the fundamental starting point of aeroacoustics [29]. He showed that these equations could be interpretated as a wave equation with a source term related to flow disturbances.

Derivation of Lighthill's equation

A fluctuating flow field occupying a limited part of a very large volume of fluid is considered. Outside of this part, the medium is assumed at rest and uniform with a speed of sound and a density written a_0 and ρ_0 respectively.

The propagation of sound in the uniform medium at rest, without sources or external forces, is a well-known classical acoustic problem which is governed by the homogeneous wave equation

$$\frac{\partial^2 \rho'}{\partial t^2} - a_0^2 \boldsymbol{\nabla}^2 \rho' = 0, \tag{1.10}$$

where $\rho' = \rho - \rho_0$ is the fluctuating density.

As for the fluctuating flow, the governing equations are given by Navier-Stokes equations (1.1) without body forces ($\boldsymbol{f} = \boldsymbol{0}$). Substracting the divergence of the momentum conservation equation (1.1b) from the time derivative of mass conservation equation (1.1a) yields

$$\frac{\partial^2 \rho}{\partial t^2} - \boldsymbol{\nabla}^2 p + \boldsymbol{\nabla} \cdot \boldsymbol{\nabla} \cdot \boldsymbol{\tau} = \boldsymbol{\nabla} \cdot \boldsymbol{\nabla} \cdot (\rho \boldsymbol{v} \otimes \boldsymbol{v}) \,. \tag{1.11}$$

Substracting each side of the equation by $a_0^2 \boldsymbol{\nabla}^2 \rho$ and rearranging the equation gives

$$\frac{\partial^2 \rho'}{\partial t^2} - a_0^2 \boldsymbol{\nabla}^2 \rho' = (\boldsymbol{\nabla} \otimes \boldsymbol{\nabla}) : \left[\rho \boldsymbol{v} \otimes \boldsymbol{v} - \boldsymbol{\tau} + (p - a_0^2 \rho) \boldsymbol{I} \right] . \tag{1.12}$$

Using Einstein's notation and defining the spatial coordinates $x_i \, (i = 1, 2, 3)$, this equation, known as Lighthill's equation, can be written

$$\frac{\partial^2 \rho'}{\partial t^2} - a_0^2 \frac{\partial^2 \rho'}{\partial x_i \partial x_i} = \frac{\partial^2 T_{ij}}{\partial x_i \partial x_j}, \tag{1.13}$$

where $\boldsymbol{T} = (T_{ij}) = (\rho v_i v_j - \tau_{ij} + (p - a_0^2 \rho) \delta_{ij})$ is Lighthill's tensor.

Interpretation of Lighthill's equation

Outside of the flow region, the term on the right-hand side of Lighthill's equation (1.13) vanishes and the latter is reduced to the homogeneous wave equation (1.10). At large distances from the turbulent region, the density fluctuations of the real flow then behave like acoustic waves in a uniform medium at rest. There is therefore an exact analogy between the density fluctuations that occur in a real flow and the ones that would result from a quadrupole source distribution of strength T_{ij} in a fictitious non-moving acoustic medium with sound speed a_0. It follows from this analogy that an aeroacoustic problem can be seen as a two-step procedure. The first step is the generation of acoustic sources by a fluctuating fluid in the region of flow. The second step is the propagation of these sources in the acoustic medium outside the region of flow (here considered at rest). An illustration of this analogy is given in Fig. 1.1.

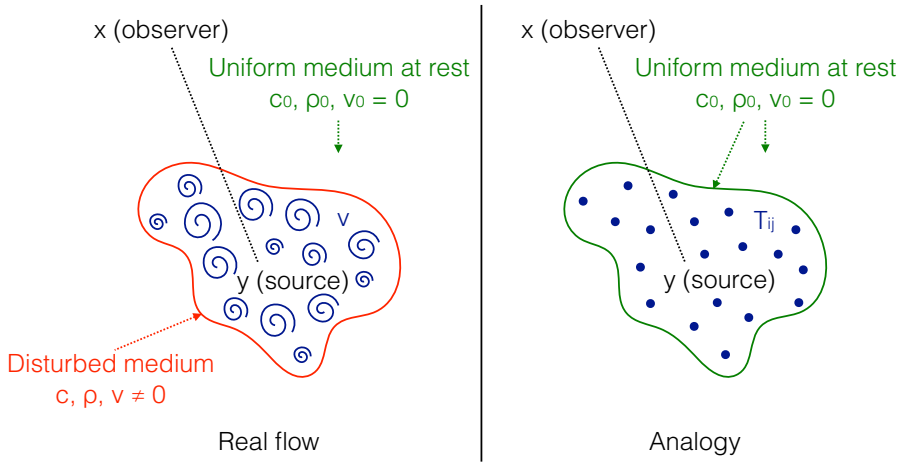

Figure 1.1: **Illustration of Lighthill's analogy**

Free field solution to Lighthill's equation

Lighthill's equation (1.13) can be solved using a generalized Green's function. The Green's function $G(\boldsymbol{y}, \tau|\boldsymbol{x}, t)$ is the solution to the wave equation where the source term is replaced by a point source in $\boldsymbol{y} = \boldsymbol{x}$ that sends a signal at time $\tau = t$. This function depends on the problem formulation and boundary conditions. In free field, it is written (for more details, see [8])

$$G(\boldsymbol{y}, \tau|\boldsymbol{x}, t) = \frac{1}{4\pi|\boldsymbol{x}-\boldsymbol{y}|}\delta(t - \tau - \frac{|\boldsymbol{x}-\boldsymbol{y}|}{a_0}), \tag{1.14}$$

where δ is the Dirac's distribution. The solution to the initial problem can then be expressed in terms of the Green's function

$$\rho'(\boldsymbol{x}, t) = \frac{1}{a_0^2}\int_{-\infty}^{+\infty}\iiint_{V(\tau)}\frac{\partial^2 T_{ij}}{\partial x_i \partial y_j}(\boldsymbol{y}, \tau)G(\boldsymbol{y}, \tau|\boldsymbol{x}, t)\, dV(\boldsymbol{y})d\tau, \tag{1.15}$$

which reduces to

$$\rho'(\boldsymbol{x}, t) = \frac{1}{4\pi a_0^2}\iiint_V \frac{1}{|\boldsymbol{x}-\boldsymbol{y}|}\frac{\partial^2 T_{ij}}{\partial x_i \partial y_j}(\boldsymbol{y}, t - \frac{|\boldsymbol{x}-\boldsymbol{y}|}{a_0})\, dV(\boldsymbol{y}). \tag{1.16}$$

Thus, provided that the source term T_{ij} is known, the acoustic density can be determined at any position and at any time. This is one of the main strengths of this analogy: the acoustic field can be derived everywhere thanks to an integral over the sources, without needing any numerical simulation in the domain.

1.2.3 Linearized theory

A different approach in aeroacoustics consists in linearizing the Navier-Stokes equations (1.3). It relies on the assumption that the magnitude of acoustic fluctuations is

much smaller than the aerodynamic one. Any flow variable can therefore be decomposed into a mean part (subscript 0) and a fluctuating part (prime symbol) much smaller than the mean part:

$$\rho = \rho_0 + \rho', \quad \rho' << \rho_0, \tag{1.17a}$$

$$\boldsymbol{v} = \boldsymbol{v_0} + \boldsymbol{v'}, \quad |\boldsymbol{v'}| << |\boldsymbol{v_0}|, \tag{1.17b}$$

$$p = p_0 + p', \quad p' << p_0, \tag{1.17c}$$

$$s = s_0 + s', \quad s' << s_0. \tag{1.17d}$$

In addition, the viscosity and heat conduction are assumed to have only a little influence on acoustic propagation and are therefore neglected ($\boldsymbol{\tau} = \boldsymbol{0}$ and $\boldsymbol{q} = \boldsymbol{0}$ in Eqs. (1.3) that become the Euler equations). By injecting the expressions (1.17) into Euler equations without body forces ($\boldsymbol{f} = \boldsymbol{0}$) and by neglecting second order terms, the following set of equations is obtained (see [8] for example for the details)

$$\frac{\partial \rho'}{\partial t} + \boldsymbol{v_0} \cdot \boldsymbol{\nabla} \rho' + \boldsymbol{v'} \cdot \boldsymbol{\nabla} \rho_0 + \rho_0 \boldsymbol{\nabla} \cdot \boldsymbol{v'} + \rho' \boldsymbol{\nabla} \cdot \boldsymbol{v_0} = 0, \tag{1.18a}$$

$$\rho_0 \left(\frac{\partial \boldsymbol{v'}}{\partial t} + \boldsymbol{v_0} \cdot \boldsymbol{\nabla} \boldsymbol{v'} + \boldsymbol{v'} \cdot \boldsymbol{\nabla} \boldsymbol{v_0} \right) + \rho' \boldsymbol{v_0} \cdot \boldsymbol{\nabla} \boldsymbol{v_0} = -\boldsymbol{\nabla} p', \tag{1.18b}$$

$$\frac{\partial s'}{\partial t} + \boldsymbol{v_0} \cdot \boldsymbol{\nabla} s' + \boldsymbol{v'} \cdot \boldsymbol{\nabla} s_0 = 0. \tag{1.18c}$$

These equations are referred to as the Linearized Euler Equations (LEE) and govern the propagation of fluctuations as long as they are some orders of magnitude smaller than the mean flow. By being linear, they are less difficult to solve than Navier-Stokes equations. In some particular flow conditions (uniform flow for example), it is possible to derive a wave equation that can be solved analytically [30]. In general configurations, a numerical simulation, less expensive than a classical CFD simulation, is needed. However, it should be kept in mind that these equations do not account for the dynamics of the flow and cannot predict the related sound sources. A prior knowledge of the acoustic sources that must be imposed on the boundaries is therefore required to solve the problem [31].

1.2.4 Chu & Kovasznay's analysis

Another approach that is similarly based on the decomposition of the flow variables into a mean part and a fluctuating part has been derived in 1957 by Chu & Kovasznay for a viscous heat-conducting compressible gas [32].

Decomposition of flow variables

To perform their analysis, Chu & Kovasznay have expanded the flow variables as power series in α (which is assumed to be small):

$$\rho = \rho_0 + \rho^{(1)} + \rho^{(2)} + ..., \tag{1.19a}$$

$$\boldsymbol{v} = \boldsymbol{v_0} + \boldsymbol{v^{(1)}} + \boldsymbol{v^{(2)}} + ..., \tag{1.19b}$$

$$p = p_0 + p^{(1)} + p^{(2)} + ..., \tag{1.19c}$$

$$s = s_0 + s^{(1)} + s^{(2)} + ..., \tag{1.19d}$$

where ρ_0, $\boldsymbol{v_0}$, p_0, s_0 are spatially and temporally averaged values and $\rho^{(n)}$, $\boldsymbol{v^{(n)}}$, $p^{(n)}$, $s^{(n)}$ are of order α^n. This is however questionable as the fluctuations of pressure and velocity have very different magnitude in a real fluid. The coordinate system is chosen to move with the mean flow such that $\boldsymbol{v_0} = \boldsymbol{0}$.

For convenience, the non-dimensional pressure and entropy are used:

$$P^{(n)} = \frac{p^{(n)}}{\gamma p_0}, \tag{1.20a}$$

$$S^{(n)} = \frac{s^{(n)}}{C_p}, \tag{1.20b}$$

with C_p the specific heat at constant pressure. The dynamic viscosity of the undisturbed medium is written μ_0 and $\nu_0 = \mu_0/\rho_0$ is the kinematic viscosity. The speed of sound is given by $a_0 = \sqrt{\gamma p_0/\rho_0}$ and the Prandtl number $Pr = \mu_0 C_p/K_T$ where K_T is the thermal conductivity of the fluid is assumed to be equal to 3/4 (for simplifying the algebra).

Identification of the three modes of fluctuations

When neglecting terms of order α^2 and higher powers of α, the governing equations of first-order fluctuations are obtained (see [32] for more details)

$$\boldsymbol{\nabla} \cdot \boldsymbol{v^{(1)}} + \frac{\partial P^{(1)}}{\partial t} - \frac{\partial S^{(1)}}{\partial t} = \frac{m}{\rho_0}, \tag{1.21a}$$

$$\frac{\partial \boldsymbol{v^{(1)}}}{\partial t} + a_0^2 \boldsymbol{\nabla} P^{(1)} - \nu_0^2 \boldsymbol{\nabla}^2 \boldsymbol{v^{(1)}} - \frac{1}{3}\nu_0 \boldsymbol{\nabla}(\boldsymbol{\nabla} \cdot \boldsymbol{v^{(1)}}) = \boldsymbol{f}, \tag{1.21b}$$

$$\frac{\partial S^{(1)}}{\partial t} - \frac{4}{3}\nu_0 \boldsymbol{\nabla} S^{(1)} - \frac{4}{3}(\gamma - 1)\nu_0 \boldsymbol{\nabla}^2 P^{(1)} = \frac{Q}{\rho_0 C_p T_0}. \tag{1.21c}$$

m represents the rate of mass production and Q the rate of heat addition per unit volume. From now, the superscript (1) is suppressed for clarity. Two new kinematic

variables are introduced, the vorticity $\boldsymbol{\omega}$ and the specific dilatation rate q

$$\boldsymbol{\omega} = \boldsymbol{\nabla} \times \boldsymbol{v}, \tag{1.22a}$$

$$q = \boldsymbol{\nabla} \cdot \boldsymbol{v}. \tag{1.22b}$$

The flow variables are written in the form

$$\boldsymbol{\omega} = \boldsymbol{\omega_\omega} + \boldsymbol{\omega_p} + \boldsymbol{\omega_s}, \tag{1.23a}$$

$$q = q_\omega + q_p + q_s, \tag{1.23b}$$

$$P = P_\omega + P_p + P_s, \tag{1.23c}$$

$$S = S_\omega + S_p + S_s, \tag{1.23d}$$

$$\boldsymbol{v} = \boldsymbol{v_\omega} + \boldsymbol{v_p} + \boldsymbol{v_s}. \tag{1.23e}$$

A few manipulations of the above equations can conveniently lead to three subsystems of equations as follows (details in [32]). The first set of equations is written, by choosing to denote the related variable by ω

$$\frac{\partial \boldsymbol{\omega_\omega}}{\partial t} - \nu_0 \boldsymbol{\nabla}^2 \boldsymbol{\omega_\omega} = \boldsymbol{\nabla} \times \boldsymbol{f}, \tag{1.24a}$$

$$P_\omega = 0, \quad S_\omega = 0, \quad q_\omega = 0, \tag{1.24b}$$

$$\boldsymbol{\nabla} \times \boldsymbol{v_\omega} = \boldsymbol{\omega_\omega}, \quad \boldsymbol{\nabla} \cdot \boldsymbol{v_\omega} = 0. \tag{1.24c}$$

Those equations are identical with the ones describing the production, convection and dissipation of weak vorticity in a viscous incompressible medium. The associated mode will therefore be called the vorticity mode. A flow satisfying these equations does not generate pressure or entropy fluctuations.

The second set of equations is written with the variables denoted by p and gives

$$\boldsymbol{\omega_p} = \boldsymbol{0}, \tag{1.25a}$$

$$\begin{aligned} \frac{\partial^2 P_p}{\partial t^2} - a_0^2 \boldsymbol{\nabla}^2 P_p - \frac{4}{3}\gamma\nu_0 \frac{\partial}{\partial t}\boldsymbol{\nabla}^2 P_p = \left(\frac{\partial}{\partial t} - \frac{4}{3}\nu_0\boldsymbol{\nabla}^2\right)\frac{m}{\rho_0} \\ - \boldsymbol{\nabla}\cdot\boldsymbol{f} + \frac{\partial}{\partial t}\frac{Q}{\rho_0 C_p T_0}, \end{aligned} \tag{1.25b}$$

$$\frac{\partial S_p}{\partial t} - \frac{4}{3}\nu_0 \boldsymbol{\nabla}^2 S_p = \frac{4}{3}(\gamma - 1)\nu_0 \boldsymbol{\nabla}^2 P_p, \tag{1.25c}$$

$$q_p = -\frac{\partial P_p}{\partial t} + \frac{\partial S_p}{\partial t} + \frac{m}{\rho_0}, \tag{1.25d}$$

$$\boldsymbol{\nabla} \times \boldsymbol{v_p} = \boldsymbol{0}, \quad \boldsymbol{\nabla} \cdot \boldsymbol{v_p} = q_p. \tag{1.25e}$$

This set of equation is similar to the one describing the production, propagation and dissipation of pressure waves in a viscous compressible heat-conductive medium and will therefore represent the sound mode. The associated velocity field is irrotational.

The third and final set of equations, written with the variables denoted by s, is given by

$$\boldsymbol{\omega_s} = \mathbf{0}, \quad P_s = 0, \tag{1.26a}$$

$$\frac{\partial S_s}{\partial t} - \frac{4}{3}\nu_0 \boldsymbol{\nabla}^2 S_s = \frac{Q}{\rho_0 C_p T_0}, \tag{1.26b}$$

$$q_s = \frac{\partial S_s}{\partial t}, \tag{1.26c}$$

$$\boldsymbol{\nabla} \times \boldsymbol{v_s} = \mathbf{0}, \quad \boldsymbol{\nabla} \cdot \boldsymbol{v_s} = q_s. \tag{1.26d}$$

The equations are the same as the ones describing the production, convection and diffusion of hot spots in a heat-conducting fluid medium and will consequently be associated with the entropy mode. Such a flow does not generate pressure fluctuations and the resulting velocity field is irrotational.

Of course, other ways of splitting Eqs. (1.21) exist but Chu & Kovasznay chose this one to reduce to the three basic modes of fluctuations that are familiar in fluid mechanics. These modes are all present in a fluctuating flow and the solution of Eqs. (1.21) can always be seen as a superposition of them. However, not all the modes will be significant in a particular problem. Chu & Kovasznay also explained that in the absence of solid boundaries, the three modes evolve as though the others were absent and can be solved independently.

Interaction between the three modes of fluctuations

By decomposing the variables up to second order terms, Chu & Kovasznay explained the interaction between the three modes as a result of the non-linearity of Navier-Stokes equations. For example, the sound field (sound mode) is resulting from four types of interaction: the sound-sound, the vorticity-vorticity, the sound-vorticity and the sound-entropy interactions. The vorticity-vorticity interaction is responsible for the generation of sound mode, as it was explained by Lighthill's analogy. The three other interactions are responsible for scattering effects [32].

1.2.5 Application to the prediction of fan tonal noise

The fundamental theories presented above allow to face an aeroacoustic problem in different ways. The first and most natural way is the direct approach. It consists in solving the Navier-Stokes equations which govern both the fluid dynamics and the acoustics. However, the resolution of these equations cannot be done analytically (except in some canonical cases) and numerical simulations are used in practice. The other way is the hybrid approach, based on Lighthill's analogy. The fluctuating flow

is responsible for equivalent sources that are computed in a first step and propagated in a second step.

Direct approach

The direct approach consists in solving directly both flow and sound fields thanks to a CFD simulation [33]. Because no particular assumption is made, this approach should be ideal. However, it requires huge computational ressources. The simulation is necessarily compressible to allow the presence of acoustic waves and it must be of "acoustic quality" i.e. it must capture the small acoustic fluctuations (1 Pa is equivalent to 94 dB) and the errors related to the discretization must be handled correctly. Its use is therefore still limited. In most applications, either the turbulence is (at least partially) modeled or the geometry is simplified.

Aside from the computational ressources that are needed, the other challenge in using a direct approach is the analysis of the computed fluctuations. As shown by Chu & Kovasznay [32], the fluctuations can be decomposed into three modes: the vorticity, the sound and the entropy modes. The fluctuations that would result from a CFD simulation will consequently be composed of those three modes, and the isolation of the sound one (in which we are interested in) is not obvious. In a fan module (cold stream), the temperature fluctuations are very small so that the entropy mode is generally neglected. However, the vorticity mode will be significant, essentially in the fan-blade and OGV wakes. Therefore, the real challenge will be to separate the vorticity and the sound modes [21, 34]. The direct approach will be applied in the present study to provide noise predictions without any important assumptions.

Hybrid approach

In an hybrid approach, the computation of the sources and their propagation are dealt separately. A minimum knowledge about the noise mechanisms is required because the sources must be isolated. A lot of different methods exist for the source computation and for the sound propagation and are very dependent on the application. Concerning fan tonal noise, the main noise mechanisms have been listed in the introduction. In subsonic regimes, the noise is linked to interaction phenomena: interaction of fan-blade wakes with OGV and interaction of distortion with fan blades. As it was mentionned, these mechanisms are responsible for unsteady loadings on OGV and fan blades respectively. These unsteady loadings are considered as the equivalent sources that need to be computed and then propagated [35, 21]. In transonic regimes, the steady loading noise and the shock noise appear. The steady loading can also be considered as an equivalent source on the surface of fan blades. As for the shock noise, its localization is not evident and its study is not dealt with hybrid approaches usually.

The computation of the equivalent sources are first discussed. The interaction of fan-blade wakes with the OGV is taken here as a representative example. The wakes impact periodically the different vanes, thus creating unsteady loadings on the lat-

ter. These unsteady loadings are the equivalent sources and can be computed either numerically or analytically. If done numerically, unsteady Navier-Stokes equations must be simulated similarly to the direct approach, except that the simulation does not need to be compressible nor of "acoustic quality". The equivalent sources are indeed caused by aerodynamics only and there is no need to propagate acoustic waves in the simulation. Such a simulation is therefore less expensive than the one needed for a direct acoustic prediction. But the sources can also be computed analytically, thanks to a response model. This kind of models usually decompose the excitation (here the wake) into elementary gusts and determine the resulting loading variations under assumptions on the geometry of the vanes and on the flow [17].

As for the propagation of the equivalent sources, different methods exist again. It can be done by solving the LEE to account for the most complex geometries and flow conditions. Such a simulation is far less expensive than a classical CFD simulation but still requires computational ressources [36, 37]. The other way is the use of a Green's function, as shown in subsection 1.2.2. Assumptions are often made on the geometry and flow conditions to get a wave equation that can be solved thanks to a Green's function. In most cases, the resulting Green's function is determined analytically but it can require sometimes a numerical solving [38].

The hybrid approach will also be used in this work to increase the understanding of the impact of distortion on fan tonal noise. The equivalent sources on fan blades, OGVs and even IGVs will be extracted and will be propagated thanks to analytical models. In the interest of going deeper in the analysis of the noise mechanisms, these sources will also be computed analytically by extracting the excitations (wakes, distortion) from the simulations and by applying a response model.

Summary of the section

Aeroacoustics is the study of the sound generated by the flow and is fully described by Navier-Stokes equations. These equations do not have an explicit solution for complex configurations and CFD simulations must be used. These simulations allow for a direct evaluation of the noise but require huge ressources because they have to be able to capture the acoustic fluctuations which are very small compared to aerodynamic values. Lighthill introduced an analogy which allows to deal with aeroacoustics in a different way. He showed that Navier-Stokes equations could be written in the form of a wave equation, with a source term depending on the aerodynamics. Thus, any aeroacoustic problem could be interpretated into two successive steps: the first step is the generation of the sources (aerodynamics) and the second one is the propagation of these sources (acoustics). The methods based on this principle are referred to as hybrid methods. The sources can be determined by a CFD simulation but analytical models also exist for simple configurations. Concerning the propagation, it can be handled either numerically, by solving the LEE for example, or analytically (in general) with the use of a Green's function. In

any case, it is less expensive than performing a complete CFD simulation but it introduces some assumptions. In this study, CFD simulations will be performed and both direct and hybrid acoustic predictions will be done in order to deliver a deep analysis of the noise mechanisms.

1.3 Acoustic energy

The quantification of the noise caused by acoustic fluctuations is done by the acoustic energy. The latter is known to be simply the product of pressure and velocity fluctuations outside of the flow region but more becomes more complex inside the flow (typically in an engine). Its formulation is given in this section.

1.3.1 Acoustic energy in a stagnant uniform fluid

Historically, an acoustic energy conservation law for stagnant uniform fluid has been first derived by Kirchhoff, but with an *ad hoc* procedure [39]. Myers has then proposed a more rigorous way of deriving this energy conservation law and has obtained the same result [40]. Both methods are presented in this section.

Derivation from the linearized conservation equations

Kirchhoff has proposed to start from the linearized conservation equations [39]. The fluid is assumed to be inviscid ($\boldsymbol{\tau} = 0$) and non-conducting ($\boldsymbol{q} = 0$). Using Eqs. (1.18) and adding the body force term $\boldsymbol{f} = \boldsymbol{f_0} + \boldsymbol{f'}$ yields

$$\frac{\partial \rho'}{\partial t} + \boldsymbol{v_0} \cdot \boldsymbol{\nabla} \rho' + \boldsymbol{v'} \cdot \boldsymbol{\nabla} \rho_0 + \rho_0 \boldsymbol{\nabla} \cdot \boldsymbol{v'} + \rho' \boldsymbol{\nabla} \cdot \boldsymbol{v_0} = 0, \tag{1.27a}$$

$$\rho_0 \left(\frac{\partial \boldsymbol{v'}}{\partial t} + \boldsymbol{v_0} \cdot \boldsymbol{\nabla} \boldsymbol{v'} + \boldsymbol{v'} \cdot \boldsymbol{\nabla} \boldsymbol{v_0} \right) + \rho' \boldsymbol{v_0} \cdot \boldsymbol{\nabla} \boldsymbol{v_0} = -\boldsymbol{\nabla} p' + \rho_0 \boldsymbol{f'} + \rho' \boldsymbol{f_0}, \tag{1.27b}$$

where the subscript 0 denotes the mean part and the prime symbol the fluctuating part of the flow variables. The mean flow is additionally assumed to be quiescent and uniform. As a consequence, there is no mean source ($\boldsymbol{f_0} = \boldsymbol{0}$) and the equations reduce to

$$\frac{\partial \rho'}{\partial t} + \rho_0 \boldsymbol{\nabla} \cdot \boldsymbol{v'} = 0, \tag{1.28a}$$

$$\rho_0 \frac{\partial \boldsymbol{v'}}{\partial t} + \boldsymbol{\nabla} p' = \rho_0 \boldsymbol{f'}. \tag{1.28b}$$

The homentropic assumption ($ds = 0$) implies that Eq. (1.6) is valid and gives

$$p' = a_0^2 \rho' \tag{1.29}$$

Multiplying Eq. (1.28a) by p'/ρ_0 and Eq. (1.28b) by $\boldsymbol{v'}$, adding the two equations and expressing density fluctuations in terms of pressure ones using Eq. (1.29) yields

$$\frac{1}{2\rho_0 a_0^2}\frac{\partial p'^2}{\partial t} + \frac{1}{2}\rho_0 \frac{\partial v'^2}{\partial t} + \boldsymbol{\nabla}\cdot(\rho'\boldsymbol{v'}) = \rho_0 \boldsymbol{f'}\cdot\boldsymbol{v'}, \tag{1.30}$$

with $v'^2 = |\boldsymbol{v'}|^2$. This equation can be written in the form

$$\frac{\partial E}{\partial t} + \boldsymbol{\nabla}\cdot\boldsymbol{I} = -D, \tag{1.31}$$

where E, $\boldsymbol{I}$ and D are given by

$$E = \frac{p'^2}{2\rho_0 a_0^2} + \frac{\rho_0 v'^2}{2}, \tag{1.32a}$$

$$\boldsymbol{I} = p'\boldsymbol{v'}, \tag{1.32b}$$

$$D = -\rho_0 \boldsymbol{f'}\cdot\boldsymbol{v'}. \tag{1.32c}$$

and are defined as the acoustic energy density, flux and dissipation respectively. Theses definitions have been derived from the linearized conservation equations and cannot therefore account for the non-linearities of the flow. They all are a combination of products of two first order terms and are consequently second order terms. The use of the linearization (thus eliminating second order terms in the governing equations) to obtain a result which is a second order term is not a rigorous procedure. Indeed, nothing can ensure that no other second order term may not be included in the above expressions. This is why another approach, inspired by the work of Myers [40] is developed in the next subsection.

Derivation from the real conservation equations

The starting point of this approach is the original equation of energy conservation in its non-linear form (1.1c), without friction ($\boldsymbol{\tau} = \boldsymbol{0}$) nor heat conduction ($\boldsymbol{q} = \boldsymbol{0}$). It can be written

$$\frac{\partial E_{tot}}{\partial t} + \boldsymbol{\nabla}\cdot\boldsymbol{I_{tot}} = -D_{tot}, \tag{1.33}$$

where E_{tot}, $\boldsymbol{I_{tot}}$ and D_{tot} are the total fluid energy density, flux and dissipation respectively and are given by

$$E_{tot} = \rho E = \rho e + \frac{1}{2}\rho v^2, \tag{1.34a}$$

$$\boldsymbol{I_{tot}} = \rho E\boldsymbol{v} + p\boldsymbol{v} = \rho e\boldsymbol{v} + \frac{1}{2}\rho v^2\boldsymbol{v} + p\boldsymbol{v}, \tag{1.34b}$$

$$D_{tot} = -\rho \boldsymbol{f}\cdot\boldsymbol{v}. \tag{1.34c}$$

e is the internal energy of the fluid and $v^2 = |\boldsymbol{v}|^2$. The goal is now to expand the quantities (1.34a), (1.34b) and (1.34c) up to second order. Same decomposition as the one shown in Eq. (1.17) is done. With $\boldsymbol{v_0} = \boldsymbol{0}$ and $\boldsymbol{f_0} = \boldsymbol{0}$ (quiescent and uniform fluid), it is straightforward to show that, up to second order,

$$\frac{1}{2}\rho v^2 = \frac{1}{2}\rho_0 v'^2, \tag{1.35a}$$

$$p\boldsymbol{v} = (p_0 + p')\boldsymbol{v'}, \tag{1.35b}$$

$$\rho\boldsymbol{f}\cdot\boldsymbol{v} = \rho_0\boldsymbol{f'}\cdot\boldsymbol{v'}. \tag{1.35c}$$

The decomposition of the term ρe is done by expanding it as power series in ρ'

$$\rho e = \rho_0 e_0 + \left(\frac{\partial \rho e}{\partial \rho}\right)_s\bigg|_0 \rho' + \left(\frac{\partial^2 \rho e}{\partial \rho^2}\right)_s\bigg|_0 \frac{\rho'^2}{2} + \dots . \tag{1.36}$$

The fundamental law of thermodynamics

$$T\,ds = de + p\,d(\rho^{-1}), \tag{1.37}$$

yields, for isentropic perturbations,

$$\left(\frac{\partial e}{\partial \rho}\right)_s = \frac{p}{\rho^2}. \tag{1.38}$$

Thus, the derivatives of ρe become, with h the enthalpy and the use of Eq. (1.5),

$$\left(\frac{\partial \rho e}{\partial \rho}\right)_s = e + \frac{p}{\rho} = h, \quad \left(\frac{\partial^2 \rho e}{\partial \rho^2}\right)_s = \frac{a^2}{\rho}. \tag{1.39a}$$

It follows that

$$\rho e = \rho_0 e_0 + h_0\rho' + \frac{a_0^2}{2\rho_0}\rho'^2 + \dots . \tag{1.40}$$

Therefore, the quantities (1.34a), (1.34b) and (1.34c) become up to second order

$$E_{tot} = \rho_0 e_0 + h_0\rho' + \frac{a_0^2}{2\rho_0}\rho'^2 + \frac{1}{2}\rho_0 v'^2, \tag{1.41a}$$

$$\boldsymbol{I_{tot}} = (h_0\rho_0 + h_0\rho' + p')\boldsymbol{v'}, \tag{1.41b}$$

$$D_{tot} = -\rho_0\boldsymbol{f'}\cdot\boldsymbol{v'}. \tag{1.41c}$$

With the use of the continuity equation (1.1a) and noting that the steady state is constant, it can be shown that the zeroth and first order terms of energy conservation (1.33) vanish, which gives

$$\frac{\partial}{\partial t}\left(\frac{p'^2}{2\rho_0 a_0^2} + \frac{\rho_0 v'^2}{2}\right) + \boldsymbol{\nabla}\cdot(p'\boldsymbol{v'}) = \rho_0\boldsymbol{f'}\cdot\boldsymbol{v'}. \tag{1.42}$$

The same acoustic energy density E, flux $\boldsymbol{I}$ and dissipation D as the ones derived by Kirchhoff are obtained

$$E = \frac{p'^2}{2\rho_0 a_0^2} + \frac{\rho_0 v'^2}{2}, \tag{1.43a}$$

$$\boldsymbol{I} = p'\boldsymbol{v'}, \tag{1.43b}$$

$$D = -\rho_0 \boldsymbol{f'} \cdot \boldsymbol{v'}. \tag{1.43c}$$

The procedure followed here is a proof that the expression obtained by Kirchhoff is the consistent approximation of the energy equation of the real flow and not only an energy-like equation of the approximate flow.

1.3.2 Acoustic energy in a homentropic non-uniform fluid

Myers developed a more general acoustic conservation law with the same approach as the one described above but considering a homentropic non-uniform flow [40]. The total enthalpy $H = e + p/\rho + v^2/2$ is introduced into energy conservation law (1.1c) for convenience. Without friction ($\boldsymbol{\tau} = \boldsymbol{0}$) nor heat conduction ($\boldsymbol{q} = \boldsymbol{0}$), it is therefore written

$$\frac{\partial}{\partial t}(\rho H - p) + \boldsymbol{\nabla} \cdot (\rho H \boldsymbol{v}) = \rho \boldsymbol{f} \cdot \boldsymbol{v}. \tag{1.44}$$

With the use of the continuity (1.1a) and the momentum (1.1b) equations and noting that the steady state is constant, Myers obtained an exact energy corollary (details in [40])

$$\frac{\partial E_{exact}}{\partial t} + \boldsymbol{\nabla} \cdot \boldsymbol{I_{exact}} = -D_{exact}, \tag{1.45}$$

where E_{exact}, $\boldsymbol{I_{exact}}$ and D_{exact} are given by

$$E_{exact} = \rho(H - H_0) - (p - p_0) - \rho_0 \boldsymbol{v_0} \cdot (\boldsymbol{v} - \boldsymbol{v_0}), \tag{1.46a}$$

$$\boldsymbol{I_{exact}} = (H - H_0)(\rho \boldsymbol{v} - \rho_0 \boldsymbol{v_0}), \tag{1.46b}$$

$$\begin{aligned} D_{exact} = {} & (\rho \boldsymbol{v} - \rho_0 \boldsymbol{v_0}) \cdot (\boldsymbol{\omega} \times \boldsymbol{v} - \boldsymbol{\omega_0} \times \boldsymbol{v_0}) - (\rho \boldsymbol{f} - \rho_0 \boldsymbol{f_0}) \cdot (\boldsymbol{v} - \boldsymbol{v_0}) \\ & -(\rho - \rho_0)\boldsymbol{f} \cdot \boldsymbol{v_0} - (\rho_0 - \rho)\boldsymbol{f_0} \cdot \boldsymbol{v}. \end{aligned} \tag{1.46c}$$

$\boldsymbol{\omega} = \boldsymbol{\nabla} \times \boldsymbol{v}$ is the vorticity and the subscript 0 stands for mean values. The resulting terms (1.46) are exact under the homentropic assumption and have the important property of being composed only of quadratic terms when expanded to acoustic perturbation (the zeroth and first order terms vanish similarly to the uniform case). Therefore, their expansion to second order yields a general definition of acoustic

energy density, flux and dissipation

$$E = \frac{p'^2}{2\rho_0 a_0^2} + \frac{\rho_0 v'^2}{2} + \rho' \boldsymbol{v_0} \cdot \boldsymbol{v'}, \tag{1.47a}$$

$$\boldsymbol{I} = \left(\frac{p'}{\rho_0} + \boldsymbol{v_0} \cdot \boldsymbol{v'} \right) (\rho_0 \boldsymbol{v'} + \rho' \boldsymbol{v_0}), \tag{1.47b}$$

$$D = -\rho_0 \boldsymbol{v_0} \cdot (\boldsymbol{\omega'} \times \boldsymbol{v'}) - \rho' \boldsymbol{v'} \cdot (\boldsymbol{\omega_0} \times \boldsymbol{v_0}) - (\rho_0 \boldsymbol{f'} - \rho' \boldsymbol{f_0}) \cdot (\boldsymbol{v'} + \rho' \boldsymbol{v_0}/\rho_0), \tag{1.47c}$$

where the prime symbol denotes the fluctuating quantities. These expressions have been obtained earlier by Cantrell & Hart [41] and are consequently often referred to as Cantrell & Hart's acoustic energy density, flux and dissipation. By its procedure, Myers brought out a clear physical interpretation of those quantities and has shown that they were exact in a general homentropic flow. It is worth to note that the vorticity has been treated as non-acoustic because it has been gathered in the dissipation term. Of course, these expressions reduce to the ones obtained with the uniform flow assumption (1.43) when taking $\boldsymbol{v_0} = \boldsymbol{0}$.

1.3.3 Notion of acoustic power

General definition

The acoustic energy density E, flux $\boldsymbol{I}$ and dissipation D have been defined above by deriving an acoustic conservation law of the form

$$\frac{\partial E}{\partial t} + \boldsymbol{\nabla} \cdot \boldsymbol{I} = -D. \tag{1.48}$$

Integrating this conservation law (1.48) over a fixed volume V enclosed by the surface S with outer normal vector $\boldsymbol{n}$ and using Gauss's theorem gives

$$\frac{d}{dt} \iiint_V E \, dV + \iint_S \boldsymbol{I} \cdot \boldsymbol{n} \, dS = - \iiint_V D \, dV. \tag{1.49}$$

Considering a periodic acoustic field and averaging Eq. (1.49) over a period yields the definition of the acoustic power P across the surface S

$$P = \iint_S \overline{\boldsymbol{I} \cdot \boldsymbol{n}} \, dS = - \iiint_V \overline{D} \, dV. \tag{1.50}$$

Acoustic power is a very useful quantity to characterize the sound emitted by some sources because it is conserved as soon as the surface S encloses them (the terms in the volume integral will be zero outside the region of sources). In practice, it is more convenient to store data on surfaces rather than volumes and the determination of the acoustic power is done by performing the surface integral of the projected acoustic energy flux.

In this study, the noise will be evaluated in the duct engine only. The surfaces that will be chosen for the evaluation of the acoustic power will therefore be perpendicular to the duct axis. If the duct is along the x-direction (of unit vector $\boldsymbol{e_x}$), the acoustic power will be expressed as

$$P^{\pm} = \mp \iint_S \overline{I_x}\, dS, \tag{1.51}$$

where the upper sign and the lower sign denote the cases where the surface is upstream ($\boldsymbol{n} = -\boldsymbol{e_x}$) and downstream the sources ($\boldsymbol{n} = \boldsymbol{e_x}$) respectively. I_x is the acoustic energy flux along the x-axis.

Stagnant uniform fluid

If the axial component of velocity disturbances is written u', it can be shown from Eq. (1.43b) that, for a stagnant uniform fluid, I_x is given by

$$I_x = p'u'. \tag{1.52}$$

Homentropic non-uniform fluid

Writing the mean velocity $\boldsymbol{v_0} = (U_0, V_0, W_0)$ and the velocity disturbances $\boldsymbol{v'} = (u', v', w')$ and using Eq. (1.47b) yields the expressions of I_x for homentropic non-uniform fluid

$$I_x = \left(\frac{p'}{\rho_0} + U_0 u' + V_0 v' + W_0 w'\right)(\rho_0 u' + \rho' U_0)\,. \tag{1.53}$$

Frequential formulation

Being interesting in fan tonal noise, it would be of great interest to be able to evaluate the contribution of each tone to the total acoustic power. This is the purpose of this section. A useful property of periodic cross-correlation function will be needed in the following derivations and is introduced here. The cross-correlation function

$$\overline{f_1^*(t) f_2(t+\tau)} = \frac{1}{T}\int_0^T f_1^*(t) f_2(t+\tau)\, dt, \tag{1.54}$$

of two any periodic functions f_1 and f_2 (period T, associated pulsation $\omega = 2\pi/T$) satifies the relation

$$\overline{f_1^*(t) f_2(t+\tau)} = \sum_{s=-\infty}^{+\infty} f_{1s}^* f_{2s} e^{-is\omega\tau}. \tag{1.55}$$

f_{1s} and f_{2s} are the Fourier components of the functions f_1 and f_2 respectively

$$f_1(t) = \sum_{s=-\infty}^{+\infty} f_{1s} e^{-is\omega t}, \tag{1.56a}$$

$$f_2(t) = \sum_{s=-\infty}^{+\infty} f_{2s} e^{-is\omega t}, \tag{1.56b}$$

$$f_{1s} = \frac{1}{T} \int_0^T f_1(t) e^{is\omega t}, \tag{1.56c}$$

$$f_{2s} = \frac{1}{T} \int_0^T f_2(t) e^{is\omega t}. \tag{1.56d}$$

Stagnant uniform fluid

If p_s and u_s are the s^{th} harmonic of pressure and axial velocity disturbances respectively, the use of Eqs. (1.52) and (1.55) (with $f_1 = u'$, $f_2 = p'$ and $\tau = 0$) gives

$$\overline{I_x} = \sum_{s=-\infty}^{+\infty} p_s u_s^*. \tag{1.57}$$

The quantity $\overline{I_{xs}} = p_s u_s^*$ is introduced so that

$$\overline{I_x} = \sum_{s=-\infty}^{+\infty} \overline{I_{xs}}. \tag{1.58}$$

$\overline{I_{xs}}$ can be interpretated as the average axial acoustic energy flux carried by the s^{th} harmonic of the sound field and is therefore called the intensity spectrum. Eq. (1.55) (with $f_1 = u' = u'^*$ and $f_2 = p'$) shows that it is the s^{th} harmonic of the cross-correlation function

$$\Gamma(\tau) = \overline{p'(t+\tau)u'(t)} = \sum_{s=-\infty}^{+\infty} \overline{I_{xs}} e^{-is\omega\tau}. \tag{1.59}$$

The above considerations lead to the definition of the acoustic power $P_s^{\pm}$ carried by the s^{th} harmonic

$$P_s^{\pm} = \mp 2 \iint_S \overline{I_{xs}}\, dS, \tag{1.60}$$

where the upper sign and the lower sign denote again the cases where the surface is upstream and downstream the sources respectively. The factor 2 arises because both $\overline{I_{xs}}$ and $\overline{I_{x(-s)}}$ contribute to the power in the s^{th} harmonic.

Homentropic non-uniform fluid

Similar procedure can be done with the axial acoustic energy flux given by Eq. (1.53) in a general homentropic non-uniform fluid. Using the relation (1.29), defining the

Mach number components $M_{x0} = U_0/a_0$, $M_{y0} = V_0/a_0$, $M_{z0} = W_0/a_0$ and writting ρ_s, u_s, v_s and w_s the s^{th} harmonic of density and velocity disturbances along the x, y and z-axis respectively, the intensity spectrum $\overline{I_{xs}}$ reduces to

$$\begin{aligned}\overline{I_{xs}} = \left(1 + M_{x0}^2\right) p_s u_s^* + \frac{M_{x0}}{\rho_0 a_0} |p_s|^2 + \rho_0 M_{x0} a_0 |u_s|^2 \\ + M_{x0} M_{y0}\, p_s v_s^* + M_{x0} M_{z0}\, p_s w_s^* \\ + \rho_0 M_{y0} a_0\, u_s v_s^* + \rho_0 M_{z0} a_0\, u_s w_s^*. \quad (1.61)\end{aligned}$$

The formulation becomes clearly identical with the one obtained for stagnant uniform fluid when $M_{x0} = M_{y0} = M_{z0} = 0$. Similarly to the previous case, the acoustic power P_s carried by the s^{th} harmonic is determined from $\overline{I_{xs}}$ by

$$P_s^{\pm} = \mp 2 \iint_S \overline{I_{xs}}\, dS. \quad (1.62)$$

Summary of the section

The concept of acoustic energy has been introduced. In a stagnant uniform fluid, an acoustic conservation law has been derived and the resulting acoustic energy flux was shown to be simply given by the product of pressure and velocity fluctuations. The integral of this flux over a closed surface is the acoustic power and remains constant as soon as the surface encloses the sources. It is therefore a very useful measure to quantify the sound radiated by a source which is independent of the position contrary to the Sound Pressure Level (SPL). A more complex expression of this flux in a general non-uniform homentropic flow has been derived by Cantrell & Hart and Myers proposed an exact energy corollary which gives a clear interpretation of the resulting quantities. This flux is again conserved when integrated on a surface enclosing the sources only if vorticity is considered as non-acoustic, which is a reasonable assumption following the work of Chu & Kovasznay. A frequency-domain expression of the acoustic quantities has been derived and will be used in this study to quantify the sources contributing to fan tonal noise.

1.4 Direct noise predictions

Direct noise predictions consists in solving directly the Navier-Stokes equations that contain the acoustic fluctuations. The application of this method is described in this section, from the numerical solving of the equations to the filtering of the non-acoustic fluctuations.

1.4.1 CFD simulations

Conventional CFD simulations solve the Navier-Stokes equations (1.1). One of the main challenges lies in the development of accurate schemes of discretization of the

spatial and temporal differential operators [42]. Alternate methods also exist such as the Lattice Boltzmann Method (LBM) in which the discrete Boltzmann's equation that describes the statistical behavior of the fluid particles is solved [43, 44].

Direct Numerical Simulations

The flow inside a turbomachine is turbulent and characterized by a wide range of scale of vortices. The maximum scale is imposed by the characteristic dimension of the problem and the minimum scale, the Kolmogorov scale, is dependent on the fluid viscosity. To compute the flow properly, it is therefore necessary to solve all these scales. The simulated domain should then be big enough to include the big scale vortices and refined enough to be able to capture the smallest ones. Simulations that solve the flow until the Kolmogorov scale are called Direct Numerical Simulations (DNS) because the equations of fluid dynamics are solved directly (the discretization in space and time is the only approximation). Current informatic capabilities limit this kind of simulations to academic configurations only. The mesh sizes required to solve these vortice scales are too big on industrial configurations. It can be shown that the number of mesh points required with such approach is about $Re_L^{37/14}$ where $Re_L = UL/\nu$ is the Reynolds number based on the characteristic size of the geometry L with U the mean velocity of the flow and ν the kinematic viscosity [45]. For a fan, the Reynolds number typically ranges from 10^6 to 10^7 [46] and the mesh should therefore contain 10^{16}-10^{17} mesh points, which is far above current capabilities. The state-of-the-art simulations reach relatively high Reynolds number ($\sim 10^5$) on simplified geometries (airfoil or isolated vane) [47, 48, 49].

Large Eddy Simulations

The Large Eddy Simulations (LES) are based on a spatial averaging of the governing equations of fluid dynamics. The largest vortices are fully resolved whereas the smallest ones, assumed to have mainly an isotropic and dissipative role, are predicted by a subgrid scale model [50, 51]. The instantaneous turbulence is therefore accessible thanks to these simulations, up to the resolved scale at least. They are also less expensive than DNS because the mesh does not need to capture down to the Kolmogorov scale. However, the mesh near the walls still needs to be well-refined and estimates of Choi & Moin gives a total number of points of about $Re_L^{13/7}$ [45]. This is still expensive and wall-resolved LES are often limited to academic configurations at low Reynolds number. Industrial configurations on a sector of a turbomachine can be studied but requires huge computational ressources. For instance, Gourdain performed a wall-resolved LES of one axial compressor stage over $2\pi/10$ that requires a mesh of approximately 1 billion points [52]. In order to reduce the computational cost of LES, wall laws are often used to model the flow near the walls. The wall-modeled LES requires significantly less points (estimates are at the order of Re_L [45]) and allows for the study of more complex configurations [53, 54, 55, 16]. Another approach that can be adopted in the field of turbomachinery consists of reducing the size of the computational domain by using phase-lagged boundary conditions [56].

Reynolds-Averaged Navier-Stokes simulations

Simulations of the Reynolds-Averaged Navier-Stokes (RANS) equations are based on a statistical averaging (or Reynolds averaging) over several possible realizations of the governing equations. This statistical averaging removes all stochastic phenomena, including turbulence which is consequently modeled. If the flow is unsteady and the phase average is synchronized with the fundamental frequency of the unsteady phenomenon, this statistical averaging keeps the unsteadiness of the flow and the simulations are referred to as Unsteady Reynolds-Averaged Navier-Stokes (URANS) simulations [57]. Because the present study is limited to the tonal noise which is caused by periodic phenomena, URANS simulations are sufficient and will be used [58, 59]. More details on the URANS formalism, the turbulence modeling and the discretization techniques are given in App. A.1.

1.4.2 Filtering of non-acoustic perturbations

The fluctations that will be extracted from the simulations result from three contributions according to Chu & Kovasznay's analysis: the entropic, the vortical and the acoustic mode. A filtering procedure is needed to isolate the acoustic part of the fluctuations. Two types of methods are generally used. They are only briefly presented here but more details will be given in Chap. 4.

Local identification of the convective wavenumber

The idea behind this filtering technique is simple. It comes from the observation that vorticity fluctuations are convected with the flow while acoustic fluctuations are propagated at the speed of sound. The filtering is realized by simply removing the part of the fluctuations that are convected with the flow.

In practice, the procedure is applied locally by following the fluctuations over the streamlines. The filtering can be done from two or more axial planes or even from the whole volumic data if available. Kopitz *et al.* developed a method using several planes to isolate the acoustic waves represented in terms of the Riemann invariants [60]. This method can be implemented easily because it requires only the temporal informations over some (typically 3) planes.

As for Bonnneau *et al.* [21], the volumic data is exploited to perform the detection of the fluctuations that are convected with the flow over each axial line of the mesh (that approximate the streamlines). A Discrete Fourier Tranform (DFT) that includes a windowing to avoid spurious modes due to non-periodicity has been done to identify those fluctuations. This method is much more expensive because it requires the storage of volumic data during the iterations. However, it is expected to be more precise because the axial evolution of the fluctuations is entirely described. A similar filtering is developed and tested in this study. More details are given Sec. 4.6.3.

Mode-matching technique

The other family of filtering consists in the decomposition of the fluctuations over acoustic modes. This type of filtering is usually applied to couple CFD and CAA simulations [61]. The principle is to make the pressure and velocity fluctuations (that both contribute to the acoustic power according to Eq. (1.61)) extracted from the CFD simulation consistent with the equations of CAA that describe acoustics. The decomposition is generally done over the duct modes that will be introduced in Sec. 1.6.1. A filtering technique inspired from this mode-matching technique is also developed in this work and is evaluated in Sec. 4.6.3.

Summary of the section

Direct noise predictions consist in solving the flow and the acoustics simultaneously thanks to a CFD simulation. Three types of simulations have been presented (DNS, LES and URANS simulations), characterized by different levels of turbulence modeling. In this study, URANS simulations that are suited for the prediction of deterministic phenomena will be performed. The fluctuations that will be extracted from the simulations will contain vorticity fluctuations that need to be filtered to provide noise estimates. Two different types of filtering methods (one based on a local identification of the convected fluctuations and one based on a modal decomposition) have been briefly presented and will be used in this study.

1.5 Hybrid noise predictions: source determination

Analytical models that determine the acoustic sources from a known excitation are presented in this section. The focus is put on Amiet's theory which predicts the acoustic response of an isolated airfoil with zero thickness and zero camber placed in a turbulent flow. A brief review of the extensions of this theory that have been developped throughout the years to account for more complex geometries and flow conditions is also given.

1.5.1 Amiet's model

Amiet proposed a theory in 1975 which allows evaluating the acoustic response of an airfoil placed in a turbulent flow [62]. He derived an analytical expression of the unsteady pressure jump on the airfoil and of the resulting far-field acoustic pressure. The focus is put on the derivation of the unsteady pressure jump only (the equivalent source). The analytical propagation of known sources will be detailed in the next section.

General formulation

An airfoil of chord $2b$, span $2d$ and with zero thickness is placed in a fluid with a mean density ρ_0 and a mean flow U_0. The frame associated with this airfoil is defined in Fig. 1.2 where the vector $\boldsymbol{r}$ denotes the point on the airfoil of coordinates $(x, y, z = 0)$. The chordwise and spanwise directions are represented by the x-axis and the y-axis respectively and the mean flow is aligned with the airfoil so that it has only an axial component.

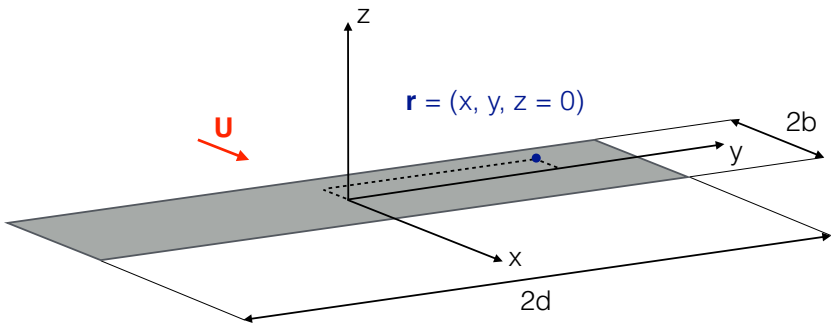

Figure 1.2: **Frame associated with the airfoil**

The incoming perturbation is characterized by the turbulent velocity normal to the chord (or upwash) w, which is assumed to be frozen i.e. constant in the moving frame. The axial coordinate in the moving frame $\tilde{x}$

$$\tilde{x} = x - U_0 t, \tag{1.63}$$

with t the time, is introduced so that the turbulent velocity w can be expressed as a function of $\tilde{x}$ and y only. The latter is decomposed into elementary gusts

$$w(\tilde{x}, y) = \int_{-\infty}^{+\infty} \int_{-\infty}^{+\infty} \widehat{\widehat{w}}(k_x, k_y) e^{i(k_x \tilde{x} + k_y y)} \, dk_x dk_y, \tag{1.64}$$

where the gusts $\widehat{\widehat{w}}(k_x, k_y)$ are determined by the inverse relation

$$\widehat{\widehat{w}}(k_x, k_y) = \frac{1}{(2\pi)^2} \int_{-\infty}^{+\infty} \int_{-\infty}^{+\infty} w(\tilde{x}, y) e^{-i(k_x \tilde{x} + k_y y)} \, d\tilde{x} dy. \tag{1.65}$$

These elementary gusts correspond to skewed gusts where k_x and k_y denote the wavenumbers along the x-axis and the y-axis respectively. The characterization of a gust with its wavenumbers is represented in Fig. 1.3.

The change of variable $\tilde{x} \to x - U_0 t$ yields the expression of the turbulent velocity in the fixed frame (which now depends on time t)

$$w(x, y, t) = \int_{-\infty}^{+\infty} \int_{-\infty}^{+\infty} \widehat{\widehat{w}}(k_x, k_y) e^{i[k_x(x - U_0 t) + k_y y]} dk_x dk_y. \tag{1.66}$$

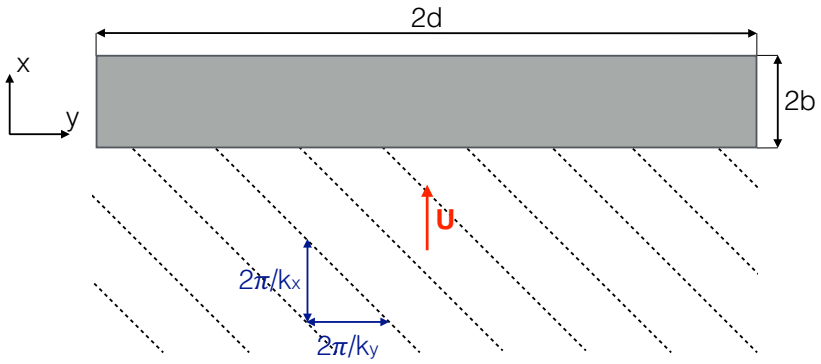

Figure 1.3: **Skewed gust incident on airfoil**

The airfoil pressure jump $\Delta P_g(x, y, t)$ caused by one skewed gust of wavenumbers k_x and k_y can be derived analytically and will be detailed later. It is here expressed thanks to a transfer function $g(x, k_x, k_y)$. For an elementary gust of the form

$$w_g = w_0 e^{i[k_x(x-U_0t)+k_y y]}, \tag{1.67}$$

the pressure jump is expressed as

$$\Delta P_g(x, y, t) = 2\pi\rho_0 U_0 b w_0 g(x, k_x, k_y) e^{i(k_y y - k_x U_0 t)}. \tag{1.68}$$

The total pressure jump $\Delta P(x, y, t)$ caused by the contribution of all gusts can therefore be written:

$$\Delta P(x, y, t) = 2\pi\rho_0 U_0 b \int_{-\infty}^{+\infty} \int_{-\infty}^{+\infty} \widehat{\widehat{w}}(k_x, k_y) g(x, k_x, k_y) e^{i(k_y y - k_x U_0 t)}\, dk_x dk_y. \tag{1.69}$$

A temporal Fourier transform is then performed to obtain the harmonics of the total pressure jump

$$\widehat{\Delta P}(x, y, \omega) = \frac{1}{2\pi} \int_{-\infty}^{+\infty} \Delta P(x, y, t) e^{i\omega t}\, dt. \tag{1.70}$$

Using Eq. (1.69) and the relation

$$\frac{1}{2\pi} \int_{-\infty}^{+\infty} e^{i(\omega - k_x U_0)t}\, dt = \delta(\omega - k_x U_0), \tag{1.71}$$

yields

$$\widehat{\Delta P}(x, y, \omega) = 2\pi\rho_0 U_0 b \int_{-\infty}^{+\infty} \widehat{\widehat{w}}(K_x, k_y) g(x, K_x, k_y) e^{ik_y y}\, dk_y, \tag{1.72}$$

where $K_x = \omega/U_0$. This derivation stresses that the pressure jump at a given frequency is produced only by the elementary gusts with the axial wavenumber K_x. Other gusts will not produce any pressure jump at this frequency. In practice, the term $\widehat{\widehat{w}}(K_x, k_y)$ is given as an input and is determined from the decomposition of the excitations (wake or distortion profile).

Transfer function between skewed gust and airfoil pressure jump

The final expression of the total pressure jump (1.69) involves the transfer function $g(x, k_x, k_y)$ that has not been detailed yet. This transfer function expresses the pressure jump caused by the elementary gust of wavenumber k_x and k_y. It is obtained by solving successively the diffraction problems at leading and trailing edges thanks to Schwarzschild's solution [63]. The expression of this function depends on the subcritical (subsonic phasis velocity) or supercritical (supersonic phasis velocity) character of the gust. Its derivation is a long task and only the results are shown here. More details can be found in [64], [65] or [66].

The transfer function $g(x, k_x, k_y)$ is the addition of two terms, g_1 which corresponds to the diffraction at the leading edge assuming an infinite chord, and g_2 which corresponds to the trailing edge correction. Several notations are used in the transfer functions and are detailed here. $\bar{x} = x/b$ is the dimensionless axial coordinate $(-1 \leq \bar{x} \leq 1)$ and $\bar{k}_x = k_x b$ and $\bar{k}_y = k_y b$ are the dimensionless wavenumber along the x-axis and y-axis respectively. The Mach number $M_0 = U_0/a_0$ with a_0 the mean speed of sound is introduced. κ is defined by $\kappa^2 = \mu^2 - \bar{k}_y^2/\beta_0^2$ with $\beta_0^2 = 1 - M_0^2$ and $\mu = \bar{k}_x M_0/\beta_0^2 = \bar{k}_x^* M_0$ where $\bar{k}_x^* = \bar{k}_x/\beta_0^2$.

For a supercritical gust, $\kappa > 0$ and the transfer functions are given by

$$g_1(\bar{x}, k_x, k_y) = \frac{e^{-i\pi/4}}{\pi\sqrt{\pi(\bar{k}_x + \beta_0^2\kappa)(\bar{x}+1)}} e^{-i(\kappa - \bar{k}_x^* M_0^2)(\bar{x}+1)}, \tag{1.73a}$$

$$g_2(\bar{x}, k_x, k_y) = \frac{e^{-i\pi/4}}{\pi\sqrt{2\pi(\bar{k}_x + \beta_0^2\kappa)}} \left[1 - (1+i)E^*(2\kappa(1-\bar{x}))\right] e^{-i(\kappa - \bar{k}_x^* M_0^2)(\bar{x}+1)}, \tag{1.73b}$$

where $E^*(X)$ is the conjugate of Fresnel integral $E(X)$

$$E(X) = \int_0^X \frac{e^{ix}}{\sqrt{2\pi x}}\, dx. \tag{1.74}$$

For a subcritical gust, $\kappa < 0$ and the transfer functions become

$$g_1'(\bar{x}, k_x, k_y) = \frac{e^{-i\pi/4}}{\pi\sqrt{\pi(\bar{k}_x + i\beta_0^2\kappa')(\bar{x}+1)}} e^{i(\bar{k}_x^* M_0^2 + \kappa')(\bar{x}+1)}, \tag{1.75a}$$

$$g_2'(\bar{x}, k_x, k_y) = \frac{e^{-i\pi/4}}{\pi\sqrt{2\pi(\bar{k}_x + i\beta_0^2\kappa')}} \left\{1 - erf\left[(\sqrt{2\kappa'(1-\bar{x})})\right]\right\} e^{i(\bar{k}_x^* M_0^2 + \kappa')(\bar{x}+1)}, \tag{1.75b}$$

with $\kappa'^2 = -\kappa^2 = \bar{k}_y^2/\beta_0^2 - \mu^2$ and $erf(X)$ the error function

$$erf(X) = \frac{2}{\sqrt{\pi}} \int_0^X e^{-x^2}\, dt. \tag{1.76}$$

1.5.2 Extensions

The final expressions obtained with Amiet's theory (1.69), (1.73) and (1.75) are purely analytical and can provide a very fast estimation of the unsteady pressure jump on an airfoil as soon as the excitation is decomposed into elementary gusts. However, it should be kept in mind that this theory introduces a lot of assumptions on both the geometry and the flow. The blade/vane is represented by a two-dimensional zero thickness airfoil without camber nor steady loading, the flow is assumed purely axial and uniform and the gusts are two-dimensional.

A lot of extensions of this theory have been developed throughout the years. For example, three-dimensional gusts have been considered by Moreau *et al.* [67] and methods of matched asymptotic expansions have been used by Myers & Kerschen [68] and by Evers & Peake [69] to account for geometrical effects (camber, thickness), angle of attack and steady loading. All these models consider isolated airfoils. When the number of blade (or vane) of a rotor (or stator) becomes important or when the stagger angle becomes high, the adjacent blades (or vanes) have a significant influence on the response of a particular blade (vane) and the isolated airfoil assumption becomes invalid. This phenomenon is often referred to as cascade effect.

More recent models account for this cascade effect. It was originally studied by Kaji & Okazaki using the semi-actuator disk theory [70] and the acceleration potential method [71] for evaluating the acoustic transmission through a row. Methods based on the Wiener-Hopf technique have simultaneously emerged, first by neglecting the interaction between leading and trailing edges [72], and then by including it with a backscattering [73]. Peake has adapted these theories to the prediction of the unsteady loadings on the blades for a two-dimensional rectilinear cascade [74]. Glegg [75], Posson *et al.* [76] and De Laborderie [17] have extended Peake's model for three-dimensional cascades using a strip-theory approach.

Another approach has emerged recently and is based on a mode-matching technique: modal expressions are written in each subdomain (upstream of the row, downstream of the row and in the inter-vane channel) and are matched using the conservation laws of fluid dynamics [77, 78]. This approach is uniformly valid and can be easily extended to three-dimensionnal cascades without needing to resort to classical strip-theory approaches [79].

In this study, Amiet's model only will be used even if a lot of other models that account for a better representation of the geometry or the flow exist. Indeed, the "real" unsteady loadings will be already known from the simulations. The idea here is just to use a relatively simple model to understand the relation at first order between the excitation (distortion, wake) and the unsteady loadings on the blades and vanes.

Summary of the section

Amiet's theory shows how an airfoil produces sound in a turbulent flow. This theory is valid for two-dimensional isolated airfoils without thickness, camber or angle of attack and consider two-dimensional gusts only. It is a fast way to predict the unsteady loadings on the blades or vanes caused by a known excitation (distortion, wake) that must be decomposed into elementary gusts. Even if more complex models that make less assumptions exist, this relatively simple model will be used in this study in the interest of establishing easily a relation at first order between the excitation and the unsteady loadings.

1.6 Hybrid noise predictions: sound propagation

Some analytical methods that are used to propagate known acoustic sources are described in this section.

1.6.1 Goldstein's analogy

Lighthill's analogy [29] has been successively extended by Curle to include fixed solid boundaries [80], by Ffowcs Williams & Hawkings to account for moving solid boundaries [81] and by Goldstein to deal with the propagation in ducts [8]. Goldstein's analogy is particularly adapted for fan noise prediction and is used in most studies [82, 83]. The main results are given below and the whole derivation can be found in App. B.

Convected wave equation

The same notations as the ones used in Sec. 1.2.2 (Lighthill's analogy) are used here. x_i $(i = 1, 2, 3)$ denotes the coordinates, t the time, ρ' the fluctuating density, a_0 the speed of sound in the uniform flow and T_{ij} the component (i, j) of Lighthill's tensor. Contrary to Lighthill's analogy, the fluid is no more considered as quiescent and a uniform flow at speed U_0 along the x_1-axis is defined. The frame that moves with the flow is Galilean because it is uniformly translated from the absolute frame which is Galilean. Lighthill's equation (1.13) is therefore also valid in the moving frame. By denoting by the tild symbol the variables in the moving frame, it is written

$$\frac{\partial^2 \rho'}{\partial t^2} - a_0^2 \frac{\partial^2 \rho'}{\partial \tilde{x}_i^2} = \frac{\partial^2 \tilde{T}_{ij}}{\partial \tilde{x}_i \partial \tilde{x}_j}. \tag{1.77}$$

The coordinates and velocities in the moving frame can be expressed by

$$\tilde{x}_i = x_i - \delta_{1i} U_0 t, \quad \tilde{v}_i = v_i - \delta_{1i} U_0, \tag{1.78}$$

where δ_{1i} is the Kronecker's symbol. Using the preceeding relations and expressing the differential operators of Lighthill's equation (1.77) in the fixed frame yields

$$\frac{D^2 \rho'}{Dt^2} - a_0^2 \frac{\partial^2 \rho'}{\partial x_i^2} = \frac{\partial^2 \tilde{T}_{ij}}{\partial x_i \partial x_j}, \tag{1.79}$$

where D/Dt is the convected derivative operator

$$\frac{D}{Dt} = \frac{\partial}{\partial t} + U_0 \frac{\partial}{\partial x_1}. \tag{1.80}$$

The wave equation (1.79) is said to be convected and characterizes the acoustic propagation in a uniform flow.

Goldstein's formula

Goldstein proposed to solve the convected wave equation (1.79) with the use of a generalized Green's function. The Green's function is the solution to the homogeneous wave equation with a point source in space and time. If $\boldsymbol{y}$ and τ denote the position and the emission time of the source and $\boldsymbol{x}$ and t the position and the reception time of the observer, then the Green's function is written $G(\boldsymbol{y}, \tau | \boldsymbol{x}, t)$ and satisfies

$$\frac{D^2 G}{Dt^2} - a_0^2 \frac{\partial^2 G}{\partial x_i^2} = \delta(\boldsymbol{x} - \boldsymbol{y})\delta(t - \tau). \tag{1.81}$$

Goldstein showed that, in the presence of solid boundaries, the solution to the non-homogeneous convected wave equation can be expressed as

$$\begin{aligned}
\rho'(\boldsymbol{x}, t) = \frac{1}{a_0^2} \int_{-\infty}^{+\infty} \iiint_{V(\tau)} \tilde{T}_{ij}(\boldsymbol{y}, \tau) \frac{\partial^2}{\partial x_i \partial y_j} \left\{ G(\boldsymbol{y}, \tau | \boldsymbol{x}, t) \right\} dV(\boldsymbol{y}) d\tau \\
+ \frac{1}{a_0^2} \int_{-\infty}^{+\infty} \iint_{S(\tau)} f_i(\boldsymbol{y}, \tau) \frac{\partial}{\partial x_i} \left\{ G(\boldsymbol{y}, \tau | \boldsymbol{x}, t) \right\} dS(\boldsymbol{y}) d\tau \\
+ \frac{1}{a_0^2} \int_{-\infty}^{+\infty} \iint_{S(\tau)} \rho_0 \tilde{V}_n(\boldsymbol{y}, \tau) \frac{D}{D\tau} \left\{ G(\boldsymbol{y}, \tau | \boldsymbol{x}, t) \right\} dS(\boldsymbol{y}) d\tau,
\end{aligned} \tag{1.82}$$

where $S(\tau)$ represents the solid surfaces of the domain, $V(\tau)$ the volume that include these surfaces, f_i their force applied to the fluid, $\tilde{V}_n$ their normal velocity expressed in the moving frame and ρ_0 the mean density.

Through this formula (1.82), often referred to as Goldsein's formula, three terms can be distinguished:

- the first term represented by Lighthill's tensor is the shear noise and can be modeled by a volumic repartition of quadrupoles in the volume enclosing the sources;
- the second term linked to the fluctuation of the forces f_i on the surfaces is the loading noise and can be seen as a surface distribution of dipoles;
- and the third term due to the displacement of fluid by the surfaces is the thickness noise and is equivalent to a surface distribution of monopoles.

Duct Green's function

Solving the convected wave equation is therefore reduced to the determination of the Green's function that is adapted to the configuration. An analytical solution is proposed by Goldstein for propagation in circular ducts that has then been extended for annular ducts. The duct is considered as infinite and is defined by its hub radius R_h and tip radius R_t. From now, cylindrical coordinates are used and the observer and source coordinates become $\boldsymbol{x} = (x, r, \theta)$ and $\boldsymbol{y} = (y, r_y, \theta_y)$ respectively. The annular duct and its associated frame are represented in Fig. 1.4. The flow is at speed U_0 along the duct axis (x-axis).

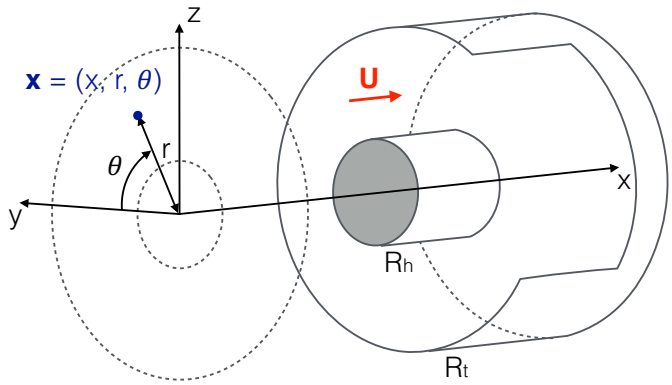

Figure 1.4: **Definition of the annular duct and its associated frame**

The Green's function is shown to be expressed as a function of duct modes (see App. B.1 for more details) defined by

$$\psi_{mn}(r,\theta) = \left[A_{mn}J_m(\alpha_{mn}r) + B_{mn}Y_m(\alpha_{mn}r)\right] e^{-im\theta}, \tag{1.83}$$

where m and n are called the azimuthal and radial mode order which correspond to the number of zeros in the azimuthal and the radial direction respectively. A_{mn}, B_{mn} and α_{mn} are duct coefficients that are obtained from the rigid wall boundary conditions at hub and shroud and J_m and Y_m are the Bessel functions of order m of first and second kinds respectively. The duct modes satisfy the orthogonality relation

$$\int_0^{2\pi}\int_{R_h}^{R_t} \psi_{mn}(r,\theta)\overline{\psi_{m'n'}}(r,\theta)\, r dr d\theta = \delta_{mm'}\delta_{nn'}\Gamma_{mn}, \tag{1.84}$$

where Γ_{mn} is the norm of the eigenfunction

$$\Gamma_{mn} = \int_0^{2\pi}\int_{R_h}^{R_t} |\psi_{mn}(r,\theta)|^2\, r dr d\theta. \tag{1.85}$$

By writing the Mach number $M_0 = U_0/a_0$, the wavenumber $k_0 = \omega/a_0$, $\beta_0^2 = 1 - M_0^2$ and $k_{mn}^2 = k_0^2 - \beta_0^2\alpha_{mn}^2$, the axial wavenumber $\gamma_{mn}^{\pm}$ of the mode (m, n) is given by

$$\gamma_{mn}^{\pm} = \frac{M_0 k_0}{\beta_0^2} \pm \frac{k_{mn}}{\beta_0^2}. \tag{1.86}$$

The upper sign and the lower sign denote the wave travelling in the upstream and downstream directions respectively. An important notion specific to the propagation of sound in ducts appears here and it is linked to the nature of the discriminant k_{mn}. If k_{mn} is real ($k_{mn}^2 \geq 0$), the axial wavenumber $\gamma_{mn}^{\pm}$ is real and the mode (m, n) is propagative (or cut-on). On the contrary, if k_{mn} is imaginary ($k_{mn}^2 < 0$), the axial wavenumber $\gamma_{mn}^{\pm}$ becomes complex, with an imaginary part necessarily positive to keep a physical meaning, and the mode will be evanescent (or cut-off). Because $\alpha_{mn} \to \infty$ whenever m or n becomes infinite, only a finite number of modes will be cut-on at a given frequency. This number of cut-on modes will increase with the frequency because $k_0 = \omega/a_0$.

Using all these notations, the duct Green's function can be shown to reduce to (see App. B.2 for more details)

$$G^{\pm}(\boldsymbol{y},\tau|\boldsymbol{x},t) = \frac{i}{4\pi}\sum_{m=-\infty}^{+\infty}\sum_{n=0}^{+\infty}\frac{\overline{\psi_{mn}}(r,\theta)\psi_{mn}(r_y,\theta_y)}{\Gamma_{mn}} \int_{-\infty}^{+\infty}\frac{e^{-i[\gamma_{mn}^{\pm}(x-y)+\omega(t-\tau)]}}{k_{mn}}\,d\omega. \quad (1.87)$$

Computation of acoustic fluctuations

To pursue its analogy, Goldstein considered that the dipole sources were dominant in the fan module. This is generally true, except for transonic regimes where the quadrupole source term might also be taken into account. Only the dipole source term in Goldstein's formula (1.82) is therefore kept

$$\rho'^{\pm}(\boldsymbol{x},t) = \frac{1}{a_0^2}\int_{-\infty}^{+\infty}\iint_{S(\tau)} f_i(\boldsymbol{y},\tau)\frac{\partial}{\partial x_i}\left\{G^{\pm}(\boldsymbol{y},\tau|\boldsymbol{x},t)\right\}dS(\boldsymbol{y})d\tau, \quad (1.88)$$

where the surface of integration $S(\tau)$ is limited to the blades and/or vanes. From now, the prime symbol is not written anymore for clarity. Using the expression of the duct Green's function (1.87) yields

$$\rho^{\pm}(\boldsymbol{x},t) = \int_{-\infty}^{+\infty}\frac{i}{4\pi a_0^2}\sum_{m=-\infty}^{+\infty}\sum_{n=0}^{+\infty}\frac{\overline{\psi_{mn}}(r,\theta)e^{-i\gamma_{mn}^{\pm}x}}{\Gamma_{mn}k_{mn}} \int_{-\infty}^{+\infty}\iint_{S(\tau)}\frac{\partial}{\partial x_i}\left\{\psi_{mn}(r_y,\theta_y)e^{i\gamma_{mn}^{\pm}y}\right\}f_i(\boldsymbol{y},\tau)e^{i\omega\tau}\,dS(\boldsymbol{y})d\tau\,e^{-i\omega t}\,d\omega. \quad (1.89)$$

This expression can be simplified for the two mechanisms considered in this study: the wake-stator interaction and the distortion-rotor interaction. It is shown in App. B.3 that both mechanisms radiate only at multiples of the BPF for an homogeneous rotor. If B denotes the number of rotor blades and Ω the engine rotational speed, Eq. (1.89) can therefore be expressed as Fourier series

$$\rho^{\pm}(\boldsymbol{x},t) = \sum_{s=-\infty}^{+\infty}\rho_{sB}^{\pm}(\boldsymbol{x})e^{-isB\Omega t}, \quad (1.90)$$

where the components are given by

$$\rho_{sB}^{\pm}(\boldsymbol{x}) = \frac{1}{2a_0^2} \sum_{m=-\infty}^{+\infty} \sum_{n=0}^{+\infty} \frac{\overline{\psi_{mn}}(r,\theta) e^{-i\gamma_{mn}^{\pm} x}}{\Gamma_{mn} k_{mn}} S_{mn}^{\pm}, \tag{1.91}$$

and where $S_{mn}^{\pm}$ represents the source term. Its expression depends on the noise mechanism. For the wake-stator interaction, it is given by

$$S_{mn}^{\pm}(sB) = i \iint_S \frac{\partial}{\partial x_i} \left\{ \psi_{mn}(r_y, \theta_y) e^{i\gamma_{mn}^{\pm} y} \right\} f_{i,sB}(\boldsymbol{y})\, dS(\boldsymbol{y}), \tag{1.92}$$

and involves only the BPF harmonics of the vane loadings $f_{i,sB}(\boldsymbol{y})$. When the stator of V vanes is homogeneous, it can be shown that only the modes that satisfy the relation $m = sB - kV$ (with k any integer) emerge (more details in App. B.3). For the distortion-rotor interaction, the source term is written

$$S_{mn}^{\pm}(s-m) = i \iint_S \frac{\partial}{\partial x_i} \left\{ \psi_{mn}(r_y, \tilde{\theta}_y) e^{i\gamma_{mn}^{\pm} y} \right\} f_{i,(s-m)}(\tilde{\boldsymbol{y}})\, dS(\tilde{\boldsymbol{y}}), \tag{1.93}$$

and involves all the RF harmonics of the blade loadings $f_{i,(sB-m)}^{1}(\tilde{\boldsymbol{y}})$. The tilde symbol is used here to denote the variables expressed in the rotating frame.

Computation of acoustic power

Analytical expression of the acoustic power caused by the stator or rotor sources can be derived. The Cantrell & Hart's formulation, valid for a general homentropic fluid, has been introduced in Sec. 1.3 and is used here. Eq. (1.62) allows for expressing the acoustic power carried by the sB^{th} harmonic

$$P_{sB}^{\pm} = \mp 2 \iint_S \overline{I_{xsB}}\, dS, \tag{1.94}$$

where $\overline{I_{xsB}}$ is given by Eq. (1.61) with $M_0 = M_{x0}$ and $M_{y0} = M_{z0} = 0$

$$\overline{I_{xsB}} = \left(1 + M_0^2\right) p_{sB} u_{sB}^{*} + \frac{M_0}{\rho_0 a_0} |p_{sB}|^2 + \rho_0 M_0 a_0 |u_{sB}|^2 . \tag{1.95}$$

Using Eq. (1.91) and limiting the sum over the cut-on modes (which are the only ones that contribute to the upstream and downstream power because the duct is infinite) yields

$$\rho_{sB}^{\pm}(\boldsymbol{x}) = \sum_{m=-\infty}^{+\infty} \sum_{\substack{n=0 \\ k_{mn}^2 \geq 0}}^{+\infty} \rho_{mn}^{\pm}(\boldsymbol{x}), \tag{1.96}$$

where $\rho_{mn}^{\pm}$ is implicitly dependent on the harmonic sB (not written for clarity) and is given by

$$\rho_{mn}^{\pm}(\boldsymbol{x}) = \frac{1}{2a_0^2} \frac{\overline{\psi_{mn}}(r,\theta) e^{-i\gamma_{mn}^{\pm} x}}{\Gamma_{mn} k_{mn}} S_{mn}^{\pm}. \tag{1.97}$$

Because the flow is isentropic, Eq. (1.29) gives the modal decomposition of the pressure fluctuations

$$p_{sB}^{\pm}(\boldsymbol{x}) = \sum_{m=-\infty}^{+\infty} \sum_{\substack{n=0 \\ k_{mn}^2 \geq 0}}^{+\infty} p_{mn}^{\pm}(\boldsymbol{x}), \tag{1.98}$$

with

$$p_{mn}^{\pm}(\boldsymbol{x}) = \frac{1}{2} \frac{\overline{\psi_{mn}}(r,\theta) e^{-i\gamma_{mn}^{\pm} x}}{\Gamma_{mn} k_{mn}} S_{mn}^{\pm}. \tag{1.99}$$

From the axial component of the momentum conservation equation (1.1b), it can be shown that the axial velocity disturbances are given by

$$u_{sB}^{\pm}(\boldsymbol{x}) = \sum_{m=-\infty}^{+\infty} \sum_{\substack{n=0 \\ k_{mn}^2 \geq 0}}^{+\infty} u_{mn}^{\pm}(\boldsymbol{x}), \tag{1.100}$$

with

$$u_{mn}^{\pm}(\boldsymbol{x}) = \frac{1}{2\rho_0 a_0} \frac{\lambda_{mn}^{\pm} \overline{\psi_{mn}}(r,\theta) e^{-i\gamma_{mn}^{\pm} x}}{\Gamma_{mn} k_{mn}} S_{mn}^{\pm}, \tag{1.101}$$

and where $\lambda_{mn}^{\pm}$ is expressed as

$$\lambda_{mn}^{\pm} = \frac{-M_0 k_0 \mp k_{mn}}{k_0 \pm M_0 k_{mn}}. \tag{1.102}$$

Combining the above equations and using the property of orthogonality of the modes (1.84) yields

$$P_{sB}^{\pm} = \frac{k_0 \beta_0^4}{2\rho_0 a_0} \sum_{m=-\infty}^{+\infty} \sum_{\substack{n=0 \\ k_{mn}^2 \geq 0}}^{+\infty} \frac{|S_{mn}^{\pm}|^2}{\Gamma_{mn} k_{mn} (k_0 \pm M_0 k_{mn})^2}. \tag{1.103}$$

With this expression, it is possible to compute analytically the power radiated by stator or rotor sources as soon as their unsteady loading is known. The acoustic power is expressed as a sum of modal powers and is characterized by its upstream and downstream values. Naturally, only the cut-on modes contribute to the power in the duct which is assumed to be infinite.

1.6.2 Extension to a slowly varying duct

The main limitation of Goldstein's analogy presented above is that the formalism is valid only for straight ducts with uniform and axial mean flow. However, the turbofan duct, such as the one sketched in Fig. 2, is far from being straight and the

duct flow is highly non-uniform.

An extension of this analogy to slowly varying duct has been proposed by Rienstra in 1999 [84] and has been validated against numerical results when mode transitions do not occur [85]. An axially varying duct geometry and flow properties is allowed and the solution becomes a multiple-scales solution rather than a simple modal expansion. Similarly to Goldstein's analogy, the solution is determined analytically and is exact. Moreover, the calculational complexities are no greater than for the classical straight duct model.

Problem formulation

The flow is a compressible inviscid perfect isentropic irrotational gas flow, consisting of a mean flow and acoustic perturbations. The mean flow variables are written with the subscript 0 while the acoustic perturbations are denoted by the prime symbol

$$\rho = \rho_0 + \rho', \tag{1.104a}$$

$$\boldsymbol{v} = \boldsymbol{v_0} + \boldsymbol{v'}, \tag{1.104b}$$

$$p = p_0 + p', \tag{1.104c}$$

$$a = a_0 + a'. \tag{1.104d}$$

The flow is essentially axial and the axial mean flow velocity is written U_0. The duct is considered here as hard-walled but lining can be considered. The duct hub radius R_h and tip radius R_t are assumed to vary slowly:

$$R_h = R_h(X), \quad R_t = R_t(X), \quad X = \varepsilon x, \tag{1.105}$$

where x is the axial coordinate, X the slowly varying axial coordinate and ε a small parameter. The latter is necessary to legitimize and support the systematic perturbation method used by Rienstra but will be absent from the final results. Only the main results obtained by Rienstra will be shown in this section because all important features of duct acoustics have already been introduced in Sec. 1.6.1.

Mean flow

With the above assumptions, Rienstra showed that the mean flow can be characterized by two constants E and F defined by

$$E = \frac{1}{2}|\boldsymbol{v_0}(X)|^2 + \frac{a_0^2(X)}{\gamma - 1} = \text{constant}, \tag{1.106a}$$

$$F = \rho_0(X)U_0(X)\left[R_t^2(X) - R_h^2(X)\right] = \text{constant}. \tag{1.106b}$$

E is similar to the Bernouilli's constant and F represents the mass-flow rate. The mean density $\rho_0(X)$ must be determined numerically for each X by solving (with

Newton's method for example)

$$\frac{1}{2}\left[\frac{F}{\rho_0(X)(R_t^2(X)-R_h^2(X))}\right]^2+\frac{1}{\gamma-1}\rho_0^{\gamma-1}(X)=E. \tag{1.107}$$

All other mean flow variables can then be obtained

$$U_0(X)=\frac{F}{\rho_0(X)\left[R_t^2(X)-R_h^2(X)\right]}, \tag{1.108a}$$

$$p_0(X)=\frac{1}{\gamma}\rho_0^{\gamma}(X), \tag{1.108b}$$

$$a_0(X)=\rho_0^{\frac{\gamma-1}{2}}(X). \tag{1.108c}$$

Acoustic field

By linearizing Navier-Stokes equations (1.1), rearranging them to get a general convected wave equation and using the Wentzel-Kramers-Brillouin (WKB) method [86], Rienstra showed that the acoustic field in the duct can be represented as a summation of slowly varying modes. Using Goldstein's formalism of Sec. 1.6.1, the fluctuating density (given by Eq. (1.91) in a straight duct) becomes

$$\rho_{sB}^{\pm}(\boldsymbol{x})=\frac{1}{2a_0^2(X)}\sum_{m=-\infty}^{+\infty}\sum_{\substack{n=0\\ k_{mn}^2(X)\geq 0}}^{+\infty}\frac{\overline{\psi_{mn}}(X,r,\theta)}{\Gamma_{mn}(X)k_{mn}(X)}S_{mn}^{\pm}\,e^{-i/\varepsilon\int^X\gamma_{mn}^{\pm}(\xi)\,d\xi}. \tag{1.109}$$

The functions $\psi_{mn}(X,r,\theta)$ are the slowly varying modes and are defined by

$$\psi_{mn}(X,r,\theta)=\left[A_{mn}(X)J_m(\alpha_{mn}(X)r)+B_{mn}(X)Y_m(\alpha_{mn}(X)r)\right]e^{-im\theta}. \tag{1.110}$$

where the duct coefficients $A_{mn}(X)$, $B_{mn}(X)$ and $\alpha_{mn}(X)$ are computed for each X, based on hub and tip radii $R_h(X)$ and $R_t(X)$ respectively. $\Gamma_{mn}(X)$ is the norm of the eigenfunction ψ_{mn}

$$\Gamma_{mn}(X)=\int_0^{2\pi}\int_{R_h(X)}^{R_t(X)}|\psi_{mn}(X,r,\theta)|^2\;rdrd\theta. \tag{1.111}$$

$k_{mn}(X)$ is the discriminant at position X and is determined by

$$k_{mn}^2(X)=k^2(X)-\beta_0^2(X)\alpha_{mn}^2(X). \tag{1.112}$$

where $k(X)=\omega/a_0(X)$ and $\beta_0^2(X)=1-M_0^2(X)$ with $M_0(X)=U_0(X)/a_0(X)$. The term $S_{mn}^{\pm}$ depends on the mechanism considered. The expressions for heterogeneous stator and rotor sources are given by

$$S_{mn}^{\pm}=\begin{cases} i\iint_S\frac{\partial}{\partial x_i}\left\{\psi_{mn}(Y,r_y,\theta_y)e^{i/\varepsilon\int^Y\gamma_{mn}^{\pm}(\xi)\,d\xi}\right\}f_{i,sB}(\boldsymbol{y})\,dS(\boldsymbol{y}) & \text{(stator)}\\ i\iint_S\frac{\partial}{\partial x_i}\left\{\psi_{mn}(Y,r_y,\tilde{\theta}_y)e^{i/\varepsilon\int^Y\gamma_{mn}^{\pm}(\xi)\,d\xi}\right\}f_{i,(sB-m)}(\tilde{\boldsymbol{y}})\,dS(\tilde{\boldsymbol{y}}) & \text{(rotor)}\end{cases}, \tag{1.113}$$

where Y stands for the slowly varying axial coordinate of the source points. The same simplifications as the ones done in App. B.3 can be done when considering an homogeneous stator. Pressure and axial velocity fluctuations can be expressed as a summation of slowly varying ducts similarly to the density and the acoustic power can be found in the same way as in Sec 1.6.1.

Accounting for transition points

It should be noted that the cut-on condition $k_{mn}^2(X) \geq 0$ in Eq. (1.109) is here ambiguous because the sign of k_{mn}^2 can change along the duct. In that case, k_{mn} necessarily goes through zero and the solution (1.109) becomes singular. Such modes are said to be transitional (cut-on/cut-off transition or cut-off/cut-on transtion). A further extension of Rienstra's theory has been made by Ovenden [87] to account for these modes via a composite solution. Comparisons against numerical results have validated the formulation [88].

In this work, this extension has not been implemented. Even if it shows big improvements of the solution obtained when a transition occurs, by predicting the transmitted and reflected wave generated, it is not expected to have a big effect in practice in the context of total noise prediction. Indeed, only a very small number of modes will be concerned by this transition behavior and the modes that are expected to be dominant will not be subject to transition.

1.6.3 First-order approximation of swirl effects

Strong swirling flow is present between the rotor and the stator and is known to have a considerable effect on noise generation and propagation. Studies started with Kerrebrock [89] who showed that the vortical, entropic and acoustic disturbances were coupled in the presence of swirl. The mean swirling flow is shown to affect significantly the vortical disturbances, such as the fan-blade wakes, and therefore the noise generation [90, 91]. It has also an important impact on the noise propagation [92]. An acoustic analogy including swirl effects (and shear flow effects) has been recently developed by Posson & Peake and results in a sixth-order wave equation with source terms depending on the swirl [38]. Applications of this analogy to the prediction of fan-trailing edge noise and fan-OGV broadband noise have been done by Posson & Peake [93] and Masson *et al.* [94] respectively and have shown a significant modification of the acoustic power caused by the swirling flow. Contrary to Goldstein's analogy presented in Sec. 1.6.1, the Green's function is computed numerically and is much more difficult to implement.

Another approach proposed by Topol [95] consists in approximating the swirl effects by a simple Doppler shift in the frequencies. The duct modes are computed considering an axial flow but replacing, for each mode of azimuthal order m, the actual frequency ω by $\omega - mU_\theta(r)/r$ where U_θ is the mean azimuthal velocity of the flow. If $U_\theta(r)/r$ is not constant along the span, the value at tip is generally taken [96]. This is a very simple way to deal with swirling flow and Posson & Peake have shown a good agreement with their analogy [38] when the swirl is simply a

solid-body rotation (i.e. $U_\theta(r)/r$ is constant). However, in the presence of a general swirling flow, they have shown that the effect of swirl can only be evaluated with the complete analogy.

Only the Doppler shift in frequencies will be used in this study for simplicity. The assumption of solid-body swirl will be evaluated in Part 4.

1.6.4 Further extensions

A lot of other models that consider more complex geometry and flow conditions exist. Concerning assumptions on the flow, Lilley has proposed in 1974 an acoustic analogy that accounts for shear flows [97]. This effect has also been included in the general Posson & Peake's acoustic analogy [38] and in Rienstra's sound propagation theory [98]. However, these theories are difficult to implement and are beyond the scope of the present study. About the geometry, the restriction of circular or annular ducts can be removed. Rienstra developed a theory for sound propagation that is valid in a slowly varying duct of arbitrary cross-section, which may be useful when dealing with asymmetric geometries [99]. Yet, it requires the numerical solving of an eigenvalue problem that is not straightforward and is therefore not considered in this study.

Another effect that is expected to impact a lot the sound propagation concerns the rotor (and stator) shielding effect. When a wave coming from the OGV travels upstream and encounters the fan, a part is transmitted and a part is reflected. Similarly for a wave coming from the fan that travels downstream and interacts with the OGV. The sound transmission through a cascade has therefore been extensively studied, first by considering two-dimensional rectilinear configuration [70, 71, 100], and then by considering quasi-three-dimensional and annular configurations [96]. The noise levels measured in the inlet are shown to be significantly affected by the rotor shielding, and the scattering into modes and frequencies different from those of the input waves has been highlighted. More recently, a linearized Euler based approach has been used to evaluate the transmission through a realistic three-dimensional rotor and has shown an important radial modes scattering which impacts significantly the transmission evaluation [101].

Summary of the section

Goldstein's analogy, which gives the sound propagation in an annular duct with uniform and axial flow, has been derived and will be used in this study. It allows to understand the generation of fan noise sources as well as the specific features of duct acoustics. However, the assumptions on the geometry or the flow are quite strong and extensions have been introduced. The theory of Rienstra which accounts for slowly varying ducts has been presented and will be used. In this theory, the duct geometry and the flow are allowed to vary "smoothly" in the axial direction. Swirl effects between the fan and the

OGV will also be included by a simple Doppler shift in frequencies.

1.7 Conclusion

The methods that can be used for the prediction of fan tonal noise have been introduced. Solving directly the equations of fluid dynamics to capture the acoustic fluctuations is possible thanks to CFD simulations. This solution, called the direct approach, is expensive and requires a filtering step to identify the acoustic part of the fluctuations that are extracted . These difficulties can be avoided by considering the aeroacoustic problem as a two-step procedure: generation of the sources and then propagation of the sources. This is the principle of the hybrid approach. Both approaches will be used in this thesis and some details have been given for each method. The concept of acoustic energy has also been introduced and will be used to quantify the sound generated by the fan module.

Chapter 2

Numerical simulations of a fan stage with bifurcations and inlet distortion

Contents

2.1 Introduction

This chapter aims at introducing the simulations performed in this PhD thesis to study the effects of distortion on the tonal noise. The engine model is first presented in Sec. 2.2. The numerical setup is described in Sec. 2.3 and convergence in terms of performance coefficients and acoustics is evaluated. A basic flow analysis, without including discussion about distortion, is finally provided in Sec. 2.4 in order to evaluate the main performances of the engine.

2.2 Engine model

The necessity to account for all fan tonal noise mechanisms to bring out any conclusion on the contribution of distortion has been explained in the introduction. A complete fan module therefore needs to be considered. Its characteristics are given in this section.

2.2.1 Geometry

A typical full-annulus turbofan composed of an air inlet duct, a fan, IGVs and OGVs is chosen in this work and is represented in its meridional view in Fig. 2.1. The domain is limited to the IGVs in the primary stream: the compressor, the combustion chamber and the turbine are not included in the computational domain.

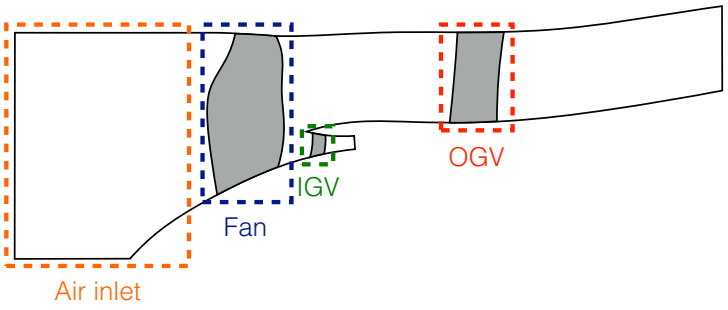

Figure 2.1: **Sketched meridional view of the configuration**

The fan has 18 identical blades and there are 93 identical IGVs and 48 non-identical OGVs, including two structural bifurcations (the pylon) at 6 and 12 o'clock and two struts at 3 and 9 o'clock as illustrated in Fig. 2.2. The heterogeneous OGV is typical of current engine architectures.

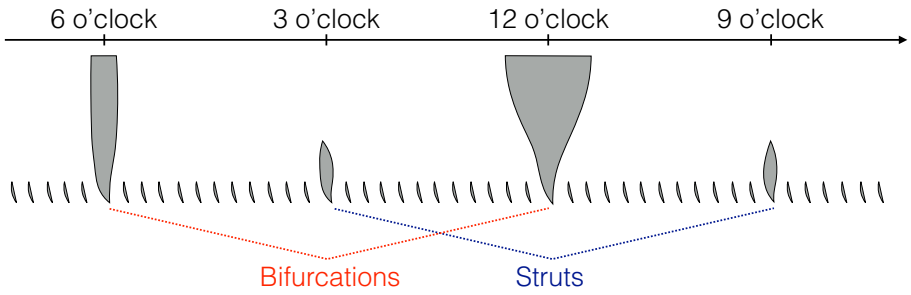

Figure 2.2: **Sketched geometry of the OGV row**

In order to isolate the effect of inlet distortion on the noise, two different geometries of air inlet duct are considered. The first one is perfectly axisymmetric and thus does not produce any distortion. The other one is asymmetric and has been designed for the purpose of the study to generate a level of distortion typical of the ones expected for UHBR engines. Fig. 2.3 shows the duct lines of both air inlets in the 6 o'clock - 12 o'clock plane (vertical plane). The asymmetric air inlet duct (red dashed lines) is slightly deviated downwards to offset the deflection of the flow in cruise conditions.

An overview of the geometry is proposed in Fig. 2.4 (in which an iso-surface of Q-criterion colored by vorticity modulus has been added). Because of the heterogeneity and the asymmetry of the configuration, the full-annulus geometry has to be part of the computational domain. The different elements listed above are highlighted. Only the flow inside the duct is simulated.

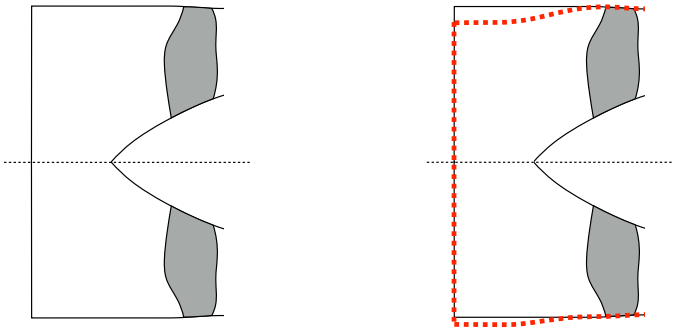

(a) Axisymmetric air inlet

(b) Asymmetric air inlet

Figure 2.3: **Sketched air-inlet duct geometries**

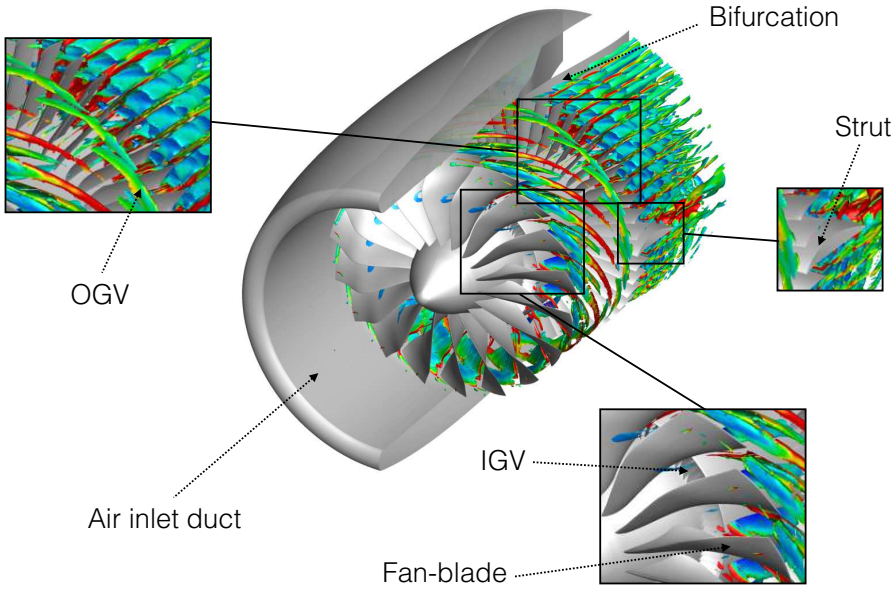

Figure 2.4: **Overview of the computational domain**

2.2.2 Operating points

The normalized experimental operating line of the studied turbofan is plotted in Fig. 2.5. The positions of the three acoustic certification points defined by ICAO [2] are given. The effect of distortion on fan tonal noise will be evaluated for each of these points. Therefore, six different configurations will be simulated and compared (three different regimes and two different air inlet geometries).

For each certification point, the normalized mass-flow rate $\dot{m}$ and total pressure ratio π are given in Tab. 2.1. The percentage of nominal speed %Nn and the relative tip Mach number M_{tip} are also added. Both the approach and the cutback regimes are subsonic ($M_{tip} < 1$) and the sideline one is transonic ($M_{tip} > 1$). The issue of shock noise therefore appears for the sideline point only. The cutback point is a high subsonic regime (M_{tip} slightly below 1) and shocks are expected to develop but

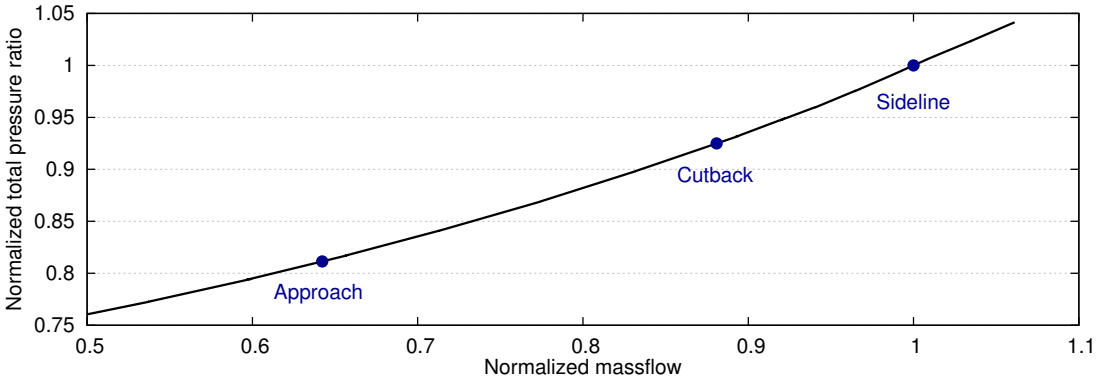

Figure 2.5: **Normalized experimental operating line**

without propagating in the inlet duct.

Regime	**%Nn**	**$\dot{m}$**	**Π**	**M_{tip}**
Approach	60	0.64	0.81	around 0.7
Cutback	80	0.88	0.92	slightly below 1
Sideline	90	1.00	1.00	around 1.1

Table 2.1: **Main characteristics of the studied operating points: %Nn is the percentage of nominal speed, $\dot{m}$ the normalized mass-flow rate, Π the normalized total pressure ratio and M_{tip} the relative tip Mach number**

Summary of the section

The engine model that has been chosen to study the effects of distortion is composed of an air inlet, a fan, an IGV row and a completely heterogeneous OGV row including struts and bifurcations. Two air inlet geometries are considered to isolate the effects of inlet distortion: one is axisymmetric and does not produce any distortion and the other is asymmetric and produces a distortion typical of the one expected in future UHBR engines. The three regimes that correspond to the three acoustic certification operating points are studied.

2.3 Numerical setup and convergence

The numerical setup is described in this section and the convergence of performance coefficients and unsteady pressure distribution on blades and vanes is evaluated.

2.3.1 Numerical setup

The elsA software

The URANS equations (A.8) are solved using Onera's CFD solver *elsA* which is based on a cell-centered finite volume approach on a structured multi-block grid [102].

Mesh

The mesh is built with a O4H topology for each blade/vane and a C topology for the splitter nozzle (which separates primary and secondary fluxes). A butterfly topology is adopted in the air inlet to account for the cylindrical domain.

Two different mesh refinements are considered. All six configurations are run on meshes M1 suited for the propagation of acoustic waves at the BPF. To study mesh convergence (and to allow the analysis at higher frequencies), one configuration (the sideline point with asymmetric air inlet duct) is also run on a mesh M2 designed for direct acoustic prediction at 2BPF. Test cases detailed in App. C.1 have shown that, with the schemes used (detailed below), 20 points per wavelength were needed to propagate a wave correctly. This criterion is respected for both upstream and downstream acoustic waves propagating at the BPF for M1 meshes, and for the ones at 2BPF for the M2 mesh. For practical reasons, the M2 mesh has first been achieved and the M1 mesh has been built by taking one in every two points of the M2 mesh in each direction.

Stretching zones have also been added at the inlet and the outlets of the domain to avoid wave reflections at the boundaries. The same strategy was successfully employed by Bonneau *et al.* [21] with the same solver and one-dimensional test cases have validated the parameters used for the stretching (see App. C.2).

M1 meshes are composed of 70 million points, with approximately 100 and 900 points in the radial and azimuthal directions respectively. Gaps between the fan-blade tips and the casing are included and are discretized with 19 points. The maximum size of the cells in the axial direction is such that there are at least 20 points per wavelength for acoustic waves propagating upstream at the BPF. The downstream waves have a longer wavelength and are necessarily discretized with more points. This last criterion is satisfied for 2BPF acoustic waves for the M2 mesh. The latter is characterized by approximately 200 and 1800 points in the radial and azimuthal directions respectively and by 37 points across the tip gaps. The total number of points of the M2 mesh is about 570 millions. These figures are summarized in Tab. 2.2.

In total, seven simulations are performed. They are listed in Tab. 2.3 with their short names that will be used in the rest of the manuscript. The number, "A", "N" and "R" stand for the percentage of nominal speed, "axisymmetric", "non-axisymmetric" and "refined" respectively. The present manuscript focuses on the

Mesh	N_{tot}	N_r	N_θ	N_x/λ^+_{1BPF}	N_{gap}
M1	70 M	100	900	20	19
M2	570 M	200	1800	40	37

Table 2.2: **Mesh characteristics: total number of points N_{tot}, number of points in the radial direction N_r, number of points in the azimuthal direction N_θ, number of points per wavelength for acoustic waves propagating upstream at the BPF N_x/λ^+_{1BPF} and number of points across the tip gaps N_{gap}**

comparison between axisymmetric and asymmetric configurations and only the results obtained with M1 meshes are shown. The effects of the mesh resolution are however studied for the sideline asymmetric configuration in App. D.

Regime	Air inlet	Mesh	Name
Approach	Axisymmetric	M1	60A
Approach	Asymmetric	M1	60N
Cutback	Axisymmetric	M1	80A
Cutback	Asymmetric	M1	80N
Sideline	Axisymmetric	M1	90A
Sideline	Asymmetric	M1	90N
Sideline	Asymmetric	M2	90NR

Table 2.3: **List of the performed simulations and associated names**

Turbulence modeling

The $k-\omega_t$ turbulence model by Wilcox [103] detailed in App. A.2 is chosen. In order to reduce the dependency on inlet turbulence, Zheng's limiter is added [104].

Discretization schemes

Spatial discretization is done with Roe's scheme with the MUSCL reconstruction (third-order accuracy) described in App. A.3. The temporal discretization is achieved with the implicit backward Euler scheme with a Dual Time Step (DTS) sub-iteration algorithm (second order accuracy). For M1 meshes, one blade passage is described by 100 time steps, leading to a total of 1800 time steps per rotation. For the M2 mesh, 200 time steps per blade passage are computed (3600 time steps per rotation) to study also the effects of time discretization.

Boundary conditions

All the walls are considered as adiabatic. A uniform flow is specified at the inlet, a mass-flow rate is imposed at the exit of the primary flux (downstream of the IGV row) and a pressure condition is used at the exit of the secondary flux (downstream

of the OGV row). This pressure condition satisfies the radial equilibrium and a valve law sets the value of pressure p_{piv} at a specified point during the time marching to be as close as possible to a targeted operating point (mass-flow rate and mean pressure). The valve law is written

$$p_{piv} = p_{ref} + \lambda \left(\frac{\dot{m}}{\dot{m}_{ref}} \right)^2 , \tag{2.1}$$

where p_{ref} and $\dot{m}_{ref}$ are specified reference pressure and mass-flow rate, $\dot{m}$ the mass-flow rate at current iteration and λ the relaxation coefficient.

Rotor-stator interfaces

Three rotor-stator interfaces are present in the computational domain:

- between the fixed air inlet duct and the rotating fan;
- between the rotating fan and the fixed IGV row;
- and between the rotating fan and the fixed OGV row.

The transfer of information through all these parts is dealt with sliding non-conformal interfaces [105].

2.3.2 Convergence

The convergence is shown here for the simulation 60A only but all other configurations show similar behaviour.

Performance coefficients

The evolution of the normalized mass-flow rate at inlet and outlet, the normalized total pressure ratio and the normalized isentropic efficiency are given in Fig. 2.6. At $t \approx 2.5$ rotations, the valve relax has been adjusted in order to be closer to the experimental operating line. After approximately 7 rotations, all coefficients reach a plateau and inlet and outlet mass-flow rate becomes coincident.

Same procedure has been applied to all configurations to be sufficiently close to the experimental operating line. The converged values of the resulting normalized mass-flow rate and normalized total pressure ratio are reported in the experimental fan map given in Fig. 2.7. All simulations are inside the $\pm 1\%$ error region (maximum tolerance acceptable) and axisymmetric and asymmetric simulations operate at very similar operating conditions for all regimes.

Mean blade and vane forces

The convergence of the flow around blades and vanes must also be checked. Global convergence is first evaluated by computing the module of the integrated pressure force F on a blade or on a vane as:

$$F = \left| \iint_S p\mathbf{n}\, dS \right| . \tag{2.2}$$

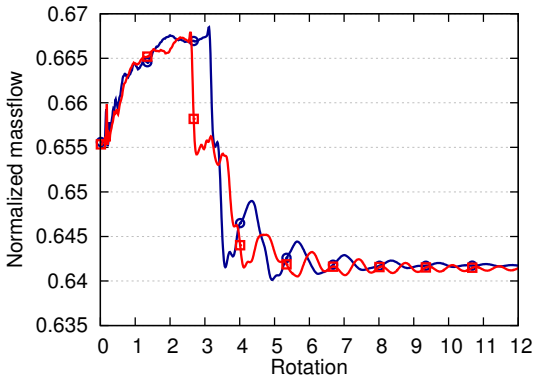

(a) Normalized mass-flow rate: inlet, outlet

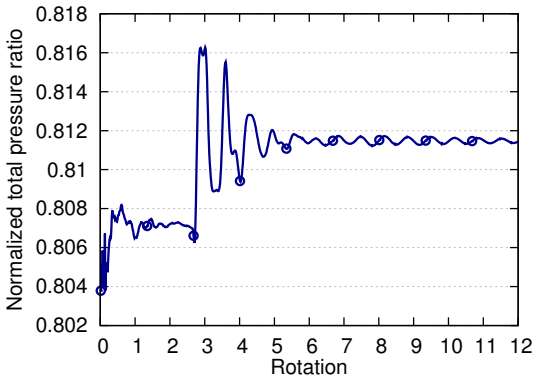

(b) Normalized total pressure ratio

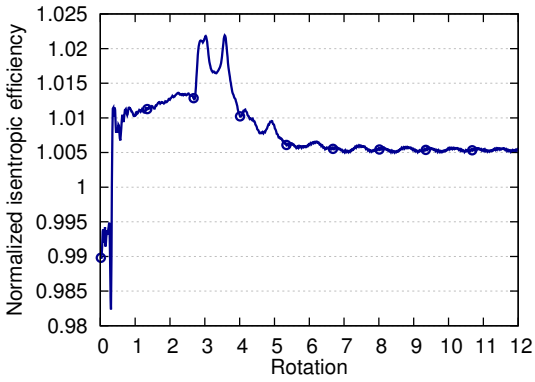

(c) Normalized isentropic efficiency

Figure 2.6: **Evolution of performance coefficients during the simulation (60A)**

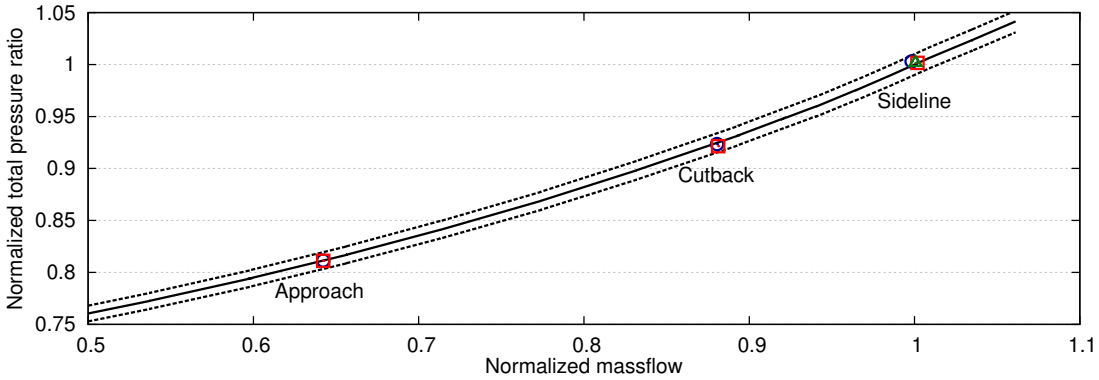

Figure 2.7: **Fan map: — experimental line, --- limits of the ±1% error region, ○ 60A/80A/90A simulations, □ 60N/80N/90N simulations, △ 90NR simulation**

p is the static pressure on the surface S of the blade/vane and $\mathbf{n}$ the normal to the wall. The evolution of this force integrated over one fan-blade, one (classical) OGV and one IGV during the last iterations is represented in Fig. 2.8. The sliding

average, computed by averaging the signal at each timestep over the last rotation, is also shown. The forces are normalized by their converged mean values.

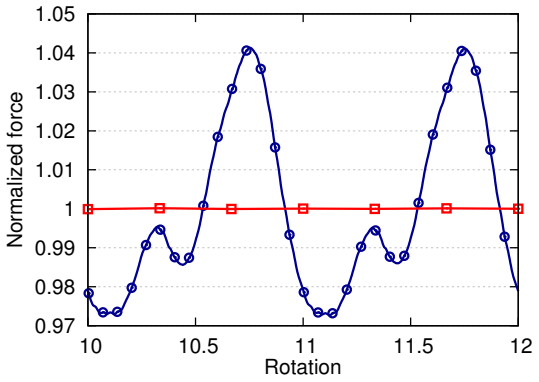

(a) Fan-blade force

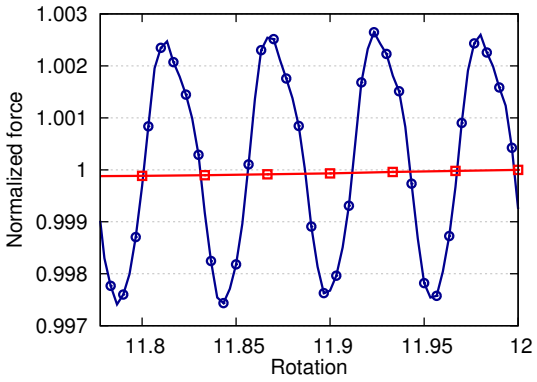

(b) OGV force

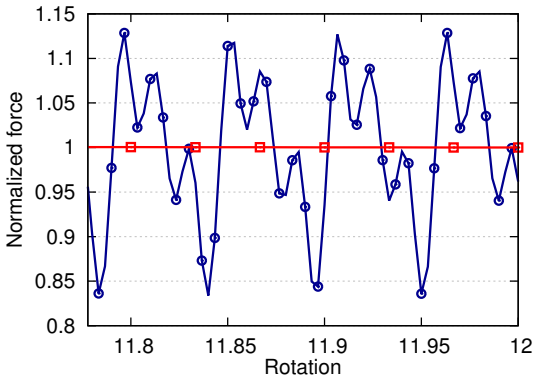

(c) IGV force

Figure 2.8: **Evolution of one fan-blade force, one (classical) OGV force and one IGV force normalized by their converged mean values: —o— instantaneous evolution, —□— sliding average**

On the one hand, the evolution of the fan force presents one major lobe (amplitude of 6.5% of the mean value) and one less important one (amplitude of 1.5% of the mean value), due to the passage of the fan blade in front of the upper pylon (the largest one, at 12 o'clock) and the lower one (the smaller one, at 6 o'clock) respectively. The mean value of the fan force is well converged because no variation of the sliding average during the last two rotations is observed. On the other hand, the evolution of both the OGV and the IGV forces show a pattern related to the number of fan blades (18), caused by the impacts of the fan-blade wakes. Two ninths of a rotation are represented here for these forces so that 4 lobes are oberved. For the OGV, the relative amplitude (0.5% of the mean value) is lower than the one observed in the fan force while it is of greater amplitude for the IGV (30% of the mean value). As it was the case for the fan-blade force, the OGV and IGV mean forces are well converged.

Unsteady blade and vane forces

The convergence of unsteady flow features must also be checked when dealing with acoustics. It has been shown in the introduction that most sources of fan tonal noise were associated with unsteady blade and vane loadings. Temporal Fourier transforms of the integrated pressure forces (2.2) are therefore computed and results are shown in Fig. 2.9 for particular harmonics. The RF and its first two harmonics are represented for the fan to highlight the interaction with the distortion. For the OGV and IGV, the BPF and its harmonics, illustrating the interaction with the fan-blade wakes, are chosen. The results have been normalized by the converged values of the corresponding mean force. All frequencies reach a plateau after 10 rotations which ensures the convergence of the integrated unsteady loadings.

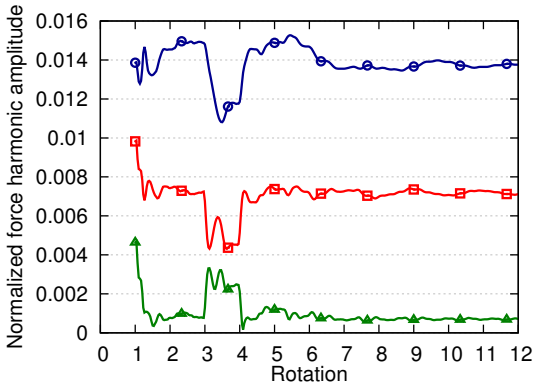

(a) Fan-blade force

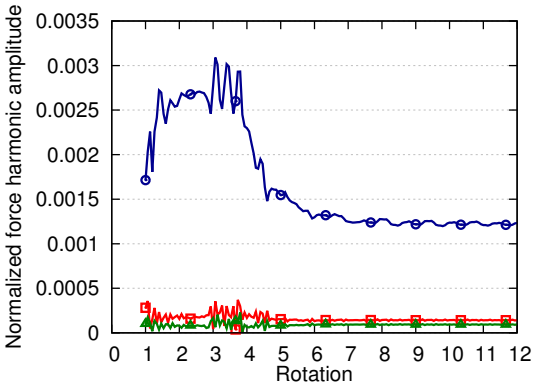

(b) OGV force

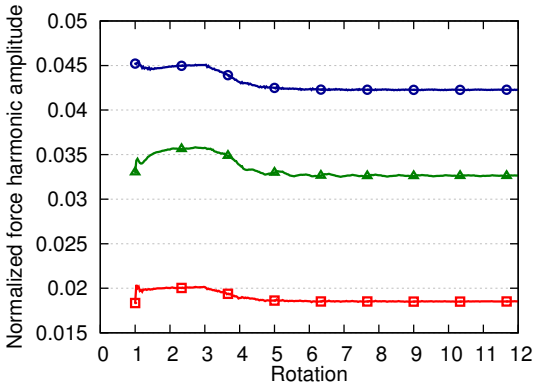

(c) IGV force

Figure 2.9: **Evolution of the normalized amplitude of the pressure force harmonics of one fan-blade, one (classical) OGV and one IGV: fundamental frequency (RF for fan and BPF for OGV/IGV), 1^{st} harmonic, 2^{nd} harmonic**

Pressure distribution

This assessment of global convergence can mask local variations of the flow. In order to ensure local convergence, Fourier harmonics of the pressure distribution

over one fan blade, one OGV and one IGV are computed over the last two rotations and are compared in Fig. 2.10. Again, the RF is shown for the fan and the BPF is chosen for both OGV and IGV. The distribution is plotted at 50% and 95% of blade/vane height only but similar results were obtained at all spanwise locations.

Excepted one silent point on the fan blade (very low absolute value), the harmonic pressure distributions computed during the last two rotations are very similar and the local unsteady loadings can be considered as converged.

Summary of the section

Full-annulus URANS simulations of the complete fan module have been performed to study the effects of inlet distortion on the tonal noise. The performance coefficients are converged after approximately 7 rotations and are found to be similar between the axisymmetric and the asymmetric configurations, making their comparison legitimate. The acoustic convergence is also ensured by comparing the loading harmonics over the blades and vanes computed during the last two rotations.

2.4 Basic flow features

An analysis of the basic flow features without inlet distortion is proposed in this section. The main flow patterns are highlighted and the global engine performances are evaluated for the three regimes considered.

2.4.1 Extractions planes and normalization

Several areas of interest are identified for the analysis of the results. They are shown in Fig. 2.3. Eight axial planes are defined: planes P1, P2 (upstream of the fan), P3, P4, P5 (interstage), P6, P7 (downstream of the OGVs) and P8 (downstream of the IGVs). Four cuts at constant vane heights are also specified: 25%, 50%, 75% and 95% of vane height.

All the results in the manuscript are normalized. From now:

- mean velocities are normalized by $V_0 = R_{tip}\ \Omega_{90\%Nn}$ with R_{tip} the fan-blade tip radius and $\Omega_{90\%Nn}$ the engine rotational speed at sideline;
- mean angles are normalized by the maximum stagger angle of fan blades;
- mean pressures (both static and total) are normalized by the formula $(p - p_0)/(0.5\rho_0 V_0^2)$ with p the static or total pressure and p_0 and ρ_0 the reference pressure and reference density respectively;
- and fluctuating velocities and pressure are normalized by an arbitrary value;

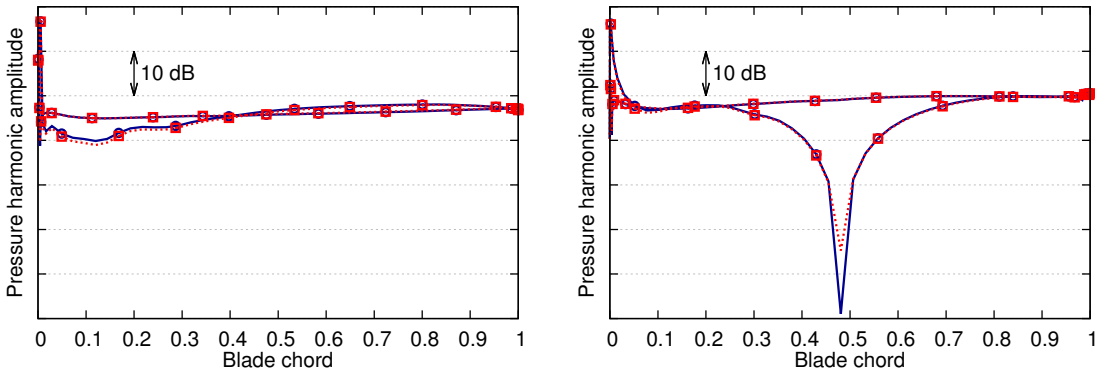

(a) Fan - 50% of blade height

(b) Fan - 95% of blade height

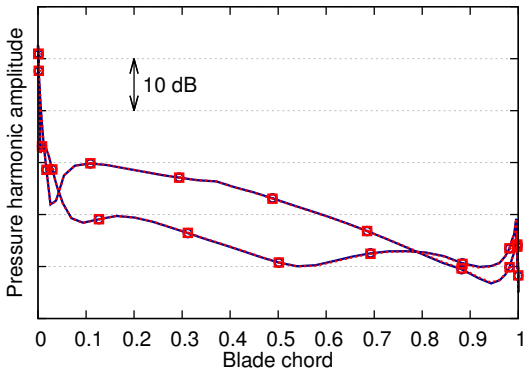

(c) OGV - 50% of vane height

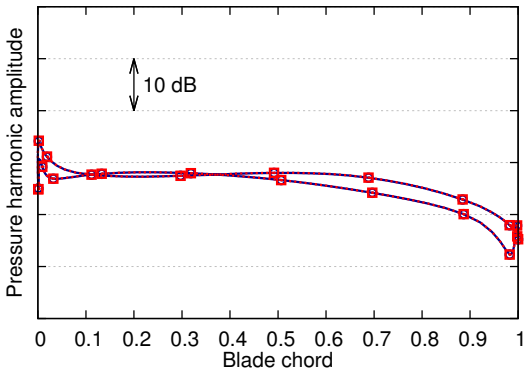

(d) OGV - 95% of vane height

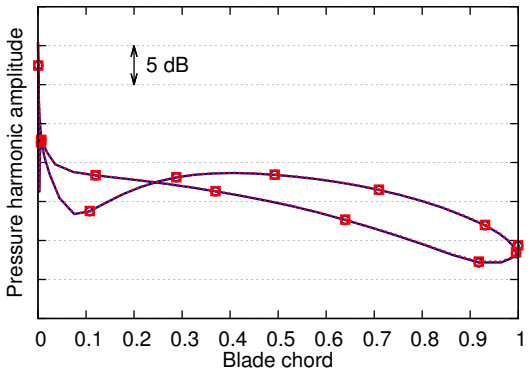

(e) IGV - 50% of vane height

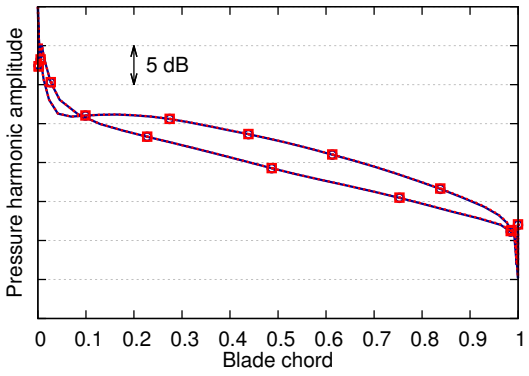

(f) IGV - 95% of vane height

Figure 2.10: **Pressure distribution over one fan-blade, one OGV and one IGV at 50% and 95% of blade/vane height at the frequency of interest (RF for the fan and BPF for the OGV and IGV): —o— harmonics computed during the second to last rotation, ··□·· harmonics computed during the last rotation**

2.4.2 Instantaneous flow

Contour maps

Instantaneous contour maps of static pressure and axial velocity are first given at different vane heights in Figs. 2.12 and 2.13 respectively. Only the maps at approach

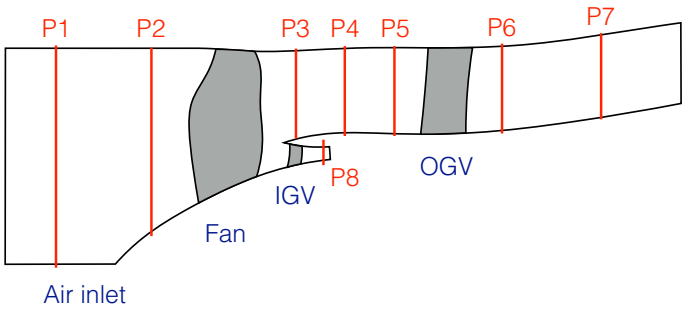

(a) Axial planes

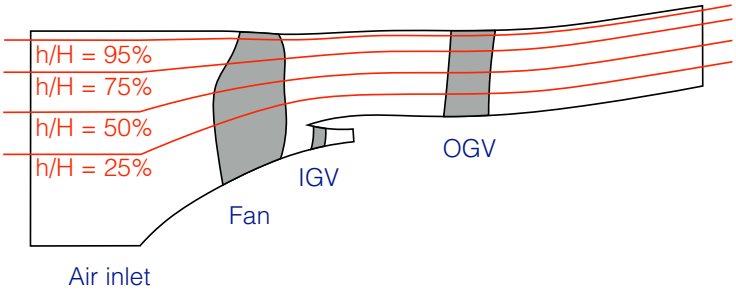

(b) Constant vane heights

Figure 2.11: **Sketched air-inlet duct geometries**

without inlet distortion are shown but similar patterns (with different absolute values) are obtained at cutback and sideline. The static pressure is increased from the inlet to the outlet thanks to the work transmitted by the fan to the fluid. The circumferential inhomogeneity of the flow is clearly visible at all vane heights and seems to be maximum close to the pylon. This heterogeneity is caused by the potential effect of the pylon and is decreasing in the upstream direction. It is also present in the axial velocity contour maps and it is possible to see that the high pressure areas correspond to the areas where the flow is slown down by the pylon. Upstream of the fan, the flow is still distorted and this is better shown in the axial velocity maps. Those maps also highlight the fan-blade wakes impacting the OGVs that slice them into lumps of low-momentum. The OGV wakes are spread far in the bypass duct. At some vane heights, the wake of the visible strut is deviated consequently so that it crosses the wake of its neighbour vane. At 95% of vane height, the velocity of the flow is less important than at the other represented vane heights, probably because of the proximity of the casing.

Flow around blades and vanes

The flow around the blades and the vanes is of paramount importance to ensure a correct operation of the engine. Axial velocity contours around fan blades, OGVs and IGVs are therefore shown at mid-span in Fig. 2.14, again at approach conditions. The acceleration of the flow is observed along the suction side of each blade and vane. The flow around the different fan blades is nearly the same but inhomogeneities are observed around the IGVs and OGVs. This is caused by the distortion coming from

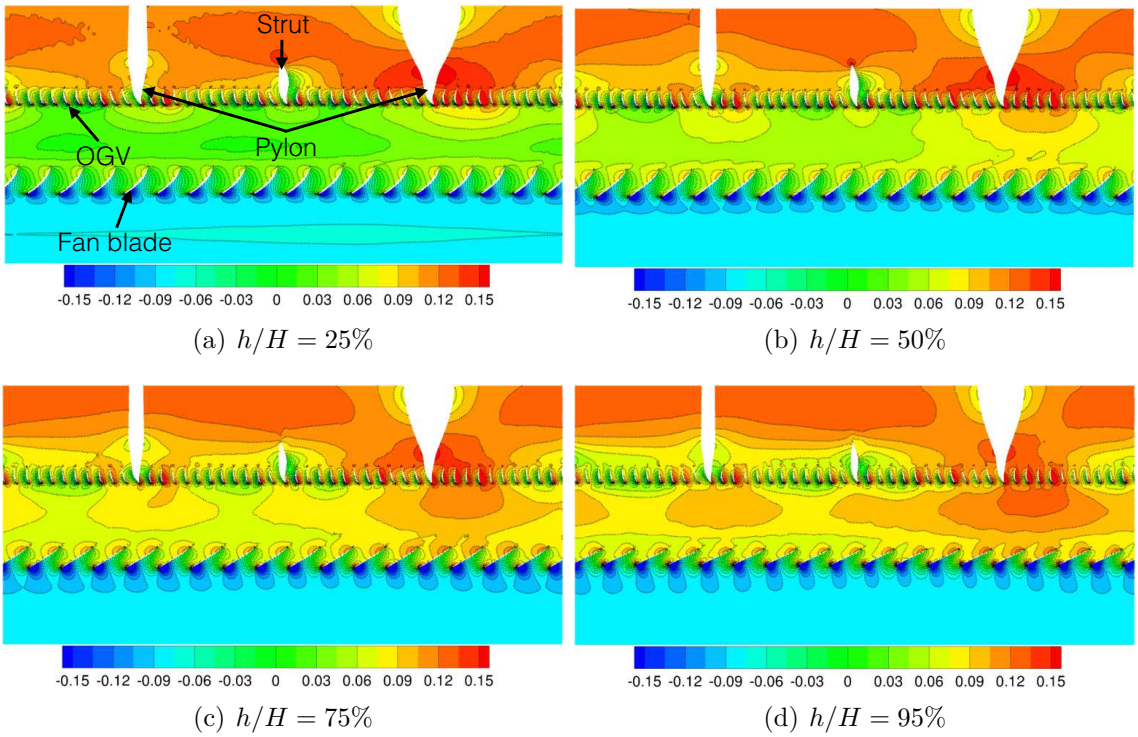

(a) $h/H = 25\%$ (b) $h/H = 50\%$

(c) $h/H = 75\%$ (d) $h/H = 95\%$

Figure 2.12: **Instantaneous contour maps of normalized static pressure at 25%, 50%, 75% and 95% of vane height (60A)**

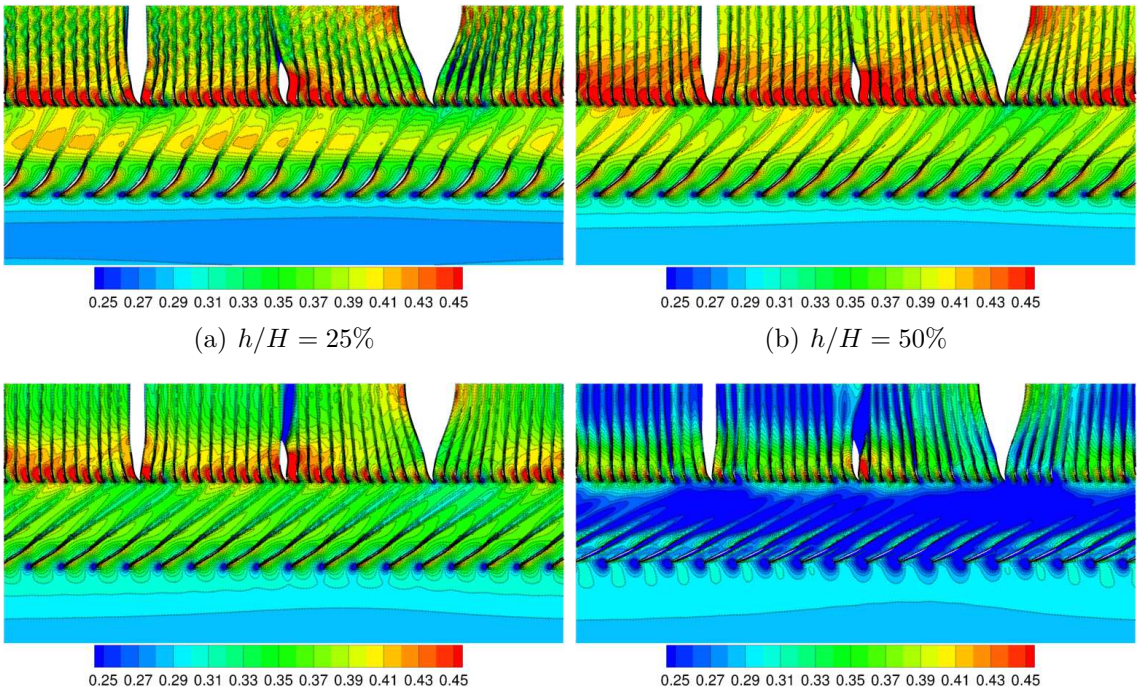

(a) $h/H = 25\%$ (b) $h/H = 50\%$

(c) $h/H = 75\%$ (d) $h/H = 95\%$

Figure 2.13: **Instantaneous contour maps of normalized axial velocity at 25%, 50%, 75% and 95% of vane height (60A)**

the potential effect of the pylon and it is naturally much more important around the OGVs.

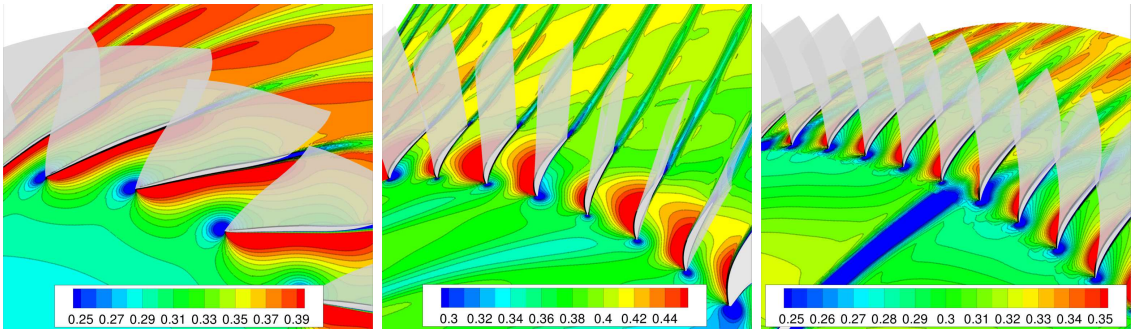

(a) Fan (b) OGV (c) IGV

Figure 2.14: **Instantaneous normalized axial velocity contours at mid-span around fan blades, OGVs and IGVs (60A)**

Shocks at sideline

At sideline, shocks develop on the suction side of the blades and propagate in the inlet. In order to visualize them, the density gradient normalized by the density $\boldsymbol{\nabla}\rho/\rho$ is represented on a cut at 95% of vane height and on a three-dimensional isosurface in Fig. 2.15. As expected, the shocks propagate via an helicoid movement in the inlet and with a decreasing amplitude [106].

(a) Cut at $h/H = 95\%$ (b) 3D isosurface

Figure 2.15: **Visualization of the normalized density gradient in the inlet duct (90A)**

Secondary flows

An iso-surface of Q-criterion colored by vorticity modulus was shown in Fig. 2.4 and highlights some flow features. The fan-blade wakes and the OGV wakes propagate far in the bypass duct and a flow separation on the visible strut is observed.

Secondary flows are evidenced, such as the fan-blade tip vortices which impinge on the OGVs. Hub corner vortices also appear to develop along the OGVs.

2.4.3 Mean flow

The instantaneous flow analysis has highlighted some of the main flow patterns in the engine. The focus will now be put on the mean flow in order to evaluate the main performances of the engine. The mean flow is computed by averaging the instantaneous flow during the last rotation.

Meridional plane

A convenient way to look at the mean flow patterns is to use the meridional plane. The meridional plane is obtained by first defining a target grid with a specified number of points in the axial and radial directions. For each point (x, r), a value is represented and corresponds to the azimuthal average, weighted by the axial momentum, of the corresponding variable. The meridional planes of normalized axial velocity, static pressure, total pressure and flow angle at approach conditions are given in Fig. 2.16. Blades are highlighted by black solid lines.

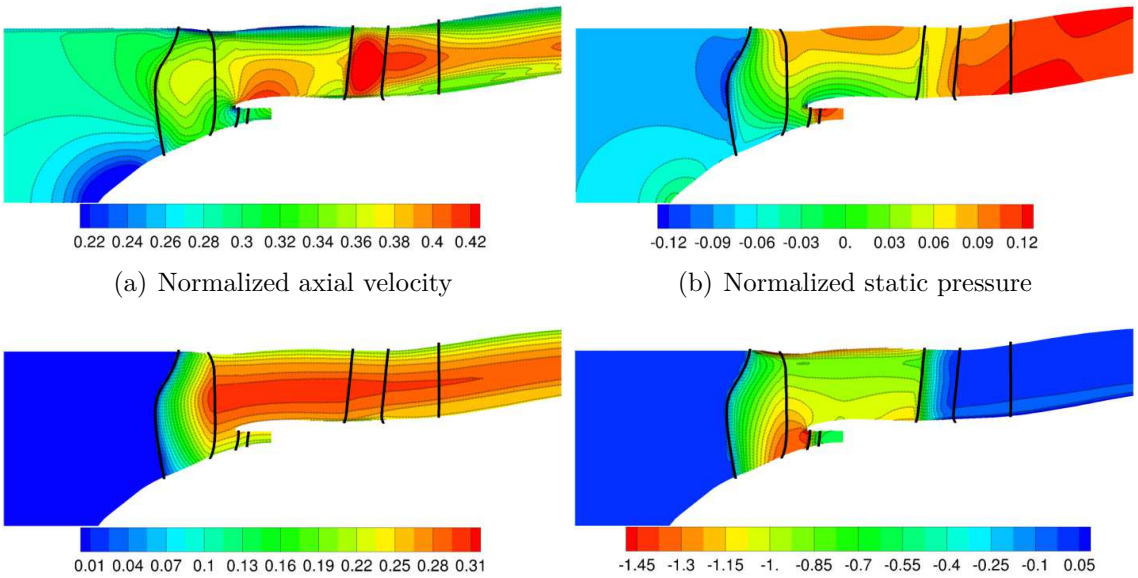

(a) Normalized axial velocity

(b) Normalized static pressure

(c) Normalized total pressure

(d) Normalized flow angle

Figure 2.16: **Meridional planes (60A)**

The acceleration of the flow through the fan-OGV stage is visible on these maps, as well as the increase of both static and total pressure. The flow angle map shows how the flow is rotating in the fan-OGV interstage and redressed by the OGVs. Radial non-uniformity is also clearly present. With different magnitude, similar maps could be drawn at cutback and sideline. In the following sections, the axial and radial evolutions of the flow are adressed more precisely and the regimes are compared.

Axial flow evolution

The axial evolution of the mean flow is obtained by averaging the meridional plane at each axial position (average weighted by the axial momentum). This procedure is applied to the normalized axial velocity, static pressure, total pressure and flow angle and results are given in Fig. 2.17 for the three operating points.

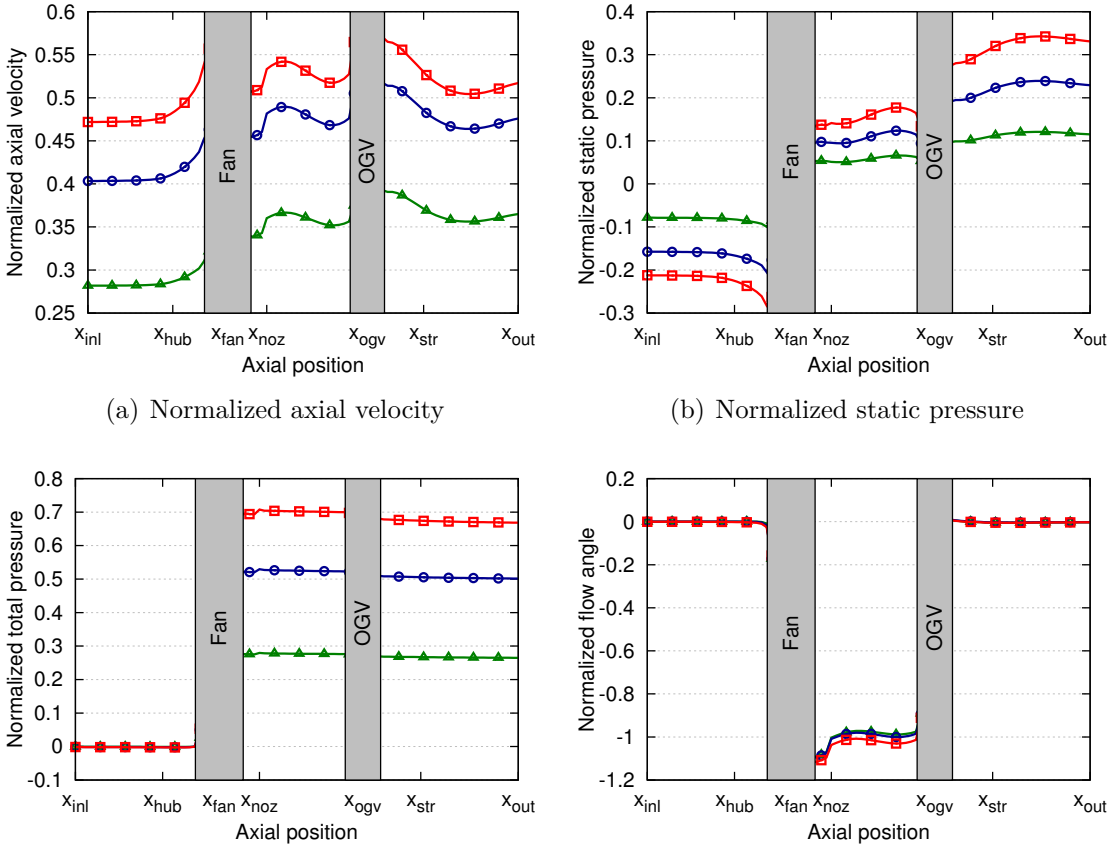

(a) Normalized axial velocity

(b) Normalized static pressure

(c) Normalized total pressure

(d) Normalized flow angle

Figure 2.17: **Axial evolution of the mean flow: approach, cutback, sideline**

At the entrance of the engine, the total pressure p_t is constant and similar between all regimes and is determined by the atmospheric total pressure. It is related to the static pressure p and the Mach number of the flow M by the isentropic relation

$$\frac{p_t}{p} = \left(1 + \frac{\gamma - 1}{2} M^2\right)^{\frac{\gamma}{\gamma - 1}}, \tag{2.3}$$

where γ is the ratio of specific heats. The mass-flow rate determines the axial velocity of the flow and the Mach number (angle equal to 0 at inlet) and finally the static pressure. Because the mass-flow rate increases with the regime, the axial velocity is also increased (0.28 velocity units at approach, 0.40 at cutback and 0.47 at sideline) and the static pressure is decreased (-0.08 pressure units at approach, -0.16

at cutback and -0.21 at sideline) at the entrance. The reduction of the section in the engine also contributes to the acceleration of the flow. The fan provides energy to the flow which leads to a rise of the total pressure. The latter again reaches a constant value in the interstage region which increases with the regime (+0.26, +0.50 and +0.66 pressure units at approach, cutback and sideline respectively). It results in higher axial velocity and static pressure. An important part of the energy is also used to rotate the flow, as evidenced by the evolution of the flow angle. The latter reaches a value close to the maximum stagger angle of the fan blades in the interstage region and for all regimes. The OGVs straighten the flow correctly at all regimes (exit angle of the flow equal to 0) and convert the energy of the swirling flow into static pressure (+0.05, +0.11 and +0.18 pressure units at approach, cutback and sideline respectively). A slight decrease of the total pressure (up to 0.3 pressure units at sideline) is also noticed through the OGV row and is caused by aerodynamic losses.

Radial flow evolution

The radial evolution of the mean flow is now checked by extracting the profiles from the meridional plane at three different axial planes. The planes P2 (upstream of the fan), P4 (in the interstage) and P6 (downstream of the OGVs) shown in Fig. 2.11 are chosen. Results for axial velocity, static pressure, total pressure and flow angle are given in Figs. 2.18, 2.19, 2.20 and 2.21 respectively.

Upstream of the fan, the axial velocity is almost constant from 60% to 95% of channel height. The casing boundary layer is expanded over about 5% of the channel height at all regimes. Close to the hub, the axial velocity is quite low compared to the mean value over the section. This is caused by the curvature of the hub close to the plane P2 (see Fig. 2.16) which leads to a radial component of the velocity vector. Downstream of the fan, the contraction contributes to accelerate the flow close to the hub while the curvature of the tip slows the flow. Downstream of the OGVs, the radial profile of axial velocity is close to a classical pipe flow profile except that a hump is observed close to the hub because of the development of corner vortices along the vanes. The increase of axial velocity with regime is conserved at all radii. In terms of static pressure, the radial evolution is globally the opposite of the one of the axial velocity, but without boundary layers. At the exit of the engine, the static pressure is therefore almost constant in the radial direction. The total pressure is perfectly homogeneous at inlet and equal to the atmospheric total pressure (normalized value equal to 0) and the evolution is quite smooth in the interstage and downstream of the OGVs, with a maximum level at mid-span and lower values close to the hub and tip (linked to the dynamic pressure which is low close to the boundaries). As for the azimuthal flow angle, it is constant and equal to 0 upstream of the fan. In the interstage region, its value is almost constant and equal to the maximum stagger angle of fan blades, except close to the tip where the absolute value is maximum (because of the tip-leakage vortices). The flow is well straightened by the OGVs because the flow angle is almost zero along the span downstream of the OGVs. Close to the hub however, the flow has a small angle (around 0.1 angle unit) that can be attributed to corner vortices.

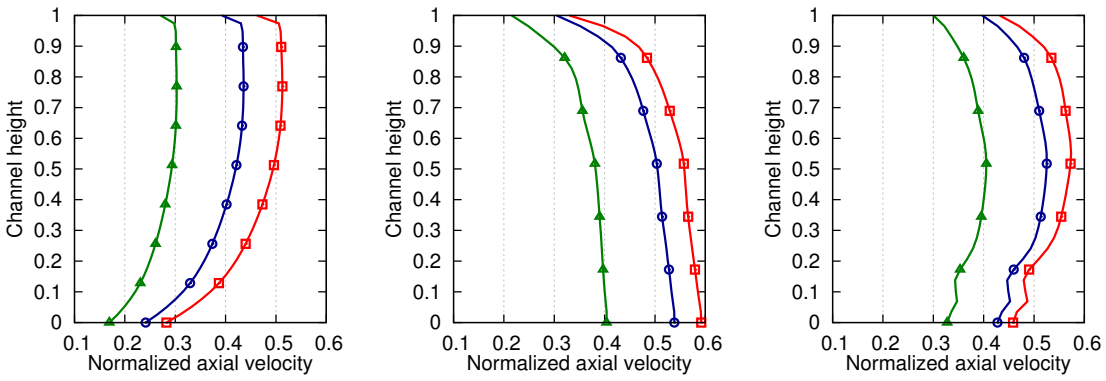

(a) Plane P2 (b) Plane P4 (c) Plane P6

Figure 2.18: **Radial evolution of the normalized axial velocity: approach, cutback, sideline**

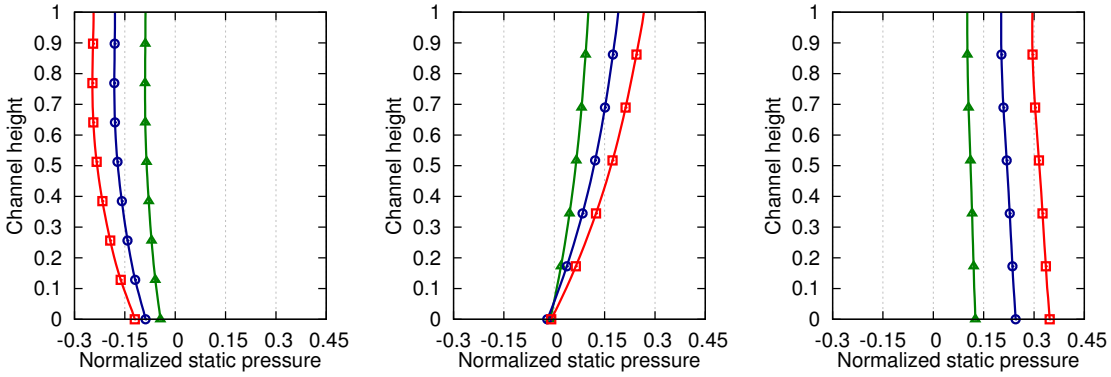

(a) Plane P2 (b) Plane P4 (c) Plane P6

Figure 2.19: **Radial evolution of the normalized static pressure: approach, cutback, sideline**

Summary of the section

Basic flow features have been analyzed on the axisymmetric configurations (i.e. without inlet distortion). Instantaneous contour maps highlighted the fan-blade wakes impinging on the OGVs, the distortion that comes from the potential effect of the pylon and the shocks that propagate upstream at sideline conditions. The performance of the engine at approach, cutback and sideline points has been evaluated from the axial and the radial evolution of the mean flow. The energy brought by the fan is transmitted to the fluid and results in a increase of outlet static pressure. Secondary flows have also been pointed out and described.

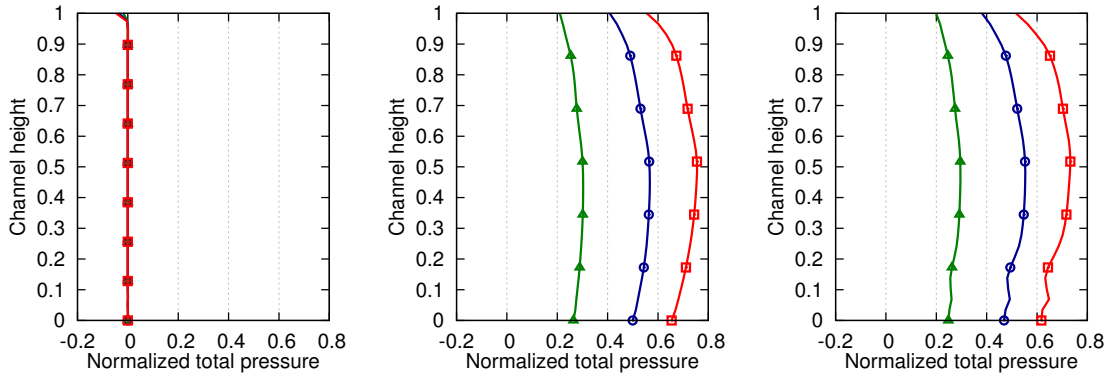

(a) Plane P2 (b) Plane P4 (c) Plane P6

Figure 2.20: **Radial evolution of the normalized total pressure: approach, cutback, sideline**

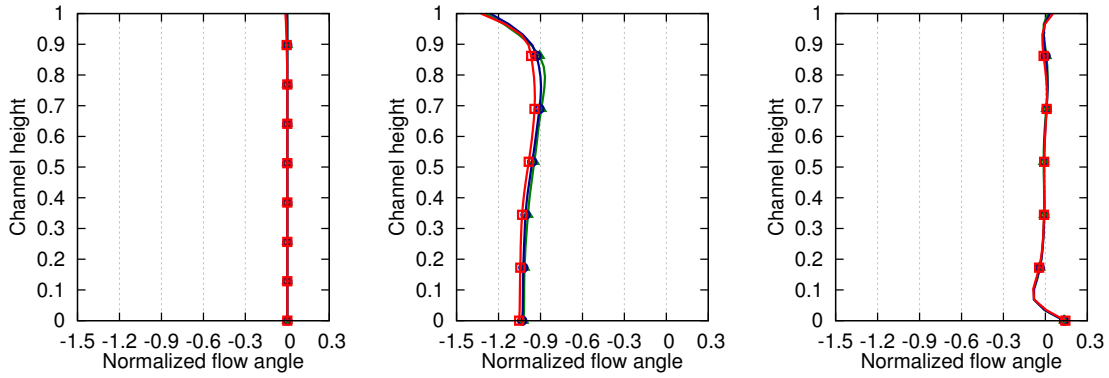

(a) Plane P2 (b) Plane P4 (c) Plane P6

Figure 2.21: **Radial evolution of the normalized flow angle: approach, cutback, sideline**

2.5 Conclusion

This chapter introduced the numerical simulations that have been performed to study the impact of distortion on fan tonal noise. The engine model is composed of an air inlet, a fan, an IGV row and a completely heterogeneous OGV row including struts and bifurcations. Full-annulus URANS simulations have been run at each certification point for two inlet geometries (axisymmetric vs. asymmetric) in order to isolate the effects of inlet distortion (the main source of distortion in the fan plane). The performance coefficients and the equivalent acoustic sources are converged after 7 rotations. The fan module is shown to operate correctly by converting the energy brought by the fan into an increase of static pressure. Secondary flows such as tip-leakage and corner vortices have also been pointed out.

Chapter 3

Characterization of the distortion and impact on aerodynamics

Contents

3.1 Introduction

In this chapter, the distortion caused by the potential effect of the bifurcations is first discussed in Sec. 3.2. Its shape and its evolution along the engine is studied and a quantification is proposed. A similar analysis is then performed on the air inlet distortion in Sec. 3.3. The impact of both kinds of distortion on unsteady aerodynamics is finally evaluated in Sec. 3.4.

3.2 Distortion caused by the potential effect of the pylon

The analysis and the quantification of the distortion that comes from the potential effect of the pylon is performed in this section by focusing on the configurations with axisymmetric air inlets.

3.2.1 Characterization of the potential effect near the pylon

As shown previously in the normalized static pressure and axial velocity contour maps in Figs. 2.12 and 2.13, the pylon and the struts are responsible for an important potential effect that goes upstream, up to the fan. Axial cuts of the mean flow are performed in plane P5 right upstream of the OGV row (see Fig. 2.11) in order to visualize it. Results for normalized axial velocity and static pressure are shown in Fig. 3.1 at approach conditions.

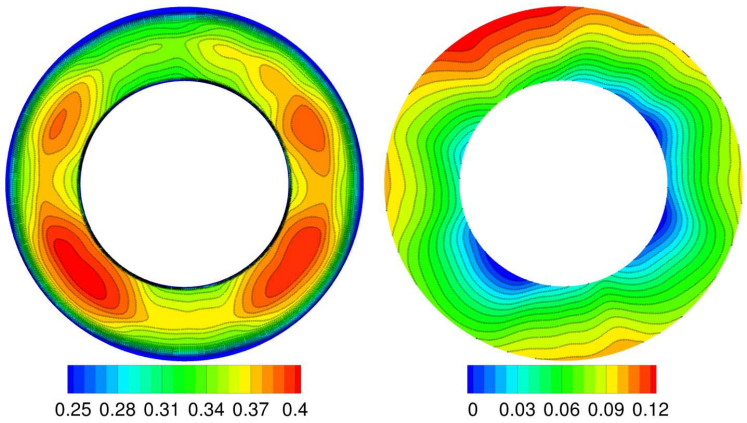

(a) Normalized axial velocity (b) Normalized static pressure

Figure 3.1: **Mean flow in plane P5 right upstream of the OGVs (60A)**

The reduction of normalized axial velocity caused by the different obstacles (pylon and struts) is observed. There are four zones of reduced velocity: in the order of importance, at 12 o'clock (big bifurcation), at 6 o'clock (small bifurcation) and at 3 and 9 o'clock (struts). The potential effect of the classical OGV (the 44 other vanes) is not visible. By comparing both maps, it can be noticed that high pressure are found in the areas with small axial velocity. The maximum value of normalized static pressure is slightly deviated in the counter-clockwise direction, which corresponds to the direction opposite to the swirling flow.

Some profiles are extracted from these maps at different vane heights to provide a more quantitative description of the potential effect. They are shown in Fig. 3.2. The corresponding azimuthal mode distribution obtained by performing an azimuthal Fourier transform is also given. Only the first 10 modes are represented

because higher orders are not significant.

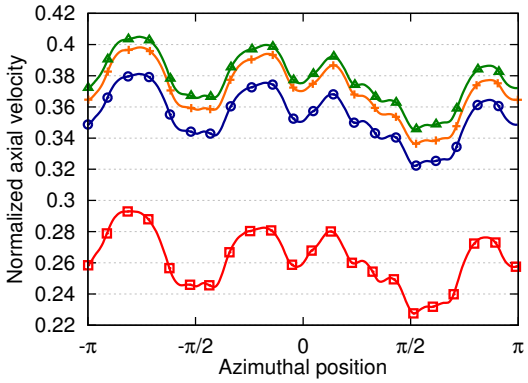

(a) Axial velocity - profile

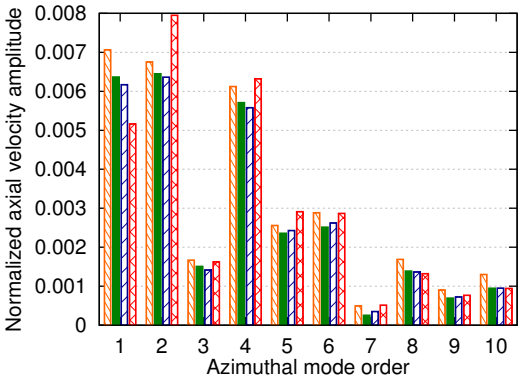

(b) Axial velocity - modes

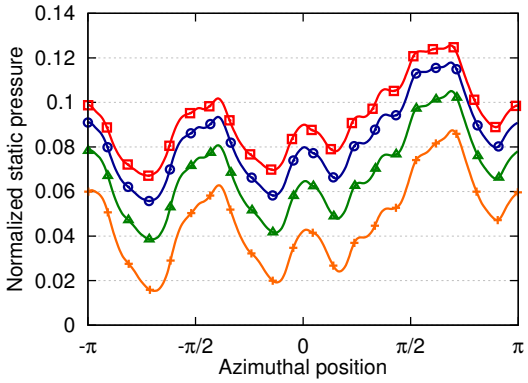

(c) Static pressure - profile

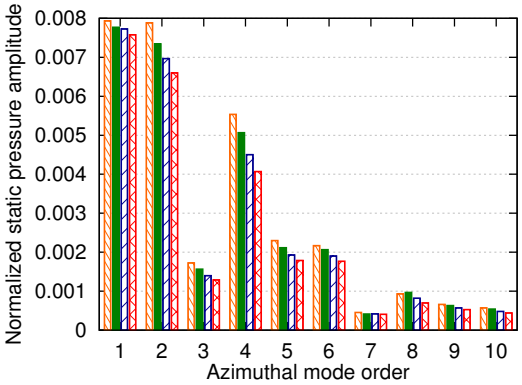

(d) Static pressure - modes

Figure 3.2: **Mean azimuthal profile and mode distribution at different vane heights - plane P5 - 60A: / 25%, / 50%, / 75%, / 95%**

At all radii, both the axial velocity and the static pressure present a similar azimuthal variation around different mean values. As a consequence, the mode distribution of all curves are comparable. There are 4 main lobes corresponding to the 4 irregular vanes (the 2 bifurcations and the 2 struts) which are responsible for the strong amplitude of mode 4. The low velocity areas are located around $\pi/2$ (in front of the upper bifurcation), $-\pi/2$ (in front of the lower bifurcation) and 0 and $\pm\pi$ (in front of the struts). The four lobes have different shapes and amplitude so that modes of lower orders are also significant. Most of the information is contained in the first six azimuthal modes, with a clear domination of the modes 1, 2 and 4. The mode distribution of normalized axial velocity and static pressure are similar. However, the evolution of the mode levels with the vane height is clearer for the static pressure signal, with a slight decrease with the radius (maximum decrease of about 30% for mode 4).

At cutback and sideline, similar plots could be drawn with different magnitudes.

To compare the distortion in plane P5 between all regimes concisely, only the azimuthal profile of axial velocity at 50% of vane height is shown with its corresponding mode distribution in Fig. 3.3.

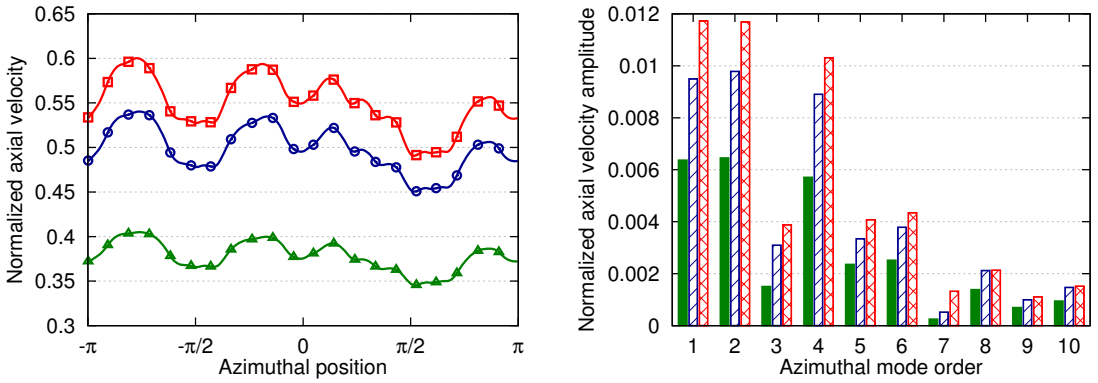

(a) Azimuthal profile

(b) Mode distribution

Figure 3.3: **Mean normalized axial velocity profile and mode distribution at $h/H = 50\%$ in plane P5: / approach, / cutback, / sideline**

The locations of the low and high axial velocities areas are preserved with the regime and the lowest velocity is always reached around $\pi/2$, in front of the big bifurcation. The azimuthal variations increase with the regime which results in higher mode levels. For the three dominant modes 1, 2 and 4, the ratio between cutback and approach levels is around 1.5 and the one between sideline and approach levels is around 1.8.

3.2.2 Evolution of the shape with distance

The potential effect is expected to decrease with distance. This is shown at approach conditions in Fig. 3.4 where axial velocity maps are plotted from plane P1 to plane P5 (defined in Fig. 2.11).

In plane P4 (at mid-distance between the fan and the OGV), only two zones of reduced velocities are observed which might indicates that the potential effect of the two struts has vanished. When going further upstream (planes P1 and P2), it seems that the potential effect of the lower bifurcation (the small one) also completely vanishes because only one area of reduced velocity is visible. In addition, the location of this area is deviated in the clockwise direction in planes P1 and P2 (discussed later).

The evolution of the shape of the potential effect and the corresponding mode distribution with distance are given in Fig. 3.5 at 75% of vane height and at approach conditions as a representative example. The azimuthal evolution of axial velocity and the amplitudes of azimuthal modes are plotted from plane P1 to plane P5.

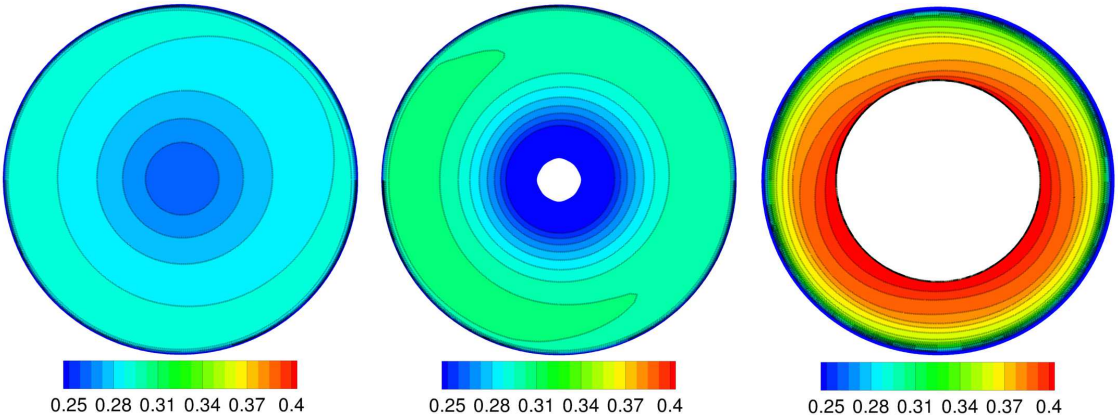

(a) Plane P1 (b) Plane P2 (c) Plane P3

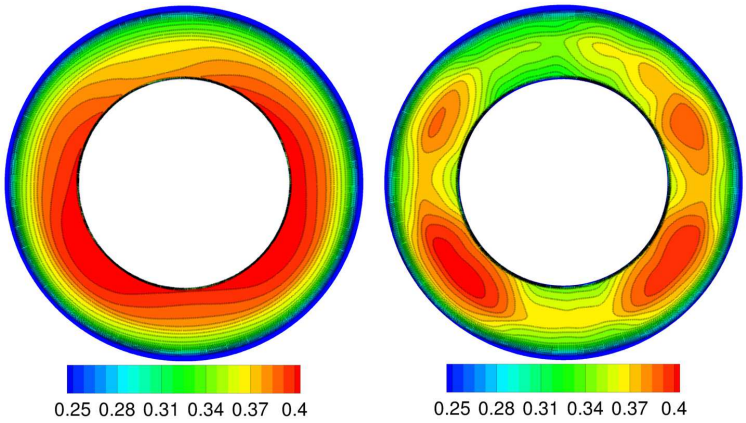

(d) Plane P4 (e) Plane P5

Figure 3.4: **Normalized axial velocity maps from plane P1 to plane P5 at approach conditions (axisymmetric)**

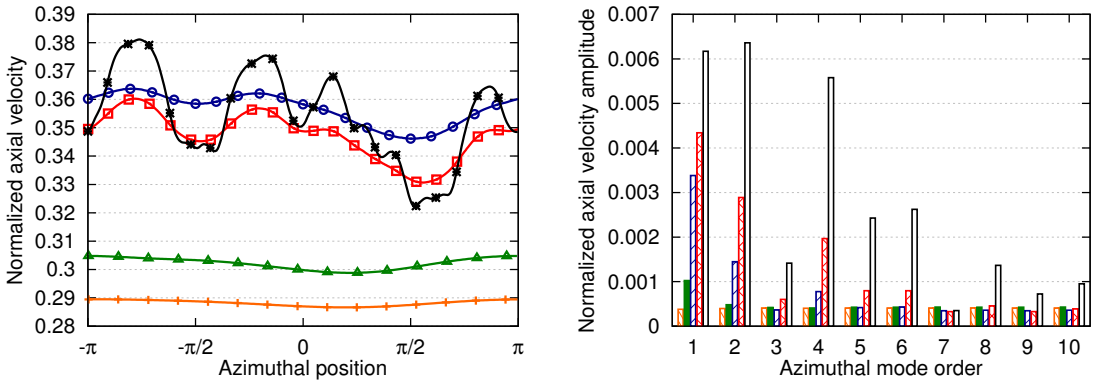

(a) Azimuthal profile (b) Mode distribution

Figure 3.5: **Mean normalized axial velocity profile and mode distribution at $h/H = 75\%$ at approach conditions: — / ▨ plane P1, —▲— / ▬ plane P2, —○— / ▨ plane P3, —□— / ▨ plane P4 and —✱— / ▭ plane P5**

The decrease in amplitude is different from one mode to another. As shown in the maps in Fig. 3.4, the level of the mode 4 becomes insignificant from plane P3 and the mode 2 becomes insignificant from plane P2. In plane P1, the distortion profile seems to be spread over all modes and no particular mode dominates. This decrease in mode amplitude with distance is better shown in Fig. 3.6 where the axial evolution of modes 1, 2, 3 and 4 is plotted for approach conditions.

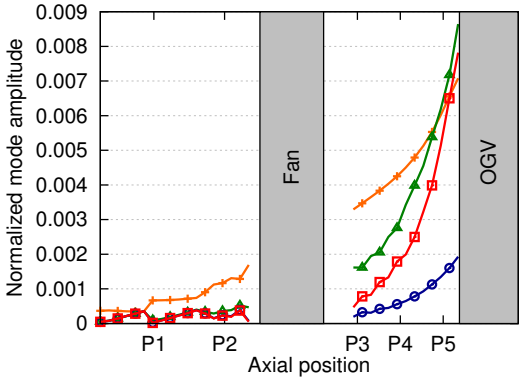

Figure 3.6: **Axial evolution of azimuthal mode amplitudes at 75% of vane height for approach conditions: mode 1, mode 2, mode 3, mode 4**

Right upstream of the pylon, the modes 1, 2 and 4 have similar amplitudes (maximum difference of 20%) but the mode 3 is negligible (almost 4 times lower). All modes decrease while going upstream but modes 2 and 4 decrease more severely than mode 1. As a result, only the mode 1 is still significant right upstream of the fan (15% of its initial value). These observations agree with the potential flow theory. Indeed, the velocity disturbance of the flow upstream of a cylinder decreases with the square of distance and is proportional to the square of the cylinder diameter [107]. The bifurcations are bigger than the struts and the associated potential effect is logically observed farther. In addition, the distortion with higher harmonic orders is expected to decrease faster axially according to Parker's findings [108, 109]. Similar evolutions are obtained at cutback and sideline as represented in Fig. 3.7, where the mean velocity at $h/H = 75\%$ of vane height is plotted over the 5 planes P1 to P5.

3.2.3 Deviation with distance

In the maps of Fig. 3.4, the location of the pattern of distortion has been observed to be deviated in the clockwise direction while going upstream. This effect is quantified here by following the location of the lowest velocity in the axial direction. Results are shown at approach conditions in Fig. 3.8(a) for different vane heights.

Right upstream of the pylon, the lowest velocity is located around $\pi/2$ because of the presence of the upper bifurcation (the largest one). In the interstage region, the location of this minimum velocity is slightly deviated in the counter-clockwise direction (positive azimuthal direction) by about $\pi/16$ at all radii. Through the

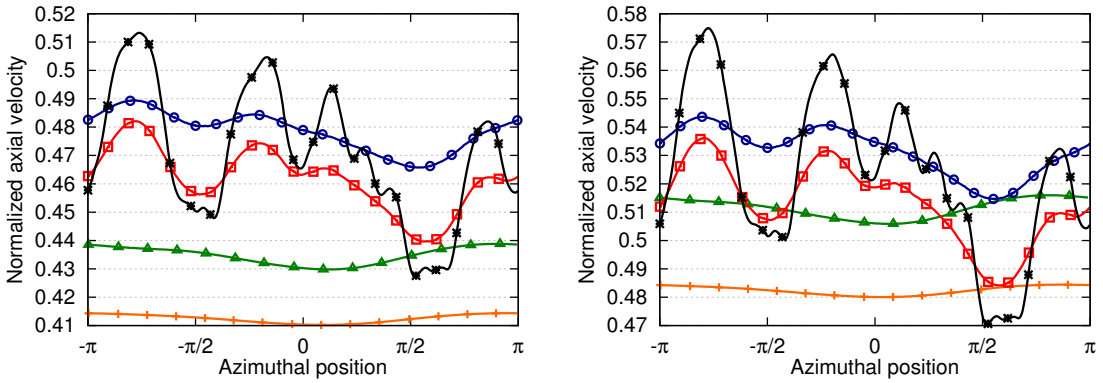

(a) Cutback (b) Sideline

Figure 3.7: **Mean normalized axial velocity profile at $h/H = 75\%$ at cubtack and sideline conditions: plane P1, plane P2, plane P3, plane P4 and plane P5**

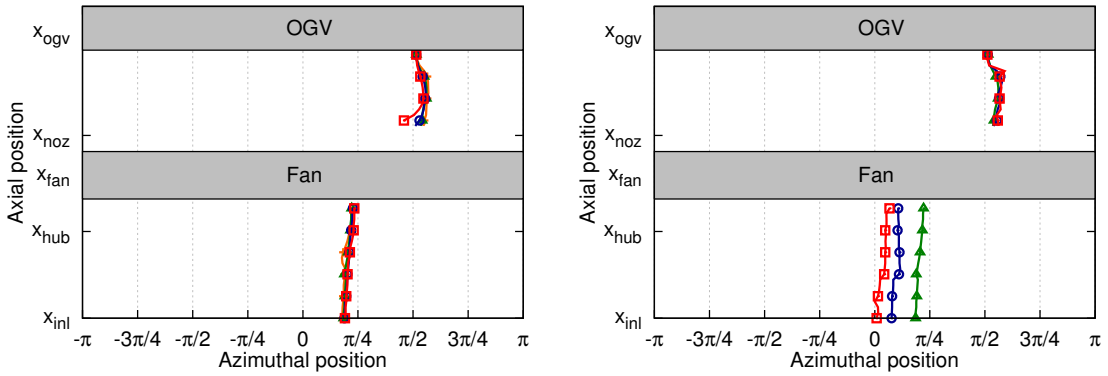

(a) At approach conditions for different vane heights: 25%, 50%, 75%, 95%

(b) At mid-span for all regimes: approach, cutback, sideline

Figure 3.8: **Tracking of the lowest normalized velocity**

fan, the pattern is significantly shifted in the clockwise direction by about $5\pi/16$. This deviation occurs in the direction of the flow (the fan rotates in the negative azimuthal direction). The pattern of distortion is therefore probably transported by the fan while rotating.

In Fig. 3.8(b), the location of the lowest velocity is now compared between the three regimes. This is done at mid-span only because there is no particular evolution with the vane height. In the interstage region, the lowest velocity follows the same path for all regimes. However, the deviation of the distortion pattern through the fan is increased with the regime. This is consistent with the hypothesis of transportation of the pattern with the fan. The azimuthal deviation through the fan varies linearly with the regime as shown in Fig. 3.9. The coefficient of the resulting line is around 4 ms.

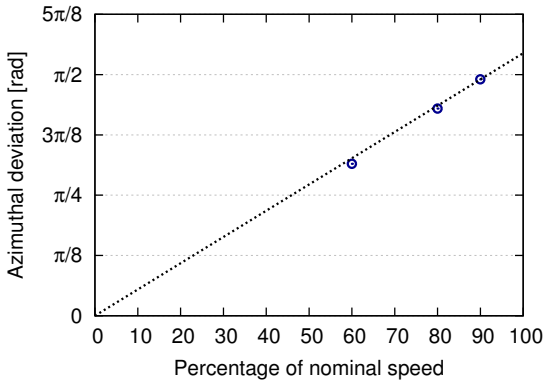

Figure 3.9: **Evolution of the azimuthal deviation through the fan with the regime**

3.2.4 Decrease of the intensity with distance

As already mentionned and observed above, the intensity of the potential effect decreases with distance. This is quantified here by introducing the Circumferential Distortion Coefficient (CDC) at different axial positions x for a constant channel height h/H, defined as:

$$CDC(x, h/H) = \frac{\mathrm{Max}_\theta\left[M(x, h/H, \theta)\right] - \mathrm{Min}_\theta\left[M(x, h/H, \theta)\right]}{\mathrm{Mean}_\theta\left[M(x, h/H, \theta)\right]}. \tag{3.1}$$

$\mathrm{Max}_\theta\left[M(x, h/H, \theta)\right]$, $\mathrm{Min}_\theta\left[M(x, h/H, \theta)\right]$ and $\mathrm{Mean}_\theta\left[M(x, h/H, \theta)\right]$ are the azimuthal maximum, minimum and mean values of the temporally-averaged Mach number at position (x, h/H) respectively. The coefficient is normalized by its maximum value. It is plotted at approach conditions along the machine rotational axis at 25%, 50%, 75% and 95% of vane height in Fig. 3.10.

The maximum value is logically reached right upstream of the pylon. It then decreases while going upstream with a kind of exponential function. The levels obtained at 25%, 50% and 75% of vane height are similar but higher values are reached at 95% of vane height. The remaining level in the fan region is around 5 to 10% of the maximum value. Similar behavior with the vane height is observed at cutback and sideline. The CDC obtained for the three regimes are therefore only compared at 50% and 95% of vane height. Results are given in Fig. 3.11.

At mid-span, the CDC is increased with the regime. This is consistent with the potential flow theory that predicts a potential effect proportional to the mean velocity [107]. Right upstream of the OGV, the CDC equals 0.55, 0.72 and 0.77 at approach, cutback and sideline respectively. Right downstream of the fan, the CDC values are reduced (0.07, 0.09 and 0.10 at approach, cutback and sideline respectively) but the ratio between regimes is conserved (around 1.3 between approach

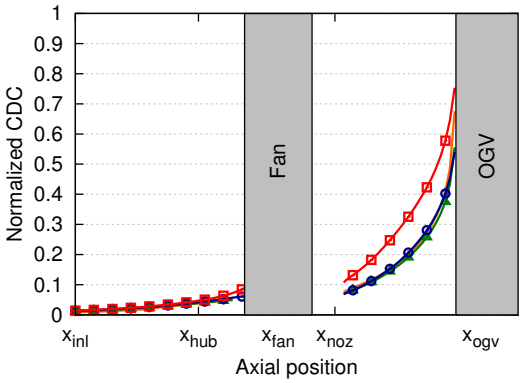

Figure 3.10: **Axial evolution of the CDC at approach conditions and at different vane heights: 25%, 50%, 75%, 95%**

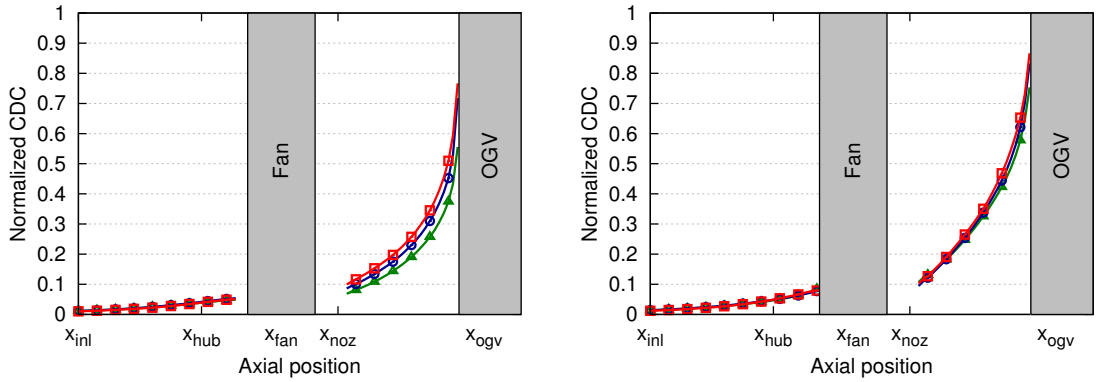

(a) $h/H = 50\%$ (b) $h/H = 95\%$

Figure 3.11: **Axial evolution of the CDC at 50% and 95% of vane for the different regimes: approach, cutback, sideline**

and cutback values and 1.4 between approach and sideline values). At 95% of vane height, the differences between the regimes are small (less than 10%), probably because of the reduced mean velocity caused by the proximity of the casing.

3.2.5 Radial evolution

The evolution of the CDC with the vane height is studied more precisely here. The radial variation of this coefficient from plane P1 to plane P5 is plotted in Fig. 3.12 at approach conditions.

In the interstage region (planes P3, P4 and P5), the shape is conserved. From 5% to 90% of channel height, the CDC is almost constant and close to the hub and the casing, the values are higher (approximately multiplied by 2). Right upstream of the fan (plane P2), this radial variation is less important and the distortion is almost constant along the span. However, in the cylindrical inlet duct (plane P1), the distortion index is zero at the axis and increases with radius. This is probably

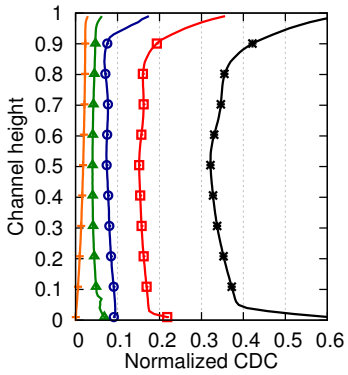

Figure 3.12: **Radial evolution of the CDC at approach conditions on different planes: plane P1, plane P2, plane P3, plane P4 and plane P5**

due to the presence of the hub that masks the potential effect of the pylon at low radii.

The three regimes are compared in 3 planes: one upstream of the fan (plane P2), one at mid-distance between the fan and the OGV (plane P3) and one right upstream of the OGV (plane P5). Results are shown in Fig. 3.13.

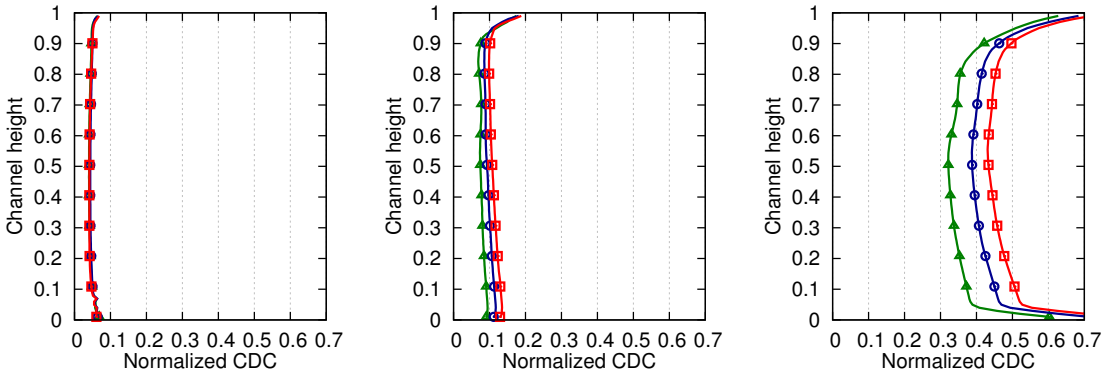

(a) Plane P2 (b) Plane P3 (c) Plane P5

Figure 3.13: **Radial evolution of the CDC in planes P2, P3 and P5 for the different regimes: approach, cutback, sideline**

The radial variation of the CDC is similar between all regimes, and same behavior is obtained in planes P1 and P4 that are not represented here. In the interstage region, the increase of the distortion with the regime that has been observed in Fig. 3.11 is evidenced and constant at all radii, except close to the casing where the curves becomes superimposed. Upstream of the fan, the radial evolution of the CDC does not change with the regime.

3.2.6 Distortion downstream of the stators

Up to now, the focus has been put on the upstream evolution of the distortion caused by the potential effect of the pylon. This potential effect will interact with the rotating fan and then be responsible of unsteady loadings. The flow features downstream of the OGV and IGV row are briefly presented here. Contour maps of normalized static pressure downstream of the OGV (plane P6) and the IGV (plane P8) at approach conditions are therefore given in Fig. 3.14. Normalized static pressure has been chosen instead of normalized axial velocity in order to focus on the distortion of the flow without the presence of the vane wakes.

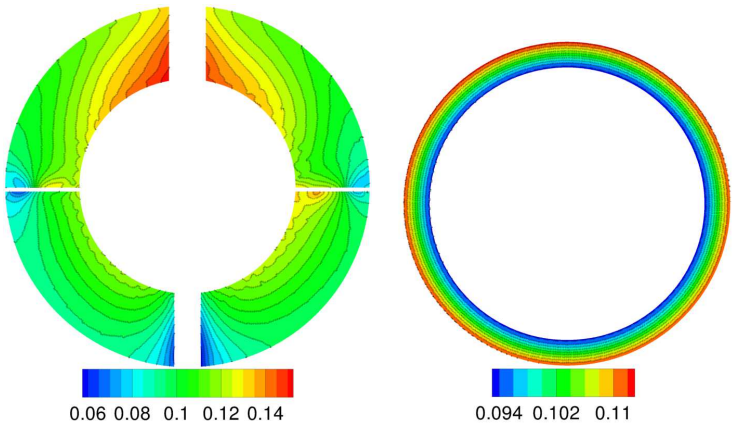

(a) Plane P6 (downstream of the OGV) (b) Plane P8 (downstream of the IGV)

Figure 3.14: **Normalized static pressure contour maps downstream of the OGV and IGV at approach conditions (axisymmetric)**

In plane P6, the pylon and the struts are still present (the four holes) and the flow is distorted. The pylon is extended up to the exit of the engine and this distortion pattern is therefore present in the whole duct downstream of the OGV. This inhomogeneity of the flow in this region might alter the acoustic fluctuations that propagate in the downstream direction. However, downstream of the IGV (plane P8), the flow seems axisymmetric. The primary stream is indeed protected from the potential effect of the pylon by the nozzle. Similar features are found at cutback and sideline.

Summary of the section

When the inlet is axisymmetric, the distortion only comes from the potential effect of the pylon and struts. While going upstream, the initial shape of this distortion composed of 4 lobes changes and only one major lobe remains. This lobe is due to the upper bifurcation, the largest one, which slows down the flow. By going through the fan, this lobe is deviated in the clockwise direction by an angle that varies linearly with the regime. The distortion caused by the

pylon increases with the regime in the interstage and reaches higher values close to the casing.

3.3 Distortion caused by the inlet asymmetry

The inlet distortion caused by the non-axisymmetric air inlet geometry is studied in this section. It is not possible to isolate the inlet distortion as it was done for the distortion that comes from the potential effect because the pylon is included in all configurations. Therefore, the characterization of the inlet distortion is done by comparison of the simulations with axisymmetric and non-axisymmetric air inlet geometries.

3.3.1 Characterization of the inlet distortion

The inlet distortion is shown in Fig. 3.15 where axial velocity contours in the vertical plane of the inlet duct are given for both geometries at approach conditions.

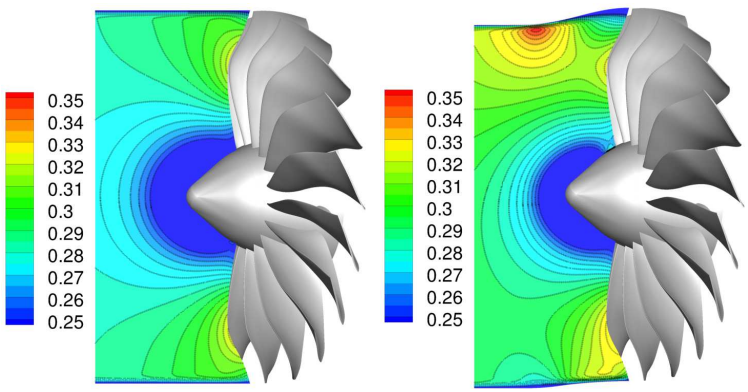

(a) Axisymmetric inlet (b) Asymmetric inlet

Figure 3.15: **Contour maps of normalized axial velocity in the inlet duct at approach conditions for both inlet geometries**

The flow with the axisymmetric inlet is logically axisymmetric (because the distortion that comes from potential effect of the pylon is largely reduced in the inlet). The non-axisymmetric inlet is responsible for a strong inhomogeneity of the flow, especially close to the casing. Right at the entrance, where the casing lines are still straight, the velocity of the flow is higher at the top. At the point where the casing lines start to curve, the axial velocity close to the tip becomes reduced at the top (divergent duct) and increased at the bottom (convergent duct). The contour maps of axial velocity in planes P1 and P2 are given for both inlet geometries in Fig. 3.16 to have a better representation of this inhomogeneity.

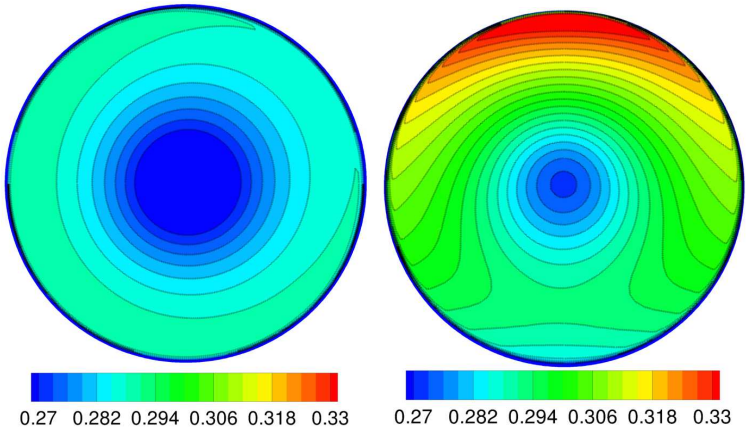

(a) Plane P1 - Axisymmetric inlet (b) Plane P1 - Asymmetric inlet

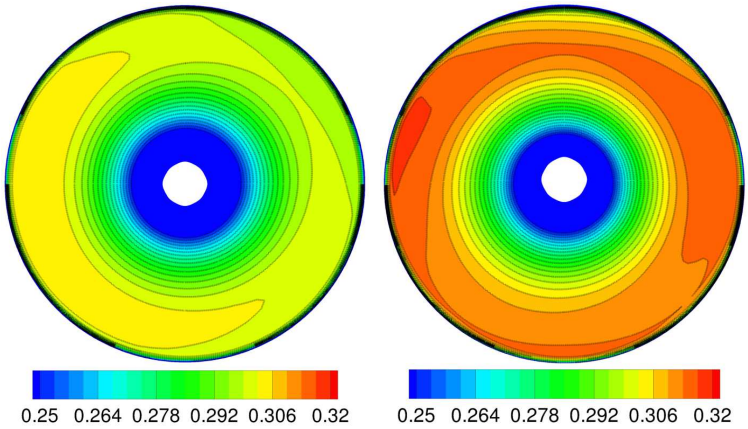

(c) Plane P2 - Axisymmetric inlet (d) Plane P2 - Asymmetric inlet

Figure 3.16: **Contour maps of normalized axial velocity in planes P1 and P2 at approach conditions for both inlet geometries**

Right upstream of the fan (plane P2), the normalized axial velocity presents a minimum value at the tip and a maximal one at the bottom, as expected with non-axisymmetric air inlets [26, 3]. The azimuthal evolution of the mean velocity in plane P2 and the associated mode distribution are shown in Fig. 3.17 at approach conditions for both air inlet geometries.

At all vane heights, the azimuthal profiles are modified by the inlet distortion. The minimum velocities were reached around $\pi/4$ in the axisymmetric configuration (dashed lines) and this is not the case anymore with the inlet asymmetry (solid lines). At 25% and 50% of vane height, the minimum is localized close to the bottom (around $-\pi/2$) while at 75% and 95% of vane height, it is reached at the top ($\pi/2$). The amplitude of the inhomogeneity is increased, in particular at 95% of vane height. This is well observed on the mode distribution. The impact of the inlet distortion is spread over the first 4 modes only. From mode 5 to 10, the amplitudes are the same between both inlet geometries (black dots and bars at the same level).

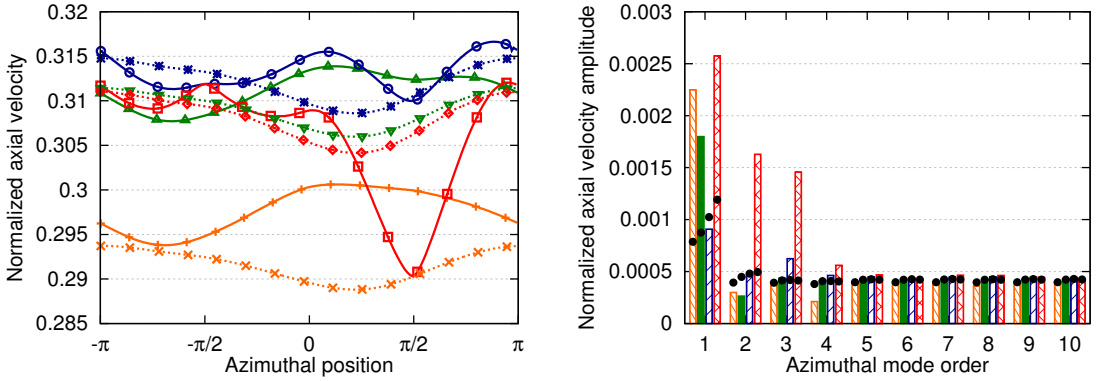

(a) Azimuthal profile (b) Mode distribution

Figure 3.17: **Mean azimuthal profile and mode distribution at approach conditions in plane P2 and at different vane heights: + / 25%, △ / 50%, ○ / 75%, □ / 95% for asymmetric inlet and × / • 25%, △ / • 50%, ✳ / • 75%, ◇ / • 95% for axisymmetric inlet**

The mode 1 is the most impacted mode, with a level multiplied by more than 2 at 25%, 50% and 95% of vane height. At 75% of vane height, there is a small decrease of the amplitude of this mode. On other modes, the impact occurs essentially at 95% of vane height, with levels multiplied approximately by 3 for modes 2 and 3. Similar results are obtained at cutback and sideline. The azimuthal velocity profiles and corresponding mode distribution are plotted in Fig. 3.18 for all regimes at 95% of vane height, where the impact is maximum.

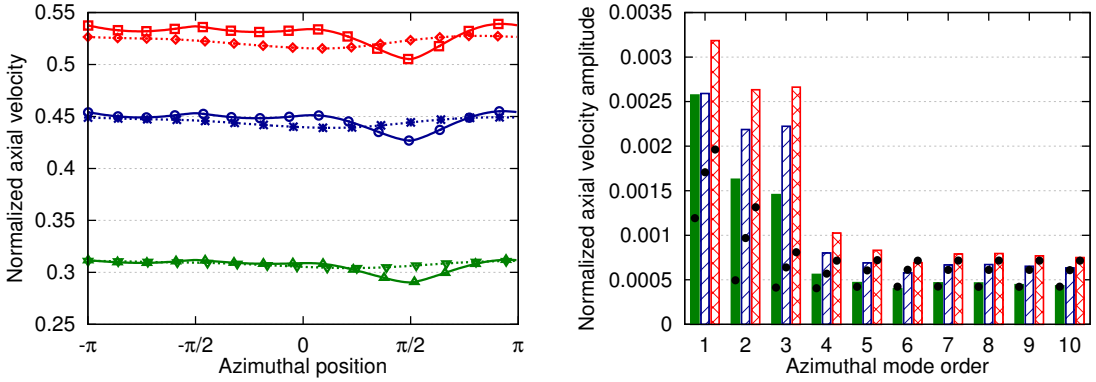

(a) Azimuthal profile (b) Mode distribution

Figure 3.18: **Mean azimuthal profile and mode distribution in plane P2 and at 95% of vane height for all regimes: △ / approach, ○ / cutback, □ / sideline for asymmetric inlet and △ / • approach, ✳ / • cutback, ◇ / • sideline for axisymmetric inlet**

Inlet distortion acts similarly at all regimes. It significantly increases the amplitudes of modes 1 to 4 (multiplication by 1.5 to 3) while other modes are rather unaffected. The amplitude of the modes increases with the regime, as well as the

mean velocity. For all regimes, the minimum velocity is located at $\pi/2$, at the top (because of the divergence of curvature of the casing), which differs from the location without inlet distortion (determined by the potential effect and the angular deviation by the fan).

3.3.2 Evolution of the shape with distance

The impact of the inlet distortion on the flow downstream of the fan is now analyzed. Contour maps in plane P3 at approach conditions are first given in Fig. 3.19, right downstream of the fan, for both inlet geometries.

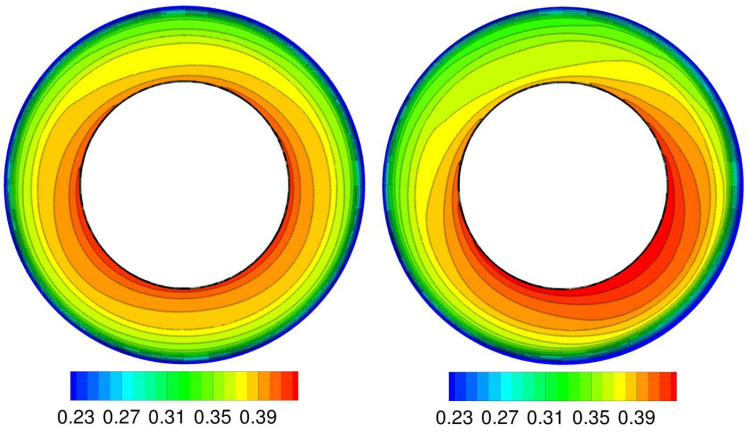

(a) Plane P3 - Axisymmetric inlet (b) Plane P3 - Asymmetric inlet

Figure 3.19: **Contour maps of normalized axial velocity in plane P3 at approach conditions for both inlet geometries**

Differences are observed between the axisymmetric and the non-axisymmetric configurations. The inhomogeneity of the flow is increased by the inlet distortion and the pattern seems to deviate towards the counter-clockwise direction. This is best assessed in Fig. 3.20 where the azimuthal velocity profiles and corresponding mode distribution are given at different vane heights.

At 25%, 50% and 75% of vane height, the location of the minimum velocity is not modified (still at $\pi/2$, upstream of the upper pylon) but the amplitudes of the profile are accentuated by the inlet distortion. Only the mode 1 is affected at those heights and it is significantly increased (multiplied by a factor going from 2 to 3). At 95% of vane height, the impact is further emphasized. The location of the minimum velocity is deviated in the counter-clockwise direction as observed in Fig. 3.19 and the amplitudes of the first three modes have been considerably increased (multiplied by 2.5 to 4).

The axial evolution of the distortion is better shown in Fig. 3.21 by plotting together the azimuthal velocity profiles and mode distributions in planes P2, P3 and P5 at approach conditions. These profiles are represented at 95% of vane height,

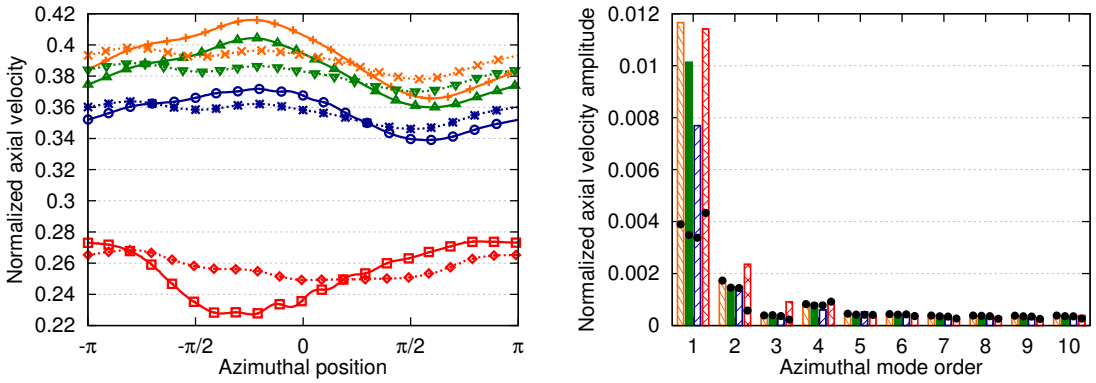

(a) Azimuthal profile (b) Mode distribution

Figure 3.20: **Mean azimuthal profile and mode distribution at approach conditions in plane P3 and at different vane heights: / 25%, / 50%, / 75%, / 95% for asymmetric inlet and / • 25%, / • 50%, / • 75%, / • 95% for axisymmetric inlet**

where the impact of the distortion is maximum.

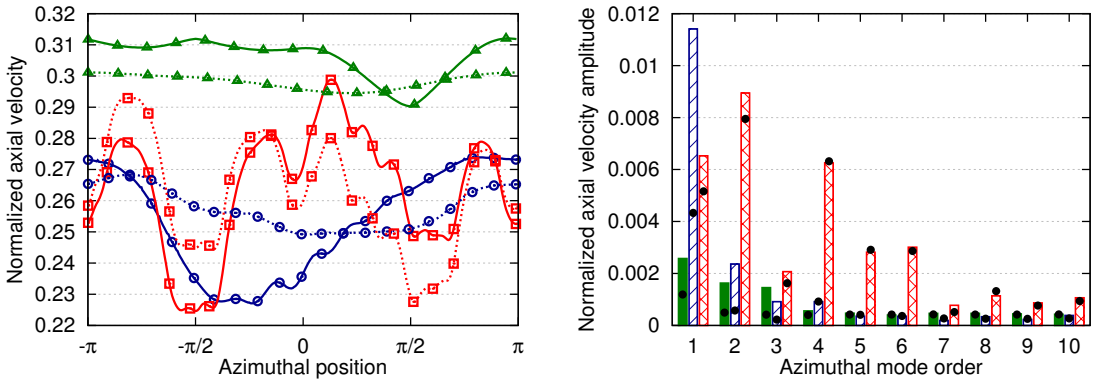

(a) Azimuthal profile (b) Mode distribution

Figure 3.21: **Mean axial velocity profile and mode distribution at $h/H = 95\%$ at approach conditions: / plane P2, / plane P3, / plane P5 for asymmetric inlet and / • plane P2, / • plane P3, / • plane P5 for axisymmetric inlet**

Even in plane P5 (right upstream of the OGV), the inlet distortion has an impact. The characteristic shape of the azimuthal velocity profile with the four lobes is conserved, but with a shift towards lower levels in the bottom part (from $-\pi$ to 0) and a shift towards higher levels in the top part (from 0 to π). As observed before, the main impact is on the first three modes. In planes P2 and P3 (around the fan), the rise in amplitudes is important (multiplication by 2 or 3) while in plane P5, the increase is around 20%. At cutback and sideline, same observations could be done, as evidenced by the similar azimuthal velocity profiles at 95% of vane height given

in Fig. 3.22.

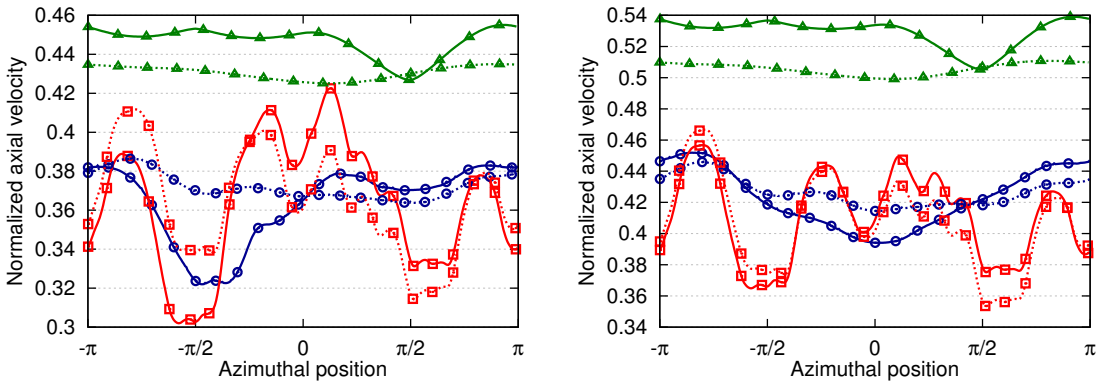

(a) Cutback (b) Sideline

Figure 3.22: **Mean normalized axial velocity profile at $h/H = 95\%$ at cubtack and sideline conditions: plane P2, plane P3, plane P5 for asymmetric inlet and plane P2, plane P3, plane P5 for axisymmetric inlet**

3.3.3 Evolution of the intensity with distance

As it was done previously for the distortion created by the potential effect of the pylon, the intensity of the distortion is evaluated thanks to the CDC. Its axial evolution at approach conditions is represented in Fig. 3.23 for different vane heights.

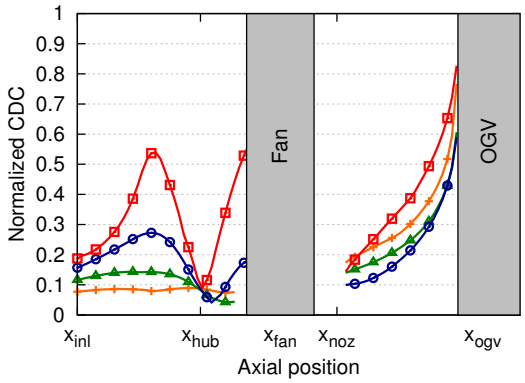

Figure 3.23: **Axial evolution of the CDC at approach conditions and at different vane heights: 25%, 50%, 75%, 95%**

In addition to the distortion created by the potential effect (maximum right upstream of the OGV), the inlet distortion is responsible for an important inhomogeneity of the flow in the middle of the inlet duct and right upstream of the fan. This inlet distortion is essentially dominant close to the tip. At 95% of vane height, the CDC is almost 60% as high as the distortion caused by the pylon. The heterogeneity in the fan region is increased when comparing with the case without inlet

distortion given in Fig. 3.10. The value of the CDC seen by the fan at 95% of vane height goes from 0.1 to 0.55. Similar evolution with the vane height is also observed at cutback and sideline. The values of CDC at 50% and 95% of vane height reached for the different regimes are compared in Fig. 3.24. The focus has been put on the region of interest, from the beginning of the hub to the OGV row.

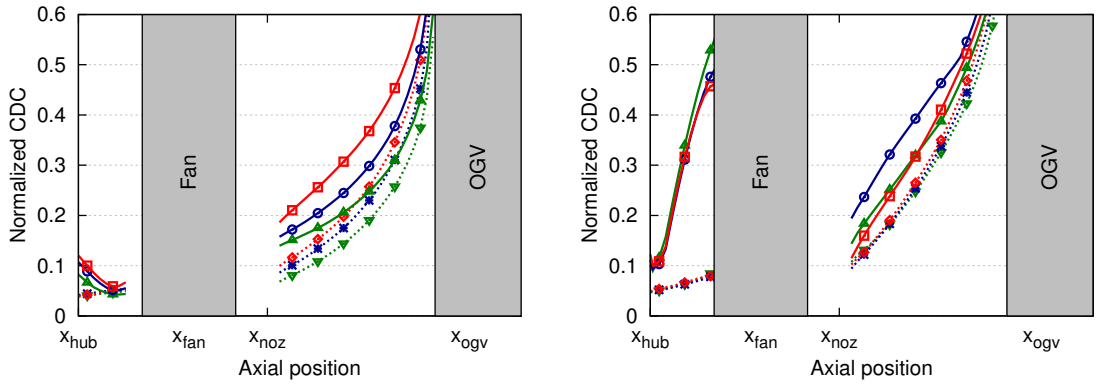

(a) $h/H = 50\%$ (b) $h/H = 95\%$

Figure 3.24: **Axial evolution of the CDC at 50% and 95% of vane for the different regimes: approach, cutback, sideline for asymmetric inlet and approach, cutback, sideline for axisymmetric inlet**

At mid-span, there is no major differences in CDC levels computed upstream of the fan between the different regimes and the different air inlet geometries. However, just downstream of the fan, the CDC is increased (multiplication by 2) with the asymmetric air inlet. The differences are attenuated while approaching the OGV, because of the dominant potential effect of the pylon. At 95% of vane height, the increase of CDC in the interstage region is still observed, but it is less evident at sideline. The major impact of inlet distortion occurs right upstream of the fan, where the levels of CDC have been multiplied by 4 to 6 at all regimes. The values obtained at cutback and sideline are very close while the ones at approach are almost 20% higher.

3.3.4 Radial evolution

The radial evolution of the CDC is analyzed here by plotting the evolution of the CDC with the channel height for planes P1 to P5 at approach conditions. Results are given in Fig. 3.25.

The distortion that is created by the non-axisymmetric inlet is increasing with the radius in plane P1 and is dominant close to the hub and the casing in plane P2. In planes that are located downstream of the fan, the radial shape of the distortion is close to the one obtained without inlet distortion, but with increasing levels at almost all radii. The direct comparison of the radial shapes between axisymmetric and non-axisymmetric configurations is done in Fig. 3.26 in planes P2, P3 and P5

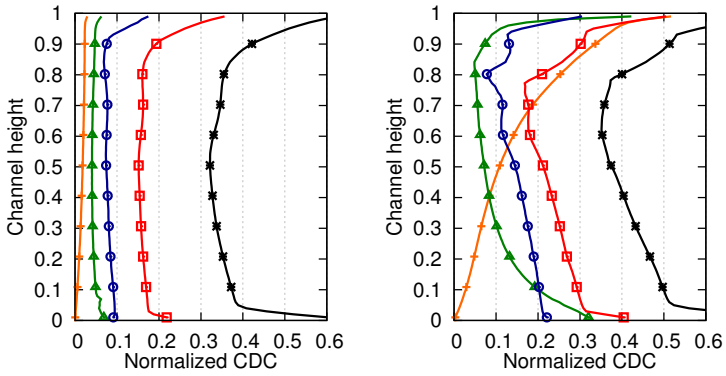

(a) Axisymmetric inlet (b) Asymmetric inlet

Figure 3.25: **Radial evolution of the CDC at approach conditions in different planes: plane P1, plane P2, plane P3, plane P4 and plane P5**

for all regimes.

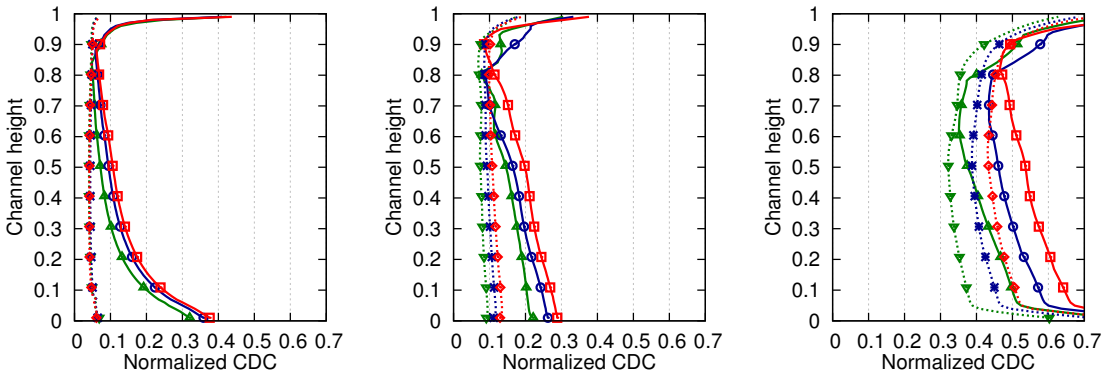

(a) Plane P2 (b) Plane P3 (c) Plane P5

Figure 3.26: **Radial evolution of the CDC in planes P2, P3 and P5 for the different regimes: approach, cutback, sideline for asymmetric inlet and approach, cutback, sideline for axisymmetric inlet**

In plane P2, the addionnal inlet distortion has modified the almost constant profile into a highly-radially distorted profile, with extrema values at hub and tip almost 3 to 5 times the values at mid-span. The behavior is similar in all regimes but the CDC from the hub to 90% of channel height is slighlty increased with the regime (around 10% higher at sideline than at approach). In plane P3, the shape is again modified by the inlet distortion. The differences in CDC that were observed in axisymmetric configurations are further emphasized. The values of CDC at hub and tip have been approximately multiplied by 3 and 2 respectively. In plane P5, unlike other planes, the maximum value of the CDC is not considerably affected by the inlet distortion because the potential effect is dominant in this region. However, between 5% and 50% of vane height, the CDC is significantly increased (up to 40%

at approach to 30% at cutback and sideline). Above 50% of channel height, levels of CDC are also increased but in a less regular way. On 80% of channel height, the CDC is increased with the regime (approximately +0.08 in average between approach and cutback and between cutback and sideline). In the tip region, the behavior with the regime is less clear, probably because of the separation that occurs on fan blades and that impacts the mean flow.

Summary of the section

The asymmetry of the inlet duct lines creates a distortion in the fan plane that is characterized by a low-velocity region at the top close to the casing. This additional distortion increases the inhomogeneity of the flow right upstream of the fan, essentially close to the tip, where the CDC has been multiplied by 4 to 6 depending on the regime. The effect in the interstage region is also significant, with an increase of the amplitudes of the modes 1 to 3 (that can more than double) at the different analyzed planes.

3.4 Impact of distortion on unsteady aerodynamics

The impact of the distortion described in previous sections on unsteady aerodynamics is analyzed in this section.

3.4.1 Fan-blade wakes

In Figs. 3.11 and 3.24, the distortion has been shown to be important in the interstage region. The mean flow values are therefore different around one vane or another. The behavior of unsteady flow, and in particular of fan-blade wakes, is discussed here. The velocity deficit is plotted during the last three blade passage periods in Fig. 3.27 at approach conditions and without inlet distortion. It is represented in planes P3, P4 and P5 at 25%, 50%, 75% and 95% of vane height and for two azimuthal positions θ_1 and θ_2. These positions are spaced by $2\pi/3$ (equivalent to the space between six blades) so that they are supposed to see the passage of fan-blade wakes at the same time.

Right downstream of the fan (plane P3), the velocity deficit is of similar magnitude between all vane heights but with varying shape. While going dowstream, the wake is diffused and the velocity deficit is reduced. In some curves, a difference between the two azimuthal positions (difference between solid and dotted lines) is observed. These differences are more important at 95% of vane height in plane P3 right downstream of the fan and at all vane heights in plane P5, right upstream of the OGV. This is caused by the distortion which is responsible not only for a circumferentially-varying mean flow but also for a circumferentially-varying unsteady flow. The vanes of the OGV row are therefore impacted by different fan-blade

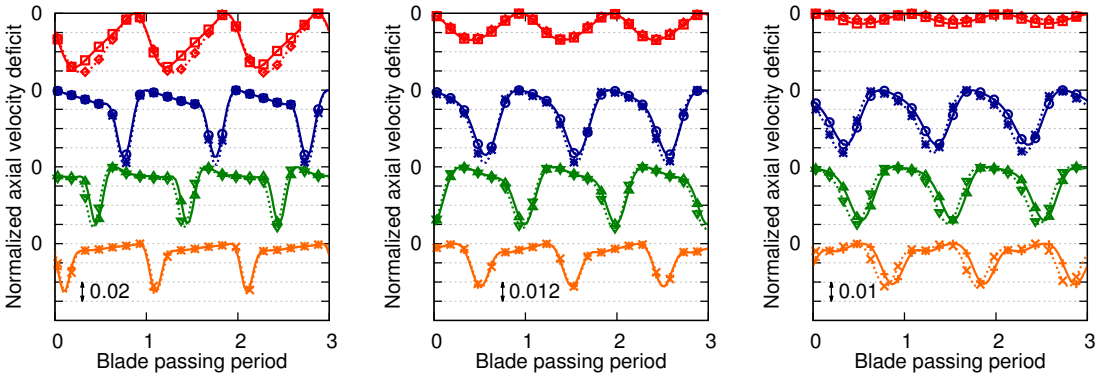

(a) Plane P3 (b) Plane P4 (c) Plane P5

Figure 3.27: **Normalized velocity deficit in planes P3, P4 and P5 for the axisymmetric approach configuration at different positions:** $h/H = 25\%$, $h/H = 50\%$, $h/H = 75\%$, $h/H = 95\%$ **for** θ_1 **and** $h/H = 25\%$, $h/H = 50\%$, $h/H = 75\%$, $h/H = 95\%$ **for** θ_2

wakes depending on their azimuthal positions, which will result in different unsteady loadings from one vane to another. The same plot is now given in Fig. 3.28 for the non-axisymmetric configuration.

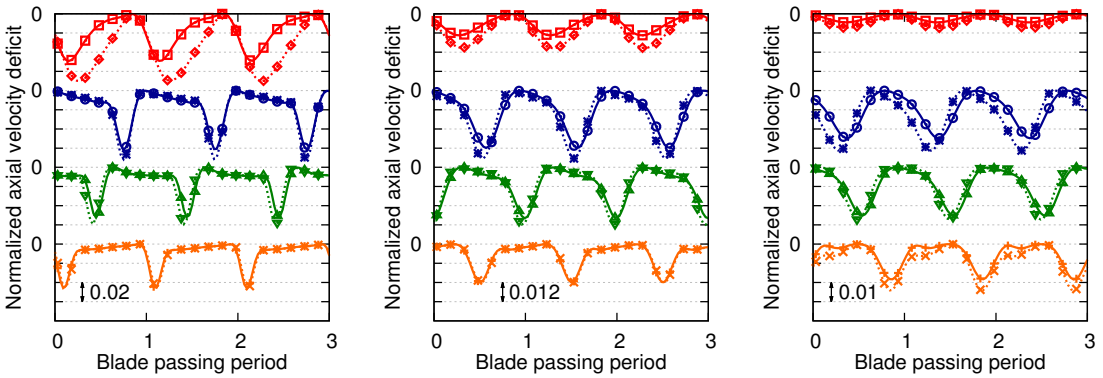

(a) Plane P3 (b) Plane P4 (c) Plane P5

Figure 3.28: **Normalized velocity deficit in planes P3, P4 and P5 for the asymmetric approach configuration at different positions:** $h/H = 25\%$, $h/H = 50\%$, $h/H = 75\%$, $h/H = 95\%$ **for** θ_1 **and** $h/H = 25\%$, $h/H = 50\%$, $h/H = 75\%$, $h/H = 95\%$ **for** θ_2

The differences in velocity deficit between the two azimuthal positions is further increased by the inlet distortion, particularly close to the casing at 75% and 95% of vane height. A comparison of the levels reached in Figs. 3.27 and 3.28 shows that the inlet distortion has an impact on the velocity deficits. This is better evaluated in Fig. 3.29 where the velocity deficit with and without inlet distortion are directly compared at two positions. The positions are taken for $\theta = \theta_2$ in plane P5 (right upstream of the OGV, representative of the interaction with the vanes) at 75% and

95% of vane height.

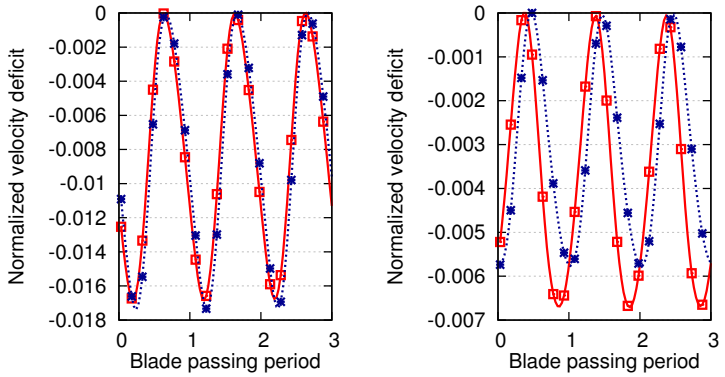

(a) $h/H = 75\%$ (b) $h/H = 95\%$

Figure 3.29: **Normalized velocity deficit at approach conditions in plane P5 at $\theta = \theta_2$ and at 75% and 95% of vane height: axisymmetric inlet, asymmetric inlet**

At 75% of vane height, the velocity deficit is slightly decreased (by 3%) when the inlet distortion is added. However, at 95% of vane height, it is significantly increased (by almost 20%) and a shift in time is also observed. The impact of inlet distortion on the wakes therefore depends on the position. These differences in velocity deficits are also observed at cutback and sideline. This is illustrated in Fig. 3.30 where the velocity deficit, with and without inlet distortion, is plotted for $\theta = \theta_1$ at $h/H = 75\%$ and in plane P5.

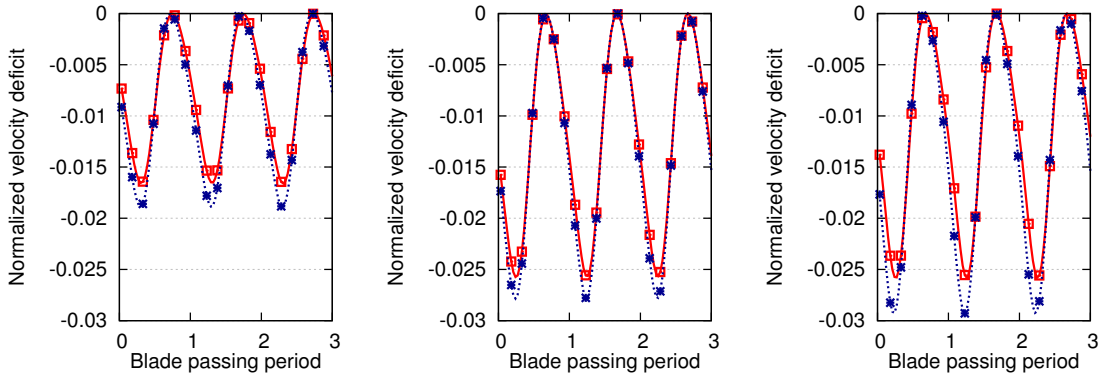

(a) Approach (b) Cutback (c) Sideline

Figure 3.30: **Normalized velocity deficit in plane P5 at $\theta = \theta_1$ and at 75% of vane height for approach, cutback and sideline regimes: axisymmetric inlet, asymmetric inlet**

The velocity deficit is increased with the regime. At this particular position, the velocity deficit is decreased when inlet distortion is added for all regimes. The

decrease is about 10% at approach and cutback, and 15% at sideline. The velocity deficit can be increased at some positions or decreased at some others as shown in Fig. 3.29 which makes the acoustic response of the stator vanes completely heterogeneous. This is evaluated here by plotting in Fig. 3.31(a) the maximum velocity deficit computed on several azimuthal positions. It is done at different vane heights right usptream of the OGV (in plane P5) and for approach conditions. In Fig. 3.31(b), the minimum, maximum and mean values of the corresponding velocity deficits are given in order to quantify more precisely the inhomogeneity of the wakes.

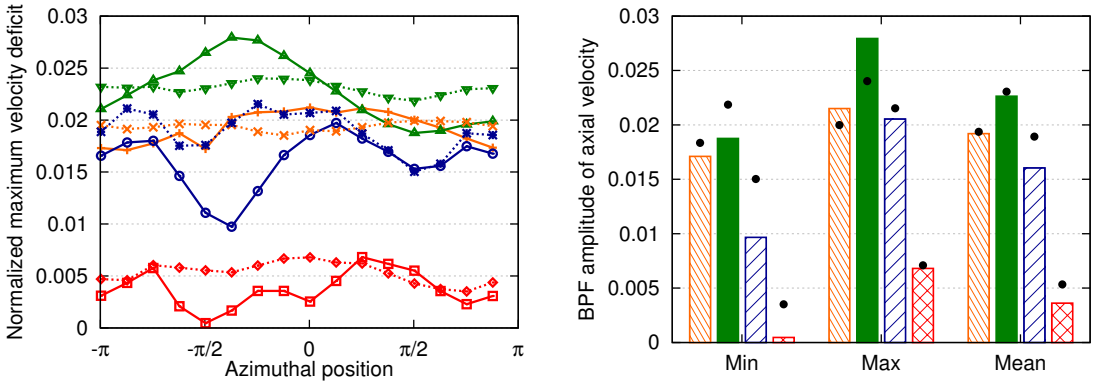

(a) Azimuthal evolution

(b) Statistics

Figure 3.31: **Azimuthal evolution and statistics of the maximum normalized velocity deficit computed in plane P5 at approach conditions: / 25%, / 50%, / 75%, / 95% for asymmetric inlet and / • 25%, / • 50%, / • 75%, / • 95% for axisymmetric inlet**

The azimuthal inhomogeneity of the wakes is observed at all vane heights even in the axisymmetric configuration (dashed lines). The levels (represented by the black dots) vary by 8%, 9%, 34% and 67% at 25%, 50%, 75% and 95% of vane height respectively. At 25% and 50% of vane height, the shape is nearly the same but the levels are approximately 20% higher at mid-span. The inhomogeneity is therefore increased with the radius. When the inlet distortion is added, the inhomogeneity is strongly increased and the azimuthal shape (solid lines) is modified. The variability of wake intensity has been increased by more than 2 at all vane heights. It becomes 23%, 40%, 68% and more than 175% at 25%, 50%, 75% and 95% of vane height respectively. Similar results are observed at cutback and sideline. The minimum, maximum and mean values obtained at the same positions are given in Fig. 3.32 for comparison purposes.

The mean intensity of the wakes is globally increased with the regime. For all regimes, the averaged velocity deficit is close between axisymmetric and non-axisymmetric configurations (maximum difference of 15% at approach for 75% of vane height). When inlet distortion is added, the minimum intensity of wakes is globally reduced while the maximum intensity is increased (comparison of bars and

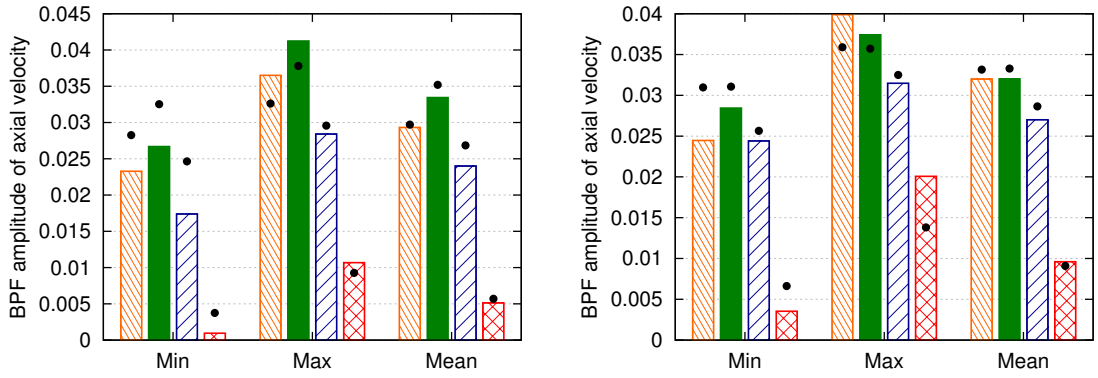

(a) Cutback (b) Sideline

Figure 3.32: **Statistics of the amplitude of the maximum normalized velocity deficit computed in plane P5 at cutback and sideline conditions: 25%, 50%, 75%, 95% for asymmetric inlet and • for axisymmetric inlet**

black dots). The inhomogeneity of the wakes is consequently increased. For example, at 50% of vane height, the variability of wake intensity goes from 9% to 40%, from 15% to 44% and from 14% to 28% at approach, cutback and sideline respectively.

3.4.2 Blade and vane unsteady loadings

Fan

The stationnary distortion interacts with the rotating fan blades and creates unsteady loadings on them. With the addition of inlet distortion, the interaction with the blades is expected to be higher and to result in more important unsteady loadings. These unsteady loadings are quantified here because they represent the equivalent acoustic sources. This is done in Fig. 3.33 where the normalized pressure distribution at RF over one fan blade is plotted at different vane heights. Results are given at approach and for both inlet geometries. Same range is applied to all plots.

Without inlet distortion, the fluctuations are found to be more important at 75% and 95% of blade height (in average +2 to +3 dB with respect to the values at 25% and 50% of vane height). The inlet distortion increases the levels at all blade heights and essentially close to the leading edge (+ 4 dB at at $h/H = 25/50\%$, +7 dB at at $h/H = 75\%$ and +8 dB at $h/H = 95\%$). The total increase is logically more important at 75 and 95% of blade height where the inlet distortion is dominant (cf. Fig. 3.23). The pressure amplitude at the RF and its harmonics (that were not shown here for conciseness) is integrated over the whole blade for both inlet geometries to quantify the overall increase of unsteadiness caused by the inlet distortion. Results are given in Fig. 3.34 for the first ten harmonics.

As it was the case for the distortion harmonics, the main unsteadiness is con-

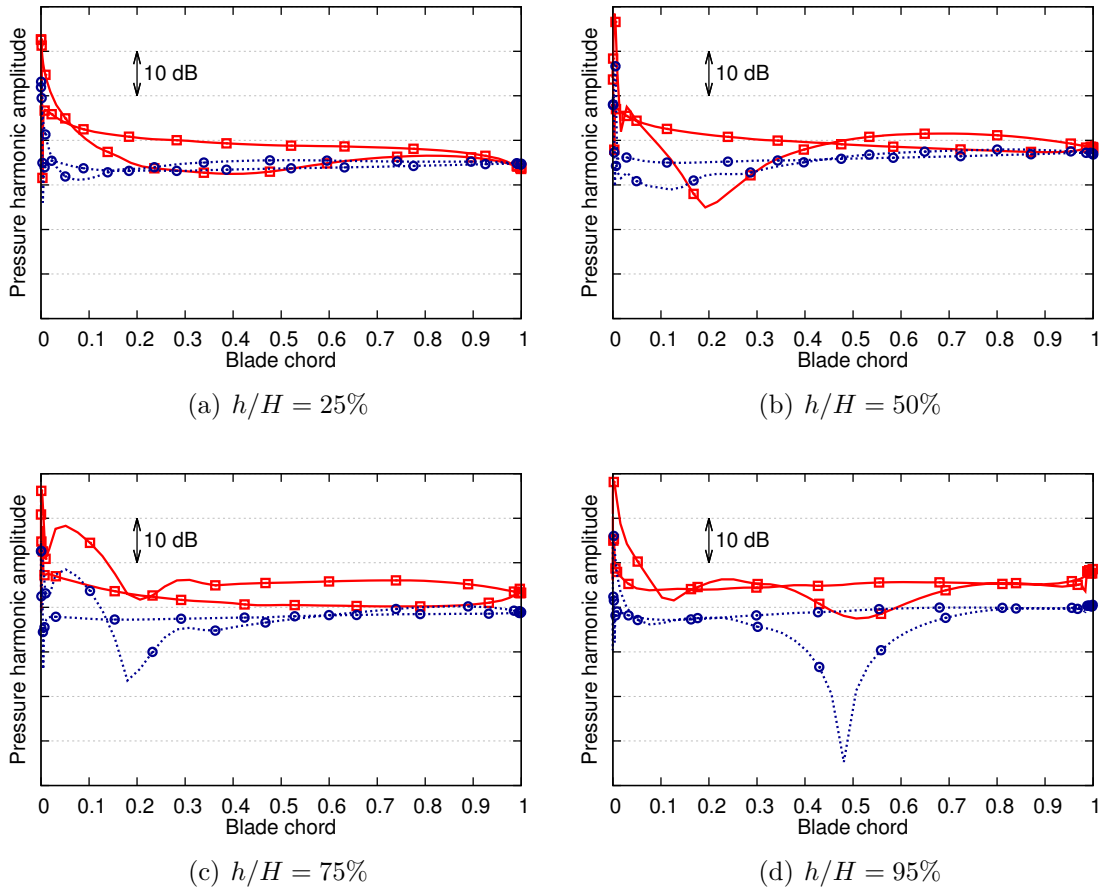

(a) $h/H = 25\%$ (b) $h/H = 50\%$

(c) $h/H = 75\%$ (d) $h/H = 95\%$

Figure 3.33: **Normalized pressure distribution at the RF over one fan-blade at 25%, 50%, 75% and 95% of blade height (approach conditions): axisymmetric inlet, asymmetric inlet**

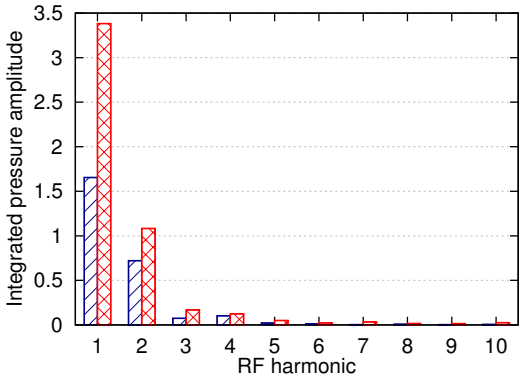

Figure 3.34: **Amplitude of one fan-blade integrated pressure fluctuations at the RF and its harmonics for approach conditions: axisymmetric inlet, asymmetric inlet**

tained in the first four harmonics, with a domination of the first two modes. When the inlet distortion is added, the levels of these harmonics are increased as expected.

The major impact is observed on the first harmonic with an amplitude multiplied by more than 2. It should be noted that the levels of integrated pressure harmonics have been obtained on one blade only. In order to compare the values reached for the different blades, the level of the first harmonic (the most important one) is plotted in Fig. 3.35 for all blades at approach conditions and for the two inlet geometries.

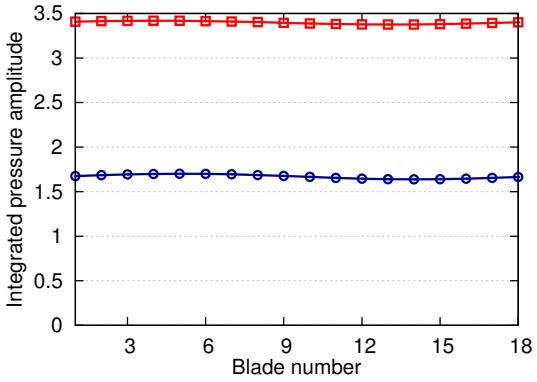

Figure 3.35: **Amplitude of the RF harmonic of integrated pressure for all fan blades (approach conditions): axisymmetric inlet, asymmetric inlet**

In both configurations, the levels are exactly the same for all blades. This is logical because all blades are identical and equally spaced and because they all interact with the same distortion (but with a phase shift). Similar behavior is observed at cutback and sideline. To give a comparison between the regimes concisely, only the RF harmonics of the integrated pressure forces are given in Fig. 3.36 for the two inlet geometries at cutback and sideline.

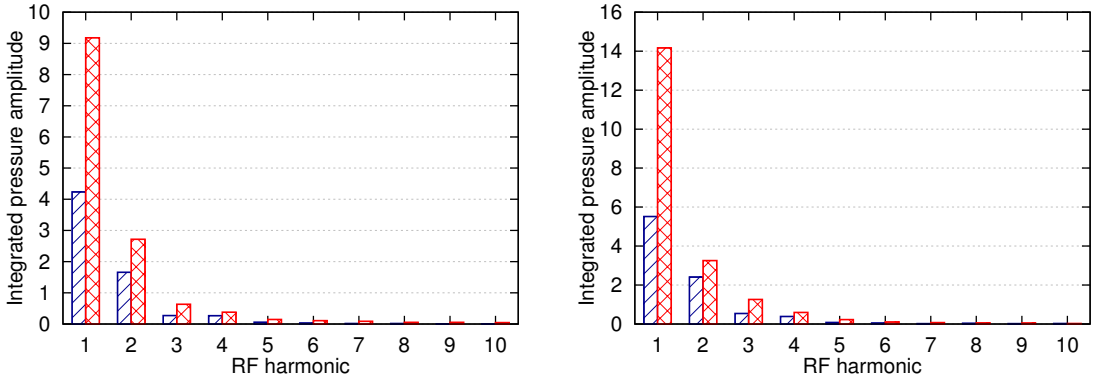

(a) Cutback (b) Sideline

Figure 3.36: **Amplitude of one fan-blade integrated pressure fluctuations at the RF and its harmonics for cutback and sideline conditions: axisymmetric inlet, asymmetric inlet**

The same harmonic distribution as the one of the approach regime is obtained,

with a domination of the first harmonic. The level of this harmonic without inlet distortion is increased with the regime (1.7, 4.2 and 5.6 at approach, cutback and sideline). The impact of inlet distortion is similar between all regimes, with a rise of all harmonics and a major increase of the first harmonic (multiplication by a factor going from 2 to 2.5).

OGV

Similar analysis is now performed on the OGV row. The wakes have been modified by the distortion as shown in Sec. 3.4.1 and the unsteady loadings on the vanes are consequently expected to be modified. The analysis is first performed on one classical OGV (located around $\pi/6$). The pressure distribution over this vane at the BPF is plotted for different vane heights in Fig. 3.37. Approach conditions are again chosen for illustration.

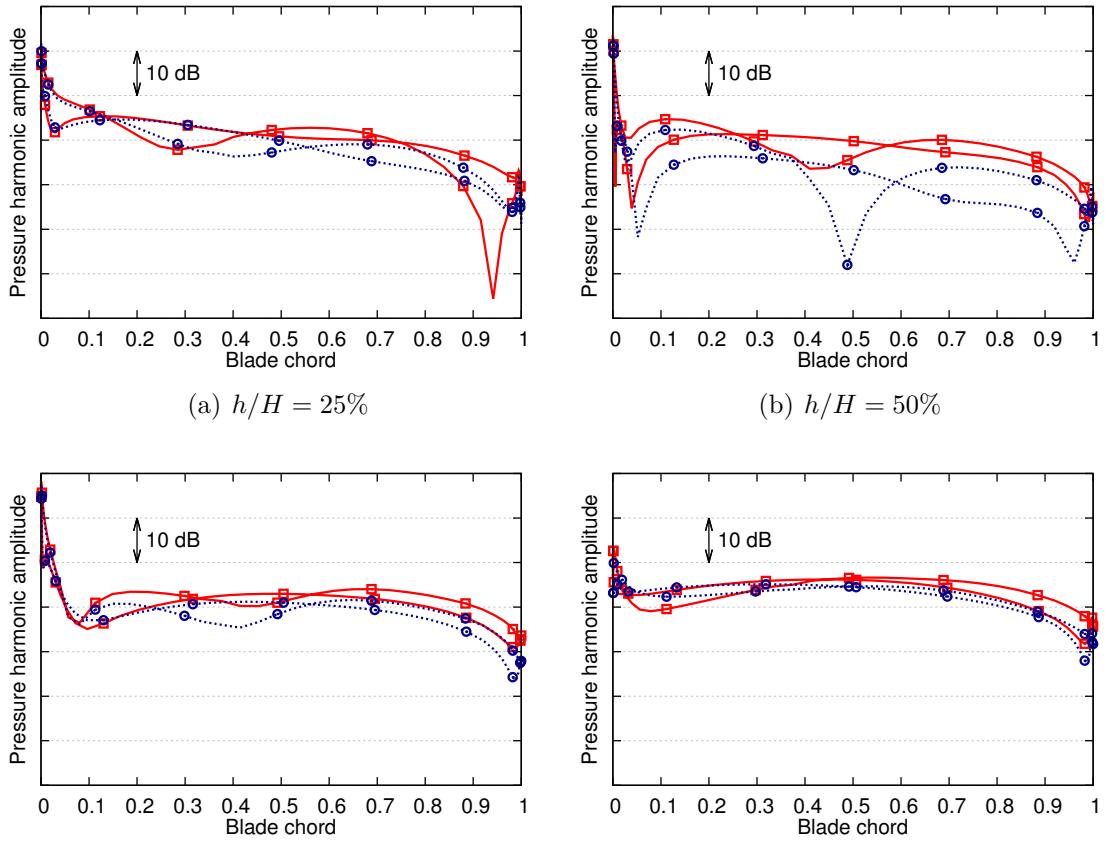

(a) $h/H = 25\%$ (b) $h/H = 50\%$

(c) $h/H = 75\%$ (d) $h/H = 95\%$

Figure 3.37: **Normalized pressure distribution at the BPF over one OGV at 25%, 50%, 75% and 95% of vane height (approach conditions): axisymmetric inlet, asymmetric inlet**

The levels reached without inlet distortion are similar between all vane heights. The pressure fluctuations are higher close to the leading edge because of the impact

of fan-blade wakes. The impact of inlet distortion is less remarkable than on the fan blade shown in Fig. 3.33. In average, the levels are slightly increased (by less than 1 dB) at 25% and 50% of vane height. At 75% and 95% of vane height, the average pressure fluctuations are reduced with the inlet distortion by 1 dB and 3 dB respectively. These variations can be linked to the modification of the wakes by the inlet distortion. When looking in Fig. 3.31(a) at the position corresponding to the present vane ($\theta = \pi/6$), a decrease of the maximum velocity deficit is observed at 50%, 75% and 95% of vane height while an increase is observed at 25% of vane height. The decrease of velocity deficit and increase of pressure fluctuations at mid-span might appear a bit contradictory. The loading fluctuations are considered to be caused by unsteady variations of the velocity normal to the vane (upwash). The velocity deficits in Fig. 3.31(a) were computed from the velocity modulus to provide a first idea and might differ from the ones computed from the normal velocity. The overall unsteadiness on this vane is quantified by integrating the pressure amplitude at the BPF and its harmonics. Results are shown in Fig. 3.38 for the first three harmonics.

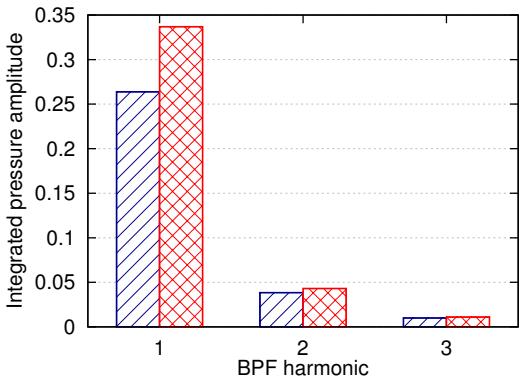

Figure 3.38: **Amplitude of one OGV integrated pressure fluctuations at the BPF and its harmonics for approach conditions: axisymmetric inlet, asymmetric inlet**

When integrated, the inlet distortion is responsible for an increase of the unsteady loading on this vane. The mean impact is observed at the BPF with a level almost 30% higher. At 2BPF and 3BPF, the impact is smaller (less than 10%). Because the wakes differ with the azimuthal positions, the unsteady loading is expected to be different from one vane to another. This is shown in Fig. 3.39 where the level of the integrated pressure at BPF is given for all vanes and for the two inlet geometries. The vanes are ordered according to their azimuthal positions: the vane 1 is located at $\theta = -\pi$ and the vane 48 at $\theta = +\pi$. The pressure distribution shown in Fig. 3.37 corresponds to the vane 38. The vanes 12 and 36 represent the lower and upper bifurcations respectively and the struts correspond to the vanes 24 et 48.

High inhomogeneity of the unsteady loadings is observed even in the absence of inlet distortion. The levels of integrated pressure are much higher for the two bifurcations, probably because of the high surface of integration. Without account-

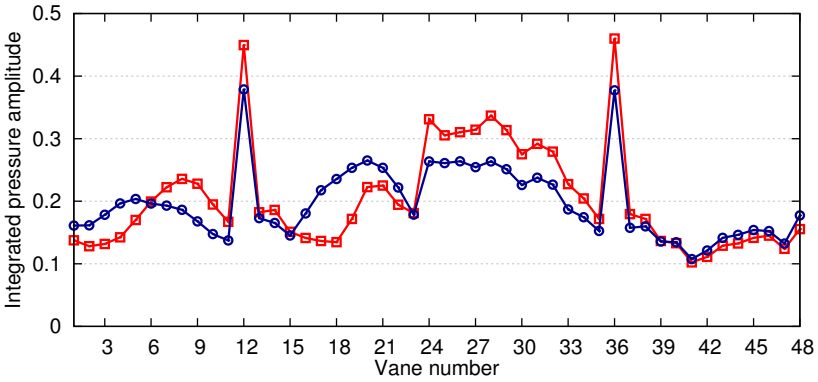

Figure 3.39: **Amplitude of the BPF harmonic of integrated pressure for all OGVs (approach conditions): axisymmetric inlet, asymmetric inlet**

ing for these bifurcations, the levels vary from from 0.11 to 0.26 (multiplication by more than 2). The inhomogeneity is further increased by the inlet distortion and the levels (still without accounting for the bifurcations) go from 0.10 to 0.34 (multiplication by more than 3). For some vanes, the integrated pressure at BPF is reduced with the inlet distortion while it is increased for some others. The reduction of the unsteady loadings from vanes 12 to 24 can be explained by the important reduction of the intensity of the wakes from $-\pi/2$ to 0 observed in Fig. 3.31(a) at 75% and 95% of vane height. At other positions, the differences between the velocity deficits obtained in the axisymmetric and non-axisymmetric configurations are lower so that the link cannot be directly done (all vane heights should be studied). This inhomogeneity reflects the complete inhomogeneity of the stator. It has also been observed at cutback and sideline but with different repartition. This is shown in Fig. 3.40 where the pressure amplitude at BPF harmonics integrated over the vane 38 is plotted for these regimes. At approach (cf. Fig. 3.38) and sideline, the levels of the first harmonics are increased by the inlet distortion while they are decreased at cutback.

IGV

The focus is now put on IGV unsteady loadings. Pressure distribution at the BPF are plotted at 25%, 50%, 75% and 95% of vane height in Fig. 3.41. Results at approach conditions are shown for the two inlet geometries.

At all vane heights, the unsteady fluctuations are higher close to the leading edge because of the impact of fan-blade wakes. The addition of inlet distortion has only a little effect on this pressure distribution (less than 1% at all radii in average). The maximum effect is observed at 25% in the region where the fluctuations are the lowest. When integrated, these unsteady loadings are therefore expected to be very close for the two configurations. This is shown for the first three BPF in Fig. 3.42.

At the BPF (most important harmonic), the differences are minor (less than

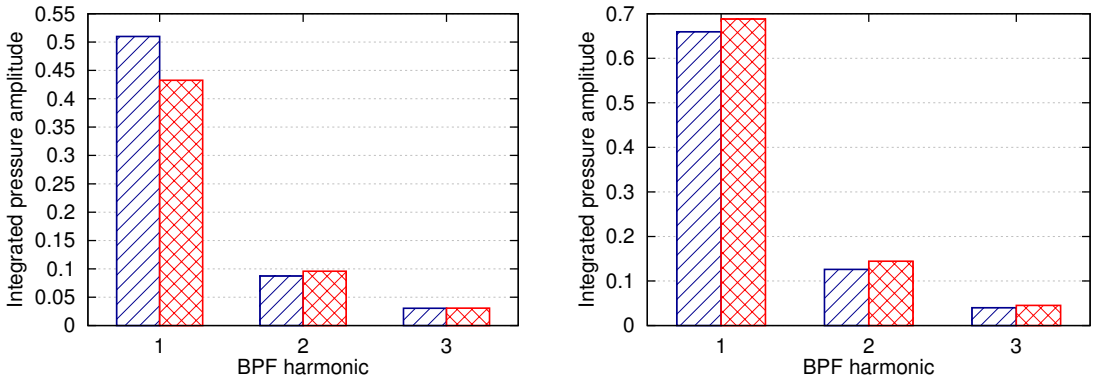

(a) Cutback (b) Sideline

Figure 3.40: **Amplitude of one OGV integrated pressure fluctuations at the BPF and its harmonics for cutback and sideline conditions: axisymmetric inlet, asymmetric inlet**

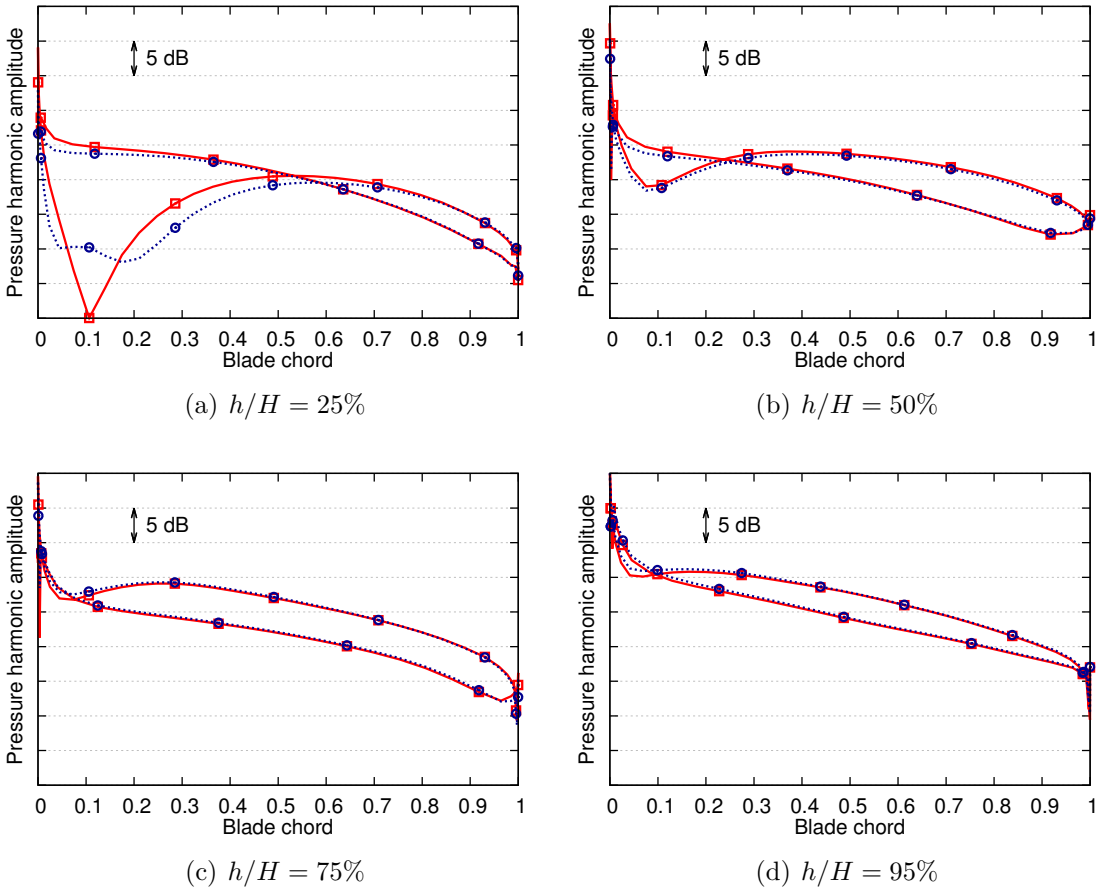

(a) $h/H = 25\%$ (b) $h/H = 50\%$

(c) $h/H = 75\%$ (d) $h/H = 95\%$

Figure 3.41: **Normalized pressure jump distribution over one IGV at 25%, 50%, 75% and 95% of vane height at the BPF (approach conditions): axisymmetric inlet, asymmetric inlet**

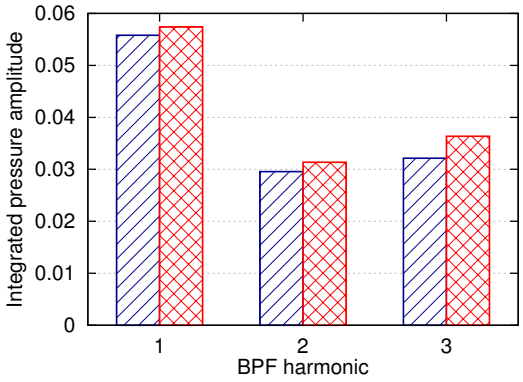

Figure 3.42: **Amplitude of one IGV force fluctuations at the BPF and its harmonics for approach conditions: axisymmetric inlet, asymmetric inlet**

3%). These differences are increased with the frequency (+6% and +13% for the 2BPF and the 3BPF respectively). This behavior indicates a modification of the fan-blade wakes that interact with the IGV because of the distortion. The levels of unsteady loading at the BPF is compared for all vanes in Fig. 3.43.

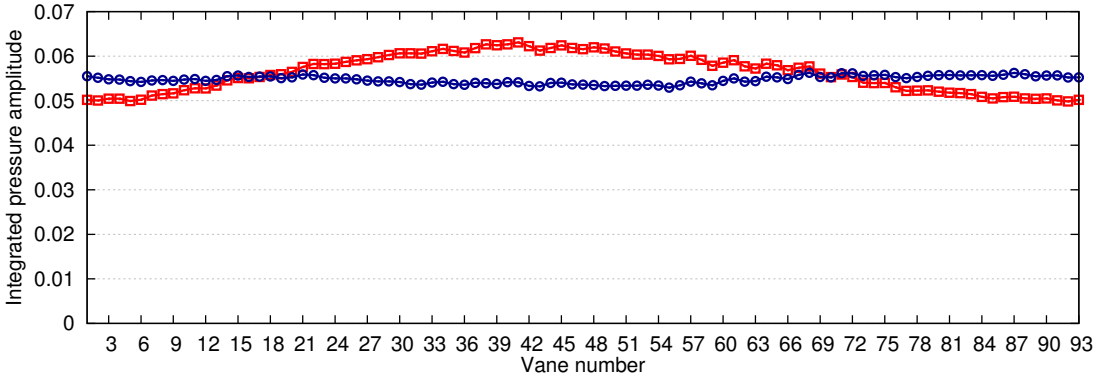

Figure 3.43: **Amplitude of the BPF harmonic of pressure force for all IGVs (approach conditions): axisymmetric inlet, asymmetric inlet**

Without inlet distortion, the levels are similar from one vane to another. This is because the distortion only comes from the potential effect of the pylon and is negligeable in the primary stream. When the inlet distortion is added, the levels are modified in a smooth way. For the vanes 20 to 70, the unsteady loadings are increased up to 15% while they are reduced up to 8% for the vanes 1 to 20 and 70 to 93. Similar behavior is obtained at cutback and sideline as shown in Fig. 3.44 where the levels of the first three BPF harmonics for the vane 67 (the one shown in Fig. 3.42) are plotted.

The differences between the levels of axisymmetric and non-axisymetric are small at all regimes (5% for the 1BPF at cutback and sideline). The impact of distortion

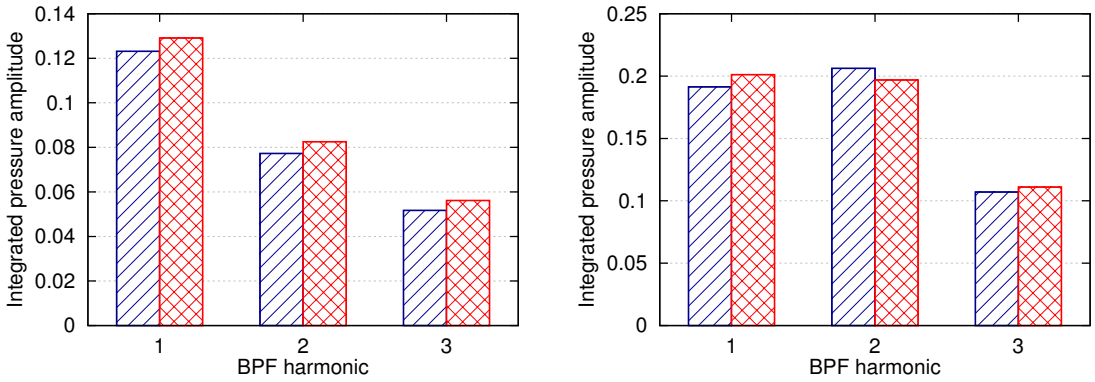

(a) Cutback (b) Sideline

Figure 3.44: **Amplitude of one IGV force fluctuations at the BPF and its harmonics for cutback and sideline conditions: axisymmetric inlet, asymmetric inlet**

on IGV sources is lower than on OGV sources and fan sources.

3.4.3 Fan-blade shocks

The unsteady loadings on fan blades are increased by the inlet distortion which means stronger acoustic sources. At sideline operating conditions, shocks also develop on the suction side of the blades and propagate upstream. Because the flow on the blades varies because of the distortion, the shocks may also be impacted. This is checked here by looking at the isentropic Mach number distribution over one fan blade. Because all blades are identical and equally spaced, they are supposed to have the same distribution (with a time lag). It is represented at $h/H = 95\%$ for the axisymmetric configuration in Fig. 3.45(a) for three equally-spaced instants of the same rotation.

On the pressure side (bottom curve), the isentropic Mach number is nearly constant. On the suction side, an important jump corresponding to the shock is observed. Its shock is located around 35% of the blade chord and has an intensity of 0.6 approximately. Local variations of less than 10% are observed during the rotation of the blade. These variations are better represented in Fig. 3.45(b) where the mean distribution is plotted along with the lower and upper envelopes. During the rotation, the position of the shock varies from 35% to 38% of blade chord and its intensity varies by about 15% (from 0.6 to 0.7). These variations are caused by the interaction with the potential effect of the pylon. Same plots are given when the inlet distortion is added in Fig. 3.46. The mean distribution obtained without inlet distortion is also added in dotted lines for comparison.

The variation of the isentropic Mach number distribution during the rotation is much more important with the inlet distortion. The area between the lower and upper envelopes is significantly increased which means that both the shock strength

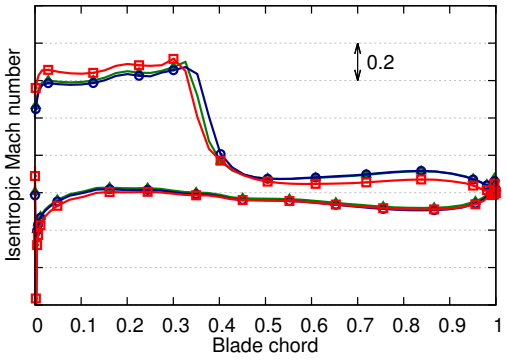

(a) Instantaneous distribution at t_1 (—▲—), t_2 (—○—) and t_3 (—□—)

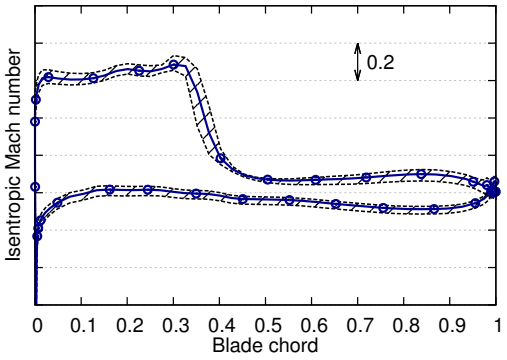

(b) Mean distribution (—○—) and envelope ▨

Figure 3.45: **Isentropic Mach number distribution (90A) over one fan blade at** $h/H = 95\%$

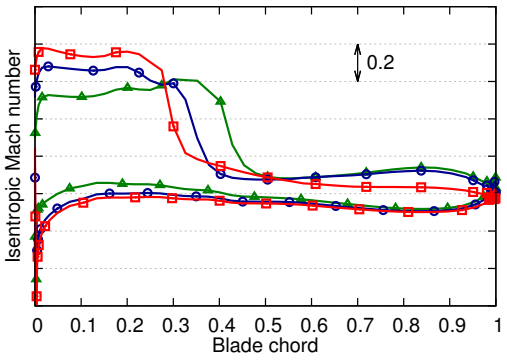

(a) Instantaneous distribution at t_1 (—▲—), t_2 (—○—) and t_3 (—□—)

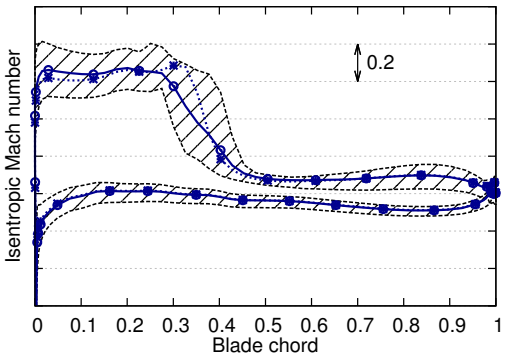

(b) Mean distribution (—○—) and envelope ▨

Figure 3.46: **Isentropic Mach number distribution (90N) over one fan blade at** $h/H = 95\%$

and shock positions are further modified. The shock position now varies approximately from 32% to 42% of the chord and the shock strength from 0.47 to 0.73 (almost 45% of variation). Because all blades are identical and equally spaced, these important variations occur on all blades during their rotations. The shocks that will propagate upstream will therefore be different depending on the azimuthal position at which they are generated. Concerning the mean distribution of isentropic Mach number, it is found to be similar between both configurations on the pressure side and on the suction side downstream of the shock. In the shock region and upstream of the shock, differences are observed. Indeed, the mean shock in presence of inlet distortion is smoothed because of the displacement of the shocks along the chord. This is just an effect of the average procedure because the shocks between both configurations have similar slopes as shown in instantaneous distributions.

Summary of the section

The impact of distortion on unsteady aerodynamic features has been highlighted. The fan-blade wakes are modified, in terms of velocity deficit particularly, even in the axisymmetric configurations. The inlet distortion further increases these inhomogeneities. It results in different unsteady loadings between the OGVs and the integrated pressure at the BPF is subjected to important variations between the different OGVs (ratio between the maximum and the minimum integrated pressure of about 2 without inlet distortion and of about 3 with inlet distortion). On the contrary, the unsteady loadings on fan blades are similar between blades because they are all identical but the levels are more than doubled by the inlet distortion at the RF. At sideline, shocks also develop on the fan blades and propagate upstream. These shocks are almost fixed in the axisymmetric configurations but their position varies over 10% of the chord and their strength varie by 45% during the rotation because of the inlet distortion.

3.5 Conclusion

The distortion has been characterized and quantified in this chapter. This distortion comes from the potential effect of the pylon and the struts and from asymmetry of the inlet duct (in the asymmetric configurations). The shape of the distortion has been discussed and its evolution with distance has been studied. A quantification based on the CDC is proposed and highlights the regions of high distortion. The impact of this distortion on unsteady aerodynamics has also been presented. A modification of the fan-blade wakes and shocks and of the unsteady loadings over the blades and vanes has been evidenced. All acoustic sources are impacted by the distortion and the consequences in terms of noise will be evaluated in the next chapter.

Chapter 4

Impact of distortion on acoustics

Contents

4.1 Introduction

The impact of distortion on acoustics is evaluated in this chapter. The first three sections 4.2-4.4 are dedicated to the analysis of each dipolar noise source (i.e. fan-OGV, distortion-fan and fan-IGV interaction) by the use of hybrid methods. These three noise sources are compared in Sec. 4.5 for all regimes. Complementary analysis is provided in Sec. 4.6 by exploiting the acoustic fluctuations extracted from the simulations directly.

4.2 Interaction of fan-blade wakes with OGVs

The interaction of fan-blade wakes with OGVs, which is expected to be the dominant noise source mechanism, is studied in this section using an hybrid approach. Different methods are used for the prediction of this noise in order to separate the contribution of different flow and geometry effects.

4.2.1 Analysis of the unsteady loadings

As shown in Goldstein's theory (cf. Sec. 1.6.1 [8]), the fan-OGV noise is caused by the unsteady loadings on the OGVs created by the impact of the fan-blade wakes. These unsteady loadings can be directly extracted from the unsteady simulations. In this subsection, they will also be computed analytically thanks to Amiet's theory (cf. Sec. 1.5.1 [62]) in order to evaluate the capabality of such a simplified model to capture the trends. This is done using the Optibrui software [83]. To account for the variation of the geometry and excitation along the span, Amiet's theory is applied for different strip bands. For each strip, the vane is modeled by a flat plate without camber and the pressure distribution over the airfoil is reduced to a distribution of pressure jump over the chord. According to Eq. (1.72), this pressure jump depends on the mean momentum, the mean Mach number and the Fourier coefficient of the upwash. The radial variation of these quantities extracted right upstream of one vane (the vane 38) is given in Fig. 4.1 at approach conditions. The upwash is shown at the BPF only.

The differences in mean momentum and Mach number caused by the air inlet distortion are small (less than 5%). The evolution of the upwash is similar between both geometries but strong local variations are observed (reduction of the level by 50% at 10% of vane height and multiplication by 100% at 95% of vane height for example). Amiet's pressure jump distribution computed from these quantities is plotted at different vane heights in Fig. 4.2. The numerical results have been added for comparison.

The analytical pressure jump distribution is slightly impacted by the inlet distortion at 25%, 50% and 75% of vane height because the input parameters are close at those radii. At 95% of vane height, an increase of more than 50% is observed

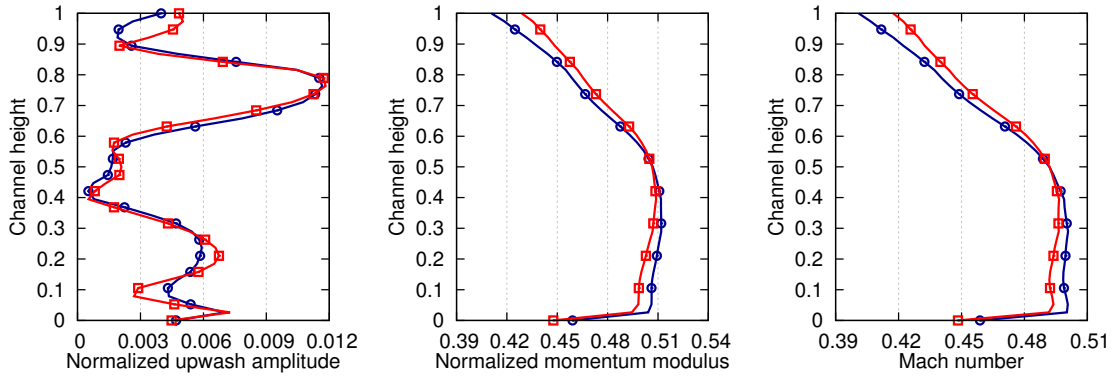

Figure 4.1: **Radial evolution of the amplitude of upwash at BPF, mean momentum and mean Mach number upstream of the vane 38 (approach conditions): axisymmetric inlet, asymmetric inlet**

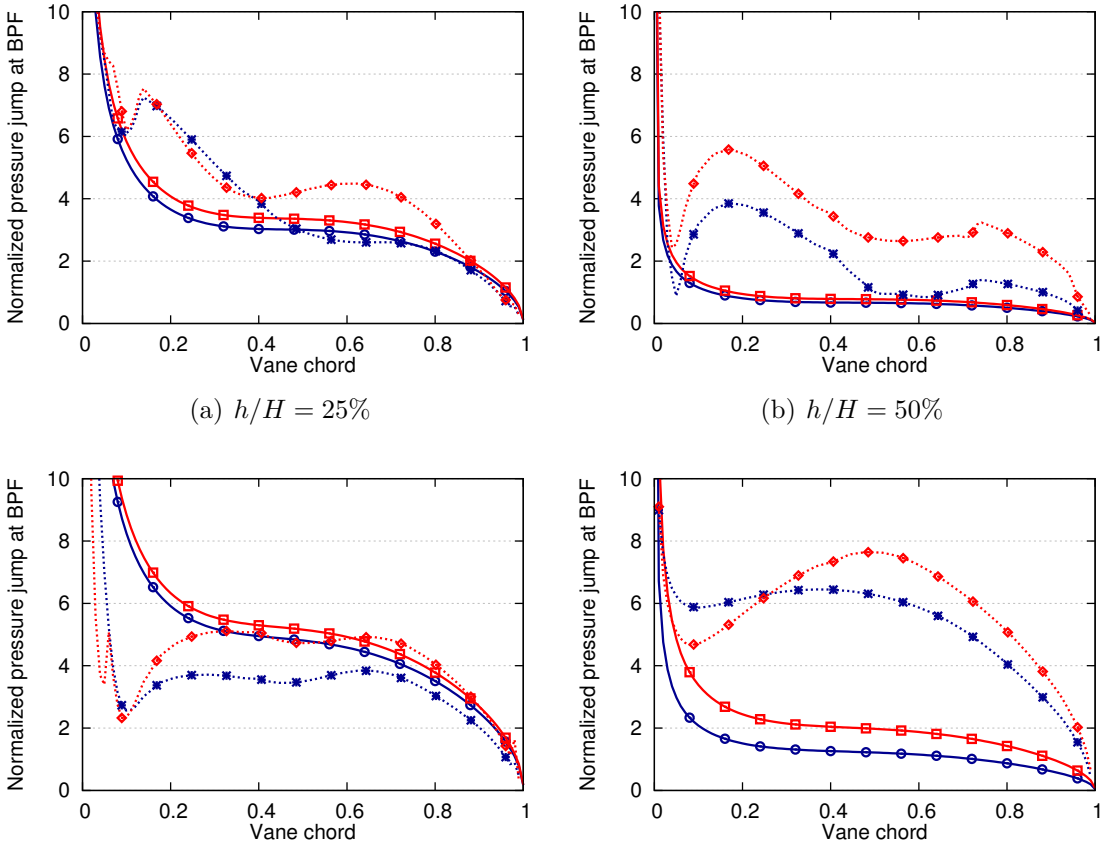

(a) $h/H = 25\%$ (b) $h/H = 50\%$

(c) $h/H = 75\%$ (d) $h/H = 95\%$

Figure 4.2: **Normalized pressure jump distribution over the vane 38 at the BPF (approach conditions): Amiet - axisymmetric inlet, Amiet - asymmetric inlet, CFD - axisymmetric inlet, CFD - asymmetric inlet**

and is related to the increase of upwash amplitude. The pressure jump distribution

computed with Amiet's theory have a characteristic shape with a dominant level at the leading edge, a stabilized level from 20% to 80% of the chord and a decrease till zero close to the trailing edge. At 25% and 50% of vane height, these evolutions compare well with the numerical results in the leading edge region but differ while following the same trend elsewhere. These differences may be caused by the cascade effect which is not accounted for in Amiet's theory. Closer to the tip, the tip-leakage flow might explain the increased differences. Amiet's model appears to be too simplified for such configuration and more complex models should be used [17]. This is out of the scope of the present study and only the numerical unsteady loadings will be considered in the rest of the section. However, it should be kept in mind that some of the trends that will be shown below could have been obtained using those analytical loadings.

4.2.2 Propagation in an annular duct

The sources represented by the numerical unsteady loadings are now propagated in the duct using Goldstein's analogy in order to evaluate the related noise. The power given by Eq. (1.103) requires the definition of a mean flow (mean density, speed of sound and axial Mach number) and a duct geometry (hub an tip radii). The sensitivity to the choice of these parameters will be discussed later. For now, the mean flow values are obtained by averaging the corresponding variables in plane P5 and plane P6 for upstream and downstream noise evaluation respectively. The duct is delimited by the minimum and maximum radii of the OGV. The acoustic power obtained at approach conditions by considering a stator composed of only one vane (the vane 38) is plotted in Fig. 4.3 for the axisymmetric and asymmetric configurations. In order to separate the effect of distortion on source generation and on noise propagation, two results are given for the asymmetric configuration: one with the mean flow computed from the axisymmetric configuration and the other with the mean flow computed from the asymmetric configuration.

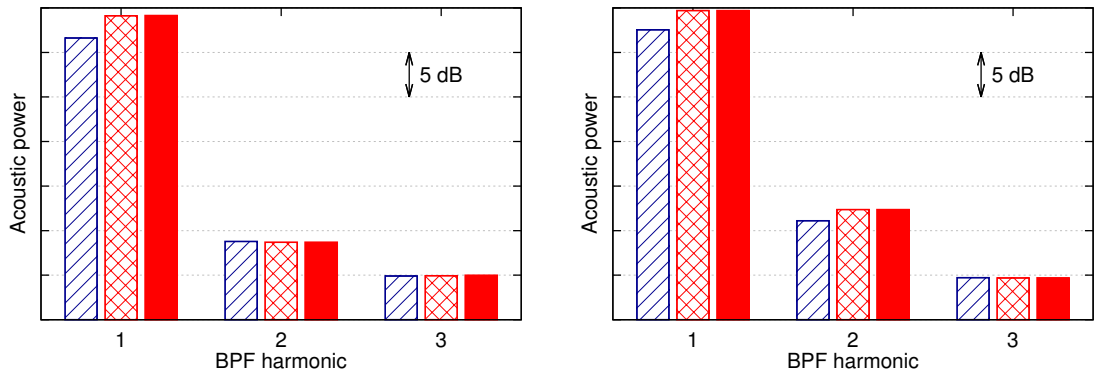

(a) Upstream (b) Downstream

Figure 4.3: **Acoustic power radiated by vane 38 at approach conditions: axisymmetric source, asymmetric source and axisymmetric flow, asymmetric source and asymmetric flow**

The choice of the flow for the asymmetric configuration does not have an effect in this case because the mean flow values around the OGV are only slightly impacted by the inlet distortion. The main impact of the inlet distortion is observed at the BPF, with an increase of about 2-3 dB in both directions, and is related to the increased level of the unsteady loadings at the BPF. Because the OGV and the excitation are heterogeneous, this trend can be reversed for other vanes as already mentionned in Sec. 3.4.2.

4.2.3 Effect of stator heterogeneity

The noise radiated by the whole OGV row is now computed in a similar way. It is compared in Fig. 4.4 with the noise radiated by the single vane 38 and by an artificial stator of 48 identical vanes (constructed using the vane 38). Results are given for the axisymmetric configuration at approach conditions.

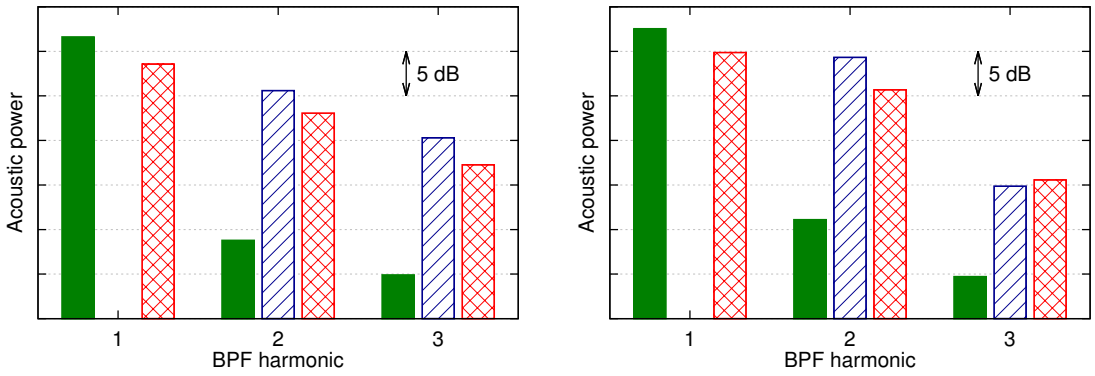

(a) Upstream (b) Downstream

Figure 4.4: **Acoustic power radiated by the OGV (60A): isolated vane homogeneous stator composed of 48 identical vanes, real heterogeneous stator**

Accounting for the entire stator instead of the isolated vane naturally results in a increase of the noise levels at 2BPF and 3BPF because more sources are present (from 10 to 20dB). However, the trend is reversed at the BPF (reduction of 2-3 dB). The results obtained for the artificial stator composed of 48 identical vanes ease the understanding of this behavior. The noise radiated from the homogeneous stator is increased by up to 5 dB at 2BPF and 3BPF when compared with the heterogeneous stator. However, the homogeneous stator does not produce any noise at the BPF because all Tyler & Sofrin modes $m = -B - kV$ are cut-off ($B = 18$ number of blades, $V = 48$ number of vanes and k any integer). This can be interpretated as destructive interferences of the acoustic field produced by each identical vane. Some vanes are similar in the real stator so that a part of these destructive interferences still occurs. The noise from the heterogeneous stator at the BPF is therefore lower than the one from the isolated vane.

These differences are further investigated by looking at the distribution of the power over the azimuthal modes. This is done by isolating the contribution of each mode m in Eq. (1.103). Using the notations of Sec. 1.6, the power of the mode m at sBPF is written

$$P^{\pm}_{sB,m} = \frac{k_0\beta^4}{2\rho_0 a_0} \sum_{\substack{n=0 \\ k^2_{mn}\geq 0}}^{+\infty} \frac{|S^{\pm}_{mn}|^2}{\Gamma_{mn} k_{mn} (k_0 \pm M_0 k_{mn})^2}. \tag{4.1}$$

The downstream azimuthal mode distribution at 2BPF is given in Fig. 4.5 as a representative example. Because the fan rotates in the negative direction, negative modes are co-rotating and positive modes are contra-rotating.

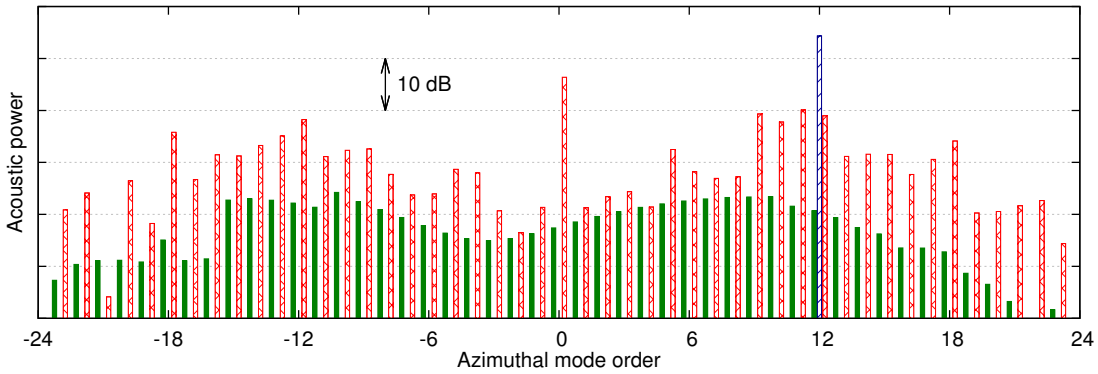

Figure 4.5: **Downstream azimuthal mode distribution at 2BPF (60A): isolated vane homogeneous stator composed of 48 identical vanes, real heterogeneous stator**

The x-axis ranges from -24 to 24 because modes of higher order are cut-off. For the reconstructed homogeneous stator, only one mode is present ($m = 12$) and corresponds to the $k = 1$ Tyler & Sofrin mode ($m = -2B + V$). For the single vane and the heterogeneous stator, the power is distributed over all cut-on modes. The mode $m = 0$ is surprisingly dominant for the real heterogeneous stator (7 dB higher than any order mode). In the rest of the section, the results are all obtained with the heterogeneous stator.

4.2.4 Influence of the regime

The downstream mode distribution at 1BPF is plotted in Fig. 4.6 at all regimes and without inlet distortion. The power is spread over all the cut-on modes and the planar mode $m = 0$ is dominant. A shift of the cut-on/cut-off transition to higher order modes with the regime is observed (last cut-on mode at $|m| = 11$, $|m| = 15$ and $|m| = 18$ at approach, cutback and sideline respectively). The total noise generated by the OGV is increased with the regime because of the higher number of cut-on modes and because of the increased levels of other modes in average (caused by higher velocity deficit as shown in Sec. 3.4.1).

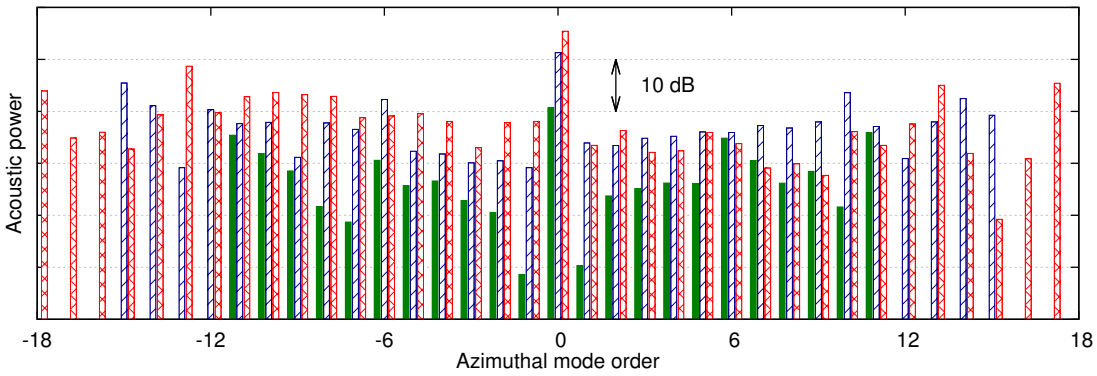

Figure 4.6: **Downstream azimuthal mode distribution at 1BPF (axisymmetric configurations): approach, cutback, sideline**

4.2.5 Effect of axial variation of flow and duct

All the noise levels predicted up to now were determined using one set of parameters in terms of mean flow and duct geometry. However, significant variations occur along the axis and the choice is not evident. Different sets of parameters are tested here in order to evaluate the impact of this choice:

- set 1: duct defined by OGV extrema radii / mean flow values extracted in plane P5 and plane P6 for upstream and downstream noise evaluation respectively (parameters used up to now);
- set 2: duct defined by duct extrema radii in plane P5 and plane P6 for upstream and downstream noise evaluation respectively / mean flow values extracted in plane P5 and plane P6 for upstream and downstream noise evaluation respectively;
- set 3: duct defined by OGV extrema radii / mean flow values extracted in plane P1 and plane P7 for upstream and downstream noise evaluation respectively;
- set 4: duct defined by duct extrema radii in plane P1 and plane P7 for upstream and downstream noise evaluation respectively / mean flow values extracted in plane P1 and plane P7 for upstream and downstream noise evaluation respectively.

The acoustic power at the first three BPF computed using these four sets are compared for the axisymmetric configuration at approach conditions in Fig. 4.7.

Differences in noise levels are observed when the mean flow values are taken at different planes (set 1 vs. set 3 and set 2 vs. set 4) and when the duct radii are modified (set 1 vs. set 2 and set 3 vs. set 4). At all BPF harmonics, there is a maximum difference of about 2 dB between the four sets. This introduces an uncertainty on the noise levels that can be mitigated by the use of Rienstra's slowly varying duct approach described in Sec. 1.6.2 [84]. This approach is used here by defining a duct without accounting for the primary stream and by using the axial mean flow computed from the CFD simulation. The resulting axial evolution of the acoustic power at the BPF is plotted in Fig. 4.8 where Goldstein's results have been

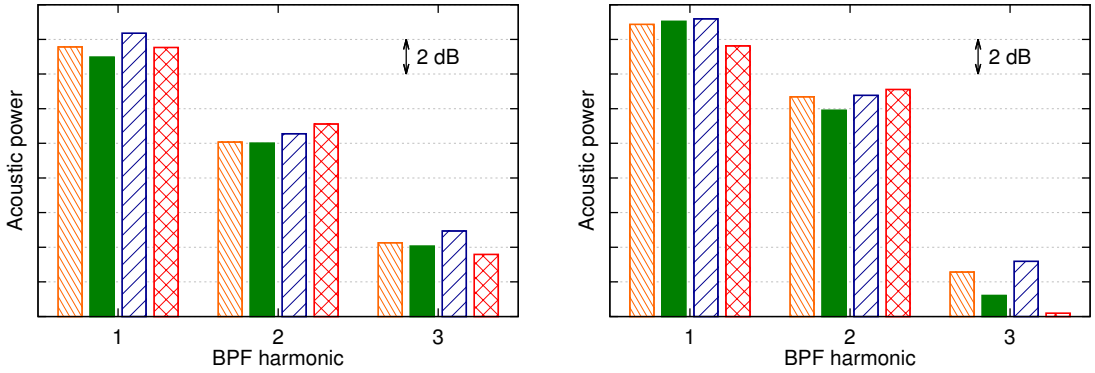

(a) Upstream (b) Downstream

Figure 4.7: **Acoustic power radiated by the heterogeneous OGV (60A) for different sets of parameters: set 1, set 2, set 3, set 4**

added for comparison.

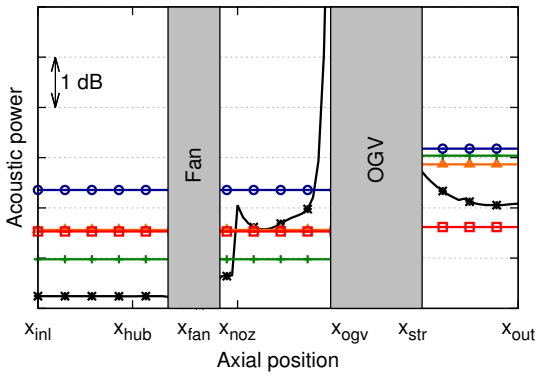

Figure 4.8: **Acoustic power radiated by the OGV (60A): Goldstein - set 1, Goldstein - set 2, Goldstein - set 3, Goldstein - set 4, Rienstra**

Downstream of the OGV, the power predicted by Rienstra's theory is between the ones predicted by Goldstein's analogy with the four sets of parameters. The maximum difference is observed with set 3 and is about 1 dB. The exponential-like decrease of the acoustic power on both sides of the OGV is caused by the evanescent modes. It is generally not present in the real acoustic power which is defined as the real part of Eq. (1.62). In this study, it has been chosen to work with the modulus of Eq. (1.62) for reasons that will be explained in Sec. 4.3.6. In any case, the difference is localized close to the source only, where the pressure associated with evanescent modes is still significant. While going towards the fan, the noise level is then reduced by almost 2 dB before reaching a plateau upstream of the fan. This decrease is linked to geometry and flow changes which are not accounted for in Goldstein's predictions. The maximum difference between Rienstra and Goldstein's predictions is about 2 dB and is again observed with set 3. In the region close to

the splitter that separate the two streams (denoted by x_{noz}), a peak is observed. It might be caused by the sudden increase of the section or by the presence of a transition point (see Sec. 1.6.2).

It should be noted that both Goldstein and Rienstra's theories are valid when there is not any obstacle in the duct. This is clearly not the case downstream of the OGV where the pylon extends up to the outlet plane and divides the duct into two parts. Such ducts are often called C-ducts because of the shape of each part. The effect of this characteristic is not studied in this manuscript but Bonneau *et al.* [21] have shown that the noise level remains unchanged when the bifurcation is thin. The mode content can however be altered by the presence of the pylon as illustrated by Redonnet & Druon [110].

4.2.6 Effect of swirling flow

A simple way to account for the swirl has been introduced in Sec. 1.6.3. It consists in introducing a Doppler shift in the frequencies: for each mode of azimuthal order m, the actual frequency ω is replaced by $\omega - mU_\theta(r)/r$ with U_θ the mean azimuthal velocity and r the radius. In order to simplify the application of this correction, $U_\theta(r)/r$ is assumed to be constant along the span and equal to Ω the rotational speed of the engine (because $U_\theta(r) \approx r\Omega$). This correction is applied in the interstage region only. Results are given in Fig. 4.9 for the approach and cutback configurations without inlet distortion.

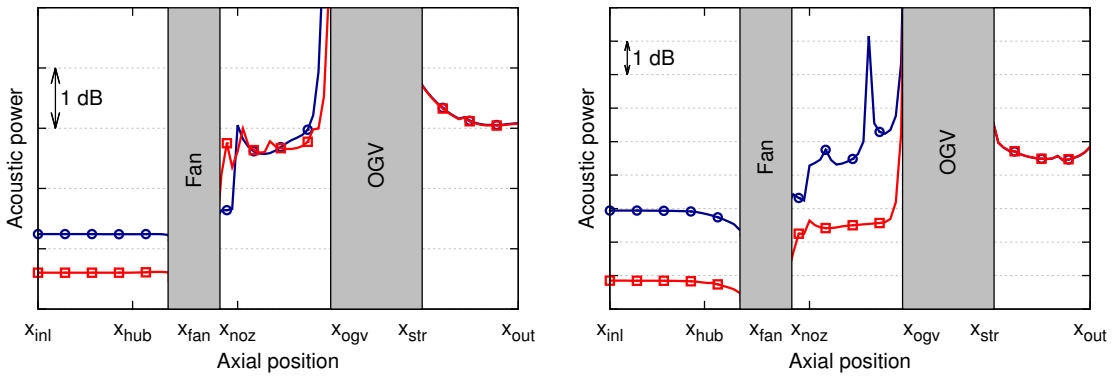

(a) Approach (b) Cutback

Figure 4.9: **Effect of swirl on the acoustic power radiated by the OGV at the BPF (60A): without, with**

The swirl is responsible for a decrease of the upstream noise levels for both regimes. The decrease is about 1 dB at approach and 2 dB at cutback. At sideline, the behavior is similar to that at cutback. Naturally, there is not any effect on the downstream noise levels. The peak observed upstream of the OGV at cutback without swirl is caused by a transitional mode. The use of Ovenden's theory [87] should avoid such behavior by predicting the transmitted and reflected waves at the tran-

sition but this is out of the scope of this PhD thesis. The reduction of the upstream noise by the swirling flow is further analyzed by looking at the mode distribution at 1BPF in the interstage region given in Fig. 4.10 for cutback conditions.

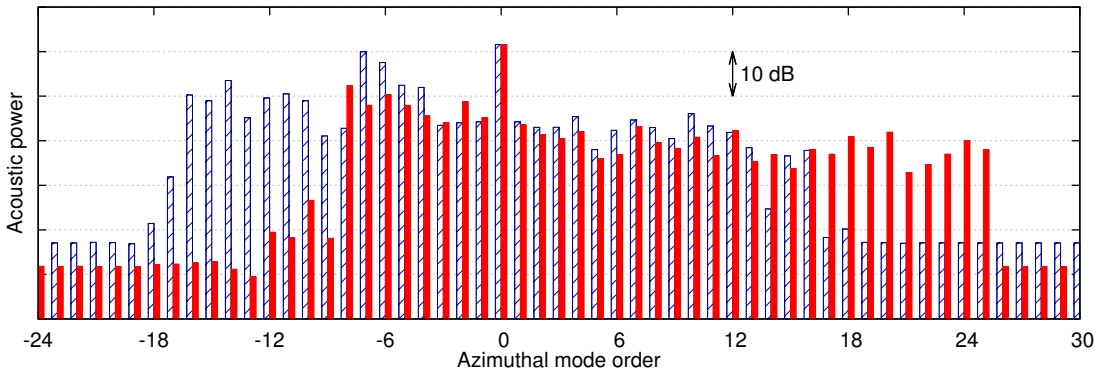

Figure 4.10: **Effect of swirl on the azimuthal mode distribution at 1BPF in the interstage region (OGV source - 80A): without swirl, with swirl**

The swirling flow modifies the transition between cut-on and cut-off modes by easying the propagation of contra-rotative modes (positive modes). In total, the same number of modes is cut-on but modes of higher order in average are present when the flow is swirling. Because higher order modes are known to propagate less efficiently due to the behavior of the higher order Bessel functions, the tonal noise is reduced [111].

4.2.7 Noise penalty induced by inlet distortion

Before evaluating the OGV noise penalty induced by inlet distortion, the issue of duct definition for the asymmetric configuration is adressed. Rienstra's theory is valid for axisymmetric ducts so that it cannot be applied directly to a non-axisymmetric configuration. Two ducts will therefore be used and compared. The first one is the same duct as the one used for the axisymmetric configuration. The other one is a reconstructed axisymmetric duct defined in order to have the same cross-section surface as the one of the real asymmetric duct at each axial position. This reconstructed duct accounts for the reduced cross-section surface of the asymmetric inlet. With this duct, both the flow extracted from the axisymmetric simulation and the one extracted from the asymmetric simulation are used in order to isolate the effects of duct geometry and mean flow definition on the propagation. Results are plotted in Fig. 4.11 at approach conditions.

The duct is not axisymmetric only upstream of the fan and the duct definition has naturally no effect downstream of it. No effect of the flow definition is also observed downstream of the fan because the averaged flow values with and without inlet distortion are close. However, some small differences (below 0.5 dB) are observed upstream of the fan. The asymmetric flow is responsible for a slight decrease

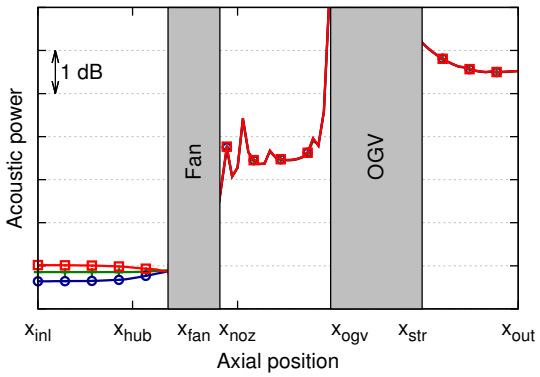

Figure 4.11: **Acoustic power radiated by the heterogeneous OGV (60N) for different flow and duct definitions: axisymmetric duct and axisymmetric flow, axisymmetric duct and asymmetric flow, equivalent asymmetric duct and asymmetric flow**

of the noise level while the reduction of the duct cross-section surface is responsible for a slight increase. These trends are not the same between all regimes but the differences always stay below 1 dB.

The penalty on OGV noise induced by inlet distortion is finally compared using the slowly varying duct theory and including the Doppler shift in frequencies in the interstage region to model the effect of swirl. For the asymmetric configurations, the predictions based on the same duct and flow parameters as the axisymmetric configurations are shown, as well as the ones based on the asymmetric flow and the reconstructed duct conserving the cross-section surface. Thus, the sources extracted from the axisymmetric and the asymmetric simulations can be compared for similar propagation conditions and also for conditions more faithful to the CFD conditions. Results are shown at the BPF in Fig. 4.12.

At all regimes, the choice of axisymmetric or asymmetric propagation properties has only a little effect on the noise levels downstream of the fan. Upstream of the fan, the effect is bigger but still low (maximum of 0.7 dB at sideline). The noise penalties induced by inlet distortion are small in the upstream direction (maximum of 0.8 dB of reduction at sideline) but they are significant in the downtream direction (2.5 dB, 2 dB and 1.6 dB at approach, cutback and sideline respectively). However, the upstream results should be taken with precaution because the swirling flow is modeled simply and rotor shielding effects are not accounted for. The noise at the BPF was shown to be caused by the heterogeneity of the OGV. In the presence of inlet distortion, the heterogeneity of the wakes is increased and consequently, the heterogeneity of the OGV unsteady loadings is also increased. Less coherence between the acoustic fluctuations radiated by each vane is therefore expected which results in less destructive interferences and then in a increased noise level.

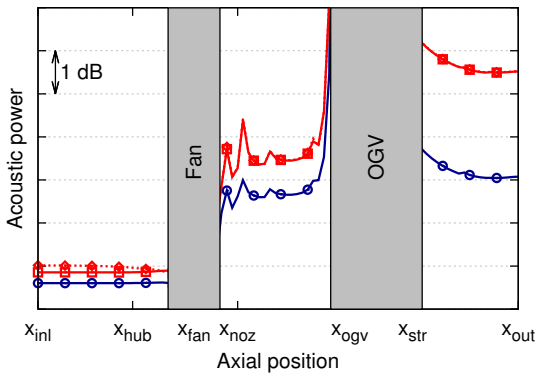

(a) Approach

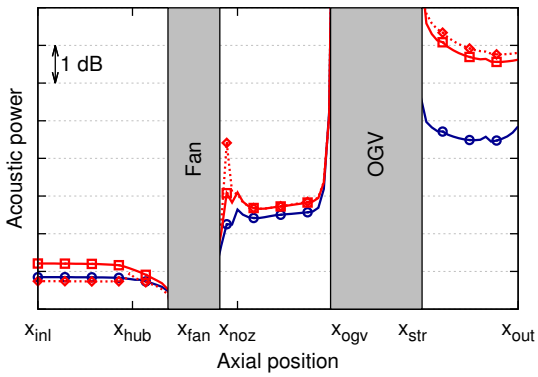

(b) Cutback

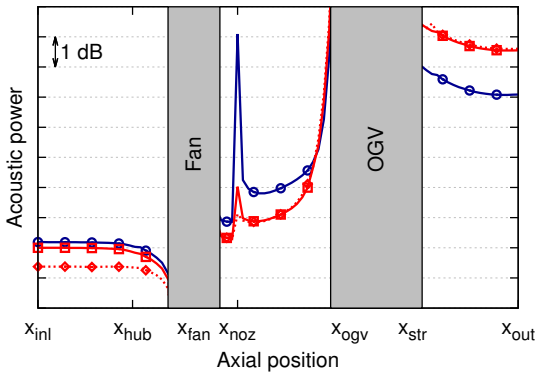

(c) Sideline

Figure 4.12: **Acoustic power radiated by the heterogeneous OGV with and without inlet distortion: axisymmetric source, asymmetric source and axisymmetric propagation properties asymmetric source and asymmetric propagation properties**

Summary of the section

The interaction of the fan-blades wakes with the OGV has been studied thanks to an hybrid approach. The limits of Amiet's model on the studied configuration have been shown even if it gives the good trends. The overlapping of the vanes is high and is probably responsible for a strong cascade effect. The numerical unsteady loadings have therefore been used for the propagation of noise in the duct. The effects of the axial variation of the flow and the duct geometry have been highlighted by the comparison of Goldstein's and Rienstra's theories and differences in noise levels of some decibels are obtained. The swirling flow has been introduced in the propagation model by a simple Doppler shift in frequencies and has been shown to move the cut-on modes towards the contra-rotating modes. The fan/OGV interaction mechanism produces noise at the BPF even if it is generally considered to be cut-off. This is due to the heteregeneity of the OGV row which generates modes that are different from the classical Tyler & Sofrin modes. The noise is therefore distributed on all the cut-on modes. The increased inhomogeneity of the fan-blade wakes in the presence of inlet distortion has been shown to increase these modes and consequently, to increase the total noise radiated by the OGV (essentially in the downstream direction and by 1 to 3 dB depending on the regime).

4.3 Interaction of distortion with fan blades

The noise resulting from the interaction of distortion with fan blades is now studied in this section. The same methods as the ones described in the previous section will be used by adapting their formulation to rotating sources.

4.3.1 Analysis of the unsteady loadings

The unsteady loadings on fan blades are created by the impact of the distortion. Amiet's theory is used in the same way as in Sec. 4.2.1 to predict analytically the pressure jump distribution. The procedure is applied to one blade only but all blades are identical and show similar distribution. The inputs of Amiet's model i.e. the mean momentum, the mean Mach number and the Fourier coefficient of the upwash are plotted in Fig. 4.13 at approach conditions for both inlet geometries. The upwash is shown at the RF only to focus on the interaction with the distortion.

The inlet geometry has only a little effect on the mean flow variables (maximum difference of 3% close to the hub). However, the impact on the upwash at RF is huge along all the span (approximately multiplied by 5). This is a consequence of the increase of the mode 1 of the distortion already observed in Fig. 3.17. The pressure jump distribution computed by Amiet's model using these inputs are given for different blade heights in Fig. 4.14. Because the inputs have been extracted

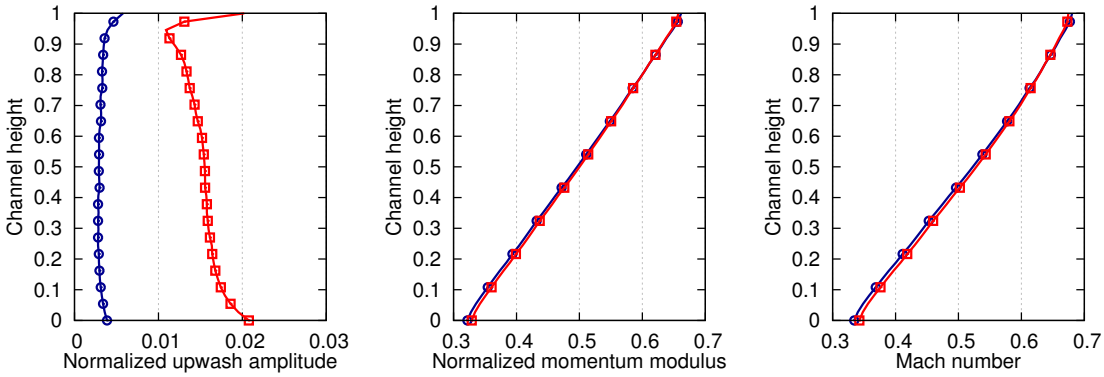

Figure 4.13: **Radial evolution of the amplitude of upwash at RF, mean momentum and mean Mach number upstream of one fan blade (approach conditions): axisymmetric inlet, asymmetric inlet**

upstream of the fan, a classical leading-edge model is used (the one described in Sec. 1.5.1). The numerical results are given for comparison.

Important discrepancies between analytical and numerical levels are observed and further investigations should be carried on to understand their origin. However, similar evolution is obtained with a peak at the leading edge and a decrease along the chord. At 75% and 95% of blade heights, humps are observed in the numerical results and might be caused by secondary flows. The similarity between the trend observed in Amiet's results and CFD's results indicates that the unsteady loadings on fan blades are effectively dominated by a leading-edge mechanism, even in the axisymmetric configuration where the distortion comes from the downstream pylon. The pressure jumps computed by Amiet's model are approximately five times higher in the presence of inlet distortion and this is directly linked to the increase of the upwash. The increase obtained from the numerical results is lower (about 2 at 25%, 50% and 95% of blade height and even lower in average at 75% of blade height). Again, more complex models could be used to understand these differences. The cascade effect should probably be included such as the camber which is significant for fan blades [17]. Only the numerical unsteady loadings will be considered in the rest of the section but it should be kept in mind that some trends could have been obtained using analytical models.

4.3.2 Propagation in an annular duct

Goldstein's analogy is used to propagate the acoustic sources represented by these unsteady loadings in an annular duct in order to evaluate the related noise. For now, the mean flow values needed for the propagation (density, speed of sound and axial Mach number) are obtained by a flow averaging in plane P2 and in plane P3 for upstream and downstream propagation respectively. Two sets of flow values are used for the propagation of the sources extracted from the asymmetric simulations: the first is obtained from the axisymmetric simulation and the other from the asymmetric simulation. The effect of inlet distortion on source generation and

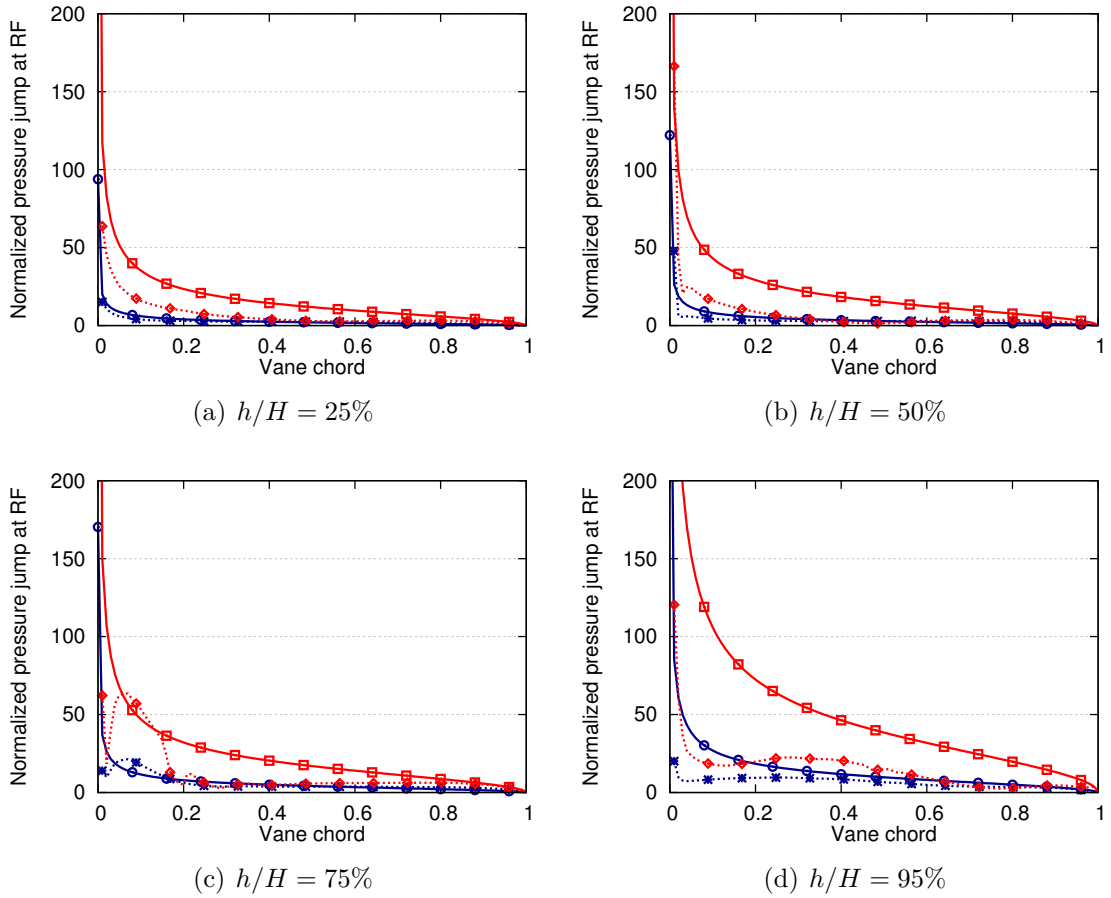

(a) $h/H = 25\%$ (b) $h/H = 50\%$

(c) $h/H = 75\%$ (d) $h/H = 95\%$

Figure 4.14: **Normalized pressure jump distribution over one fan blade at 25%, 50%, 75% and 95% of blade height at the RF (approach conditions): Amiet - axisymmetric inlet, Amiet - asymmetric inlet, CFD - axisymmetric inlet, CFD - asymmetric inlet**

noise propagation is therefore studied independently. Results are given in Fig. 4.15 at approach conditions as an example. Sources on one fan blade only have been integrated.

An increase of both upstream and downstream noise levels is observed when considering the sources in the presence of inlet distortion. At the BPF, the increase is about 2 dB upstream and 9 dB downstream. The choice of axisymmetric or asymmetric flow values for the propagation of asymmetric sources has only a little effect.

4.3.3 Assessment of the rotor homogeneity

The sources radiated from the whole rotor are now propagated in a similar way. The resulting noise is compared with the noise computed from one single blade and from one fictitious rotor of 18 blades created by duplicating one fan blade. Results are given in Fig. 4.16.

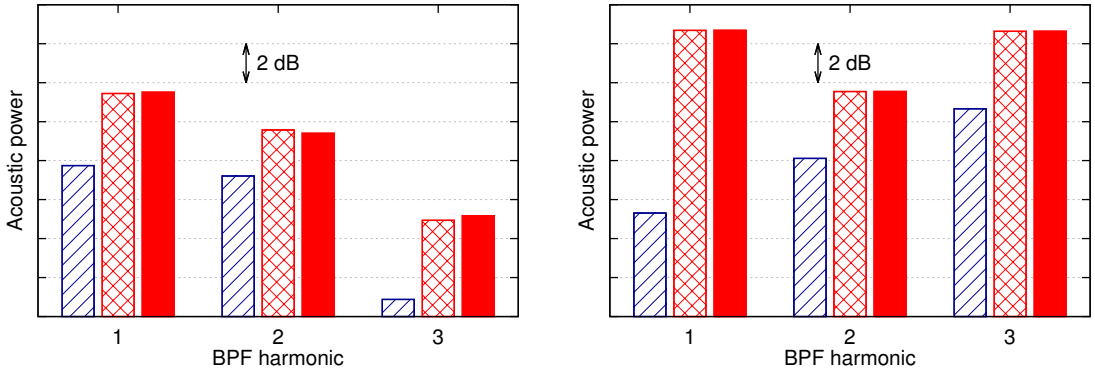

(a) Upstream (b) Downstream

Figure 4.15: **Acoustic power radiated by one fan blade at approach conditions: axisymmetric source, asymmetric source and axisymmetric flow, asymmetric source and asymmetric flow**

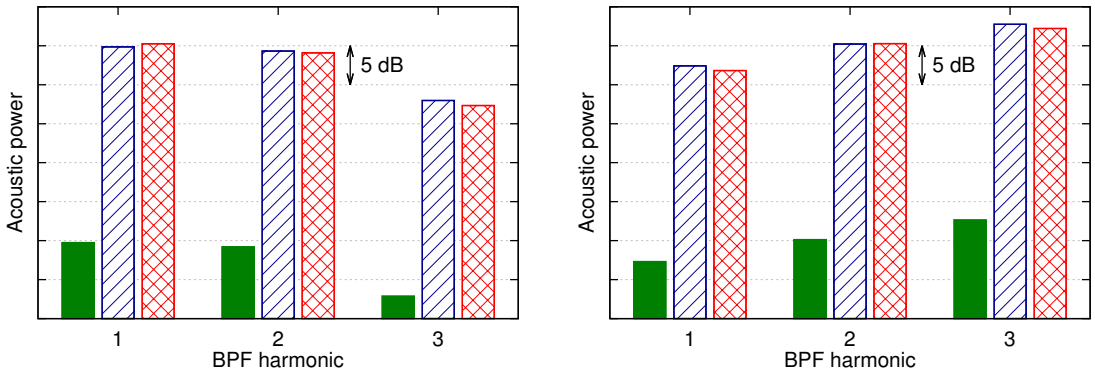

(a) Upstream (b) Downstream

Figure 4.16: **Acoustic power radiated by the fan (60A): isolated blade homogeneous rotor composed of 18 identical blades, real rotor**

Results obtained from the reconstructed rotor and the real rotor are naturally the same because the real rotor is homogeneous. The gap between the noise radiated by the single blade and the complete rotor is the same for the different frequencies and for both upstream and downstream levels. Its value is about 25 dB, which simply corresponds to the multiplication by the number of blades in dB scale ($10\log_{10}(18^2) \approx 25$ dB). Similar comparison between the three configurations is obtained on the mode distribution, as evidenced in Fig. 4.17.

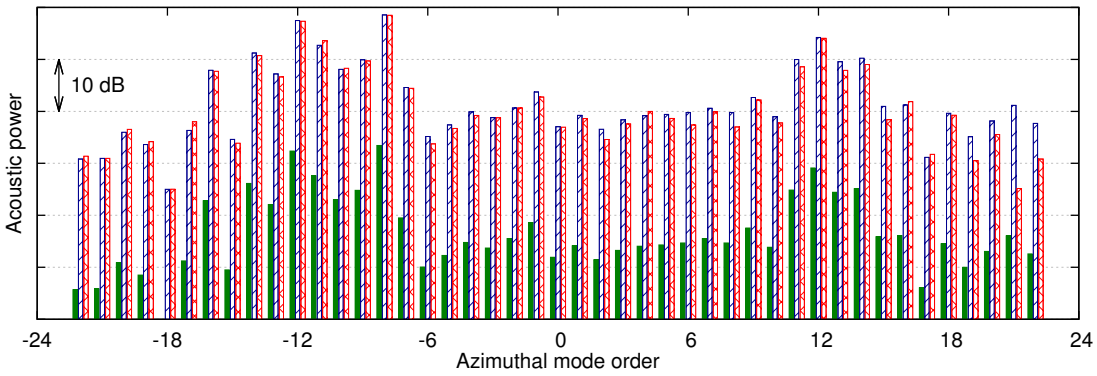

Figure 4.17: **Upstream azimuthal mode distribution at 2BPF (60A): isolated blade homogeneous rotor composed of 18 identical blades, real rotor**

4.3.4 Influence of the regime

The mode distributions obtained for the different regimes are compared at the BPF in Fig. 4.18. Upstream results obtained from the axisymmetric configurations are shown only as examples.

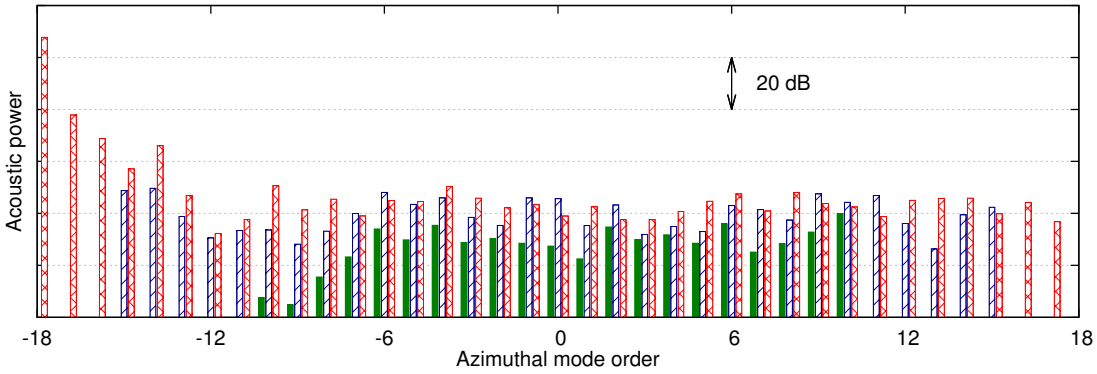

Figure 4.18: **Upstream azimuthal mode distribution at 1BPF (axisymmetric configurations): approach cutback, sideline**

As observed for the OGV noise, more modes are cut-on when the engine rotational speed is increased which results in a increased noise level. However, the shape of the distribution is different here. The rotor-locked mode $m = -18$ is far above all other modes (+30 dB) when it is cut-on i.e. at sideline only. Then, the dominant modes are the ones close to it ($m = -17$ to $m = -14$) with levels generally 20 dB higher than other modes. This behavior results from the rotation of the fan. From Eq. (B.70), it can be shown that the azimuthal mode m of harmonic sB is caused by the fluctuations of pressure on the blades at the harmonic $-sB-m$. At the BPF, $s = 1$ so that the modes $m = -17$ to $m = -14$ correspond to the fluctuations at the first to the fourth RF harmonic respectively. Because the distortion is composed of low-order modes, the acoustic field will be dominated by the azimuthal modes close

to the rotor-locked mode. The later is included here even if it does not correspond to the interaction of the fan with the distortion. This mode is linked to the steady loading ($-sB - m = 0$) and its contribution is the Gutin's noise. A strong impact of the regime on the noise caused by fan sources is expected from these observations. The modes linked to distortion are all cut-off at approach, some of them are cut-on at cutback and most of them are cut-on at sideline. At sideline, however, the rotor-locked mode is also cut-on and dominates the modes related to fan-distortion interaction.

4.3.5 Effect of axial variation of flow and duct

The results shown up to here were obtained with a single definition of the mean flow values and duct radii. As shown for the OGV noise, differences in noise levels can be obtained when a different sets of parameters is chosen in Goldstein's analogy. Same tests are performed here to evaluate the sensitivity of the noise caused by fan sources to those parameters. Four sets of parameters are tested:

- set 1: duct defined by fan extrema radii / mean flow values extracted in plane P2 and plane P3 for upstream and downstream noise evaluation respectively (parameters used up to now);
- set 2: duct defined by duct extrema radii in plane P2 and plane P3 for upstream and downstream noise evaluation respectively / mean flow values extracted in plane P2 and plane P3 for upstream and downstream noise evaluation respectively;
- set 3: duct defined by fan extrema radii / mean flow values extracted in plane P1 and plane P7 for upstream and downstream noise evaluation respectively;
- set 4: duct defined by duct extrema radii in plane P1 and plane P7 for upstream and downstream noise evaluation respectively / mean flow values extracted in plane P1 and plane P7 for upstream and downstream noise evaluation respectively.

The acoustic power at the first three BPF computed using these four sets are compared at approach conditions in Fig. 4.19.

The trends are conserved when changing the set of parameters but important differences in noise levels can be obtained between two sets. The maximum difference is obtained at the BPF (downstream radiation) with a gap of almost 3 dB. Rienstra's theory is therefore used as for the OGV noise to account for axial variation of the duct geometry and the mean flow. The resulting axial evolution of the acoustic power at the BPF is plotted in Fig. 4.20. Goldstein's results obtained with the four sets defined above are added for comparison.

Upstream of the fan, there is no major differences (less than 0.3 dB) in the noise levels predicted by Goldstein's theory and Rienstra's theory. Downstream of the fan, the differences are more important and can go up to 3 dB (for set 4). It appears that Goldstein's results are better when obtained with sets 1 and 3 i.e. when the duct radii are defined as the extrema radii of the fan blades.

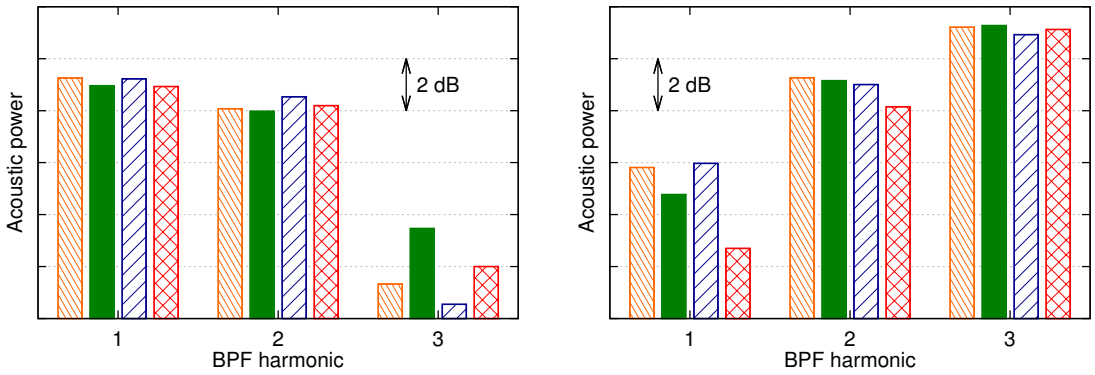

(a) Upstream (b) Downstream

Figure 4.19: **Acoustic power radiated by the fan (60A) for different sets of parameters: set 1, set 2, set 3, set 4**

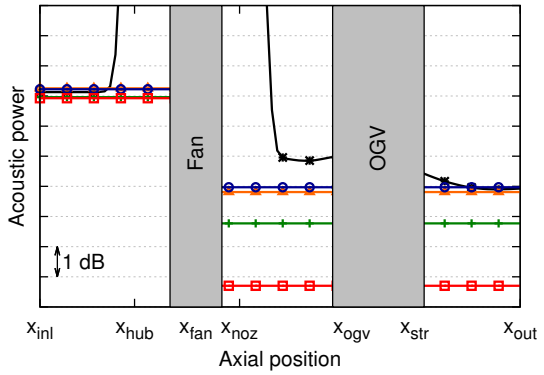

Figure 4.20: **Acoustic power radiated by the fan (60A): Goldstein (set 1), Goldstein (set 2), Goldstein (set 3), Goldstein (set 4), Rienstra**

4.3.6 Power formulation

On both sides of the fan, the power computed with Rienstra's theory reaches high values unlike the power computed with Goldstein's theory. Those high values are caused by the presence of evanescent modes close to the fan that are not accounted for in the present Goldstein's formulation. To make the explanations clearer, the acoustic power evaluated using Rienstra's theory is computed thanks to Eq. (1.62) and the real part, the imaginary part and the modulus of the result are given along the duct axis in Fig. 4.21.

Usually, the in-duct acoustic power is defined as the real part of Eq. (1.62). The result is determined by the cut-on modes and is almost constant upstream and downstream of the fan. The cut-off modes are responsible for the imaginary part of Eq. (1.62) and this is why the corresponding levels are high around the fan blades only. However, even if they do not contribute to the in-duct acoustic power, the cut-off modes may still have a significant level in terms of pressure fluctuations in

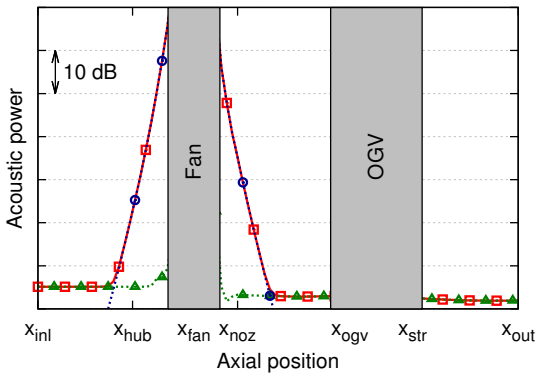

Figure 4.21: **Acoustic power radiated by the fan (60A): modulus, real part, imaginary part**

the inlet plane if the inlet duct is not long enough (as expected for UHBR engines). In such cases, a part of these cut-off modes will radiate outside of the engine and will contribute to the far-field acoustic power. Accounting properly for this contribution (by a mode-matching technique or by an LEE simulation outside of the engine for example) is out of the scope of this thesis. Therefore, this is done in the rest of the manuscript only approximately by considering the modulus of Eq. (1.62) instead of its real part. For simplicity reasons, it is still called acoustic power even if it does not match with the real in-duct acoustic power when the cut-off modes dominate (i.e. close to the sources).

4.3.7 Effect of swirling flow

The effect of swirling flow on the noise level is now studied. It is included in the same way as for the evaluation of the OGV noise. Noise predictions with and without this swirl effect are given in Fig. 4.22 at approach and cutback as examples (axisymmetric inlet geometries).

Naturally, the impact of the swirl is only observed on downstream noise levels. For both regimes, the swirling flow reduces the downstream fan noise. The reduction is about 2.5 dB at approach and more than 20 dB at cutback. At sideline, the impact is similar to at cutback. Those reductions in noise levels are far more important than the ones observed for the OGV noise. To understand this behavior, the azimuthal mode distribution at 1BPF is given in Fig. 4.23 at cutback.

As for the OGV noise, the swirl shifts the range of propagative modes towards contra-rotative modes. However, the most important modes are the co-rotative modes and especially the modes close to the rotor-locked mode. These modes are cut-on at cutback but become cut-off when the swirl is accounted for. At approach, most of these modes are already cut-off which explains the lower impact of swirl.

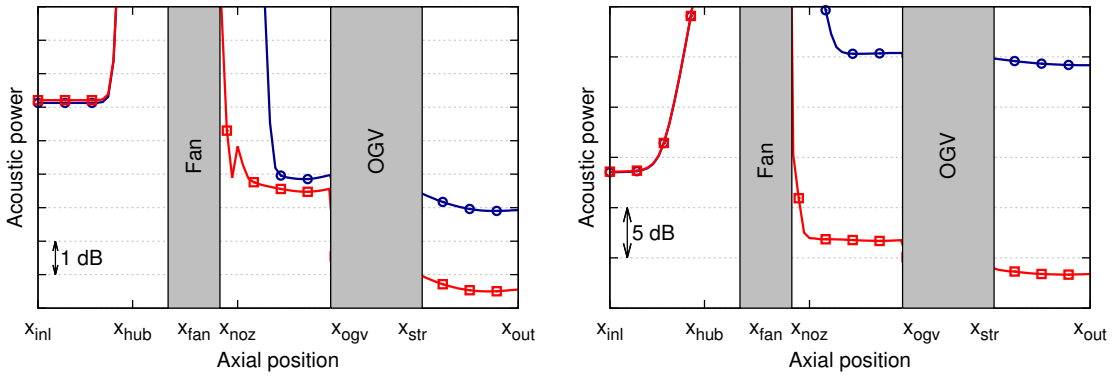

(a) Approach (b) Cutback

Figure 4.22: **Effect of swirl on the acoustic power radiated by the fan: without, with**

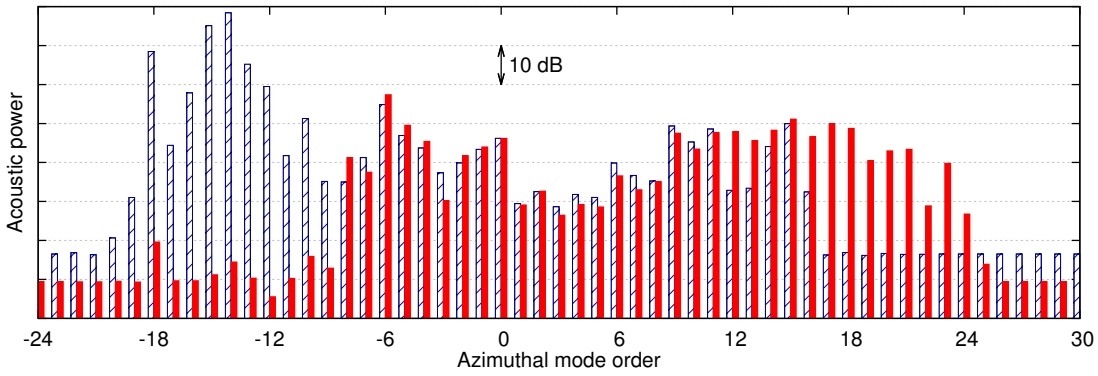

Figure 4.23: **Effect of swirl on the azimuthal mode distribution at 1BPF in the interstage region (fan source - 80A): without swirl, with swirl**

4.3.8 Noise penalty induced by inlet distortion

As it was done for the OGV noise, the choice of duct and flow for non-axisymmetric configurations is first discussed. The same definitions are compared: axisymmetric duct and axisymmetric flow, axisymmetric duct and asymmetric flow, equivalent asymmetric duct and asymmetric flow. Results are given in Fig. 4.24 at both approach and cutback.

At approach, the choice of duct and flow has only a little influence (less than 0.3 dB). However, at cutback, the impact of this choice is significative. Using the axial flow extracted from the axisymmetric simulation instead of the one from the asymmetric simulation is responsible for an increase of 7 dB. This trend is reversed by accounting for the equivalent asymmetric duct with a reduced cross-section which causes a decrease of 10dB. In total, a difference of 4 dB is obtained at cutback depending on the condition of propagation (axisymmetric properties or asymmetric properties). In the following, both predictions are kept because they allow to sepa-

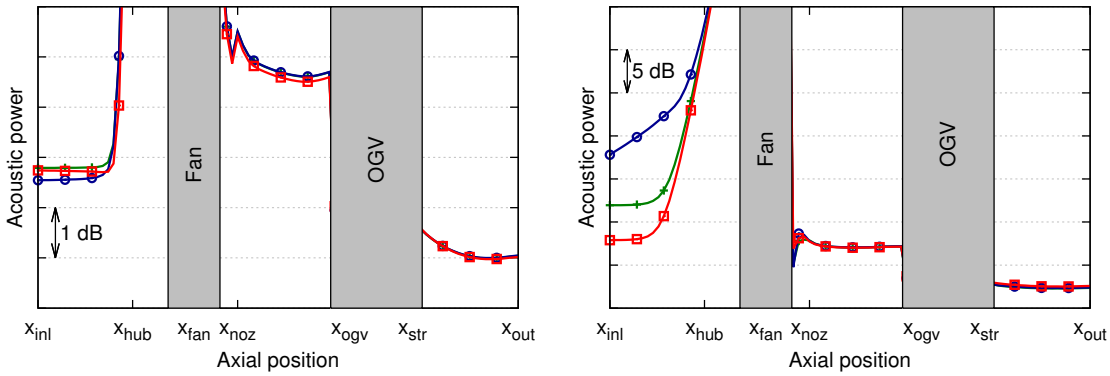

(a) Approach (b) Cutback

Figure 4.24: **Acoustic power radiated by the fan (60N) for different flow and duct definitions: axisymmetric duct and axisymmetric flow, axisymmetric duct and asymmetric flow, equivalent asymmetric duct and asymmetric flow**

rate the effect of distortion on source generation and noise propagation.

The impact of inlet distortion on the noise radiated by the fan is finally estimated here at all regimes. Rienstra's theory is used to propagate the sources extracted from the whole rotor and a Doppler shift in frequencies is introduced in the interstage region to model the swirl. Results are given in Fig. 4.25 for the BPF.

At all regimes, the noise radiated by the fan is more important in the upstream direction than in the downstream one because of the swirl. When considering similar propagation properties, the noise penalty caused by inlet distortion is large at approach and cutback in both directions (about +4 dB and +8 dB in upstream and downstream direction at approach and about +3 dB and +4 dB at cutback). At sideline, the penalty downstream of the OGV is around 1 dB and there is no impact upstream because the rotor-locked mode, which is linked to the steady loading and is therefore not directly affected by distortion, is cut-on. Nevertheless, accounting for the different propagation properties modifies these conclusions at cutback and sideline. The decrease of cut-off modes depends on the flow conditions and on the duct geometry. At approach, the important modes (the ones caused by the interaction with distortion) are well cut-off because they are far from the cut-on/cut-off transition. Slightly modifying the flow and duct geometry does not have an important impact because the modes still stay strongly evanescent. However, at cutback and sideline, those important modes are close to the cut-on/cut-off transition or are slighlty cut-off so that a parameter variation can have a big influence. The impact is observd only upstream where these modes are close to the transition. For both regimes, considering the asymmetric propagation properties instead of the axisymmetric ones for the evaluation of the asymmetric sources is responsible for an important decrease of the upstream noise level by about 4-5 dB.

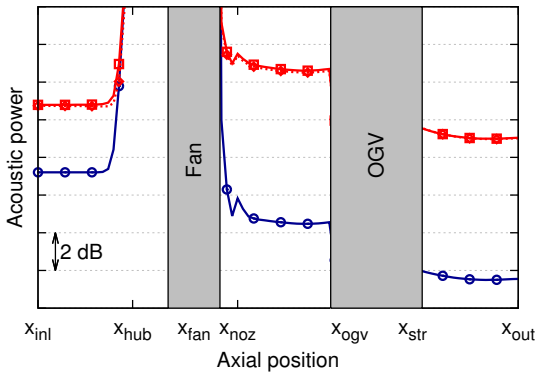

(a) Approach

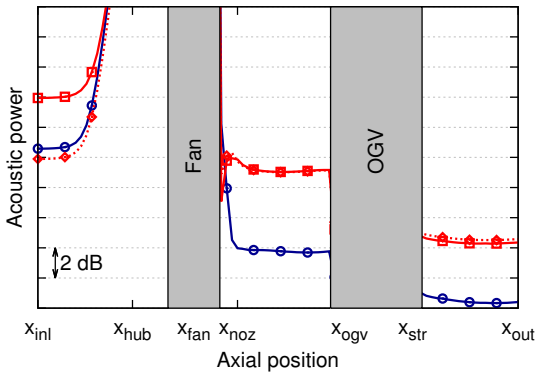

(b) Cutback

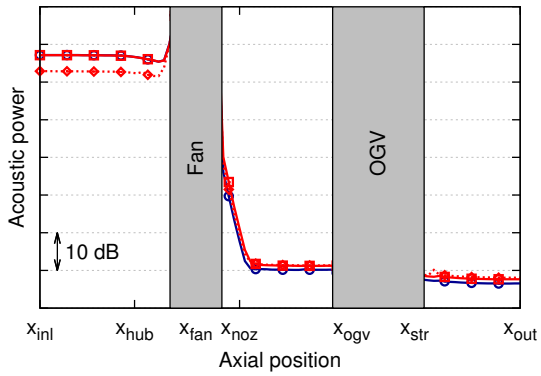

(c) Sideline

Figure 4.25: **Acoustic power radiated by fan with and without inlet distortion: axisymmetric source, asymmetric source and axisymmetric propagation properties, asymmetric source and asymmetric propagation properties**

Summary of the section

The distortion-fan interaction noise has been studied in this section. The limits of Amiet's theory are again shown on such a configuration. The limitation to straight ducts in Goldstein's theory is also responsible for differences in the noise estimates of some decibels that can however be small for a convenient choice of propagation parameters. The distortion-fan interaction is shown to produce important modes close to the rotor-locked mode $m = -18$ at the BPF (typically the mode $m = -20$, $m = -19$, $m = -17$, $m = -16$) because the distortion is essentially described by low-order harmonics. These modes are not necessarily cut-on and an important evolution of this noise with the regime is observed. At approach conditions, all these modes are cut-off and the noise is generated by modes of lower order that are caused by the interaction with the high-order harmonics of the distortion. At cutback, some of these modes become cut-on and at sideline, they are all cut-on, the rotor-locked

mode included. All these modes are co-rotating and are therefore strongly reduced by the swirling flow (-20 dB at cutback for example). With the inlet distortion, the power associated with these modes is increased at the source. For similar propagation properties, the noise radiated by the fan sources is therefore more important with inlet distortion, excepted at sideline where the rotor-locked mode $m = -18$, linked to the steady loading on the blades, dominates all other modes. However, the asymmetric air inlet is characterized by a smaller cross-section surface and it is shown to mitigate this increase of noise.

4.4 Interaction of fan-blade wakes with IGVs

In this section, the noise caused by the interaction of fan-blade wakes with the IGVs is studied. This noise is generally neglected and the validity of this assumption is evaluated here. Because this mechanism is similar to the interaction of fan-blade wakes with the OGVs, only the particularities linked to the IGV will be adressed.

4.4.1 Propagation in duct and assessment of the stator homogeneity

Goldstein's analogy is used as for the OGV noise to evaluate the noise radiated by the IGV. The IGV extrema radii are chosen for the definition of the duct and the mean flow values are extracted in plane P8 in the primary stream. Only the upstream results will be shown in this section because the noise radiated downstream of the IGV will interact with many components before reaching the exit and will be mixed with other noise sources (compressor, combustion, turbine and jet noise). Contrary to the OGV, the IGV is homogeneous because all vanes are identical. However, the distortion is responsible for non-homogeneous excitation so that the response of each vane will be different from the other. To quantify this, Goldstein's analogy is used to propagate the sources on one vane, on a fictitious stator of 93 identical vanes recomposed from one vane and on the real stator. Results are given in Fig. 4.26 for the axisymmetric configuration at approach conditions.

The fictitious homogeneous stator does not produce any sound at the first three BPF harmonics because all Tyler & Sofrin modes $m = -nB-kV$ are cut-off ($B = 18$ number of blades, $V = 93$ number of vanes and k any integer). The noise that is radiated from the real stator is not null and is therefore caused by the inhomogeneity of the excitation. It is lower by 1.5 to 3.5 dB than the noise radiated by the single vane for the first three BPF harmonics. This indicates the presence of some destructive interferences at the origin of Tyler & Sofrin modes and the residual level is caused by the slight inhomogeneity of the sources. The upstream azimuthal distribution at 2BPF is given in Fig. 4.27.

The power is distributed over all cut-on modes with a dominant planar mode $m = 0$ when considering the real stator. The mode distribution between the isolated vane

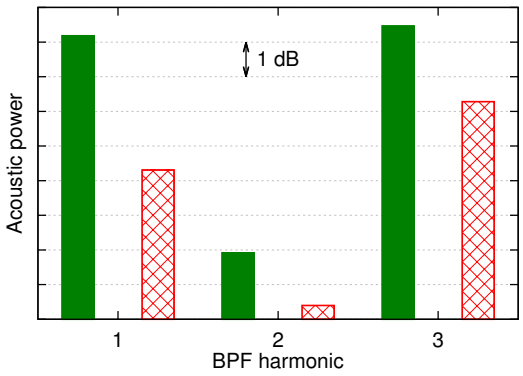

Figure 4.26: **Acoustic power radiated by the IGV (60A): isolated vane homogeneous stator composed of 93 identical vanes, real stator**

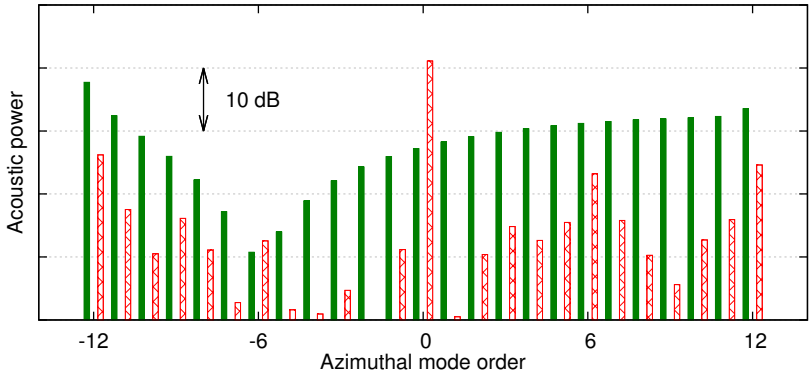

Figure 4.27: **Azimuthal mode distribution of the 2BPF radiated upstream (60A): isolated vane homogeneous stator composed of 93 identical vanes, real heterogeneous stator**

and the real stator are not similar because of the partial destructive interferences occuring with the latter.

4.4.2 Noise penalty induced by inlet distortion

The effect of axial variation of the flow and geometry and the effect of swirling flow are similar to the ones on OGV noise. The noise penalty on the IGV is directly evaluated here using Rienstra's theory and including the swirl in the interstage region. Results are given in Fig. 4.28 where the asymmetric sources are propagated with both axisymmetric propagation properties and asymmetric ones.

The choice of axisymmetric or asymmetric propagation properties does not have an influence on the upstream noise radiated from the asymmetric source, except at sideline where a difference of more than 2 dB is observed. At all regimes, the inlet distortion is responsible for an increase of the noise level radiated by the IGV. The penalty is about 0.5 dB, 2 dB and 1 dB at approach, cutback and sideline respectively. This is consistent with the previous observations. Adding the inlet distortion

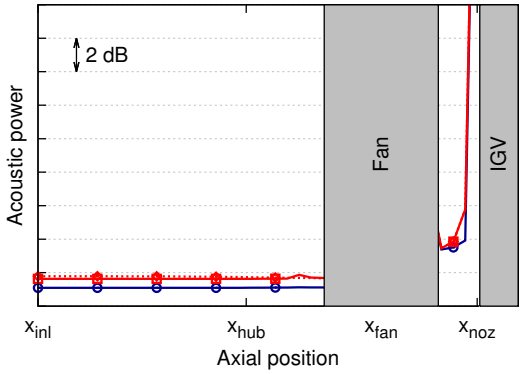

(a) Approach

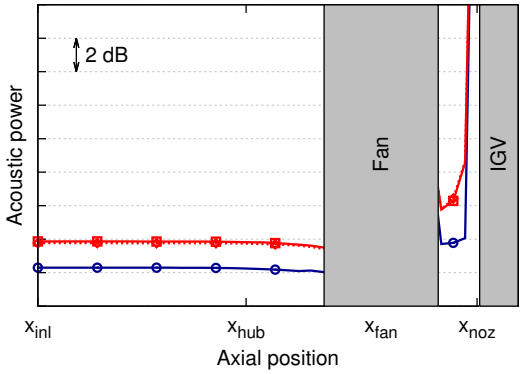

(b) Cutback

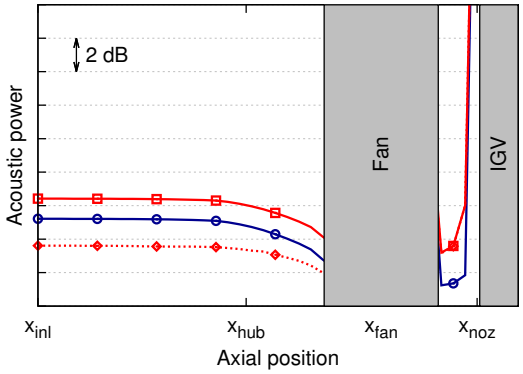

(c) Sideline

Figure 4.28: **Acoustic power radiated by the heterogeneous IGV with or without inlet distortion: axisymmetric inlet, asymmetric inlet and axisymmetric duct and flow, asymmetric inlet and equivalent asymmetric duct and flow**

increases the inhomogeneity of the excitation and consequently the inhomogeneity of the IGV unsteady loadings. The destructive interferences are therefore reduced and the residual noise level is increased.

Summary of the section

The noise caused by the interaction of the fan-blades wakes with the IGVs presents similarities with the one resulting from the interaction with the OGVs. The same conclusions can be drawn and the main difference is that the heterogeneity of the IGV is only due to the heterogeneity of the excitations (caused by the distortion) because all vanes are identical. The increased heterogeneity caused by inlet distortion is responsible for a noise penalty that can reach 2 dB.

4.5 Source breakdown using hybrid methods

The three noise sources described above are compared in this section in order to establish a classification for all regimes. This classification is based on Rienstra's predictions including the swirling flow in the interstage region by a Doppler shift.

4.5.1 Source breakdown at approach

The noise radiated at the BPF by each noise mechanism at approach conditions is given in Fig. 4.29. The comparison between the sources extracted from the axisymmetric simulations and the ones extracted from the asymmetric simulations is done for similar propagation properties (axisymmetric duct and flow) and for proper propagation properties (i.e. axisymmetric duct and flow for axisymmetric sources and equivalent asymmetric duct and flow for asymmetric sources).

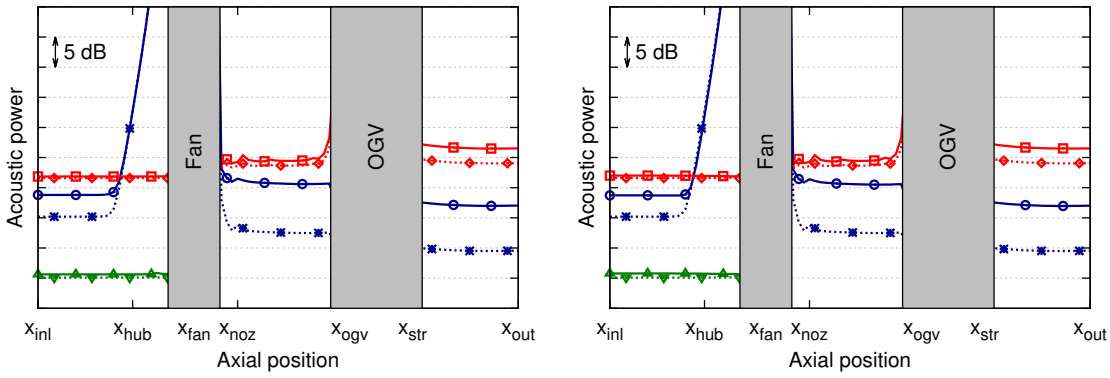

(a) Same propagation properties

(b) Proper propagation properties

Figure 4.29: **Source breakdown at approach - acoustic power at the BPF: IGV non-axi, fan non-axi, OGV non-axi, IGV axi, fan axi, OGV axi**

Using similar or proper propagation properties does not change the noise radiated by each mechanism. Upstream of the fan, the IGV noise appears to be very low

compared to fan noise and OGV noise (10 dB to 17 dB lower). The OGV noise is more important than fan noise by 7 dB approximately in inlet plane for the axisymmetric configuration. When inlet distortion is included, this difference is reduced and becomes close to 3 dB. Downstream of the OGV, the noise is largely dominated by the OGV sources in both axisymmetric and asymmetric configurations (approximately 15 dB and 10 dB higher than fan noise without and with inlet distortion respectively). These trends are linked to the fact that the important modes caused by distortion-fan interaction are cut-off at approach. This is illustrated in Fig. 4.30 where the azimuthal mode distribution at BPF extracted in the inlet plane is plotted. The modes radiated by fan and OGV sources for both inlet geometries are shown only because the IGV noise is negligible.

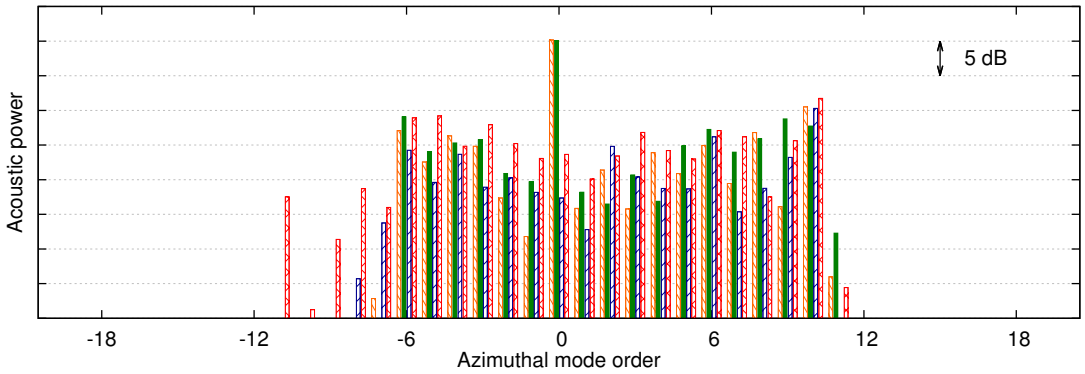

Figure 4.30: **Upstream azimuthal mode distribution at the BPF (60A): OGV axi, OGV non-axi, fan axi, fan non-axi**

The important modes caused by distortion-fan interaction that typically ranges from $m = -17$ to $m = -14$ are indeed cut-off. The planar mode dominates the OGV noise with a level higher by 10 dB than any other mode. The inlet distortion increases the fan modes but the impact on OGV modes is less clear (increase of some modes and decrease of some others). This is why the upstream OGV noise level is not affected by the distortion while the fan one is increased. Downstream of the OGV, the noise penalty induced by inlet distortion is caused by the OGV sources. In conclusion, the upstream noise is caused by fan and OGV sources and the downstream noise by OGV sources only at approach conditions. The noise penalty induced by inlet distortion is caused by the rise of fan sources at the inlet and by the rise of OGV sources at the outlet. However, the total upstream noise is probably wrongly predicted because it is mainly caused by the OGV sources which are impacted by the swirl (only simply modeled here) and by the rotor shielding (not accounted for here).

4.5.2 Source breakdown at cutback

The source breakdown is now represented at cutback in Fig. 4.31.

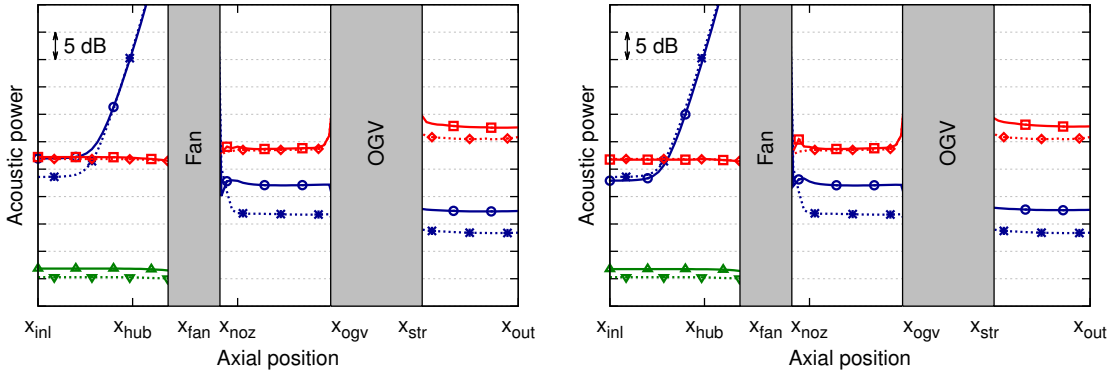

(a) Same propagation properties

(b) Proper propagation properties

Figure 4.31: **Source breakdown at cutback - acoustic power at the BPF: IGV non-axi, fan non-axi, OGV non-axi, IGV axi, fan axi, OGV axi**

Again, the IGV noise is much lower than OGV noise and fan noise in the inlet for both configurations (difference of more than 15 dB). Downstream of the OGV, the noise is dominated by the OGV sources for both inlet geometries because the swirl has significantly reduced the downstream fan noise (cf. Sec. 4.3.7). In the inlet plane, the OGV noise is more important than the fan noise in the absence of inlet distortion. With the inlet distortion and considering similar propagation properties, the OGV noise is rather unaffected and the fan noise is increased by more than 3 dB which makes the two noise mechanisms comparable. This is caused by the increase of some modes related to fan-distortion interaction that are cut-on. However, the asymmetric duct makes the upstream propagation of this noise more difficult with a reduction of 3 dB when compared to propagation in the axisymmetric duct. The reduced section of the equivalent asymmetric duct makes stricter the cut-on condition. This mitigates the increase of noise caused by the increased importance of fan sources. The azimuthal mode distribution at BPF is given in Fig. 4.32 for fan and OGV sources and for similar propagation properties.

The OGV modes distribution is concentrated on contra-rotative modes because some co-rotative modes have been cut-off by the swirling flow. The planar mode is higher than any other by almost 10 dB and is only slightly impact by the inlet distortion. The fan modes are dominated by the modes close to the rotor-locked mode (especially the modes $m = -16$, $m = -15$, $m = -14$ and $m = -13$). These modes are strongly increased by the inlet distortion (average increase of more than 5 dB). When considering asymmetric propagation properties, the modes $m = -16$ becomes cut-off and the total noise is reduced. The conclusions are therefore similar to the one obtained at approach. However, the evanescent modes have an influence over almost 60% of the inlet duct. This can have an important effect on the noise in the engines equipped with short inlet ducts. This effect will be discussed using a direct approach in Sec. 4.6.2.

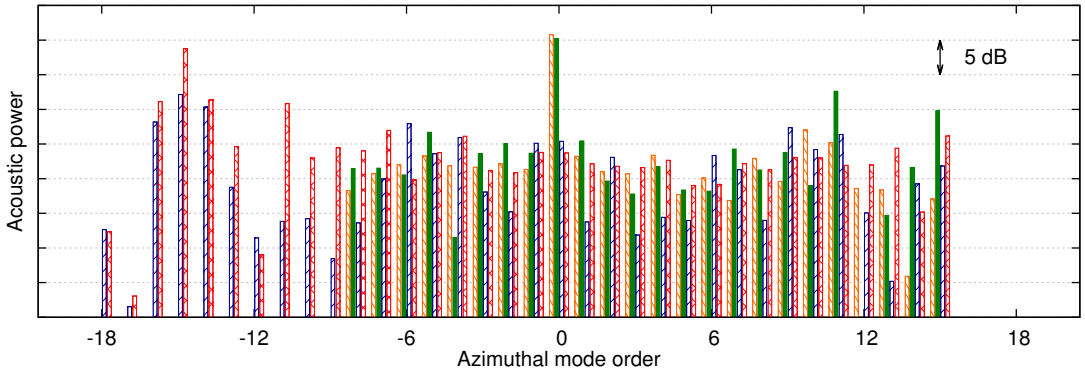

Figure 4.32: **Upstream azimuthal mode distribution at the BPF (80A): OGV axi, OGV non-axi, fan axi, fan non-axi**

4.5.3 Source breakdown at sideline

The weight of the different sources at sideline conditions is now represented in Fig. 4.33.

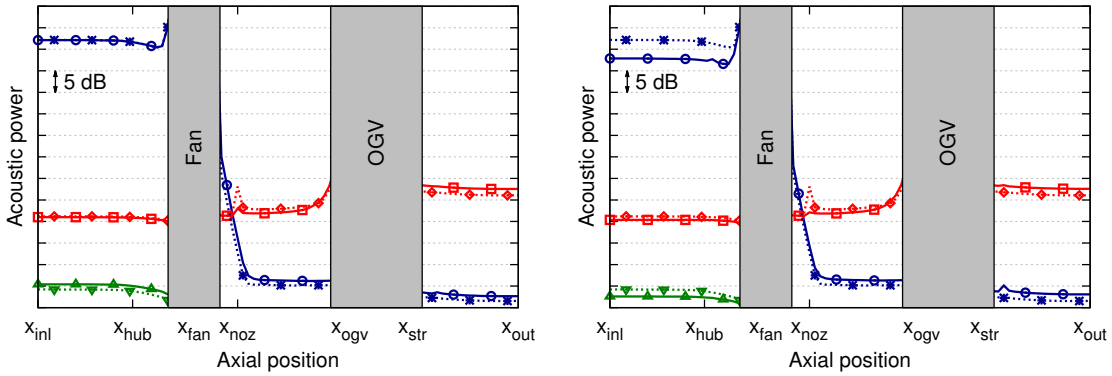

(a) Same propagation properties

(b) Proper propagation properties

Figure 4.33: **Source breakdown at sideline - acoustic power at the BPF: IGV non-axi, fan non-axi, OGV non-axi, IGV axi, fan axi, OGV axi**

Upstream of the fan, the noise radiated by OGV and IGV sources are both negligible because the noise caused by fan sources is 35 to 40 dB higher. This important difference is caused by the rotor-locked mode which becomes cut-on at sideline. This is shown in Fig. 4.34 where the azimuthal mode distribution in the inlet plane is given at the BPF. The swirling flow cuts off this mode as well as the important modes linked to distortion and makes the fan noise low compared to OGV noise in the outlet plane (approximately 25 dB lower). When considering similar propagation properties, the inlet distortion does not have any effect on the noise level upstream because the dominant rotor-locked mode is not affected by the distortion. However, an important reduction of the noise by 4 dB is observed when considering

the propagation in the asymmetric duct. This is similar to what has been observed at cutback conditions.

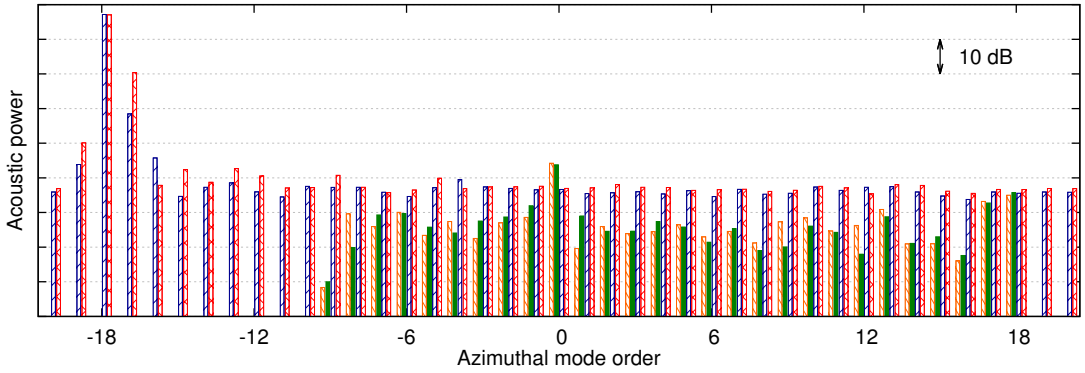

Figure 4.34: **Upstream azimuthal mode distribution at the BPF (90A): OGV axi, OGV non-axi, fan axi, fan non-axi**

At sideline, the contribution of the sources is clearer: the fan sources contribute to the upstream noise and the OGV sources contribute to the downstream noise. The upstream noise being dominated by the rotor-locked mode, no impact of ilnlet distortion is observed. Only the impact of the propagation in a duct with a smaller cross-section surface is observed. The impact of inlet distortion on the downstream noise level (about 1.5 dB) is caused by the modification of the OGV sources linked to the modification of the excitation. However, those results, especially for the fan sources, should be taken with precaution because non-linear effects occur at such supersonic tip speeds. In addition, shocks develop in the inlet at sideline and are not predicted with this theory.

Summary of the section

A comparison of the noise levels predicted by propagating the fan sources, the OGV sources and the IGV sources has been proposed. The upstream noise radiated by the IGV is shown to be negligible at all regimes. The downstream noise is dominated by the OGV sources at all operating conditions (levels higher by 10 dB at least) because of the swirling flow that cuts-off the important modes caused by the fan sources. For the upstream noise, the dominating source is less clear except at sideline where the fan sources strongly dominate because of the cut-on rotor-locked mode. With the predictions based on Rienstra's theory, the OGV sources dominate upstream at approach and cutback but their noise level is likely wrongly predicted because the swirl is only simply modeled and the rotor shielding effect is not accounted for.

4.6 Direct acoustic analysis

Important conclusions have been brought using hybrid methods for the prediction of noise. Those methods allow the study of the noise mechanism independently and have helped to establish a classification of the sources for all regimes. However, important hypothesis have been made and might have an impact on the conclusions. In particular, the swirling flow was modeled by a simple Doppler shift in frequencies and the rotor shielding effect was not accounted for. These assumptions have probably an impact on the upstream OGV noise level. In order to complete the analysis, direct methods are also used for the evaluation of the noise. They are presented in this section.

4.6.1 Direct evaluation of acoustic power

The main advantage of using direct methods for the prediction of noise is that no assumption is made on the duct geometry or on the flow. However, they are more difficult to use in practice because they require a sufficiently refined mesh and accurate numerical schemes. With the present meshes, they can be used for the prediction of the noise level at the BPF only.

A Fourier transform has been performed during the simulations using the co-processing capabilities of Antares [112]. The mean field and the field at the BPF are therefore available in the whole domain, excepted in the rotor domain. The real part of the pressure fluctuations at the BPF extracted at 75% of vane height is given in Fig. 4.35 for illustration. It corresponds to the axisymmetric simulation at approach conditions.

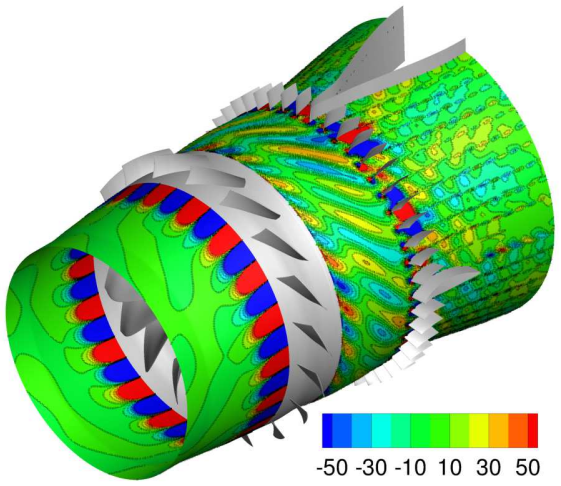

Figure 4.35: **Amplitude of pressure fluctuations at the BPF (60A) without filtering**

In the rotor domain, the map is not colored because the information is not available. Upstream of the fan, the rotor-locked mode composed of 18 azimuthal lobes is

observed close to the fan but decreases while going towards the inlet. Downstream of each fan blade and each OGV, fluctuations are observed in the vicinity of the wakes. These fluctuations are linked to vorticity and correspond to the vorticity mode of Chu & Kovasznay [32]. These vorticity (or hydrodynamic) fluctuations pollute the acoustic field and need to be filtered. To illustrate this need, the acoustic power is evaluated directly from this unfiltered fluctuations at each section by integrating Eq. (1.61). The results are given in Fig. 4.36. It should be recalled that, in this manuscript, the acoustic power is defined with the modulus of Eq. (1.62) instead of its real part (see Sec. 4.3.6). Thus, an acoustic power can be attributed to the cut-off modes while it should be zero in reality. This choice has been made to account for the possible contribution of the cut-off modes to the far-field noise when the inlet duct is short.

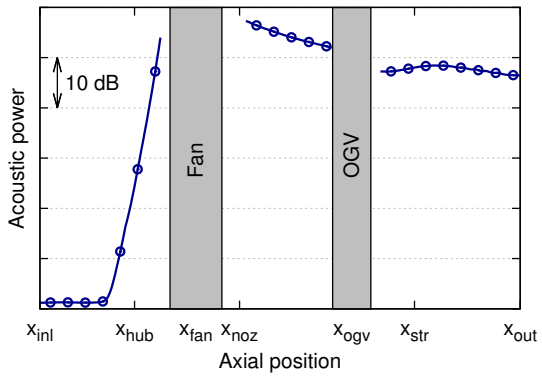

Figure 4.36: **Axial evolution of acoustic power at the BPF (60A) without filtering**

Upstream of the fan, hydrodynamic fluctuations are not present and the estimated power is reliable. However, downstream of the fan and the OGV, the absolute levels (that cannot be given for confidentialy reasons) are considerably high for acoustics. Even without accessing to the absolute level, it can be seen by the huge gap of 45 dB between the upstream noise level and the downstream one. This gap was indeed of only 5 dB in the hybrid predictions (cf. Fig. 4.29).

In order to go deeper into this analysis, an azimuthal Fourier transform is performed on the whole field at the BPF. The field associated with each azimuthal mode is recomposed and the acoustic power is then evaluated by integrating Eq. (1.61) for each mode. To make this decomposition easier, the presence of the pylon is not accounted for and the duct downstream of the OGV is assumed to be annular (i.e. not divided into two parts) where the fluctuations are set to zero in the pylon area. The evolution of the power associated with the four more important modes downstream of the OGV is given in Fig. 4.37. The determination of the more important modes is done right downstream of the OGV.

The dominant modes are the modes $m = -18$, $m = -20$, $m = -21$ and $m = -19$. These modes do not correspond to the cut-on modes generated by the OGV

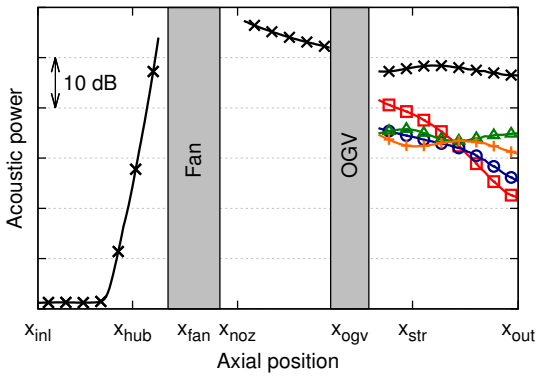

Figure 4.37: **Axial evolution of acoustic power (60A) without filtering: dominant modes (mode -18, mode -20, mode -21, mode -19 in order), total power**

(that range from $m = -12$ to $m = 12$) and are therefore not linked to acoustics. A filtering procedure to exploit the results downstream of the fan and the OGV is therefore required and will be detailed in Sec. 4.6.3.

4.6.2 Analysis of upstream power

The analysis of the upstream results is first done because no filtering is needed. The three regimes are studied successively.

At approach

The study of the upstream results is performed by analyzing the evolution of the acoustic power associated with each azimuthal mode. In order to keep clarity, only the dominant modes will be plotted. Because the modes vary axially, the dominant modes at one location may not be the dominant modes at another. This is why the determination of the dominant modes will be done at 3 different axial positions. These positions are defined by the ratio L/D between the distance to the fan L and the diameter of the fan D: $L/D = 0$, $L/D = 0.2$ and $L/D = 0.4$. $L/D = 0$ is chosen because it will evidence the modes close to the source, $L/D = 0.2$ because it is representative of the size of UHBR engines and $L/D = 0.4$ because it is representative of the size of current HBR engines [113]. In order to ease the comparison between axisymmetric and asymmetric simulations, one set of dominant modes is determined at each position for both configurations. Results at approach conditions are given in Figs. 4.38, 4.39 and 4.40 for the dominant modes at $L/D = 0$, $L/D = 0.2$ and $L/D = 0.4$ respectively. On each plot, six modes are represented so that the first three dominant modes of both axisymmetric and asymmetric simulations are plotted at least. The same range is used between all plots and the power computed in the axisymmetric simulation is added in black dotted line in the asymmetric plot to ease the comparison.

The rotor-locked mode $m = -18$ is the most important mode at source but is

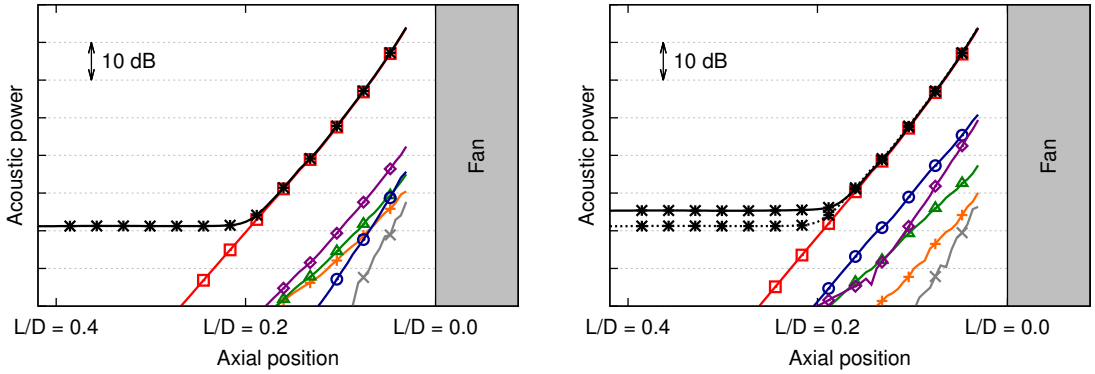

(a) Axisymmetric air inlet (b) Asymmetric air inlet

Figure 4.38: **Axial evolution of acoustic power at the BPF at approach: dominant modes at $L/D = 0$ (mode -18, mode -17, mode -19, mode -16, mode -14, mode -22), total power**

cut-off. It is nevertheless responsible for most part of the noise up to $L/D = 0.2$. This mode is linked to the steady loading on the blades and is therefore not directly impacted by the inlet distortion. The orders of the other important modes at $L/D = 0$ (-17, -19, -16, etc.) are all close to -18 and indicate that these modes are linked to distortion-fan interaction. They are indeed significantly increased by the inlet distortion (+7 dB for $m = -17$ and +15 dB for $m = -19$ for example) but they are all evanescent so that they do not contribute to the upstream noise.

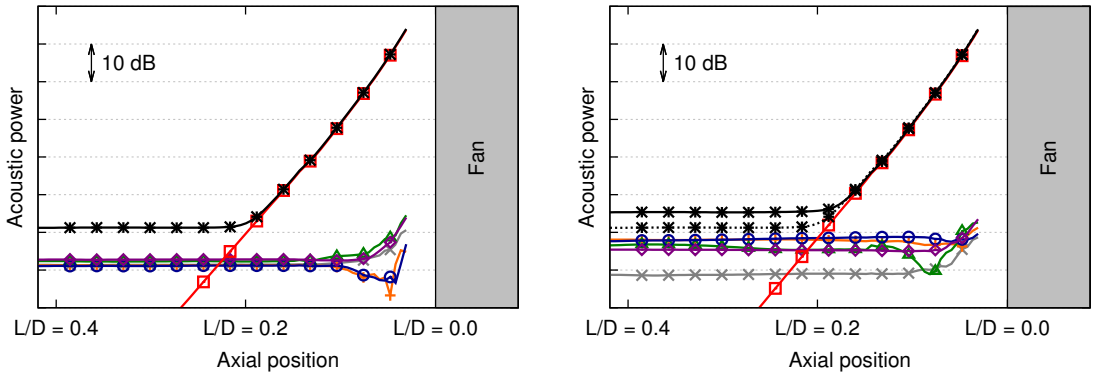

(a) Axisymmetric air inlet (b) Asymmetric air inlet

Figure 4.39: **Axial evolution of acoustic power at the BPF at approach: dominant modes at $L/D = 0.2$ (mode -18, mode -2, mode -5, mode -10, mode -6, mode 2), total power**

When going upstream and looking at the dominant modes at $L/D = 0.2$, the modes linked to distortion-fan interaction do not appear anymore because they are cut-off. However, while being cut-off, the rotor-locked mode is still present and contribute to the total noise. The other modes that become dominant in this region

are low-order modes (-2, -5, -10, etc.) and are therefore probably linked to the interaction of fan-blade wakes with the OGVs. Most of these modes are increased by the inlet distortion via the modification of the wakes.

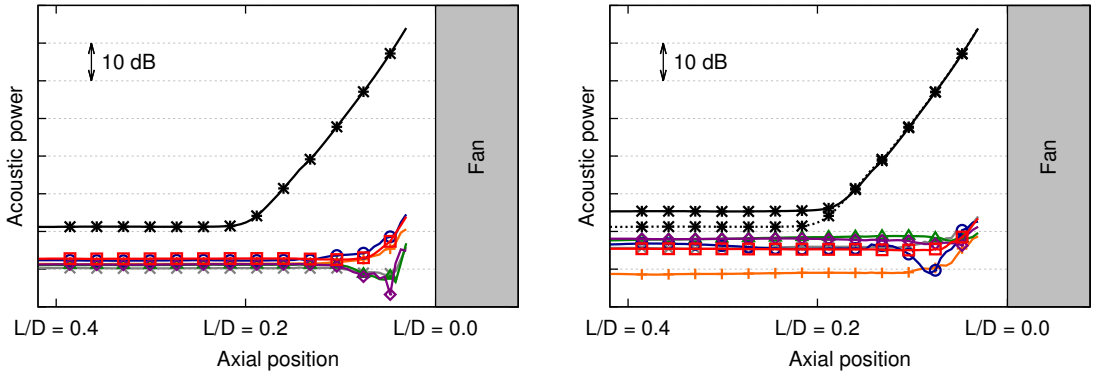

(a) Axisymmetric air inlet

(b) Asymmetric air inlet

Figure 4.40: **Axial evolution of acoustic power at the BPF at approach: dominant modes at $L/D = 0.4$ (mode -2, mode -6, mode -10, mode -5, mode 2, mode -7), total power**

At $L/D = 0.4$, the dominant modes are almost the same as at $L/D = 0.2$ except the rotor-locked mode that has become unsignificant. From $L/D = 0.2$ to $L/D = 0.4$, all the cut-off modes become unsignificant and only the cut-on modes remain. The levels of these modes are constant up to the inlet plane and the penalty induced by inlet distortion at the inlet is around 5 dB. A comparison of these results with the predictions based on hybrid methods is given in Fig. 4.41. The noise radiated by the fan, the OGV and the IGV sources computed using Rienstra's theory is given.

The domination of the OGV sources was already found using Rienstra's theory. However, both the fan noise and the OGV noise computed analytically are greater than the total acoustic power predicted directly. For the OGV noise, this overestimation is probably due to the simple model of swirling flow and to the rotor shielding effect that is not accounted for in the present work. For the fan noise, the overestimation is probably linked to the fact that all the important modes that are linked to the interaction with the distortion are cut-off. The remaining modes (the low-order modes) that causes the noise are linked to the unsteady loadings on fan blades at higher frequencies that may be more easily polluted by hydrodynamics. The noise penalty induced by inlet distortion of 4 dB is greater than the one predicted with Rienstra's theory (1 dB if we consider only the OGV sources and 1.5 dB if we consider all sources).

At cutback

The same analysis is now performed at cutback. Results are given in Figs. 4.42, 4.43 and 4.44 for the dominant modes at $L/D = 0$, $L/D = 0.2$ and $L/D = 0.4$

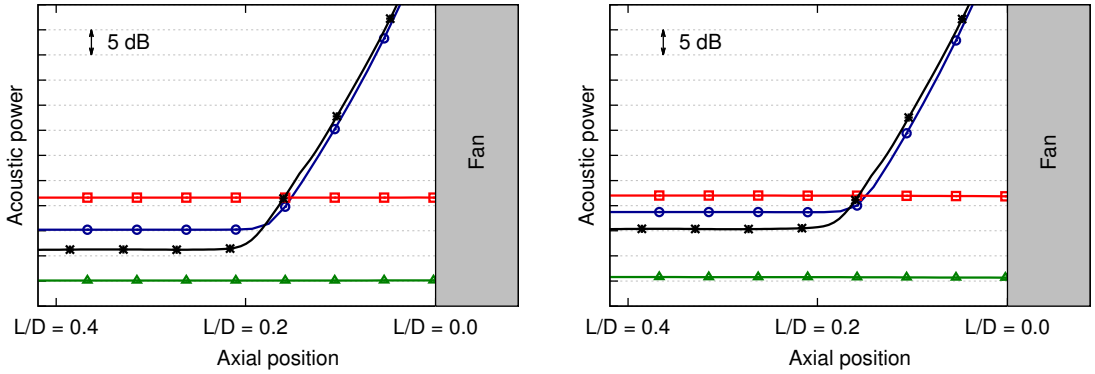

(a) Axisymmetric air inlet (b) Asymmetric air inlet

Figure 4.41: **Axial evolution of acoustic power at the BPF at approach: Rienstra - IGV, Rienstra - fan, Rienstra OGV, direct method**

respectively.

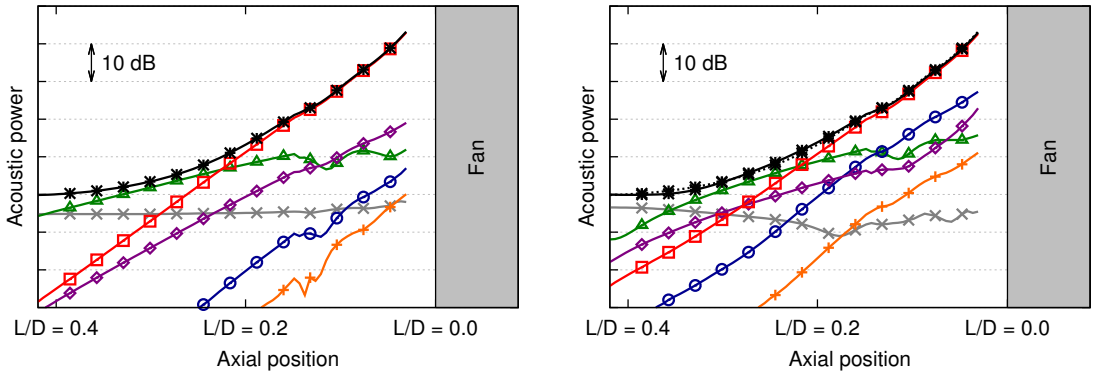

(a) Axisymmetric air inlet (b) Asymmetric air inlet

Figure 4.42: **Axial evolution of acoustic power at the BPF at cutback: dominant modes at $L/D = 0$ (mode -18, mode -17, mode -19, mode -16, mode -20, mode -14), total power**

In Fig. 4.42, the dominant modes at source ($L/D = 0$) are the same as the ones observed at approach: the rotor-locked mode (-18) and the modes linked to distortion-fan interaction (-17, -19, -16, etc.). Again, the rotor-locked mode is not altered by the inlet distortion on the contrary of the other modes that are strongly increased (+3 dB for $m = -17$ and almost +20 dB for $m = -19$ for example). The decrease of the modes is more important for high order modes and this is consistent with the theory.

Contrary to what has been observed at approach, the modes linked to distortion-fan interaction are still dominant at $L/D = 0.2$ in Fig. 4.43. The lower decreasing of

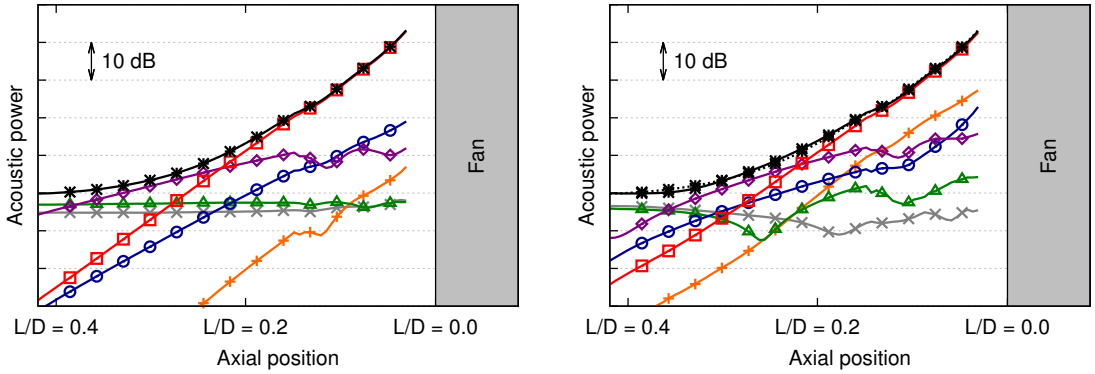

(a) Axisymmetric air inlet (b) Asymmetric air inlet

Figure 4.43: **Axial evolution of acoustic power at the BPF at cutback: dominant modes at $L/D = 0.2$ (mode -18, mode -16, mode -17, mode -15, mode -19, mode -14), total power**

these modes (when compared with Fig. 4.38 for example) caused by the increased rotational speed of the fan is responsible for this behavior. The most important mode is still the rotor-locked mode but the other modes also contribute significantly to the total noise at this position. Over the 6 modes that are represented, 4 are cut-off (-19 to -16) and 2 are cut-on (-14 and -15). Most of the noise at $L/D = 0.2$ is caused by the cut-off modes that might therefore have an impact for engines equipped with short inlets.

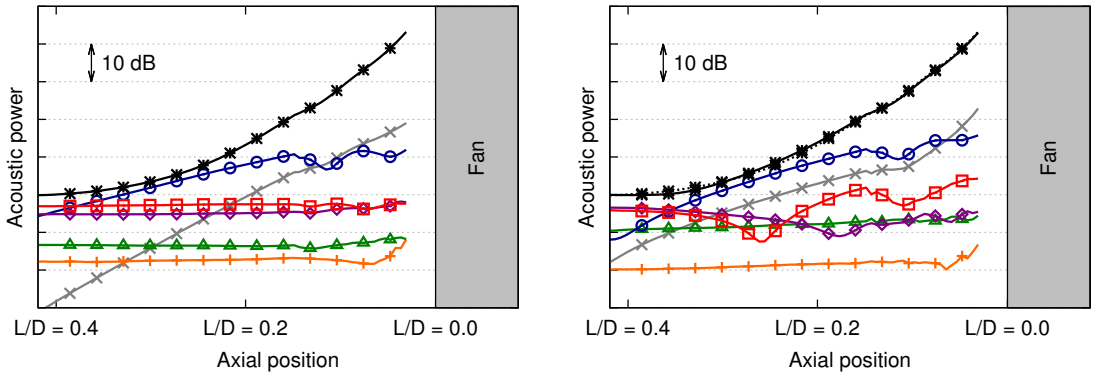

(a) Axisymmetric air inlet (b) Asymmetric air inlet

Figure 4.44: **Axial evolution of acoustic power at the BPF at cutback: dominant modes at $L/D = 0.4$ (mode -15, mode -14, mode -16, mode -13, mode -1, mode -17), total power**

When going further upstream, the distortion-fan interaction modes remain dominant. One low-order mode is also present ($m = -1$) but is 15 dB lower than other modes so that it does not contribute significantly to the total power. Because the rotor-locked mode is not significant anymore at $L/D = 0.4$ (it is "more cut-off" be-

cause of its higher order), the distortion-fan interaction modes are now responsible for most part of the noise. However, the total noise is surprisingly not increased by the inlet distortion. A stronger attenuation of the cut-off modes is observed in the asymmetric configuration and explains this behavior. For example, the mode $m = -16$ is 3 dB higher at source in the presence of inlet distortion but becomes almost 7 dB lower at $L/D = 0.4$. This stronger attenuation has also been observed with the hybrid methods when considering the equivalent asymmetric duct and is therefore a consequence of the reduction of the cross-section surface of the asymmetric air inlet. In any case, it appears that the modes caused by the interaction of distortion with the fan are the most important contributor to the upstream total noise. The comparison with the predictions based on hybrid methods is given in Fig. 4.45.

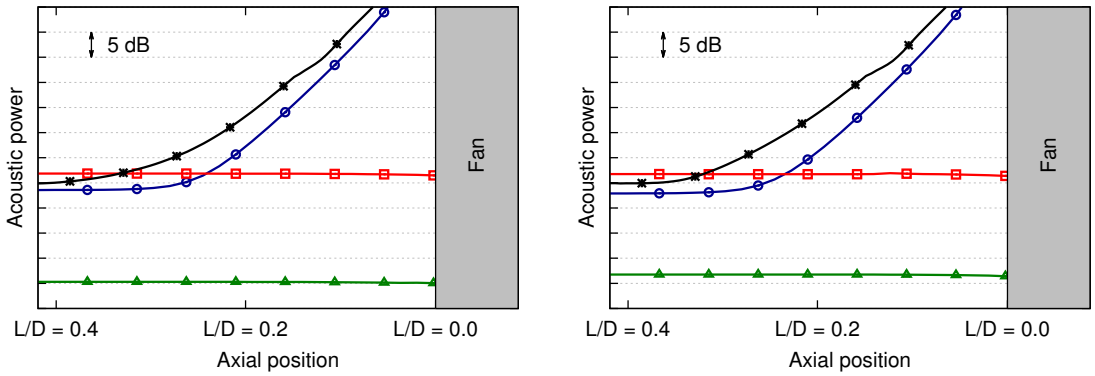

(a) Axisymmetric air inlet (b) Asymmetric air inlet

Figure 4.45: **Axial evolution of acoustic power at the BPF at cutback: Rienstra - IGV, Rienstra - fan, Rienstra OGV, direct method**

With the hybrid methods, the noise caused by the OGV sources was dominant for both inlet geometries. However, as already mentionned, this noise is probably overestimated because of the rotor shielding effect that has been neglected. The levels predicted from the fan sources are close to the total power computed directly and this is an additional evidence that the upstream noise is dominated by those sources. This level is probably better predicted than at approach conditions because some of the important modes caused by the interaction with the distortion becomes cut-on. With both methods, the penalty induced by the inlet distortion is found to be small (less than 1 dB) because of propagation effects even if the sources are significantly increased.

At sideline

At sideline, the behavior is again different because the rotor-locked mode and the important modes linked to distortion-fan interaction are cut-on. Therefore, there is no need to look at the dominant modes at several axial positions because they remain the same in the whole inlet. The results are given in Fig. 4.46.

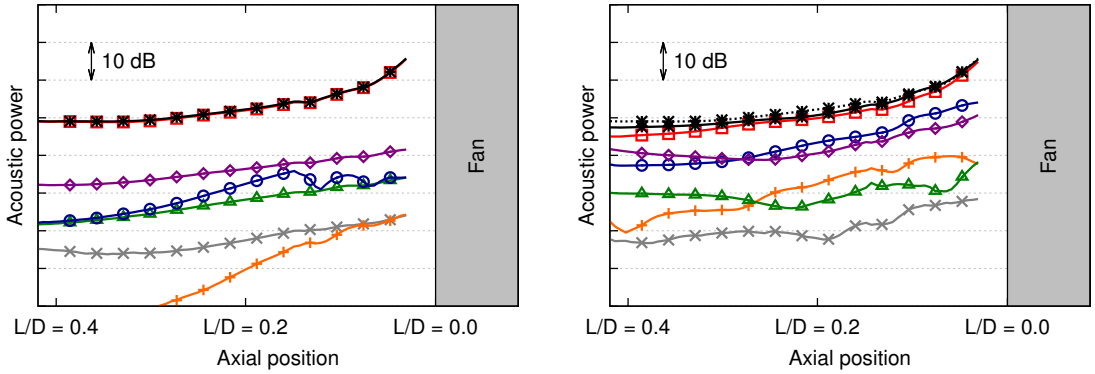

(a) Axisymmetric air inlet (b) Asymmetric air inlet

Figure 4.46: **Axial evolution of acoustic power at the BPF at sideline: dominant modes in the inlet (mode -18, mode -17, mode -19, mode -16, mode -20, mode -15), total power**

Without inlet distortion, the rotor-locked mode dominates all other modes with a level at least 15 dB greater than the second most important mode. The upstream noise level is therefore totally linked to this mode. All the other modes are the ones close to it and are linked to the interaction of the fan with the distortion. This is why these modes are significantly increased by the inlet distortion: +10 dB for $m = -17$, +8 dB for $m = -16$ and +16 dB for $m = -19$ for example. However, the rotor-locked mode, while having the same value at source, is more attenuated in the inlet. This is again an effect of propagation that can be linked to the reduction of cross-section surface according to hybrid method results. This stronger attenuation results in a lower upstream noise level but this is partially mitigated by the increased level of distortion-fan interaction modes. Those modes contribute to the upstream noise in the asymmetric configuration as evidenced by the gap of 2 dB between the total power and the power associated with the rotor-locked mode. For comparison purposes, the results obtained using Rienstra's theory are given in Fig. 4.47.

The hybrid approach successfully predicted the domination of the fan sources but considerably overestimates their noise level (by more than 15 dB). It is essentially due to the overestimation of the rotor-locked mode: its noise level at inlet plane is 28 dB and 17 dB higher than the second dominant mode $m = -17$ without and with inlet distortion respectively (see Fig. 4.34). This gap is much lower using the direct approach: 17 dB in the axisymmetric case and 4 dB in the asymmetric one at inlet plane. At supersonic tip speeds, the use of Rienstra's theory appears to be inappropriate to propagate fan sources. In addition, the rotor-locked mode at this regime also carry the energy of the shocks that are not accounted for in the present hybrid approch. Nevertheless, the reduction of the noise with the inlet distortion was predicted in both methods. Using Rienstra's approach, the noise is reduced by 4-5 dB because of the reduction of the duct section. In the direct estimations, the reduction of noise is lower (1-2 dB) even if the rotor-locked mode is also reduced by 4-5 dB also. This is due to the increased importance of distortion-fan interaction

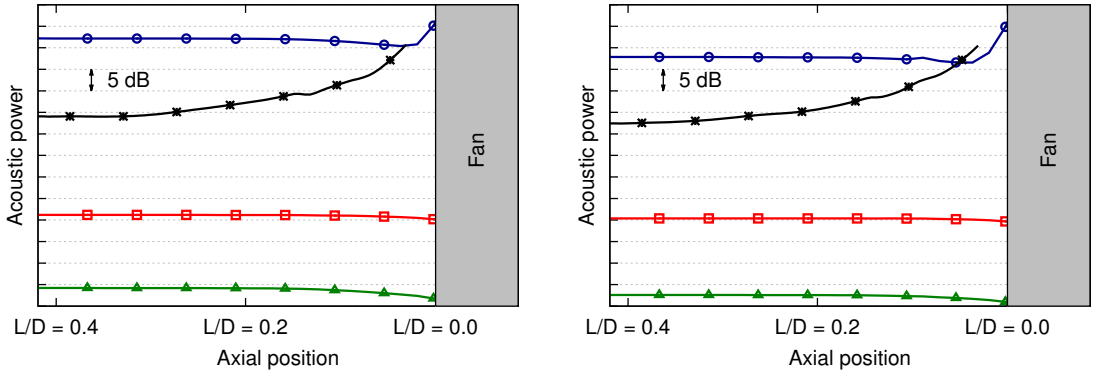

(a) Axisymmetric air inlet (b) Asymmetric air inlet

Figure 4.47: **Axial evolution of acoustic power at the BPF at sideline: Rienstra - IGV, Rienstra - fan, Rienstra OGV, direct method**

modes but also probably due to some modal scattering by the distortion [114] (see for example the exchange of the energy between modes $m = -18$ and $m = -17$ from $L/D = 0.3$).

4.6.3 Filtering of hydrodynamic fluctuations

Before proceeding to the analysis of the downstream noise, a filtering of the hydrodynamic fluctuations must be performed. Several techniques are tested and are shown in this section.

Filtering based on the convective fluctuations

The first filtering that has been performed is similar to the one used by Bonneau *et al.* [21]. It is based on the fact that vorticity fluctuations are convected with the flow. In a canonical one-dimensional case, if the mean flow velocity is U_0 and the mean speed of sound is a_0, then these fluctuations will be convected at the speed U_0 while the acoustic fluctuations will be propagated at $U_0 \pm a_0$ ($+$ for the downstream propagation and $-$ for the upstream one). The principle of the filtering is simply to remove the part convected at U_0. It is applied here by interpolating the mean flow and the field at the BPF on a Cartesian grid in order to follow the fluctuations over axial lines for each point (r, θ) of the cross-section. A Dynamic Mode Decomposition (DMD) [115] is then performed on each line to detect the amplitude related to the convection wavenumber $k_c = 2\pi f/U_0$ where f is the frequency. The definition of U_0 is discussed later. In practice, it will be defined by a range to account for the axial variation of the flow so that a range of modes will be related to convection. Each line is therefore reconstructed by accounting for all the modes except the ones related to the convection.

U_0 is first chosen as the local velocity of the line. This velocity varies along the line and is defined by its minimum and maximum values U_0^{min} and U_0^{max}. The convection wavenumber therefore lies between $k_c^{min} = 2\pi f/U_0^{max}$ and $k_c^{max} = 2\pi f/U_0^{min}$.

Even if it is not shown here for purposes of brevity, it has been observed than removing all the wavenumbers between these upper and lower limits had almost no effect on the power. A tolerance t_{filt} is therefore added to mitigate this and the wavenumbers between $(1 - t_{filt})\, k_c^{min}$ and $(1 + t_{filt})\, k_c^{max}$ are filtered. The results obtained with a tolerance of 20% are presented below. The effect of the filtering will be illustrated on the fluctuations and on the acoustic power. Considering the fluctuations, the procedure is applied to the pressure and the axial velocity fluctuations because they are both present in Eq. (1.61). The axisymmetric approach configuration is chosen as an illustration. The axial evolution of the real part of the pressure at the BPF extracted in a line around mid-span is shown in Fig. 4.48(a), before and after filtering. The signal reconstitued from all the modes found by the DMD is given to check the coherence of the decomposition. Note that the DMD is applied only to the part downstream of the struts in order to avoid the presence of OGV evanescent modes that might cause inaccuracies. The normalized wavenumbers found by the DFT are also given 4.48(b) to highlight the filtered wavenumbers. These wavenumbers are normalized by the averaged convection wavenumber $k_{norm} = 2\pi f / U_{norm}$ where U_{norm} is the axial velocity averaged over the domain downstream of the OGV.

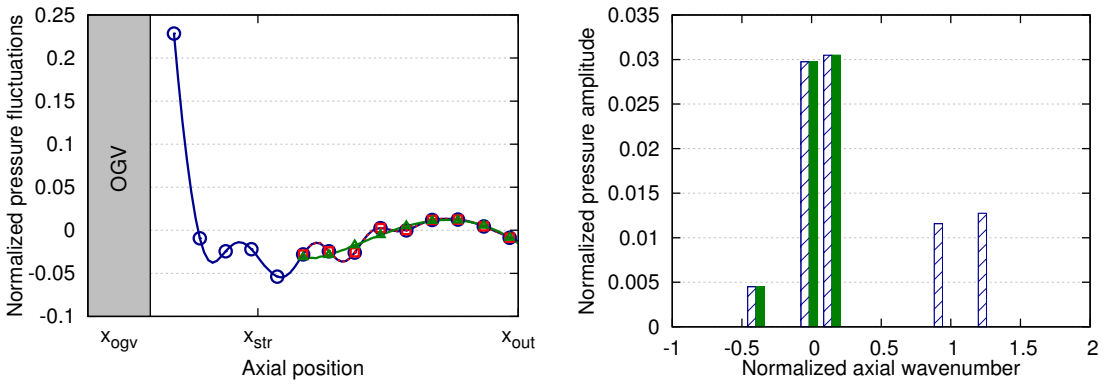

(a) Axial evolution of pressure fluctuations at BPF

(b) Axial mode decomposition at BPF

Figure 4.48: **Illustration of the filtering procedure based on local velocity (60A) - point around mid-span: initial signal, reconstructed signal from all modes, filtered signal**

The signal recomposed from all the modes found by the DMD fits well the initial signal which gives credits to the decomposition. The filtered signal no longer contains the fast variation of pressure that were convected with the flow (the two modes with normalized wavenumber around 1). The results obtained from a line extracted close to the hub are now shown in Fig. 4.49.

On this line, the convective fluctuations are not filtered by the procedure. Because the mean axial velocity is lower close to the hub, the minimum and maximum convective wavenumbers computed on the line k_c^{min} and k_c^{max} are high (around 2 after normalization). However, it appears that the hydrodynamic fluctuations are

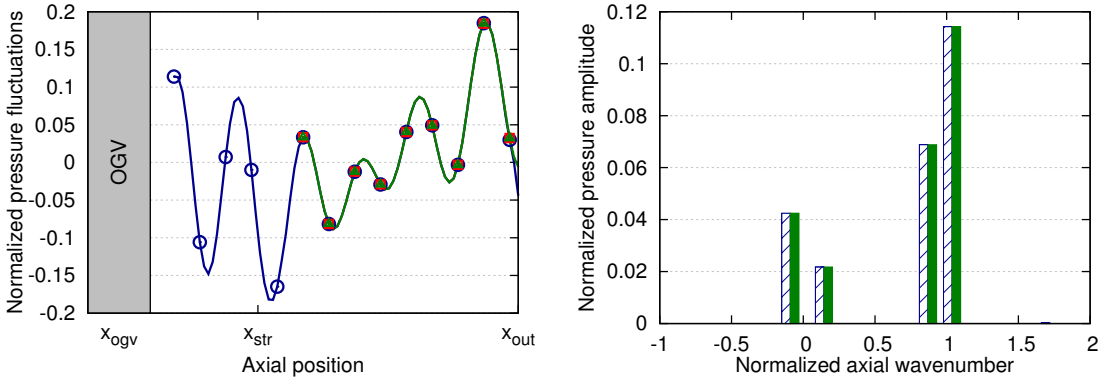

(a) Axial evolution of pressure fluctuations at BPF

(b) Axial mode decomposition at BPF

Figure 4.49: **Illustration of the filtering procedure based on local velocity (60A) - point near hub: initial signal, reconstructed signal from all modes, filtered signal**

convected with the mean flow of the section (normalized wavenumber around 1) despite the low local axial velocity. This observation limits the use of the local velocity for U_0 in the filtering procedure.

U_0 is therefore now defined as the averaged axial velocity of the section. It means that each line of the same section are characterized by the same U_0. However, U_0 is still varying along the lines and as previously, the convective wavenumbers are considered between the minimum and maximum value over the line k_c^{min} and k_c^{max}. A tolerance is similarly added. The results obtained for the same line as the one shown in Fig. 4.49 are given in Fig. 4.50.

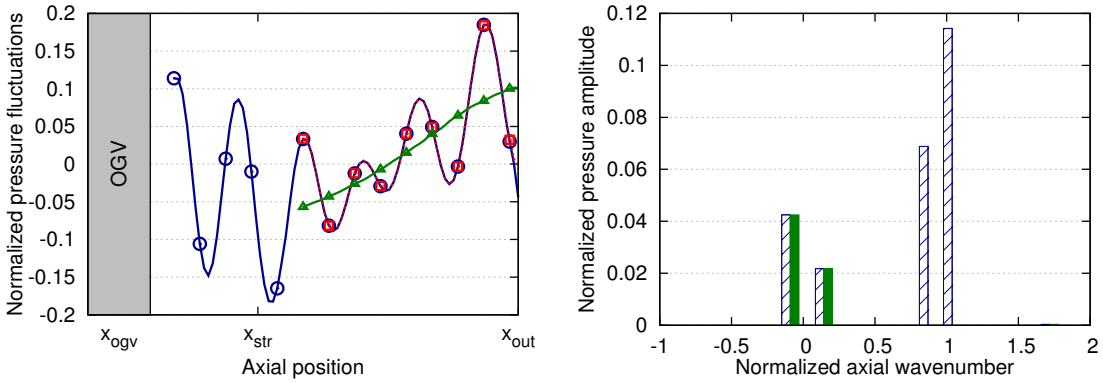

(a) Axial evolution of pressure fluctuations at BPF

(b) Axial mode decomposition at BPF

Figure 4.50: **Illustration of the filtering procedure based on global velocity (60A) - point near hub: initial signal, reconstructed signal from all modes, filtered signal**

Accounting for the velocity averaged over the section (called global velocity) instead of the local velocity to the line makes the filtering better in this region, by eliminating the two modes close to 1. However, the variation of global velocity over the line is lower than the one of the local velocity and the range of modes to be filtered $[k_c^{min}, k_c^{max}]$ is therefore smaller. This makes the filtering partially inefficient for some lines. For example, the results shown in Fig. 4.48 for the line extracted around mid-span are updated with the use of global velocity in Fig. 4.51.

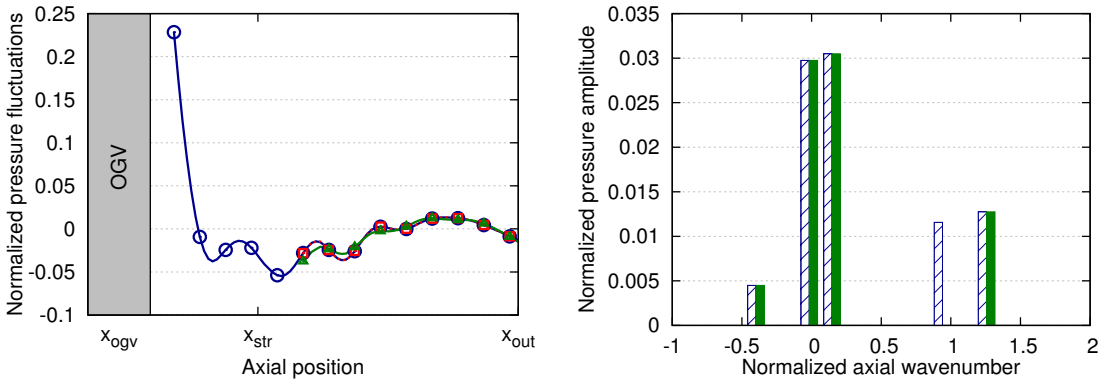

(a) Axial evolution of pressure fluctuations at BPF

(b) Axial mode decomposition at BPF

Figure 4.51: **Illustration of the filtering procedure based on global velocity (60A) - point around mid-span: initial signal, reconstructed signal from all modes, filtered signal**

This smaller range is responsible for the filtering of one mode only (the one closest to 1). The other mode is not filtered and some hydrodynamic fluctuations (high frequency variations) are still visible in the filtered signal. This behavior can be corrected by simply increasing the tolerance parameter t_{filt}. For this line, using $t_{filt} = 0.5$ removes the residual hydrodynamic fluctuations.

The filtering procedure is done on both pressure and axial velocity fluctuations and the acoustic power is evaluated from the filtered fluctuations. A comparison between the results obtained using a local definition for U_0 (with $t_{filt} = 0.2$) and a global definition (with $t_{filt} = 0.2$ and $t_{filt} = 0.5$) is given in Fig. 4.52.

For a tolerance of 20%, the use of the local velocity for the definition of the convection wavenumber instead of the global velocity filters more the hydrodynamic fluctuations (power 2 dB lower). This is caused by the more important variations of the local velocity and the resulting bigger range of modes to be filtered. This is why the filtered power is significantly decreased (-8 dB) with the global velocity definition when the tolerance is increased to 50%. The level is lower than the one obtained using the local velocity definition where the fluctuations near boundaries were not filtered because of low local velocities. On both sides of the filtered power, a strange behavior is observed and is due to the decomposition method which detects artificial

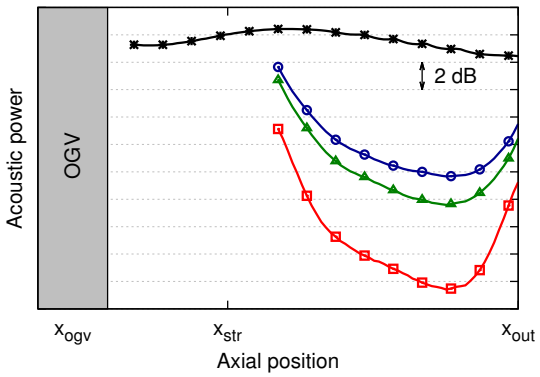

Figure 4.52: **Axial evolution of the acoustic power at the BPF (60A): without filtering, filtering based on local velocity - $t_{filt} = 0.2$, filtering based on global velocity - $t_{filt} = 0.2$, filtering based on global velocity - $t_{filt} = 0.5$**

modes with very high amplification coefficients. Therefore, the values of acoustic power obtained in these regions are not exploitable. This filtering procedure is difficult to use in practice because it strongly depends on the choice of the tolerance which cannot be known a priori. By increasing it too much, part of the acoustic fluctuations may also be removed.

Filtering based on modal decomposition

Another filtering technique is used in order to overpass the limits exposed above. It is inspired from the mode matching technique originally developed by Ovenden & Rienstra to couple CFD and CAA simulations [61]. At each section, the field at the BPF (static pressure and axial velocity) is decomposed into duct modes using the local duct radii. For example, the pressure $\widehat{p}$ at pulsation ω and at point (x, r, θ) is written, with the notations of Sec. 1.6,

$$\widehat{p}(x, r, \theta) = \sum_{m=-\infty}^{+\infty} \sum_{n=0}^{+\infty} p_{mn}(x, \omega) \psi_{mn}(x, r, \theta), \tag{4.2}$$

where

$$\psi_{mn}(x, r, \theta) = \left[A_{mn}(x) J_m(\alpha_{mn}(x) r) + B_{mn}(x) Y_m(\alpha_{mn}(x) r)\right] e^{-im\theta}. \tag{4.3}$$

The pressure modal coefficient $p_{mn}(x, \omega)$ is obtained from the simulations by a projection of the azimuthal Fourier components $p_m(x, r)$ over Bessel's functions:

$$p_{mn}(x, \omega) = \frac{2\pi}{\Gamma_{mn}} \int_{R_h}^{R_t} p_m(x, r) \left[A_{mn}(x) J_m(\alpha_{mn}(x) r) + B_{mn}(x) Y_m(\alpha_{mn}(x) r)\right] r dr. \tag{4.4}$$

This decomposition relates to Rienstra's theory in which each mode is characterized by its wavenumber $\gamma_{mn}^{\pm}$ (see Eq.(1.91) for example). + and - stand for the

upstream and downstream propagation respectively. For now, the fluctuations extracted from the CFD are assumed to propagate in the downstream direction only (i.e. no reflection on the boundaries). This assumption is evaluated later. From the axial evolution of each mode computed from the CFD, it is therefore possible to extract only what is propagated with the theoretical wavenumber γ^-_{mn} (i.e. the acoustic part of the fluctuations) using a DMD as previously. This acoustic wavenumber γ^-_{mn} varies along the duct so that a range of acoustic wavenumbers is defined in practice for each mode. Filtering by accounting for what is strictly in this range is too restrictive and several modes that are theoretically cut-on reach zero. This can be explained by the fact that this range of acoustic wavenumbers is valid only for flows that are purely axial and that are homogeneous in the radial and the azimuthal directions (assumptions in Rienstra's theory). To mitigate these tight constraints linked to the hypotheses of the theory, a tolerance must be included again. However, contrary to the previous filtering technique, the tolerance can be chosen more objectively here. Indeed, both the theoretical convective wavenumber (defined with the velocity integrated over the section because there is no more local quantities with the modal decomposition) and the acoustic wavenumber are known. It is therefore easy to choose the tolerance so that there is no overlapping. In the results presented here, the axially-averaged convective wavenumber is computed such as the axially-averaged acoustic wavenumber for each mode. If a wavenumber found by the DMD is closer to the convective wavenumber than to the acoustic wavenumber, then it is removed from the signal. The procedure is illustrated on one duct mode ($m = 6, n = 0$) in Fig. 4.53, still for the axisymmetric approach configuration.

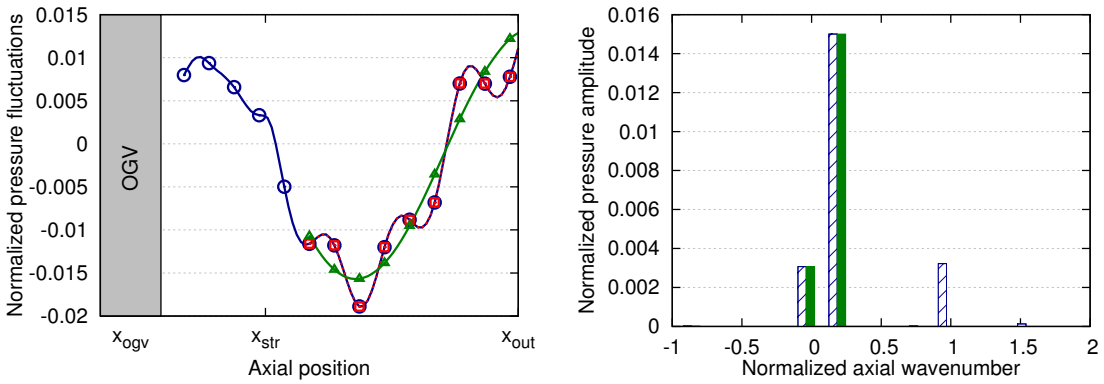

(a) Axial evolution of pressure fluctuations at BPF

(b) Axial mode decomposition at BPF

Figure 4.53: **Illustration of the filtering procedure based on modal decomposition (60A) - pressure signal - mode** ($m = 6, n = 0$)**: initial signal, reconstructed signal from all axial modes, filtered signal**

The hydrodynamic fluctuations (characterized by the normalized wavenumber near 1) are of lower amplitude than the acoustic fluctuations (characterized by the smaller wavenumbers). This is generally true for the modal pressure of all other cut-on modes. These hydrodynamic fluctuations have been completely removed by the filtering. It should also be noted that the signal reconstructed from all the modes

found by the DMD correctly recovers the initial signal. The effect of the filtering is much more important on the axial velocity signal which is known to be more affected by the hydrodynamics than the pressure one [61]. This is illustrated in Fig. 4.54 which shows the axial evolution of the the axial velocity associated with the same mode.

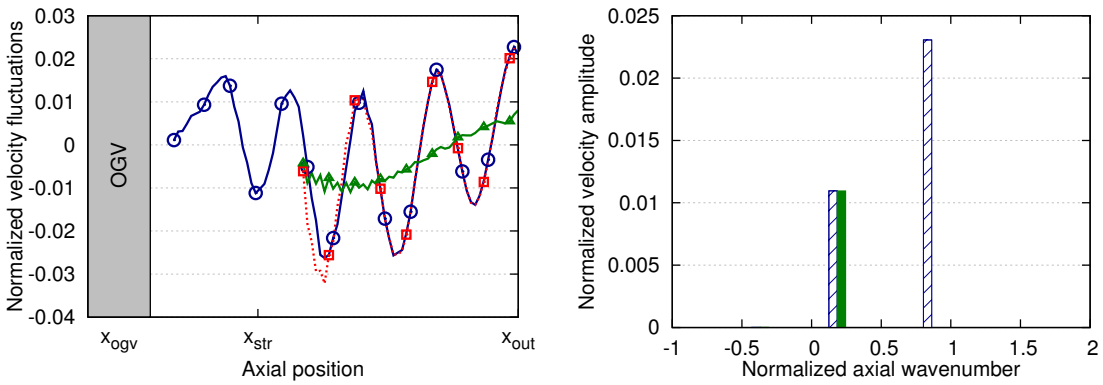

(a) Axial evolution of axial velocity fluctuations at BPF

(b) Axial mode decomposition at BPF

Figure 4.54: **Illustration of the filtering procedure based on modal decomposition (60A) - axial velocity signal - mode** $(m = 6, n = 0)$**:** ⟶○⟵ **initial signal,** □ **reconstructed signal from all axial modes,** ⟶△⟵ **filtered signal**

The hydrodynamic fluctuations are much greater than acoustic ones here, even if the mode is cut-on. This is observed for all other modes. Still, the filtering is able to isolate the acoustic part. However, the filtered signal is a bit noisy because of the presence of high wavenumbers that are not shown in the graph for clarity.

In order to avoid the difficulty linked to the filtering of the velocity signal, the modal decomposition technique offers the possibility to compute the axial velocity acoustic fluctuations directly from the pressure ones. Indeed, Eqs. (1.99) and (1.101) yields

$$u^-_{mn}(x,\omega) = \frac{\lambda^-_{mn}}{\rho_0 a_0} p^-_{mn}(x,\omega), \tag{4.5}$$

where the notations of Sec. 1.6 are used. The use of this relation not only ease the computation of the acoustic velocity fluctuations but also allows to have a consistency with the equations describing the acoustics in a slowly varying annular duct with a slowly varying axial flow. A comparison between the velocity fluctuations obtained by filtering the velocity signal of the CFD (called P+V filtering because the filtering is applied to both pressure and velocity) and the velocity fluctuations computed from the filtered pressure fluctuations using Eq. (4.5) (called P filtering because the pressure only is used form the CFD) is given in Fig. 4.55 for the same mode.

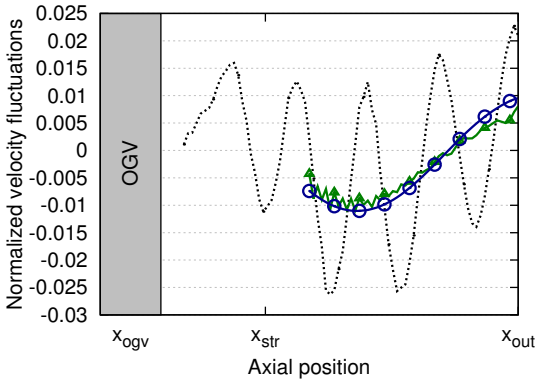

Figure 4.55: **Axial evolution of axial velocity fluctuations at BPF (60A) - mode** $(m = 6, n = 0)$**: without filtering, P+V filtering, P filtering**

When using the velocity signal from the CFD, the filtered signal is indeed a bit noisy but it is nevertheless close to the one computed theretically from the pressure signal (less than 20% of error on average). It means that, for this mode, the pressure and velocity resulting from the filtering procedure are consistent with the equations of acoustics, even without using the theoretical relationship (4.5).

In both the P and P+V filtering described above, it has been assumed that the acoustic waves were going in the downstream direction only. This is true downstream of the OGV only if the reflection of the waves by the outlet boundary condition is negligible. In the CFD simulations, stretching zones have been added at the outlet to avoid these reflections. Using the modal decomposition technique allows the decomposition into an upstream and downstream acoustic waves when using the pressure and velocity jointly. It will be done here in order to check this assumption. The pressure and axial velocity coefficients associated with the mode (m, n) can be decomposed into an upstream part and a downstream one

$$p_{mn}(x,\omega) = p^{+}_{mn}(x,\omega) + p^{-}_{mn}(x,\omega), \tag{4.6a}$$

$$u_{mn}(x,\omega) = u^{+}_{mn}(x,\omega) + u^{-}_{mn}(x,\omega), \tag{4.6b}$$

with the velocity related to the pressure by

$$u^{\pm}_{mn}(x,\omega) = \frac{\lambda^{\pm}_{mn}}{\rho_0 a_0} p^{\pm}_{mn}(x,\omega). \tag{4.7}$$

With the values of $p_{mn}(x,\omega)$ and $u_{mn}(x,\omega)$ extracted from the CFD (using Eq.

(4.4)), the upstream and downstream waves can be determined [39]:

$$p^+_{mn}(x,\omega) = \frac{\rho_0 a_0 u_{mn}(x,\omega) - \lambda^-_{mn} p_{mn}(x,\omega)}{\lambda^+_{mn} - \lambda^-_{mn}}, \tag{4.8a}$$

$$p^-_{mn}(x,\omega) = p_{mn}(x,\omega) - p^+_{mn}(x,\omega), \tag{4.8b}$$

$$u^+_{mn}(x,\omega) = \frac{\lambda^+_{mn}\left[\rho_0 a_0 u_{mn}(x,\omega) - \lambda^-_{mn} p_{mn}(x,\omega)\right]}{\rho_0 a_0 \left[\lambda^+_{mn} - \lambda^-_{mn}\right]}, \tag{4.8c}$$

$$u^-_{mn}(x,\omega) = u_{mn}(x,\omega) - u^+_{mn}(x,\omega). \tag{4.8d}$$

Because this technique requires the joint use of pressure and velocity fluctuations, it is called PV filtering in the rest of the section. The comparison of the filtered pressure and axial velocity obtained using the PV technique and the P technique is provided in Fig. 4.56 for the mode $(6, 0)$.

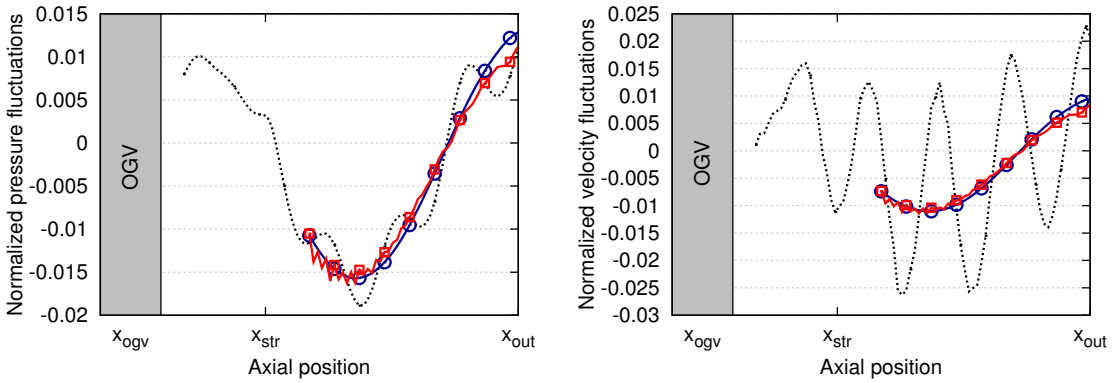

(a) Pressure

(b) Axial velocity

Figure 4.56: **Axial evolution of pressure and axial velocity fluctuations at BPF (60A) - mode** $(m = 6, n = 0)$**: without filtering, P filtering, PV filtering**

The evolution of pressure and velocity obtained with both filtering techniques are close with local differences that do not exceed 20%. The PV signal is more noisy because it uses the axial velocity signal of the CFD. This high similarity indicates that this mode is essentially propagating in the downstream direction. All the observations made above are observed for the other modes and witness a correct behavior of the filtering technique. This is evidenced by the comparison between the three types of filtering (P+V, P and PV) in terms of resulting total power in Fig. 4.57.

The impact of the filtering based on modal decomposition is much more important than the ones observed with the previous filtering technique (around -30 dB instead of -15 dB for $t_{filt} = 50\%$). The filtered power level does not depend on the formulation (P+V, P and PV) which means that

- the filtered pressure and velocity in the P+V formulation are consistent with the equations of duct acoustics (similarity of P+V noise level and P level);

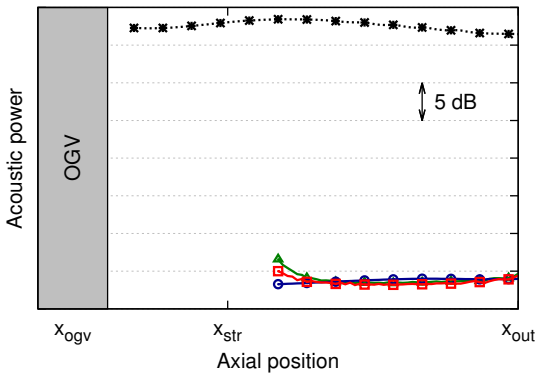

Figure 4.57: **Axial evolution of acoustic power at the BPF (60A): without filtering, P+V filtering, P filtering, PV filtering**

- the filtered power is entirely caused by the downstream acoustic waves (similarity of P noise level and PV level).

These two remarks gives credit to the filtering based on modal decomposition and to the predicted downstream noise levels. In addition, the resulting acoustic power is almost constant which is expected far from the sources. In the following of the manuscript, the downstream acoustic power levels are based on the P filtering (the less noisy).

The dominant modes downstream of the OGV that were shown in Fig. 4.37 without filtering are now recomputed after application of the P filtering. The results are given in Fig. 4.58, again for the axisymmetric approach configuration.

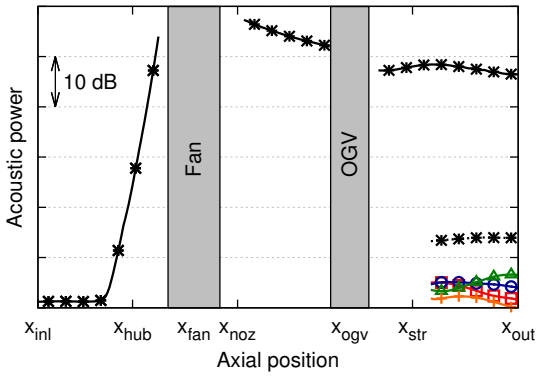

Figure 4.58: **Axial evolution of acoustic power (60A) with filtering based on modal decomposition (P): dominant modes (mode -10, mode 6, mode -6, mode 8 in order), total power, filtered power**

Contrary to what was observed before the filtering, the downstream noise is now dominated by low-order modes that are not caused by vorticity fluctuations. The dominant modes are of maximum absolute order 10 and are therefore probably caused by OGV sources.

4.6.4 Analysis of downstream power

The downstream power levels obtained after filtering are analyzed here. Such as for the upstream noise, the analysis is based on the determination of the dominant modes. For upstream noise analysis, the dominant modes were determined at different locations because of the importance of the cut-off modes in the inlet. Downstream of the OGV, the axial variation of the modes is not as crucial and the dominant modes are therefore determined at one location only (in the outlet plane).

At approach

The results at approach conditions are given in Fig. 4.59 for both inlet geometries. On the asymmetric plot, the total noise level computed from the axisymmetric simulation is added in black dotted line to ease the comparison. All the dominant modes at the outlet are low-order modes and are therefore probably linked to fan-OGV interaction. The effect of the inlet distortion is not the same on all these modes but most of them are increased. For example, the two most important modes in the asymmetric configuration $m = -7$ and $m = 6$ are increased by 7 dB and 4 dB respectively, which is responsible for a penalty of more than 3 dB in total. Important axial variations of the power carried by the different modes is also observed (up to 5 dB for $m = -7$ in the axisymmetric configuration). This indicates important modal scattering that can be caused by axial variations of the mean flow and duct radii [116], the presence of the pylon [110] or the presence of distortion (i.e. azimuthal variation of the mean flow) [114].

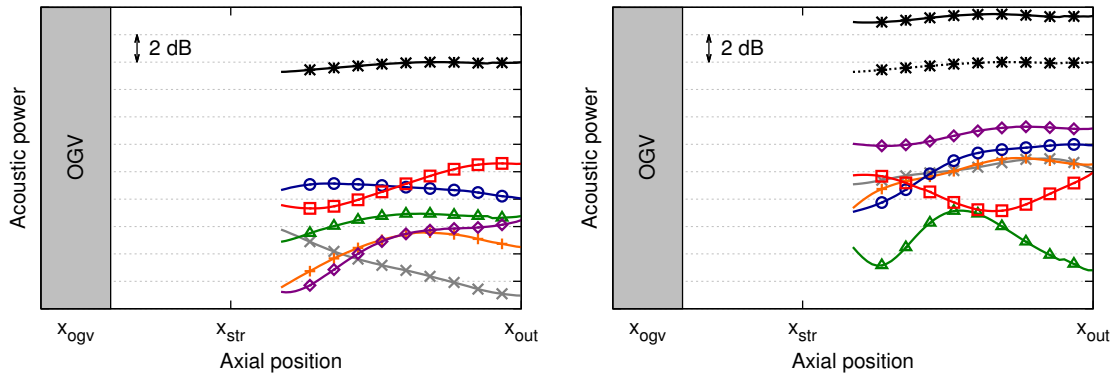

(a) Axisymmetric air inlet

(b) Asymmetric air inlet

Figure 4.59: **Axial evolution of acoustic power at the BPF at approach: dominant modes in the outlet (mode -6, mode -7, mode 6, mode 2, mode 3, mode 5), total filtered power**

The comparison with the power levels predicted with Rienstra's theory is given in Fig. 4.60. Both the noise radiated from the fan sources and from the OGV sources is represented. The domination of the OGV sources is also found in the hybrid approach with a level 14 dB and 9 dB higher for the OGV than for the fan. The noise levels that are predicted with Rienstra's theory are in good agreement with

the direct estimates (difference of less than 1 dB) and the acoustic penalties caused by inlet distortion are consequently coherent between both approaches (around 2 dB and 3 dB for the hybrid and direct approaches respectively).

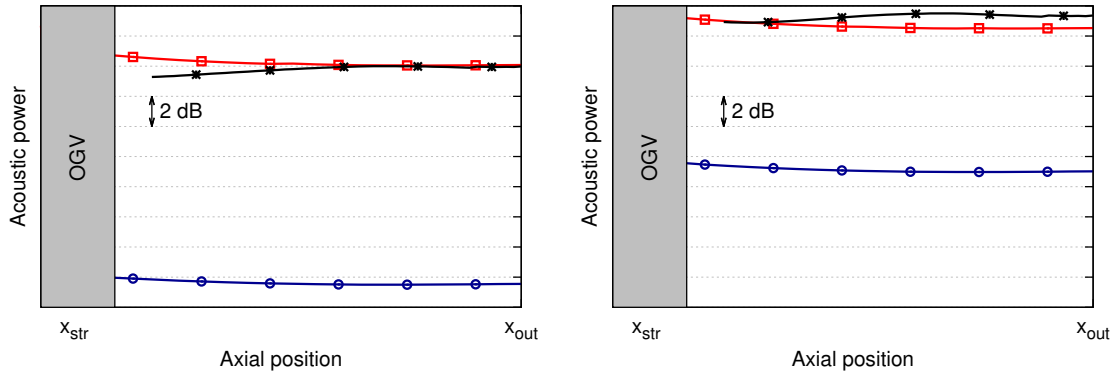

(a) Axisymmetric air inlet (b) Asymmetric air inlet

Figure 4.60: **Axial evolution of acoustic power at the BPF at approach: Rienstra - fan, Rienstra OGV, direct method**

At cutback

The same procedure is applied at cutback and results are given in Fig. 4.61. Again, the dominant modes at the outlet are of orders far from the rotor-locked mode ($m = -18$) and are probably linked to OGV sources. The energy associated with most of these modes is increased resulting in a total acoustic penalty of 2.5 dB on average. The scattering between the modes is increased when compared to approach conditions and humps are also observed for some modes ($m = 6$ for example).

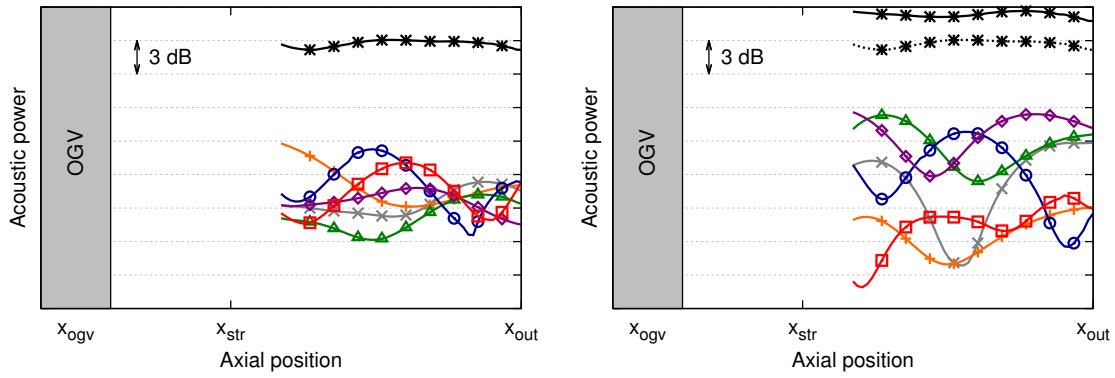

(a) Axisymmetric air inlet (b) Asymmetric air inlet

Figure 4.61: **Axial evolution of acoustic power at the BPF at cutback: dominant modes in the outlet (mode -2, mode 10, mode 6, mode -11, mode -14, mode 8), total filtered power**

The comparison with the hybrid approach results is given in Fig. 4.62. The domination of the OGV sources in the downsteam noise is again evidenced with levels 18 and 15 dB higher than the noise caused by fan sources for the axisymmetric and the asymmetric configurations. Significative differences of approximately 3 dB on average are observed between the levels predicted with both approaches. However, the noise penalty is similar between both approaches (around 2.5 dB for the direct approach and 2 dB in average for the hybrid approach).

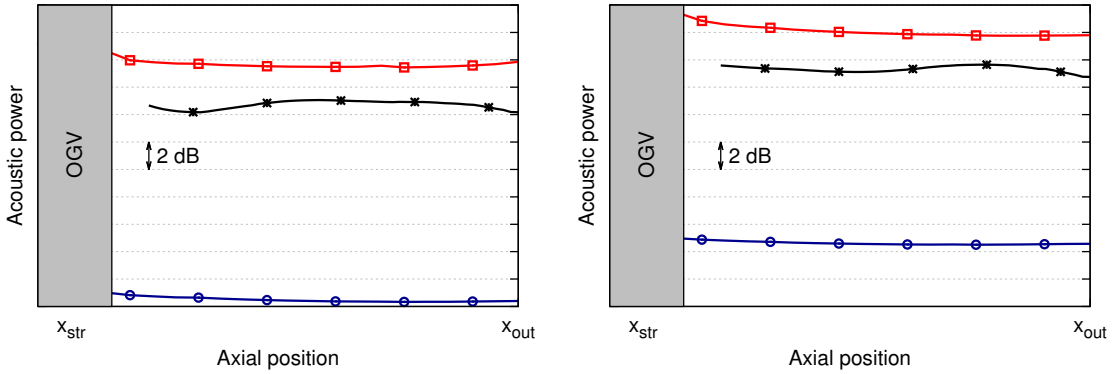

(a) Axisymmetric air inlet (b) Asymmetric air inlet

Figure 4.62: **Axial evolution of acoustic power at the BPF at cutback: Rienstra - fan, Rienstra OGV, direct method**

At sideline

Results at sideline conditions are given in Fig. 4.63. For this regime, the modes are less impacted by the inlet distortion and conserve their global shape. The increase of total noise is therefore moderate (around 1 dB in average). At sideline, the cut-on/cut-off transition occurs at a higher order than at approach and cutback and some modes of high absolute orders are therefore present in the outlet plane. It is not evident to say a priori if the modes $m = -13$ and $m = -14$ come from the interaction of the fan with the 4^{th} and 5^{th} harmonic of the distortion or from the interaction of the fan-blade wakes with the OGV. The other dominant modes are all co-rotating (and therefore far from the rotor-locked mode) and are probably caused by OGV sources.

The predominance of the OGV sources is again also evidenced with the hybrid approach as shown in Fig. 4.64. The differences between the absolute noise levels predicted by both approaches are increased when compared to the cutback and approach regimes. This is probably caused by the increased number of radial modes that become cut-on when increasing the rotational speed of the engine. However, these differences are found for both configurations and the impact on the noise induced by inlet distortion is consistent between both methods (approximately +2 dB in average).

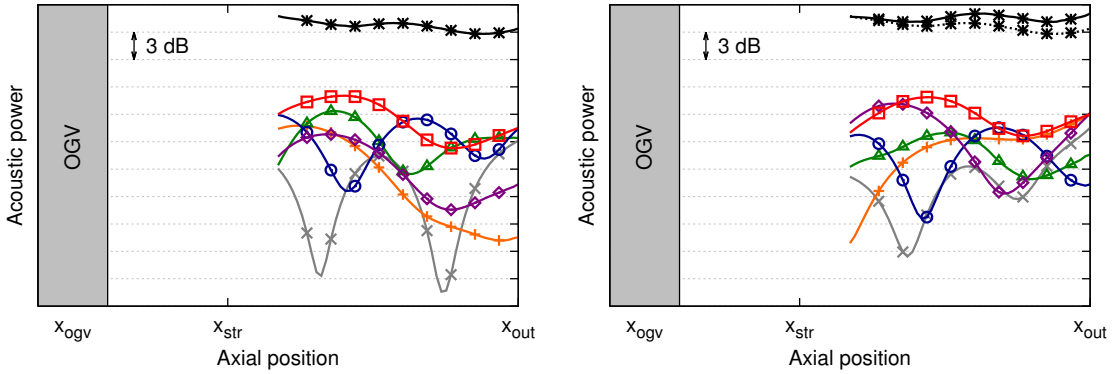

(a) Axisymmetric air inlet (b) Asymmetric air inlet

Figure 4.63: **Axial evolution of acoustic power at the BPF at sideline: dominant modes in the outlet (mode -14, mode -13, mode 8, mode 10, mode 16, mode 5), total filtered power**

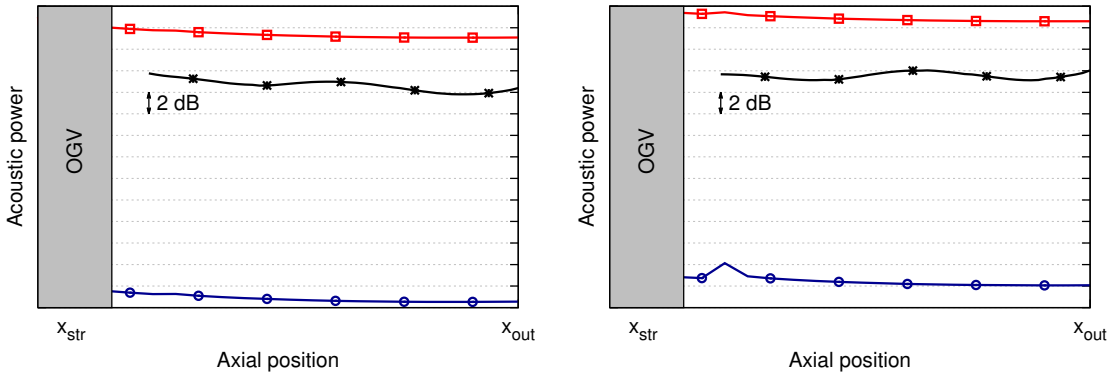

(a) Axisymmetric air inlet (b) Asymmetric air inlet

Figure 4.64: **Axial evolution of acoustic power at the BPF at sideline: Rienstra - fan, Rienstra OGV, direct method**

Summary of the section

A direct acoustic analysis has been performed in this section. The study of the downstream noise required a preliminary step that consists in filtering the hydrodynamic fluctuations. Two types of filtering were tested: one based on a local identification of the convective pertubations and the other based on a modal decomposition. The filtering based on the modal decomposition was shown to work correctly and has been applied to predict the downstream noise levels. At all regimes, the dominant modes downstream of the OGV are low-order modes that are probably caused by the OGV sources, which is consistent with the results based on Rienstra's theory. They are generally increased by the inlet distortion which results in a higher total power. However, this increase is reduced with the regime (penalty around 3 dB, 2 dB and

1 dB at approach, cutback and sideline respectively). The penalties induced by inlet distortion are in good agreement (maximum difference of 1 dB) with the ones predicted using Rienstra's theory even if differences were evidenced in the absolute noise levels. Concerning the upstream noise, a modal analysis evidenced a domination of the modes caused by distortion-fan interaction at cutback and sideline (modes around the rotor-locked mode). At approach, low-order modes dominate and are likely linked to OGV sources. The comparison with the previous results highlight the limits of the analytical propagation method used in the present work. The upstream noise radiated by the OGV sources predicted using Rienstra's theory is likely overestimated because the rotor shielding effect has not been taken into account. At sideline, the fan-blade tip speed becomes supersonic and the noise levels predicted analytically are largely overestimated.

4.7 Conclusion

The impact of distortion on the noise radiated by the fan module has been evaluated in this chapter using both an hybrid and a direct approach. The hybrid approach permitted the study of the different noise mechanisms (excepted the shock noise mechanism) separately. The impact of inlet distortion is evidenced on all mechanisms. It naturally increases the distortion-fan interaction noise but also the fan-OGV and fan-IGV interaction noise via the increased inhomogeneity of the wakes. A source breakdown based on this approach is proposed and is completed by a direct acoustic analysis (after filtering the non-acoustic part of the fluctuations via a modal decomposition). The results show that the downstream noise is dominated by the fan-OGV interaction mechanism, because of the swirling flow that cuts-off most co-rotating modes. The upstream noise seems to be dominated by OGV sources at approach and fan sources linked to the interaction with the distortion at cutback. At sideline, the rotor-locked mode is cut-on and dominates all other mode. The fan-IGV interaction noise is shown to be negligible.

Conclusions and perspectives

Recalling the objectives

The present PhD thesis concerns the study of the tonal noise generated by a fan module of a modern turbofan engine. Usually, the interaction of the fan-blade wakes with the OGVs is considered to be the dominant source of noise for subsonic operating points. In transonic regimes, the fan-self noise (steady loading and shock noise) also becomes important. The noise caused by the interaction of distortion with the fan blades is generally neglected. However, the distortion is expected to increase in UHBR engines and this source breakdown might be altered. The purpose of this PhD thesis was to evaluate the impact of this increased distortion on the noise generated by the fan module.

The study is based on full-annulus URANS simulations that include the air inlet, the fan, the IGVs and the OGVs. The OGV is heterogeneous and includes the pylon which is typical of modern architectures. Two air inlet geometries are considered (one is axisymmetric and the other is not) in order isolate the effects of inlet distortion that is the dominant source of distortion in the fan plane. The three acoustic certification points (approach, cutback and sideline) which correspond to different engine regimes are studied.

Conclusions from a physical point of view

The distortion has been characterized and quantified. When the inlet is axisymmetric, the distortion only comes from the potential effect of the pylon and struts. The potential effect of the classical vanes is indeed found to be negligible. While going upstream, the initial shape of the distortion composed of four lobes changes and only one major lobe remains. This lobe is due to the upper bifurcation (the largest one) which slows down the flow in its proximity. By going through the fan, this lobe is deviated by its rotation by an angle that varies linearly with the regime. The distortion caused by the pylon increases with the regime in the interstage region and reaches higher values close to the casing.

In addition, the asymmetry of the air inlet creates a distortion in the fan plane that is characterized by a low-velocity region at the top and a high-velocity region at

the bottom. This additional distortion increases the inhomogeneity of the flow right upstream of the fan, essentially close to the tip, where the distortion index has been multiplied by 4 to 6 depending on the regime. The effect in the interstage region is also significant, with an increase of the amplitudes of the first three harmonics of distortion which can be multiplied by more than 2.

The impact of this distortion on unsteady aerodynamic features has been described. The distortion linked to the potential effect of the pylon is responsible for important unsteady loadings on fan blades at the RF. These unsteady loadings are multiplied by more than 2 because of the inlet distortion. The modification of the fan-blade wakes has also been highlighted with the circumferential inhomogeneity of the velocity deficits. The inlet distortion further increases these inhomogeneities. Differences in the unsteady loadings between the different OGVs is therefore evidenced and are increased with the inlet distortion. At approach for example, the integrated pressure at the BPF vary from one vane to another by a factor of 2 without inlet distortion and by a factor of 3 when inlet distortion is added. At sideline, shocks also develop on the fan blades and propagate upstream. These shocks are almost fixed when the air inlet is axisymmetric but their position varies over 10% of the chord and their strength varies by 45% in the presence of inlet distortion.

The consequences in terms of noise emissions have been shown. The downstream noise appears to be effectively dominated by the OGV sources caused by the interaction with the fan-blade wakes (levels higher by 10 dB at least using predictions based on Rienstra's theory). This is essentially due to the swirl in the interstage that cuts-off the important modes caused by the interaction of the distortion with the fan. The inlet distortion increases the downstream noise by 1 to 3 dB depending on the regime by increasing the inhomogeneity of the wakes. As for the upstream noise, the fan sources are shown to be important contributors, at least at cutback and sideline. The balance at approach is less evident to establish but an increase of about 5 dB caused by the inlet distortion is computed with the direct approach. At cutback, the distortion-fan interaction modes dominate the upstream noise and some of them are increased by more than 10 dB with the inlet distortion. This is similar at sideline but the fan-self noise, carried by the rotor-locked mode and not affected by the inlet distortion at source, is also dominant. However, it appears that the propagation in the asymmetric inlet (characterized by a smaller cross-section surface) mitigates these increased levels at cutback and sideline. Finally, the contribution of the IGV sources that is generally neglected has been evaluated for the first time. Their contribution is insignificant even if the associated noise is increased by some decibels with the inlet distortion (again because of the increased heterogeneity of the impinging wakes). These conclusions are summarized in Tabs. 4.1 and 4.2 for the upstream and the downstream noise respectively. For each certification point, the dominant mechanism(s) is (are) given along with the impact caused by inlet distortion. Two symbols are given for the distortion-fan interaction at cutback and for the fan-self noise at sideline because of the mentionned propagation effects in the asymmetric duct. The first symbol stands for the effect of inlet distortion at source while the second one stands for the effect of inlet distortion in the inlet plane.

Mechanism	Approach	Cutback	Sideline
Wakes-OGV interaction	↗		
Distortion-fan interaction		↗ / =	↗
Fan self-noise			= / ↘
Wakes-IGV interaction			

Table 4.1: **Source breakdown for upstream noise: dominant mechanism, = / ↘ / ↗ evolution with inlet distortion (no effect, decrease, increase)**

Mechanism	Approach	Cutback	Sideline
Wakes-OGV interaction	↗	↗	↗
Distortion-fan interaction			
Fan self-noise			
Wakes-IGV interaction			

Table 4.2: **Source breakdown for downstream noise: dominant mechanism, = / ↘ / ↗ evolution with inlet distortion (no effect, decrease, increase)**

Conclusions from a methodological point of view

The work done during this PhD thesis is based on full-annulus URANS simulations of a whole fan module. The main conclusions of the work were obtained by comparing the simulations with and without inlet distortion that were run with the same numerical setup. An analysis of the performances has been done in order to verify the correct operating of the fan module.

Concerning acoustic predictions, several methods with different degrees of modeling have been used. First, for hybrid methods, the limits of Amiet's model to correctly predict the unsteady loadings on the blades and vanes have been shown even if it gives the good trends. The overlapping of the blades and vanes is high in the studied configuration and a strong cascade effect is expected. This justifies the use of the numerical sources for the in-duct propagation. The effects of the axial variation of the flow and the duct geometry are shown to be significant with differences in noise levels that can reach several decibels. The use of the slowly varying theory of Rienstra permits to overpass these limits. The modeling of the swirling flow by a simple Doppler shift is probably simplistic and reduces the confidence on the downstream noise levels caused by fan sources and on the upstream noise levels caused by OGV sources. This is likely not important for the fan sources because the downstream noise is found to be dominated by the OGV sources. However, the upstream noise radiated by the OGV is greater at cutback than the noise coming from fan sources. This is not in agreement with the results coming from the direct analysis. The simple modeling of the swirling flow is probably one of the reasons that explain these differences. In addition, the rotor shielding effect was not ac-

counted for in this hybrid approach and has probably an important influence on the usptream noise coming from the OGV. Finally, the limits of Rienstra's theory for the propagation of fan sources at supersonic tip speeds were shown with levels that were largely overestimated (by more than 15 dB).

The direct analysis of the downstream results required a preliminary filtering of the hydrodynamic fluctuations. Two types of filtering were compared: one based on a local identification of the convective pertubations and the other based on a modal decomposition. The filtering based on the local identification of the convective pertubations depends too much on the tolerance that is chosen arbitrarily which makes its application difficult. However, the modal decomposition technique allows for an objective choice of the tolerance based on the theoretical axial wavenumbers of the acousic mode and the vorticity fluctuations. It is shown to work correctly and gives pressure and velocity fields that are consistent with the equations of acoustics. This filtering has therefore been applied for the prediction of the downstream noise level on all configurations.

The downstream noise penalties induced by inlet distortion that are predicted from both the direct and the hybrid approach are in relatively good agreement even if differences in the absolute levels are found at cutback and sideline. Important modal scattering has also been evidenced in the outlet duct and can be explained by the presence of the pylon, the distorted flow or the axial variation of the geometry and the flow.

Future work

The different results shown in the manuscript have been obtained using data extracted from the simulations. It seems esssential to validate those numerical simulations by comparison with experiments.

Concerning the influence of distortion on the noise radiated by the fan, the problematic of shock noise should be studied more precisely. The shocks were shown to be largely influenced by the inlet distortion but the impact on the related noise has not been done because its separation from the noise caused by other sources is not straightforward. Because of this modification of the shocks, the inlet distortion might ease the emergence of Buzz-Saw Noise when the fan blades are not perfectly staggered. In addition, this study was limited to the prediction of fan tonal noise but it should also be interesting to look at the effects on the broadband noise. The impact of distortion on the fan-blade wakes was significant and a modification of turbulent gusts inside the wakes might be expected.

This PhD thesis has shown how the different elements of a turbofan engine can interact. The most illustrative evidence is the effect of the inlet distortion on the fan-blade wakes and, consequently, on the noise caused by the OGV sources. It seems necessary to stop thinking by module and to consider more integrated configurations. In this perspective, it is important to extend the study by accounting for

a real inlet geometry including the nacelle (and eventually the wing). The far-field noise might be different from the in-duct noise because of the reflections at the inlet.

The use of analytical methods permits the study of the noise mechanisms independently and eases the analysis of the results given by the direct approach. The effects of the distortion on the generation of the sources of fan tonal noise was largely discussed but the analysis of the effects on the propagation was limited because of the limitations of the models that have been used. These effects were naturally included in the direct noise estimations but they could not be isolated easily from other effects (the generation of the sources also changed). The use of methods that predict with more fidelity the in-duct propagation (by accounting for the shear flow, the swirling flow, the distortion, the asymmetry of the duct and the C-duct geometry downstream of the OGV) is therefore encouraged. Those more complex theories should reduce the gap between the noise levels predicted with the direct and the hybrid approaches and can also explain the modal scattering that has been observed in the outlet duct.

Conclusions et perspectives

Rappel des objectifs

Ce travail de thèse porte sur l'étude du bruit tonal généré par le module de soufflante d'un turboréacteur moderne. Ce bruit est généralement supposé être dominé par l'interaction des sillages des pales de la soufflante avec les OGVs en régime subsonique. Le bruit propre de la soufflante (bruit de charge stationnaire et bruit de choc) devient également important en regime transsonique. Le bruit généré par l'interaction de la distorsion avec les pales de la soufflante est généralement négligé. Cependant, cette distorsion est amenée à augmenter dans les moteurs UHBR et cet équilibre des sources pourrait être modifié. L'objectif de cette thèse est d'évaluer l'impact de cette importante distorsion sur le bruit tonal généré par le module de soufflante.

L'étude est basée sur des simulations URANS de l'ensemble entrée d'air, soufflante, IGVs et OGVs réalisées sur 360 degrés. L'OGV est hétérogène et comprend le pylône, comme dans les architectures modernes de turboréacteur. Deux entrées d'air sont considérées (une axisymétrique et l'autre non) de manière à isoler les effets de la distorsion d'entrée d'air, qui est la source dominante de distorsion au niveau de la soufflante. Les trois points de certification acoustique (approche, survol et décollage) correspondant à trois régimes différents sont étudiés.

Conclusions d'un point de vue physique

La distorsion a été caractérisée et quantifiée. Quand l'entrée d'air est axisymétrique, la distorsion est causée uniquement par l'effet potentiel du pylône et des bras supports. L'effet potentiel des aubes classiques est négligeable. En amont, la forme initiale de la distorsion composée de quatre lobes change et n'est constituée plus que d'un seul lobe principal. Ce lobe est dû à la partie supérieure du pylône (la plus large) qui est responsable d'un ralentissement de l'écoulement. En traversant la soufflante, le lobe est dévié par la rotation des pales par un angle qui varie linéairement avec le régime. La distorsion causée par le pylône augmente avec le régime entre la soufflante et les OGVs et atteint des valeurs maximales proche du carter.

L'asymétrie de l'entrée d'air crée une distorsion supplémentaire au niveau de la

soufflante qui est caractérisée par une région à basse vitesse dans la partie supérieure et une région à haute vitesse dans la partie inférieure. L'hétérogénéité de l'écoulement au niveau de la soufflante est alors augmentée, en particulier proche du carter où le coefficient de distorsion est multiplié par un facteur allant de 4 à 6 en fonction du régime. En aval de la soufflante, l'effet est également significatif, avec une augmentation des trois premières harmoniques de la distorsion qui peuvent être multipliées par un facteur supérieur à 2.

L'impact de la distorsion sur l'écoulement instationnaire a aussi été décrit. La distorsion liée à l'effet potentiel du pylône est à l'origine de niveaux importants de la charge instationnaire s'exerçant sur les pales de la soufflante à la RF. L'amplitude de cette charge instationnaire est multipliée par plus de 2 avec la distorsion d'entrée d'air. La modification des sillages des pales de la soufflante a également été mise en évidence avec l'inhomogénéité azimutale du déficit de vitesse. La distorsion d'entrée d'air augmente cette inhomogénéité. La charge instationnaire exercée sur l'OGV à la BPF varie donc d'une aube à l'autre et les différences sont d'autant plus importantes avec la distorsion d'entrée d'air. A l'approche, la charge peut varier d'un facteur 2 d'une aube à l'autre quand l'entrée d'air est axisymétrique. Quand la distorsion d'entrée d'air est ajoutée, ce facteur passe à 3. Au point de décollage, des chocs se développent en tête des pales du fait de l'écoulement localement transsonique et se propagent en amont. Ces chocs sont quasiment fixes quand l'entrée d'air est axisymétrique mais leur position varie sur 10% de la corde et leur amplitude varie de 45% dans le cas de l'entrée d'air asymétrique.

Les conséquences en termes d'émission de bruit ont également été montrées. Le bruit émis en aval est effectivement dominé par les sources sur les OGVs causées par l'interaction avec les sillages des pales de la soufflante (niveaux prédits avec la théorie de Rienstra supérieurs de 10 dB environ). Cela est essentiellement dû à la rotation de l'écoulement entre la soufflante et l'OGV qui est responsable d'une coupure prématurée des modes importants liés à la distorsion. La distorsion d'entrée d'air augmente le bruit aval de 1 à 3 dB en fonction du régime à cause de l'augmentation de l'inhomogénéité des sillages. En ce qui concerne le bruit émis en amont, la contribution des sources sur la soufflante a été mise en évidence, au moins aux points de survol et de décollage. La contribution de ces sources à l'approche est moins évidente à établir mais le niveau a été augmenté de 5 dB au total par la distorsion d'entrée d'air (estimation par l'approche directe). Au point de survol, les modes d'interaction distorsion-soufflante dominent le bruit amont et leur niveau peut être augmenté de 10 dB par la distorsion d'entrée d'air. La situation est similaire au point de décollage mais le bruit propre de la soufflante, porté par le mode attaché et non affecté par la distorsion d'entrée d'air à la source, est aussi dominant. Cependant, la propagation dans le conduit asymétrique (qui a une section plus petite) semble se faire plus difficilement que dans le conduit axisymétrique et vient contrebalancer ces augmentations aux points de survol et de décollage. Finalement, la contribution des sources sur les IGVs qui ne sont généralement pas considérées a été évaluée pour la première fois. Ces sources sont effectivement négligeables même si leur niveau a été augmenté de quelques décibels avec la distorsion d'entrée d'air (encore du fait

l'hétérogéité des sillages). Ces conclusions sont résumées dans les Tabs. 4.3 et 4.4 pour le bruit amont et le bruit aval respectivement. Pour chaque point de certification, le ou les mécanismes dominants sont donnés ainsi que l'impact causé par la distorsion d'entrée d'air sur ceux-ci. Deux symbôles apparaissent pour l'interaction de la distorsion avec la soufflante au point de survol et pour le bruit propre de soufflante au point de décollage à cause des effets de propagation mentionnés plus haut. Le premier symbôle désigne alors l'effet de la distorsion d'entrée d'air au niveau de la source alors que le second désigne l'effet de la distorsion d'entrée d'air au niveau du plan d'entrée.

Mécanisme	**Approche**	**Survol**	**Décollage**
Interaction sillages-OGV	↗		
Interaction distorsion-soufflante		↗ / =	↗
Bruit propre de soufflante			= / ↘
Interaction sillages-IGV			

Table 4.3: **Répartition des sources pour le bruit amont : mécanisme dominant, = / ↘ / ↗ évolution avec la distorsion d'entrée d'air (pas d'effet, réduction, augmentation)**

Mécanisme	**Approche**	**Survol**	**Décollage**
Interaction sillages-OGV	↗	↗	↗
Interaction distorsion-soufflante			
Bruit propre de soufflante			
Interaction sillages-IGV			

Table 4.4: **Répartition des sources pour le bruit aval : mécanisme dominant, = / ↘ / ↗ évolution avec la distorsion d'entrée d'air (pas d'effet, réduction, augmentation)**

Conclusions d'un point de vue méthodologique

Le travail réalisé durant cette thèse est basé sur des simulations numériques URANS d'un module de soufflante sur 360 degrés. Les principales conclusions ont été obtenues en comparant les simulations avec et sans distorsion d'entrée d'air qui ont été réalisées avec les mêmes paramètres numériques. Une analyse des performances a été faite pour s'assurer d'un fonctionnement correct du module.

Pour les prévisions acoustiques, plusieurs méthodes avec des dégrés de modélisation différents ont été utilisées. Premièrement, concernant les méthodes hybrides, les limites du modèle d'Amiet pour la prévision de la charge instationnaire sur les pales et les aubes ont été montrées, même si les tendances sont les bonnes. Le recouvrement des pales et des aubes est élevé dans la configuration étudiée et l'effet de

grille est donc important. Les sources extraites du calcul ont alors été directement utilisées pour les prévisions du bruit en conduit. Les effets de la variation axiale de l'écoulement et de la géométrie du conduit ont été soulignés avec des différences de bruit pouvant atteindre plusieurs décibels. L'utilisation de la théorie de Rienstra adaptée aux conduits lentement variables a permis de s'affranchir de ces limites. La modélisation de l'écoulement tournant par un simple décalage en fréquence est probablement simpliste et réduit la précision des résultats de bruit amont causé par les sources OGVs et de bruit aval causé par les sources de la soufflante. Pour le bruit aval, cela n'a probablement que peu d'importance puisqu'il est dominé par les sources OGVs. En revanche, pour le bruit amont, cela peut avoir son importance. Par exemple, le bruit amont rayonné par les sources OGVs est estimé supérieur à celui rayonné par les sources de la soufflante au point de survol. Or, les résultats issus de l'approche directe montrent le contraire. Le masquage par le fan a de plus été négligé bien qu'il ait probablement un impact important sur le bruit amont rayonné par les sources OGVs. Finalement, les limites de la théorie de Rienstra pour la propagation des sources de la soufflante aux régimes transsoniques a été mise en évidence avec des niveaux largement surrestimés (de plus de 15 dB).

L'analyse directe des résultats du bruit à l'aval a nécessité une étape de filtrage des fluctuations hydrodynamiques. Deux types de filtrage ont été testés : l'un basé sur l'identification locale des perturbations convectées avec l'écoulement et l'autre basé sur une décomposition modale. Le filtrage basé sur l'identification locale des perturbations convectées avec l'écoulement est fortement dépendant de la tolérance choisie (arbitrairement) et rend son application difficile. En revanche, la technique de décomposition modale permet un choix objectif de la tolérance basé sur les nombres d'onde axiaux théoriques des modes acoustiques et des perturbations de vorticité. Ce filtrage montre des résultats satisfaisants and donne des champs de pression et de vitesse qui sont consistents avec les équations de l'acoustique. Ce filtrage a donc été appliqué à toutes les configurations pour la prévision du bruit aval.

Les pénalités de bruit causées par la distorsion d'entrée d'air en aval issues des méthodes directe et hybride sont en bon accord, même si des différences en termes de niveaux absolus sont observées aux points de survol et de décollage. La dispersion des modes a été mise en évidence dans le conduit à l'aval et peut être expliquée par la présence du pylône, la distorsion ou alors la variation axiale de la géométrie et de l'écoulement.

Perspectives

Les différents résultats montrés dans le manuscrit ont été obtenus à partir des données extraites des simulations. Il paraît essentiel de valider ces simulations en les comparant à des résultats d'essais.

Pour ce qui est de l'influence de la distorsion sur le bruit rayonné par la soufflante, la problématique du bruit de choc devrait être étudiée plus en détail. Il a été observé une importante modification des chocs par la distorsion d'entrée d'air

mais l'impact sur le bruit généré n'a pas pu être quantifié puisqu'il est difficilement dissociable des autres sources de bruit. La modification des chocs pourrait faciliter l'émergence des FMR quand des petites différences de fabrication et d'installation des pales existent. De plus, l'étude a été limitée à la prévision du bruit tonal mais il serait également intéressant de quantifier les effets de la distorsion sur le bruit à large bande. Les sillages sont fortement impactés par la distorsion d'entrée d'air et il ne serait pas surprenant que les tourbillons le composant le soient également.

Ce travail de thèse a de plus montré comment les différents éléments d'un turboréacteur pouvaient interagir. L'exemple le plus marquant est l'effet de la distorsion d'entrée d'air sur les sillages, et donc sur les sources OGVs. Il semble nécessaire de ne plus séparer les différents modules et de considérer des configurations de plus en plus intégrées. Dans cette optique, il paraît essentiel d'étendre l'étude en prenant en compte la géométrie réelle de l'entrée d'air avec la nacelle (et éventuellement l'aile). Le bruit rayonné en champ lointain pourrait être différent de celui en conduit à cause des réflexions au niveau de l'entrée d'air.

Finalement, l'utilisation des méthodes analytiques a permis d'étudier les différents mécanismes indépendamment les uns des autres et a facilité l'analyse des résultats obtenus par la méthode directe. Les effets de la distorsion sur la génération des sources du bruit tonal ont été largement discutés mais l'analyse de ces effets sur la propagation a été limitée du fait des hypothèses faites dans les modèles utilisés. Ces effets sont naturellement inclus dans les previsions directes du bruit mais ils ne peuvent pas être dissociés des autres effets (puisque la génération des sources est également modifiée). L'utilisation de méthodes qui prédisent la propagation en conduit avec plus de fidélité (en prenant en compte le cisaillement de l'écoulement, la rotation de l'écoulement, la distorsion, l'asymétrie du conduit et la forme en C du conduit en aval de l'OGV) est donc encouragée. Ces théories plus complexes devraient permettre de réduire l'écart entre les niveaux de bruit prédits avec les approches directe et hybride et pourraient aussi expliquer la dispersion des modes observée dans le conduit de sortie.

Appendix A

Add-ons for the numerical simulations

Additional informations on the theoretical aspects of the numerical simulations (introduced in Sec. 1.4.1) are given in this appendix.

A.1 URANS formalism

RANS methods have initially been introduced for the simulation of incompressible stationary flows. They are based on a statistical approach of the turbulence where each instantaneous flow variable $f(t)$ (where t represents the time) is decomposed into a mean part $\langle f \rangle$ and a fluctuating part $f'(t)$

$$f(t) = \langle f \rangle + f'(t). \tag{A.1}$$

The mean part is defined as a statistical average (Reynolds averaging) over N independent realizations

$$\langle f \rangle = \lim_{N \to \infty} \left(\frac{1}{N} \sum_{i=1}^{N} f_i \right), \tag{A.2}$$

and the fluctuations are such that $\langle f' \rangle = 0$. Ergodicity principle allows replacing the statistical average by a temporal average over a period T (longer than the turbulent characteristic time)

$$\langle f \rangle = \lim_{T \to \infty} \left(\frac{1}{T} \int_0^T f(\tau)\, d\tau \right). \tag{A.3}$$

In URANS incompressible simulations, the same principle is applied at different time steps

$$\langle f \rangle (t) = \lim_{T \to \infty} \left(\frac{1}{T} \int_{t-T}^{t} f(\tau)\, d\tau \right). \tag{A.4}$$

The period T must be appropiately chosen to be long enough to average the turbulent fluctuations but short enough to keep the unsteady features of the flow.

When the Reynolds averaging is applied to the compressible Navier-Stokes equations, the equations become much more complex. To simplify them, Favre averaging is introduced [117]

$$f = \overline{f} + f'', \tag{A.5}$$

with

$$\overline{f} = \frac{\langle \rho f \rangle}{\langle \rho \rangle}. \tag{A.6}$$

Applying the Reynolds averaging to the system of equations (1.1) and using the definition of Favre averaging yields the URANS equations

$$\frac{\partial \langle \rho \rangle}{\partial t} + \boldsymbol{\nabla} \cdot (\langle \rho \rangle \overline{\boldsymbol{v}}) = 0, \tag{A.7a}$$

$$\frac{\partial (\langle \rho \rangle \overline{\boldsymbol{v}})}{\partial t} + \boldsymbol{\nabla} \cdot (\langle \rho \rangle \overline{\boldsymbol{v}} \otimes \overline{\boldsymbol{v}} + \langle p \rangle \boldsymbol{I} - \langle \boldsymbol{\tau} \rangle - \boldsymbol{\tau_r}) = \langle \rho \rangle \overline{\boldsymbol{f}}, \tag{A.7b}$$

$$\frac{\partial \left[\langle \rho \rangle \left(\overline{E} + k\right)\right]}{\partial t} + \boldsymbol{\nabla} \cdot \left[\langle \rho \rangle \left(\overline{E} + k\right) \overline{\boldsymbol{v}} + \langle p \rangle \overline{\boldsymbol{v}} - (\langle \boldsymbol{\tau} \rangle + \boldsymbol{\tau_r}) \cdot \overline{\boldsymbol{v}} + \langle \boldsymbol{q} \rangle + \boldsymbol{q_t}\right] = \langle \rho \rangle \overline{\boldsymbol{f}} \cdot \overline{\boldsymbol{v}}. \tag{A.7c}$$

From now, the averaging operators $\langle . \rangle$ and $\overline{.}$ are not written anymore for clarity but it should be kept in mind that ρ, p, $\boldsymbol{\tau}$ and $\boldsymbol{q}$ are Reynolds-averaged and $\boldsymbol{v}$, $\boldsymbol{f}$ and E are Favre-averaged. Without the averaging operators, the URANS equations become

$$\frac{\partial \rho}{\partial t} + \boldsymbol{\nabla} \cdot (\rho \boldsymbol{v}) = 0, \tag{A.8a}$$

$$\frac{\partial (\rho \boldsymbol{v})}{\partial t} + \boldsymbol{\nabla} \cdot (\rho \boldsymbol{v} \otimes \boldsymbol{v} + p \boldsymbol{I} - \boldsymbol{\tau} - \boldsymbol{\tau_r}) = \rho \boldsymbol{f}, \tag{A.8b}$$

$$\frac{\partial \left[\rho \left(E + k\right)\right]}{\partial t} + \boldsymbol{\nabla} \cdot \left[\rho \left(E + k\right) \boldsymbol{v} + p \boldsymbol{v} - (\boldsymbol{\tau} + \boldsymbol{\tau_r}) \cdot \boldsymbol{v} + \boldsymbol{q} + \boldsymbol{q_t}\right] = \rho \boldsymbol{f} \cdot \boldsymbol{v}. \tag{A.8c}$$

This averaging procedure has led to an open problem with the appearance of additional terms coming from the non-linearity of momentum and energy conservation equations [118]:

- the so-called Reynolds stress tensor $\boldsymbol{\tau_r} = -\langle \rho \boldsymbol{v''} \otimes \boldsymbol{v''} \rangle$;
- the turbulence kinetic energy $k = \frac{1}{2} \left\langle \rho \left| \boldsymbol{v''} \right|^2 \right\rangle / \langle \rho \rangle$;
- and the turbulence enthalpy diffusion flux $\boldsymbol{q_t} = \langle \rho \boldsymbol{v''} h'' \rangle$ (where h is the enthalpy: $h = e + p/\rho$).

In order to close the problem and allow its resolution, these terms must be modeled.

A.2 Turbulence modeling

The Boussinesq hypothesis

The classical approach consists in considering the turbulence as a dissipative process. Boussinesq introduced in 1897 the concept of turbulent dynamic viscosity μ_t [119] which links the Reynolds stress tensor $\boldsymbol{\tau_r}$ to the strain rate tensor $\boldsymbol{D}$

$$\boldsymbol{\tau_r} = -\frac{2}{3}\left(\rho k + \mu_t \boldsymbol{\nabla}\cdot\boldsymbol{v}\right)\boldsymbol{I} + 2\mu_t \boldsymbol{D}, \tag{A.9}$$

where $\boldsymbol{D}$ is written

$$\boldsymbol{D} = \frac{1}{2}\left[\boldsymbol{\nabla v} + (\boldsymbol{\nabla v})^T\right]. \tag{A.10}$$

By analogy with the mean heat flux $\boldsymbol{q}$, the turbulence enthalpy diffusion flux is classically assumed to be proportionnal to the temperature gradient

$$\boldsymbol{q_t} = -K_{T_t}\boldsymbol{\nabla} T. \tag{A.11}$$

K_{T_t} is the turbulent thermal conductivity and is given by

$$K_{T_t} = \frac{C_p \mu_t}{Pr_t}, \tag{A.12}$$

with Pr_t the turbulent Prandtl number which is often assumed to be constant (Pr_t = 0.90) [118].

Therefore, the modeling of turbulence is reduced to the evaluation of the turbulence kinetic energy k and the turbulent dynamic viscosity μ_t. A lot of turbulence models exist and differ by their application. Most of them are described by one transport equation (Spalart-Allmaras model for example [120]) or two transports equations (k-ε [121] or k-ω_t models [103] for example). More complex models that solve equation transport for each component of the Reynolds stress tensor, in addition to one equation for the dissipation of the turbulence, also exist. They are referred to as Reynolds Stress Models (RSM) [122].

Wilcox's k-ω_t two equation model

The k-ω_t turbulence model published by Wilcox in 1988 is developed here [103]. This model is suited for configurations with walls and is therefore relevant in turbomachinery applications. The turbulence kinetic energy k and the specific rate of dissipation of turbulence ω_t satisfy the following equations

$$\frac{\partial(\rho k)}{\partial t} + \boldsymbol{\nabla}\cdot\left[\rho k\boldsymbol{v} - (\mu + \sigma^*\mu_t)\boldsymbol{\nabla} k\right] = P_k - \beta^*\rho k\omega_t, \tag{A.13a}$$

$$\frac{\partial(\rho\omega_t)}{\partial t} + \boldsymbol{\nabla}\cdot\left[\rho\omega_t\boldsymbol{v} - (\mu + \sigma\mu_t)\boldsymbol{\nabla}\omega_t\right] = \frac{\gamma}{\nu_t}P_k - \beta\rho\omega_t^2. \tag{A.13b}$$

Eq. (A.13a) describes the transport of the turbulence kinetic energy k and Eq. (A.13b) the one of the specific rate of dissipation ω_t. The turbulent dynamic viscosity is expressed as

$$\mu_t = \frac{\rho k}{\omega_t}. \tag{A.14}$$

$\nu_t = \mu_t/\rho$ is the turbulent kinematic viscosity and P_k is the production term and is given by

$$P_k = \boldsymbol{\tau_r} : \boldsymbol{\nabla v}. \tag{A.15}$$

σ, σ^*, β, β^* and γ are model constants:

$$\sigma^* = \sigma = 0.5, \quad \beta^* = 0.09, \quad \beta = 0.075,$$
$$\gamma = \frac{\beta}{\beta^*} - \sigma\frac{K^2}{\sqrt{\beta^*}} \approx 0.5532 \quad \text{with} \quad K = 0.41. \tag{A.16}$$

Solving equations (A.13) gives access to the turbulence kinetic energy k and the turbulent dynamic viscosity μ and close the URANS equations (A.8).

Zheng's limiter

One of the issues in Wilcox k-ω_t turbulence model is the dependence of the determined turbulent quantities on the values imposed at the boundaries. To alleviate this dependency, Zheng *et al.* proposed to introduce one more parameter in the original model [104].

If the Reynolds stress tensor component are written τ_{ij}^r, Zheng *et al.* showed that the relation

$$\sqrt{\sum_{ij}\left(\tau_{ij}^r\right)^2} \leq 2\rho k, \tag{A.17}$$

was satisfied. Using Boussinesq assumption (A.9) and the relation (A.14) yields

$$\omega_t \geq \frac{\sqrt{3}}{2}\sqrt{P_d}, \tag{A.18}$$

with

$$P_d = 2\boldsymbol{D} : \boldsymbol{\nabla v}. \tag{A.19}$$

This lower bound of ω_t is included in the turbulence model so that

$$\omega_t = \max(\omega_{t0}, \frac{\sqrt{3}}{2}\sqrt{P_d}), \tag{A.20}$$

where ω_{t0} is the value obtained from Wilcox original k-ω_t model.

A.3 Discretization of the equations

The URANS equations (A.8), closed with the turbulence model (A.13), cannot be solved analytically and a discretization in space and time must be done. Three kinds of methods, listed below, exist for the spatial discretization [57].

- Finite differences: the flow variables are stored at each node of the mesh. The derivatives at each point is obtained through Taylor series expansions [123].
- Finite volumes: the flow variables are averaged over each cell of the mesh. Green's theorem is applied to the integral form of the equations to get integrals over the surface of the cells. The fluxes across the surfaces of each cell are computed and transferred to the adjacent cells. This method is conservative by definition [124].
- Finite elements: approximate solutions are searched among a family of arbitrary fields (polynomial usually) on each element. Galerkin method is the most common method in finite elements [125].

Finite volume approach

The CFD software that will be used in this study is based on a finite volume approach. Some details of this approach are given here. The URANS equations (A.8) integrated over a control volume Ω of boundaries $\partial\Omega$ and unitary normal vector $\boldsymbol{n}$ can be shown to reduce to, after application of Green's theorem,

$$\frac{\partial}{\partial t}\iiint_{\Omega} \boldsymbol{W}\, d\Omega + \iint_{\partial\Omega} \left[\boldsymbol{F_c}(\boldsymbol{W}) + \boldsymbol{F_d}(\boldsymbol{W})\right]\cdot \boldsymbol{n}\, d\Sigma = \iiint_{\Omega} \boldsymbol{T}(\boldsymbol{W})\, d\Omega, \tag{A.21}$$

where $\boldsymbol{W}$ is the vector of conservative variables

$$\boldsymbol{W} = \begin{bmatrix} \rho \\ \rho\boldsymbol{v} \\ \rho(E+k) \end{bmatrix}, \tag{A.22}$$

$\boldsymbol{F_c}(\boldsymbol{W})$ is the convective flux

$$\boldsymbol{F_c}(\boldsymbol{W}) = \begin{bmatrix} \rho\boldsymbol{v} \\ \rho\boldsymbol{v}\otimes\boldsymbol{v} + p\boldsymbol{I} \\ \rho\left(E+k\right)\boldsymbol{v} + p\boldsymbol{v} \end{bmatrix}, \tag{A.23}$$

$\boldsymbol{F_d}(\boldsymbol{W})$ is the diffusive flux

$$\boldsymbol{F_d}(\boldsymbol{W}) = \begin{bmatrix} 0 \\ -\boldsymbol{\tau} - \boldsymbol{\tau_r} \\ -\left(\boldsymbol{\tau}+\boldsymbol{\tau_r}\right)\cdot\boldsymbol{v} + \boldsymbol{q} + \boldsymbol{q_t} \end{bmatrix}, \tag{A.24}$$

and $\boldsymbol{T}(\boldsymbol{W})$ is the complementary term caused by the body force $\boldsymbol{f}$

$$\boldsymbol{T}(\boldsymbol{W}) = \begin{bmatrix} 0 \\ \rho \boldsymbol{f} \\ \rho \boldsymbol{f} \cdot \boldsymbol{v} \end{bmatrix}. \tag{A.25}$$

Equation (A.21) can be solved on a structured or unstructured mesh. The resolution of the equations depends on the type of mesh and a CFD solver is generally adapted to one type only. A structured mesh is characterized by a regular connectivity of the cells. In three dimensions, it is generally composed of hexahedra. Structured meshes are very useful because the data can be stored in arrays and can be accessed very easily thanks to an indexing (usually (i, j, k) in 3D). It is very efficient when there is a preferential direction, such as in the boundary layers. Meshing a whole domain is often impossible using only one block. This is why structured meshes are almost always composed of several coincident blocks (multi-block structured mesh). On the contrary, unstructured meshes have an irregular connectivity and can be composed of any type of elements. Using an unstructured mesh significantly ease the meshing procedure of complex geometries. However, they require more memory since the connectivities must be stored (absence of direct indexing). To take profit of each technique, hybrid meshes composed of both a structured part and an unstructured one also exist. Only structured meshes will be used in this study. The following equations are written in this structured mesh framework.

Each hexahedral cell of the mesh Ω is characterized by its volume

$$V(\Omega) = \iiint d\Omega, \tag{A.26}$$

and its surface

$$\partial\Omega = \sum_{i=1}^{6} \Sigma_i(\Omega), \tag{A.27}$$

where $\Sigma_i(\Omega)$ is the i^{th} face of the cell. Eq. (A.21) can therefore be approximated by

$$V(\Omega)\frac{\partial \boldsymbol{W}_{\boldsymbol{\Omega}}}{\partial t} = -\sum_{i=1}^{6} \boldsymbol{F}(\mathcal{E}_i(\Omega)) \cdot \boldsymbol{N}_{\boldsymbol{\Sigma_i}}(\Omega) - V(\Omega)\boldsymbol{T}(\boldsymbol{W}_{\boldsymbol{\Omega}}) = -\boldsymbol{R}_{\boldsymbol{\Omega}}. \tag{A.28}$$

$\boldsymbol{W}_{\boldsymbol{\Omega}}$ is the numerical approximation of the average value of $\boldsymbol{W}$ in the cell Ω. $\boldsymbol{F}(\mathcal{E}_i(\Omega))$ is the numerical flux (convective + diffusive fluxes) across the face $\Sigma_i(\Omega)$ of cell Ω. This flux is computed from the values of $\boldsymbol{W}$ at different cells depending on the spatial scheme used. The set of cells that are needed is written $\mathcal{E}_i(\Omega)$. $\boldsymbol{N}_{\boldsymbol{\Sigma_i}}(\Omega)$ is the outside normal vector of the face, defined as

$$\boldsymbol{N}_{\boldsymbol{\Sigma_i}}(\Omega) = \iint_{\Sigma_i(\Omega)} \boldsymbol{n} d\Sigma. \tag{A.29}$$

$\boldsymbol{T}(\boldsymbol{W}_{\boldsymbol{\Omega}})$ is the numerical approximation of the average value of $\boldsymbol{T}(\boldsymbol{W})$ in the cell Ω and $\boldsymbol{R}_{\boldsymbol{\Omega}}$ is defined as the numerical residue.

The semi-discrete formulation (A.28) is interesting because the spatial discretization is totally defined by the flux balance across the surfaces of the cells so that the temporal discretization can be chosen independently. The latter consists of solving a simple ordinary differential equation and only the spatial discretization is detailed below.

Spatial schemes

The purpose of spatial schemes is to evaluate the flux $\boldsymbol{F}(\mathcal{E}_i(\Omega))$. This flux is the sum of the convective flux $\boldsymbol{F_c}(\mathcal{E}_i(\Omega))$ and the diffusive flux $\boldsymbol{F_d}(\mathcal{E}_i(\Omega))$ that are often solved separately.

Convective fluxes

Jameson's scheme

The most natural way to compute the convective flux is to use a second-order central scheme. In that case, Ω_i denotes the neighbour cell of cell Ω that is adjacent to the face $\Sigma_i(\Omega)$ and the flux $\boldsymbol{F_c}(\mathcal{E}_i(\Omega))$ is written as $\boldsymbol{F_c^{cent}}(\boldsymbol{W_\Omega}, \boldsymbol{W_{\Omega_i}})$. This flux can be evaluated by:

- averaging the conservative variables at the interface and determining the associated flux

$$\boldsymbol{F_c^{cent}}(\boldsymbol{W_\Omega}, \boldsymbol{W_{\Omega_i}}) \cdot \boldsymbol{N_{\Sigma_i}}(\Omega) = \boldsymbol{F_c}\left(\frac{1}{2}\left[\boldsymbol{W_\Omega} + \boldsymbol{W_{\Omega_i}}\right]\right) \cdot \boldsymbol{N_{\Sigma_i}}(\Omega); \tag{A.30}$$

- averaging the fluxes at the interface

$$\boldsymbol{F_c^{cent}}(\boldsymbol{W_\Omega}, \boldsymbol{W_{\Omega_i}}) \cdot \boldsymbol{N_{\Sigma_i}}(\Omega) = \frac{1}{2}\left[\boldsymbol{F_c}(\boldsymbol{W_\Omega}) + \boldsymbol{F_c}(\boldsymbol{W_{\Omega_i}})\right] \cdot \boldsymbol{N_{\Sigma_i}}(\Omega). \tag{A.31}$$

To make the scheme stable, artificial dissipation $\boldsymbol{D_{\Sigma_i}}(\boldsymbol{W_\Omega}, \boldsymbol{W_{\Omega_i}})$ is added as proposed by Jameson [126] and the flux becomes

$$\boldsymbol{F_c^{Jam}}(\boldsymbol{W_\Omega}, \boldsymbol{W_{\Omega_i}}) \cdot \boldsymbol{N_{\Sigma_i}}(\Omega) = \boldsymbol{F_c^{cent}}(\boldsymbol{W_\Omega}, \boldsymbol{W_{\Omega_i}}) \cdot \boldsymbol{N_{\Sigma_i}}(\Omega) - \boldsymbol{D_{\Sigma_i}}(\boldsymbol{W_\Omega}, \boldsymbol{W_{\Omega_i}}). \tag{A.32}$$

Roe's scheme

Upwind schemes can also be used to compute the convective flux. Using an upwind scheme has the advantage of having very low dispersion errors. However, an upwind scheme is dissipative and a special attention must be put on the size of mesh cells to control the overall dissipation. Roe's scheme will be used in this study and is detailed here [127]. Roe's scheme gives an expression of the flux at the face $\Sigma_i(\Omega)$ as a function of the states at cells Ω and Ω_i. The flux is written $\boldsymbol{F_c^{Roe}}(\boldsymbol{W_\Omega}, \boldsymbol{W_{\Omega_i}})$ and is expressed as

$$\boldsymbol{F_c^{Roe}}(\boldsymbol{W_\Omega}, \boldsymbol{W_{\Omega_i}}) = \frac{\boldsymbol{F_c}(\boldsymbol{W_\Omega}) + \boldsymbol{F_c}(\boldsymbol{W_{\Omega_i}})}{2} - \frac{1}{2}\left|\boldsymbol{A}\right|\left(\boldsymbol{W_{\Omega_i}} - \boldsymbol{W_\Omega}\right), \tag{A.33}$$

where $\boldsymbol{A}$ is the Jacobian of the flux computed with Roe's state $\tilde{\boldsymbol{W}}$. This state is defined by

$$\tilde{\rho} = \sqrt{\rho_\Omega \rho_{\Omega_i}}, \tag{A.34a}$$

$$\tilde{\boldsymbol{v}} = \frac{\sqrt{\rho_\Omega}\boldsymbol{v_\Omega} + \sqrt{\rho_{\Omega_i}}\boldsymbol{v_{\Omega_i}}}{\sqrt{\rho_\Omega} + \sqrt{\rho_{\Omega_i}}}, \tag{A.34b}$$

$$\tilde{H} = \frac{\sqrt{\rho_\Omega} H_\Omega + \sqrt{\rho_{\Omega_i}} H_{\Omega_i}}{\sqrt{\rho_\Omega} + \sqrt{\rho_{\Omega_i}}}, \tag{A.34c}$$

with $H = e + p/\rho + v^2/2$ the total enthalpy. The Jacobian matrix can be diagonalized

$$\boldsymbol{A} = \boldsymbol{M_A} \boldsymbol{\lambda_A} \boldsymbol{M_A}^{-1}, \tag{A.35}$$

where $\boldsymbol{M_A}$ and $\boldsymbol{\lambda_A}$ represent the eigenvector and eigenvalue matrices respectively.

Harten's entropy correction

Roe's scheme admits discontinuities into its calculation since a Riemann problem is solved to calculate the flux at the faces between cells. In real flows, compression shocks can occur and are discontinuous, contrary to expansion waves that change the flow in an isentropic way. Using Roe's scheme in its classical form detailed above will give non-physical shocks for expansion processes and they sould be eliminated from the method. This is classically done by employing Harten's entropy correction [128]. This correction consists in modifying the eigenvalues λ_{A_i} of the matrix $\boldsymbol{\lambda_A}$ by applying them a function ψ

$$\psi(\lambda_{A_i}) = \begin{cases} |\lambda_{A_i}| & \text{if } |\lambda_{A_i}| \geq \sigma \\ \left(\lambda_{A_i}^2 + \sigma^2\right) / (2\sigma) & \text{otherwise} \end{cases}. \tag{A.36}$$

This correction has the effect of smoothing out expansion shocks, which occur near sonic points, because one of the eigenvalues tends to zero at these points. σ is the parameter of the entropy correction and has to be adjusted depending on the configuration.

Extension to higher order of accuracy

This flux is first-order accurate but higher order of accuracy can be reached using the MUSCL method of van Leer [129]. This method consists in replacing the states $\boldsymbol{W_\Omega}$ and $\boldsymbol{W_{\Omega_i}}$ by the reconstructing states on the left side of the interface $\boldsymbol{W^L_{\Sigma_i(\Omega)}}$ and on its right side $\boldsymbol{W^R_{\Sigma_i(\Omega)}}$. A lot of different possibilities exist for the reconstruction of the states $\boldsymbol{W^L_{\Sigma_i(\Omega)}}$ and $\boldsymbol{W^R_{\Sigma_i(\Omega)}}$. These states can also be written with the indices (i, j, k) for a structured mesh. To make the following explanations clearer, j and k are fixed and only i is varying. The interface between cells (i, j, k) and $(i+1, j, k)$ is considered. The left state is therefore written $\boldsymbol{W^L_{(i+\frac{1}{2},j,k)}}$ and the right one $\boldsymbol{W^R_{(i+\frac{1}{2},j,k)}}$. Van Leer

proposed the following reconstruction for the left and right states

$$\boldsymbol{W}^{\boldsymbol{L}}_{(i+\frac{1}{2},j,k)} = \boldsymbol{W}_{(i,j,k)} + \frac{1+\kappa}{4}\left(\boldsymbol{W}_{(i+1,j,k)} - \boldsymbol{W}_{(i,j,k)}\right) + \frac{1-\kappa}{4}\left(\boldsymbol{W}_{(i,j,k)} - \boldsymbol{W}_{(i-1,j,k)}\right), \tag{A.37a}$$

$$\boldsymbol{W}^{\boldsymbol{R}}_{(i+\frac{1}{2},j,k)} = \boldsymbol{W}_{(i,j,k)} - \frac{1+\kappa}{4}\left(\boldsymbol{W}_{(i+2,j,k)} - \boldsymbol{W}_{(i+1,j,k)}\right) - \frac{1-\kappa}{4}\left(\boldsymbol{W}_{(i+1,j,k)} - \boldsymbol{W}_{(i,j,k)}\right). \tag{A.37b}$$

For $\kappa = -1$, the second-order accurate, one-sided upwind scheme is obtained, and for $\kappa = 1$, the standard second-accurate central scheme. By choosing $\kappa = 1/3$, Koren [130] showed that the maximum precision is reached and the scheme becomes third-order accurate.

Diffusive fluxes

The diffusive flux is computed in two steps since $\boldsymbol{F_d}(\mathcal{E}_i(\Omega))$ is expressed thanks to gradients of velocity and temperature. The first step is the computation of the gradients present in $\boldsymbol{F_d}(\mathcal{E}_i(\Omega))$ and the second step is the discretization of the flux istelf.

The method detailed here is based on an evaluation of the gradients in the cells Ω and Ω_i (neighbour cell of cell Ω that is adjacent to the face $\Sigma_i(\Omega)$). These gradients are evaluated thanks to Green's theorem. For a variable f, it is written

$$(\boldsymbol{\nabla} f)_\Omega = \frac{1}{V(\Omega)} \iiint_\Omega f \, d\Omega = \frac{1}{V(\Omega)} \sum_{i=1}^{6} \iint_{\Sigma_i(\Omega)} f \boldsymbol{n} \, d\Sigma. \tag{A.38}$$

A simple averaging between the values on each side of the faces is made for the discrete evaluation of the gradient

$$(\boldsymbol{\nabla} f)_\Omega = \frac{1}{V(\Omega)} \sum_{i=1}^{6} \frac{1}{2} \left(f_\Omega + f_{\Omega_i}\right) \boldsymbol{N_{\Sigma_i}}(\Omega), \tag{A.39}$$

where f_Ω and f_{Ω_i} are the numerical approximations of the averaged value of f in the cell Ω and Ω_i respectively.

The balance of the diffusion fluxes for cell Ω can now be made. A simple way to compute it is to take the half sum of the flux in the cells Ω and its adjacent cell Ω_i

$$\boldsymbol{F_d}(\boldsymbol{W_\Omega}, \boldsymbol{W_{\Omega_i}}) \cdot \boldsymbol{N_{\Sigma_i}}(\Omega) = \frac{1}{2} \left[\boldsymbol{F_d}(\boldsymbol{W_\Omega}) + \boldsymbol{F_d}(\boldsymbol{W_{\Omega_i}})\right] \cdot \boldsymbol{N_{\Sigma_i}}(\Omega), \tag{A.40}$$

with $\boldsymbol{F_d}(\boldsymbol{W_\Omega})$ and $\boldsymbol{F_d}(\boldsymbol{W_{\Omega_i}})$ evaluated thanks to Eqs. (A.24) with the gradients computed with Eq. (A.39).

Appendix B

Add-ons for Goldstein's analogy

The derivations of the duct modes and the duct Green's function required in Goldstein's analogy (described in Sec. 1.6.1) are given in this appendix.

B.1 Derivation of the duct modes

The resolution of the convected wave equation (1.79) requires a decomposition of the acoustic field into basis functions called duct modes or duct eigenfunctions. These functions will be first derived by solving Eq. (1.79) without the source term. In cylindrical coordinates, it becomes

$$\left[\frac{\partial^2}{\partial t^2} + 2U_0\frac{\partial^2}{\partial t \partial x} + U_0^2\frac{\partial^2}{\partial x^2} - a_0^2\Delta\right]\rho' = 0, \tag{B.1}$$

where the Laplace operator Δ is expressed as

$$\Delta = \frac{1}{r}\frac{\partial}{\partial r}\left(r\frac{\partial}{\partial r}\right) + \frac{1}{r^2}\frac{\partial^2}{\partial \theta^2} + \frac{\partial^2}{\partial x^2}. \tag{B.2}$$

The fluctuating density $\rho'(x, r, \theta, t)$ is expressed in terms of its Fourier components

$$\rho'(x, r, \theta, t) = \int_{-\infty}^{+\infty} \widehat{\rho}(x, r, \theta, \omega)e^{-i\omega t}\, d\omega, \tag{B.3}$$

and Eq. (B.1) can be shown to reduce to the convected Helmholtz equation

$$\left[-k_0^2 - 2iM_0k_0\frac{\partial}{\partial x} + M_0^2\frac{\partial^2}{\partial x^2} - \Delta\right]\widehat{\rho} = 0, \tag{B.4}$$

where the Mach number $M_0 = U_0/a_0$ and the wavenumber $k_0 = \omega/a_0$ have been introduced. The method of separation of variables is used so that the density fluctuations $\widehat{\rho}$ are written

$$\widehat{\rho}(x, r, \theta, \omega) = e(x, \omega)\psi(r, \theta), \tag{B.5}$$

and Eq. (B.4) becomes

$$-\frac{1}{\psi}\Delta_T\psi = \frac{1}{e}\left[\beta_0^2\frac{\partial^2 e}{\partial x^2} + 2iM_0k_0\frac{\partial e}{\partial x} + k_0^2 e\right] = \text{constant} = \alpha^2, \tag{B.6}$$

where Δ_T is the transverse Laplace operator

$$\Delta_T = \frac{1}{r}\frac{\partial}{\partial r}\left(r\frac{\partial}{\partial r}\right) + \frac{1}{r^2}\frac{\partial^2}{\partial\theta^2}. \tag{B.7}$$

The focus is first put on the determination of the transverse function $\psi(r,\theta)$. Since it is 2π-periodic in θ, it can be expressed as a Fourier series

$$\psi(r,\theta) = \sum_{m=-\infty}^{+\infty}\psi_m(r)e^{-im\theta}. \tag{B.8}$$

From Eq. (B.6), it can be shown that the radial part $\psi_m(r)$ must satisfy the relation

$$\frac{d^2\psi_m}{dr^2} + \frac{1}{r}\frac{d\psi_m}{dr} + \left(\alpha^2 - \frac{m^2}{r^2}\right)\psi_m = 0. \tag{B.9}$$

This is known as Bessel equation of order m and its solution is given by

$$\psi_m(r) = A_mJ_m(\alpha r) + B_mY_m(\alpha r), \tag{B.10}$$

where α is still an unknown constant and J_m and Y_m are the Bessel functions of order m of first and second kinds respectively. The possible values for α are given by the boundary conditions which are determined from the rigid wall assumption at hub and tip radii

$$\left.\frac{d\psi_m}{dr}\right|_{R_h,R_t} = 0. \tag{B.11}$$

It can be deduced from the two boundary conditions that the possible values of α respect the relation

$$J'_m(\alpha R_h)Y'_m(\alpha R_t) - J'_m(\alpha R_t)Y'_m(\alpha R_h) = 0. \tag{B.12}$$

The solutions are the so-called duct eigenvalues α_{mn} where n corresponds to the number of zeros of $J_m(\alpha_{mn}r)$ between R_h and R_t. Thus, $\psi(r,\theta)$ can be written

$$\psi(r,\theta) = \sum_{m=-\infty}^{+\infty}\sum_{n=0}^{+\infty}\psi_{mn}(r,\theta), \tag{B.13}$$

where

$$\psi_{mn}(r,\theta) = \left[A_{mn}J_m(\alpha_{mn}r) + B_{mn}Y_m(\alpha_{mn}r)\right]e^{-im\theta}. \tag{B.14}$$

The integers m and n are called the azimuthal and radial mode order respectively.

The functions $\psi_{mn}(r,\theta)$ are often referred to as the rigid duct eigenfunctions and satisfy the orthogonality relation

$$\int_0^{2\pi}\int_{R_h}^{R_t} \psi_{mn}(r,\theta)\overline{\psi_{m'n'}}(r,\theta)\, r dr d\theta = \delta_{mm'}\delta_{nn'}\Gamma_{mn}, \tag{B.15}$$

where Γ_{mn} is the norm of the eigenfunction

$$\Gamma_{mn} = \int_0^{2\pi}\int_{R_h}^{R_t} |\psi_{mn}(r,\theta)|^2\, r dr d\theta. \tag{B.16}$$

The function $e(x)$ will now be determined. From Eq. (B.6) and the fact that α has only discrete values α_{mn}, it results that $e(x)$ will also have discrete values depending on the mode (m, n) and that $\widehat{\rho}(x,r,\theta,\omega)$ can be written in the form

$$\widehat{\rho}(x,r,\theta,\omega) = \sum_{m=-\infty}^{+\infty}\sum_{n=0}^{+\infty} e_{mn}(x,\omega)\psi_{mn}(r,\theta). \tag{B.17}$$

Injecting this expression into the convected Helmholtz equation (B.4), using Eq. (B.9), multiplying by $\psi^*_{mn}(r,\theta)$, integrating over a duct section and using the property of orthogonality of duct modes (B.15) yields

$$\beta_0^2\frac{\partial^2 e_{mn}}{\partial x^2} + 2iM_0k_0\frac{\partial e_{mn}}{\partial x} + (k_0^2-\alpha_{mn}^2)e_{mn} = 0. \tag{B.18}$$

The function e_{mn} is expressed as an inverse Fourier transform

$$e_{mn}(x,\omega) = \int_{-\infty}^{+\infty} \widehat{e_{mn}}(\omega)e^{ik_x x}\, dk_x, \tag{B.19}$$

and Eq. (B.18) reduces to the dispersion relation

$$-\beta_0^2k_x^2 - 2M_0k_0k_x + (k_0^2-\alpha_{mn}^2) = 0. \tag{B.20}$$

It is a quadratic equation of reduced discriminant k_{mn} determined by

$$k_{mn}^2 = k_0^2 - \beta_0^2\alpha_{mn}^2. \tag{B.21}$$

The solutions are written

$$k_x^{\mp} = -\gamma_{mn}^{\pm}, \tag{B.22}$$

where $\gamma_{mn}^{\pm}$ is defined by

$$\gamma_{mn}^{\pm} = \frac{M_0k_0}{\beta_0^2} \pm \frac{k_{mn}}{\beta_0^2}. \tag{B.23}$$

The upper sign and the lower sign denote the wave travelling in the upstream and downstream directions respectively and the cut-off of a mode is observed when k_{mn} is imaginary ($k_{mn}^2 < 0$) and the axial wavenumber $\gamma_{mn}^{\pm}$ becomes complex.

Finally, the density fluctuations are expressed as

$$\rho'^{\pm}(x,r,\theta,t) = \int_{-\infty}^{+\infty}\sum_{m=-\infty}^{+\infty}\sum_{n=0}^{+\infty} \widehat{e_{mn}}(\omega)\psi_{mn}(r,\theta)e^{-i(\gamma_{mn}^{\pm}x+\omega t)}\, d\omega. \tag{B.24}$$

B.2 Derivation of the duct Green's function

The Green's function is determined by solving Eq. (1.81), which becomes in cylindrical coordinates

$$\left[\frac{\partial^2}{\partial t^2} + 2U_0\frac{\partial^2}{\partial t\partial x} + U_0^2\frac{\partial^2}{\partial x^2} - a_0^2\Delta\right] G = \delta(\boldsymbol{x}-\boldsymbol{y})\delta(t-\tau), \tag{B.25}$$

with Δ given by Eq. (B.2) and the boundary conditions determined from the rigid wall assumption at hub and tip radii

$$\left.\frac{\partial G}{\partial r}\right|_{R_h,R_t} = 0. \tag{B.26}$$

The Green's function $G(\boldsymbol{y},\tau|\boldsymbol{x},t)$ depends on t and τ only in the combination $t' = t-\tau$ and is therefore written $G(\boldsymbol{y},t'|\boldsymbol{x})$. Its inverse t'-Fourier transform is written

$$G(\boldsymbol{y},t'|\boldsymbol{x}) = \int_{-\infty}^{+\infty} \widehat{G}(\boldsymbol{y},\omega|\boldsymbol{x})e^{-i\omega t'}\,d\omega, \tag{B.27}$$

where the Fourier components $\widehat{G}(\boldsymbol{y},\omega|\boldsymbol{x})$ are given by

$$\widehat{G}(\boldsymbol{y},\omega|\boldsymbol{x}) = \frac{1}{2\pi}\int_{-\infty}^{+\infty} G(\boldsymbol{y},t'|\boldsymbol{x})e^{i\omega t'}\,dt'. \tag{B.28}$$

Injecting Eq. (B.27) into (B.25) and noting that

$$\delta(t') = \frac{1}{2\pi}\int_{-\infty}^{+\infty} e^{-i\omega t'}\,d\omega, \tag{B.29}$$

yields

$$\left[-k_0^2 - 2iM_0k_0\frac{\partial}{\partial x} + M_0^2\frac{\partial^2}{\partial x^2} - \Delta\right]\widehat{G}(\boldsymbol{y},\omega|\boldsymbol{x}) = \frac{\delta(\boldsymbol{x}-\boldsymbol{y})}{2\pi}. \tag{B.30}$$

Similarly to what was done before for the density fluctuations, the frequency-domain Green's function $\widehat{G}(\boldsymbol{y},\omega|\boldsymbol{x})$ is decomposed into the duct modes of Sec. 1.6.1

$$\widehat{G}(\boldsymbol{y},\omega|\boldsymbol{x}) = \sum_{m=-\infty}^{+\infty}\sum_{n=0}^{+\infty} e_{mn}(y,\omega|\boldsymbol{x})\psi_{mn}(r_y,\theta_y). \tag{B.31}$$

Injecting this expression into Eq. (B.30), using Eq. (B.9), multiplying by $\psi^*_{mn}(r,\theta)$, integrating over a duct section and using the property of orthogonality of duct modes (B.15) yields

$$\beta_0^2\frac{\partial^2 e_{mn}}{\partial x^2} + 2iM_0k_0\frac{\partial e_{mn}}{\partial x} + (k_0^2-\alpha_{mn}^2)e_{mn} = -\frac{\delta(x-y)\psi^*_{mn}(r,\theta)}{2\pi\Gamma_{mn}}. \tag{B.32}$$

The duct is assumed to be invariant to translation and $e_{mn}(y,\omega|\boldsymbol{x})$ can be expressed as a function of $x' = x - y$ and is therefore written $e_{mn}(\omega|x', r, \theta)$. Its inverse x'-Fourier transform is written

$$e_{mn}(\omega|x', r, \theta) = \int_{-\infty}^{+\infty} \widehat{e_{mn}}(\omega|k_x, r, \theta) e^{ik_x x'}\, dk_x, \tag{B.33}$$

where the Fourier components $\widehat{e_{mn}}(\omega|k_x, r, \theta)$ are given by

$$\widehat{e_{mn}}(\omega|k_x, r, \theta) = \frac{1}{2\pi} \int_{-\infty}^{+\infty} e_{mn}(\omega|x', r, \theta) e^{-ik_x x'}\, dx'. \tag{B.34}$$

Since

$$\delta(x') = \frac{1}{2\pi} \int_{-\infty}^{+\infty} e^{ik_x x'}\, dk_x, \tag{B.35}$$

injecting Eq. (B.33) into Eq. (B.32) gives

$$\left[-\beta_0^2 k_x^2 - 2M_0 k_0 k_x + (k_0^2 - \alpha_{mn}^2)\right] \widehat{e_{mn}}(\omega|k_x, r, \theta) = -\frac{\psi_{mn}^*(r,\theta)}{(2\pi)^2 \Gamma_{mn}}. \tag{B.36}$$

The part in square brackets is similar to Eq. (B.20) and it can consequently be written in terms of its solutions

$$-\beta_0^2 k_x^2 - 2M_0 k_0 k_x + (k_0^2 - \alpha_{mn}^2) = -\beta_0^2 (k_x + \gamma_{mn}^+)(k_x + \gamma_{mn}^-). \tag{B.37}$$

The expression of $\widehat{e_{mn}}(\omega|k_x, r, \theta)$ can be therefore be shown to reduce to

$$\widehat{e_{mn}}(\omega|k_x, r, \theta) = -\frac{\psi_{mn}^*(r,\theta)}{2(2\pi)^2 \Gamma_{mn} k_{mn}} \left(\frac{1}{k_x + \gamma_{mn}^+} - \frac{1}{k_x + \gamma_{mn}^-} \right). \tag{B.38}$$

Its inverse Fourier transform (B.33) is written

$$e_{mn}(\omega|x', r, \theta) = -\frac{\psi_{mn}^*(r,\theta)}{2(2\pi)^2 \Gamma_{mn} k_{mn}} \int_{-\infty}^{+\infty} \left(\frac{1}{k_x + \gamma_{mn}^+} - \frac{1}{k_x + \gamma_{mn}^-} \right) e^{ik_x x'}\, dk_x, \tag{B.39}$$

and the use of the residue theorem gives

$$e_{mn}^{\pm}(\omega|x', r, \theta) = \frac{i\psi_{mn}^*(r,\theta)}{4\pi \Gamma_{mn} k_{mn}} e^{-i\gamma_{mn}^{\pm} x'}. \tag{B.40}$$

The expression of the duct Green's function is finally obtained by combining Eqs. (B.25), (B.31) and (B.40) and by reminding that $t' = t - \tau$ and $x' = x - y$

$$G^{\pm}(\boldsymbol{y}, \tau|\boldsymbol{x}, t) = \frac{i}{4\pi} \sum_{m=-\infty}^{+\infty} \sum_{n=0}^{+\infty} \frac{\overline{\psi_{mn}}(r,\theta)\psi_{mn}(r_y,\theta_y)}{\Gamma_{mn}} \int_{-\infty}^{+\infty} \frac{e^{-i[\gamma_{mn}^{\pm}(x-y)+\omega(t-\tau)]}}{k_{mn}}\, d\omega. \tag{B.41}$$

B.3 Simplification of the source term

Using Goldstein's formula (1.82) and the expression of the duct Green's function (1.87) yields the expression of density fluctuations

$$\rho^{\pm}(\boldsymbol{x},t) = \int_{-\infty}^{+\infty} \frac{i}{4\pi a_0^2} \sum_{m=-\infty}^{+\infty} \sum_{n=0}^{+\infty} \frac{\overline{\psi_{mn}}(r,\theta)e^{-i\gamma_{mn}^{\pm}x}}{\Gamma_{mn}k_{mn}}$$
$$\int_{-\infty}^{+\infty} \iint_{S(\tau)} \frac{\partial}{\partial x_i} \left\{\psi_{mn}(r_y,\theta_y)e^{i\gamma_{mn}^{\pm}y}\right\} f_i(\boldsymbol{y},\tau)e^{i\omega\tau}\, dS(\boldsymbol{y})d\tau\, e^{-i\omega t}\, d\omega. \quad \text{(B.42)}$$

This expression can be simplified for the two mechanisms that are considered in this study: the wake-stator interaction and the distortion-rotor interaction. B and V denote the number of rotor blades and stator vanes respectively and Ω the engine rotational speed. The rotor is assumed to be homogeneous (i.e. it has identical and evenly spaced blades) but the stator can be heterogeneous like in modern aircraft engines.

Wake-stator interaction

When interested in evaluating the noise caused by the interaction of rotor-blade wakes with stator vanes, the surface integration in Eq. (B.42) is done over the stator vanes which are fixed. The fluctuating density can therefore be written

$$\rho^{\pm}(\boldsymbol{x},t) = \int_{-\infty}^{+\infty} \frac{i}{4\pi a_0^2} \sum_{m=-\infty}^{+\infty} \sum_{n=0}^{+\infty} \frac{\overline{\psi_{mn}}(r,\theta)e^{-i\gamma_{mn}^{\pm}x}}{\Gamma_{mn}k_{mn}}$$
$$\iint_{S} \frac{\partial}{\partial x_i} \left\{\psi_{mn}(r_y,\theta_y)e^{i\gamma_{mn}^{\pm}y}\right\} \int_{-\infty}^{+\infty} f_i(\boldsymbol{y},\tau)e^{i\omega\tau}\, d\tau dS(\boldsymbol{y})\, e^{-i\omega t}\, d\omega. \quad \text{(B.43)}$$

The lift variations on stator vanes caused by the impact of blade wakes are periodic and the force components $f_i(\boldsymbol{y},\tau)$ can be expressed as Fourier series

$$f_i(\boldsymbol{y},\tau) = \sum_{s=-\infty}^{+\infty} f_{i,s}(\boldsymbol{y})e^{-is\Omega\tau}, \quad \text{(B.44)}$$

where

$$f_{i,s}(\boldsymbol{y}) = \frac{\Omega}{2\pi} \int_0^{\frac{2\pi}{\Omega}} f_i(\boldsymbol{y},\tau)e^{is\Omega\tau}\, d\tau. \quad \text{(B.45)}$$

Since the rotor blades wakes are identical and evenly spaced, the characteristic period becomes $2\pi/B\Omega$ and only the harmonics that are multiple of B contribute to the sum

$$f_i(\boldsymbol{y},\tau) = \sum_{s=-\infty}^{+\infty} f_{i,sB}(\boldsymbol{y})e^{-isB\Omega\tau}. \quad \text{(B.46)}$$

With the relation

$$\int_{-\infty}^{\infty} e^{i(\omega - sB\Omega)\tau}\, d\tau = 2\pi\, \delta(\omega - sB\Omega), \tag{B.47}$$

and Eqs. (B.43) and (B.46), it results that the fluctuating density can itself be expressed as a Fourier series

$$\rho^{\pm}(\boldsymbol{x}, t) = \sum_{s=-\infty}^{+\infty} \rho^{\pm}_{sB}(\boldsymbol{x}) e^{-isB\Omega t}, \tag{B.48}$$

with

$$\rho^{\pm}_{sB}(\boldsymbol{x}) = \frac{1}{2a_0^2} \sum_{m=-\infty}^{+\infty} \sum_{n=0}^{+\infty} \frac{\overline{\psi_{mn}}(r, \theta) e^{-i\gamma^{\pm}_{mn} x}}{\Gamma_{mn} k_{mn}} S^{\pm}_{mn}(sB), \tag{B.49}$$

and where $S^{\pm}_{mn}(sB)$ determines the amplitude of the mode $(m,\, n)$ caused by the fluctuating lift on stator vanes at pulsation $\omega = sB\Omega$ and is defined by

$$S^{\pm}_{mn}(sB) = i \iint_S \frac{\partial}{\partial x_i} \left\{ \psi_{mn}(r_y, \theta_y) e^{i\gamma^{\pm}_{mn} y} \right\} f_{i,sB}(\boldsymbol{y})\, dS(\boldsymbol{y}). \tag{B.50}$$

Particular case: homogeneous stator

When the stator vanes are all identical and evenly spaced, the wake that impacts the j^{th} vane is the same that the one that impacted the 1^{st} vane (spaced from the j^{th} vane by an angle of $\frac{2\pi}{V}(j-1)$) with a timelag of $\frac{2\pi}{V\Omega}(j-1)$

$$f_i^j(r_y, \theta_y, y, \tau) = f_i^1(r_y, \theta_y - \frac{2\pi}{V}(j-1), y, \tau - \frac{2\pi}{V\Omega}(j-1)). \tag{B.51}$$

This results in the following relationship between the Fourier components

$$f^j_{i,sB}(r_y, \theta_y, y) = f^1_{i,sB}(r_y, \theta_y - \frac{2\pi}{V}(j-1), y) e^{isB\frac{2\pi}{V}(j-1)}. \tag{B.52}$$

Writting the term (B.50) as a sum of integrals over each vane and using the relations (B.52) and (1.83) to bring the integration of the surface S_1 of the 1^{st} vane only yields

$$S^{\pm}_{mn}(sB) = \sum_{j=1}^{j=V} e^{i(sB-m)\frac{2\pi}{V}(j-1)}\, i \iint_{S_1} \frac{\partial}{\partial x_i} \left\{ \psi_{mn}(r_y, \theta_y) e^{i\gamma^{\pm}_{mn} y} \right\} f^1_{i,sB}(\boldsymbol{y})\, dS(\boldsymbol{y}). \tag{B.53}$$

From the relation

$$\sum_{j=1}^{j=V} e^{i(sB-m)\frac{2\pi}{V}(j-1)} = \begin{cases} V & \text{if } \exists k \in \mathbb{Z} \text{ such as } sB - m = kV \\ 0 & \text{otherwise} \end{cases}, \tag{B.54}$$

results what is known as Tyler & Sofrin's law. Only the modes with an azimuthal order that can be written as $m = sB - kV$ (where k is any integer) are excited by the interaction of homogeneous rotor blade wakes with homogeenous stator vanes. For such modes, $S^{\pm}_{mn}(sB)$ becomes

$$S^{\pm}_{mn}(sB) = iV \iint_{S_1} \frac{\partial}{\partial x_i} \left\{ \psi_{mn}(r_y, \theta_y) e^{i\gamma^{\pm}_{mn} y} \right\} f^1_{i,sB}(\boldsymbol{y})\, dS(\boldsymbol{y}). \tag{B.55}$$

Distortion-rotor interaction

When evaluating the noise due to the interaction of rotor blades with the distortion, the surface integration in Eq. (B.42) is done over the rotor blades which are rotating. In order to bring the integral over a fixed surface, a change of frame is needed

$$\tilde{\theta_y} = \theta_y - \Omega\tau, \tag{B.56}$$

and Eq. (B.42) becomes

$$\rho^{\pm}(\boldsymbol{x},t) = \int_{-\infty}^{+\infty} \frac{i}{4\pi a_0^2} \sum_{m=-\infty}^{+\infty} \sum_{n=0}^{+\infty} \frac{\overline{\psi_{mn}}(r,\theta) e^{-i\gamma_{mn}^{\pm} x}}{\Gamma_{mn} k_{mn}}$$
$$\iint_S \frac{\partial}{\partial x_i} \left\{ \psi_{mn}(r_y, \tilde{\theta}_y) e^{i\gamma_{mn}^{\pm} y} \right\} \int_{-\infty}^{+\infty} f_i(\tilde{\boldsymbol{y}},\tau) e^{i(\omega - m\Omega)\tau}\, d\tau dS(\tilde{\boldsymbol{y}})\, e^{-i\omega t}\, d\omega. \tag{B.57}$$

The lift variations on rotor blades vanes caused by the impact of distortion are also periodic and the force components $f_i(\tilde{\boldsymbol{y}},\tau)$ can be expressed as Fourier series

$$f_i(\tilde{\boldsymbol{y}},\tau) = \sum_{p=-\infty}^{+\infty} f_{i,p}(\tilde{\boldsymbol{y}}) e^{-ip\Omega\tau}, \tag{B.58}$$

where

$$f_{i,p}(\tilde{\boldsymbol{y}}) = \frac{\Omega}{2\pi} \int_0^{\frac{2\pi}{\Omega}} f_i(\tilde{\boldsymbol{y}},\tau) e^{ip\Omega\tau}\, d\tau. \tag{B.59}$$

Applying the identity

$$\int_{-\infty}^{\infty} e^{i(\omega-(p+m)\Omega)\tau}\, d\tau = 2\pi\, \delta(\omega - (p+m)\Omega), \tag{B.60}$$

writting $s = p+m$ and using Eqs. (B.57), (B.58) and (1.83) yields the decomposition of the fluctuating density as a Fourier series

$$\rho^{\pm}(\boldsymbol{x},t) = \sum_{s=-\infty}^{+\infty} \rho_s^{\pm}(\boldsymbol{x}) e^{-is\Omega t}, \tag{B.61}$$

with

$$\rho_s^{\pm}(\boldsymbol{x}) = \frac{1}{2a_0^2} \sum_{m=-\infty}^{+\infty} \sum_{n=0}^{+\infty} \frac{\overline{\psi_{mn}}(r,\theta) e^{-i\gamma_{mn}^{\pm} x}}{\Gamma_{mn} k_{mn}} S_{mn}^{\pm}(s-m), \tag{B.62}$$

and where $S_{mn}^{\pm}(s-m)$ determines the amplitude of the mode $(m,\, n)$ caused by the fluctuating lift on rotor blades at pulsation $\omega = (s-m)\Omega$ and is defined by

$$S_{mn}^{\pm}(s-m) = i \iint_S \frac{\partial}{\partial x_i} \left\{ \psi_{mn}(r_y, \tilde{\theta}_y) e^{i\gamma_{mn}^{\pm} y} \right\} f_{i,(s-m)}(\tilde{\boldsymbol{y}})\, dS(\tilde{\boldsymbol{y}}). \tag{B.63}$$

Since all rotor blades are identical and evenly spaced, the distortion seen by the j^{th} blade is the same as the one seen by the 1^{st} blade (spaced from j^{th} blade by an angle of $\frac{2\pi}{B}(j-1)$) with an advance in time of $\frac{2\pi}{B\Omega}(j-1)$. The forces on the j^{th} and the 1^{st} blades are therefore related by

$$f_i^j(r_y, \tilde{\theta}_y, y, \tau) = f_i^1(r_y, \tilde{\theta}_y - \frac{2\pi}{B}(j-1), y, \tau + \frac{2\pi}{B\Omega}(j-1)), \tag{B.64}$$

which gives, in terms of Fourier components

$$f_{i,p}^j(r_y, \tilde{\theta}_y, y) = f_{i,p}^1(r_y, \tilde{\theta}_y - \frac{2\pi}{B}(j-1), y) e^{-ip\frac{2\pi}{B}(j-1)}. \tag{B.65}$$

Writting the term (B.63) as a sum of integrals over each blade and using Eq. (1.83) to bring the integration of the surface S_1 of the 1^{st} blade only yields

$$S_{mn}^{\pm}(s-m) = \sum_{j=1}^{j=B} e^{-is\frac{2\pi}{B}(j-1)} i \iint_{S_1} \frac{\partial}{\partial x_i} \left\{ \psi_{mn}(r_y, \tilde{\theta}_y) e^{i\gamma_{mn}^{\pm} y} \right\} f_{i,(s-m)}^1(\tilde{\boldsymbol{y}})\, dS(\tilde{\boldsymbol{y}}). \tag{B.66}$$

Since

$$\sum_{j=1}^{j=B} e^{-is\frac{2\pi}{B}(j-1)} = \begin{cases} B & \text{if } \exists k \in \mathbb{Z} \text{ such as } s = kB \\ 0 & \text{otherwise} \end{cases}, \tag{B.67}$$

only the harmonics that are multiple of B will emerge. The flutuating density can therefore be written

$$\rho^{\pm}(\boldsymbol{x}, t) = \sum_{s=-\infty}^{+\infty} \rho_{sB}^{\pm}(\boldsymbol{x}) e^{-isB\Omega t}, \tag{B.68}$$

with

$$\rho_{sB}^{\pm}(\boldsymbol{x}) = \frac{1}{2a_0^2} \sum_{m=-\infty}^{+\infty} \sum_{n=0}^{+\infty} \frac{\overline{\psi_{mn}}(r, \theta) e^{-i\gamma_{mn}^{\pm} x}}{\Gamma_{mn} k_{mn}} S_{mn}^{\pm}(sB - m), \tag{B.69}$$

and

$$S_{mn}^{\pm}(sB-m) = iB \iint_{S_1} \frac{\partial}{\partial x_i} \left\{ \psi_{mn}(r_y, \tilde{\theta}_y) e^{i\gamma_{mn}^{\pm} y} \right\} f_{i,(sB-m)}^1(\tilde{\boldsymbol{y}})\, dS(\tilde{\boldsymbol{y}}). \tag{B.70}$$

General formulation

In any case (stator or rotor sources), the fluctuating density can be expressed as a Fourier series

$$\rho^{\pm}(\boldsymbol{x}, t) = \sum_{s=-\infty}^{+\infty} \rho_{sB}^{\pm}(\boldsymbol{x}) e^{-isB\Omega t}, \tag{B.71}$$

where the components are given by

$$\rho_{sB}^{\pm}(\boldsymbol{x}) = \frac{1}{2a_0^2} \sum_{m=-\infty}^{+\infty} \sum_{n=0}^{+\infty} \frac{\overline{\psi_{mn}}(r,\theta) e^{-i\gamma_{mn}^{\pm} x}}{\Gamma_{mn} k_{mn}} S_{mn}^{\pm}, \tag{B.72}$$

The term $S_{mn}^{\pm}$ is determined from Eq. (B.50) for heterogeneous stator sources, from Eq. (B.55) for homogeneous stator sources and from Eq. (B.70) for homogeneous rotor sources. Since only the cut-on modes have a significant level far from the sources, the sum over the modes in Eq. (B.72) can be truncated, which yields

$$\rho_{sB}^{\pm}(\boldsymbol{x}) = \frac{1}{2a_0^2} \sum_{m=-\infty}^{+\infty} \sum_{\substack{n=0 \\ k_{mn}^2 \geq 0}}^{+\infty} \frac{\overline{\psi_{mn}}(r,\theta) e^{-i\gamma_{mn}^{\pm} x}}{\Gamma_{mn} k_{mn}} S_{mn}^{\pm}. \tag{B.73}$$

Appendix C

One-dimensional validation of the numerical setup

One-dimensional test-cases are shown in this appendix to validate the numerical setup chosen for the study.

C.1 Propagation of acoustic waves

One-dimensional test cases have been run to validate the discretization used in the study. Roe's scheme with the MUSCL reconstruction (third-order accuracy) described in App. A.3 is used for the spatial discretization while the temporal discretization is achieved with the implicit backward Euler scheme with a DTS sub-iteration algorithm (second order accuracy).

The test cases consist of propagating fluctuations on a one-dimensional grid composed of cells with the size of the biggest cell of the simulations. The size of the domain is the same as the one of the simulations. An unsteady inlet condition is used to inject the fluctuations and a pressure condition is put at the outlet. The inlet condition plays the role of the fluctuations that appear on the blades or the vanes. The propagation of both upstream and downstream waves is evaluated. Since it is not possible to inject the fluctuations at the outlet with the code that is used, the upstream propagation is evaluated by artificially increasing the frequency in order to get the correct wavenumber.

The test cases are achieved with the parameters that correspond to the cutback regime. The fluctuations are injected at the BPF (the frequency at which the noise predictions are made) and an axial flow is defined using the mean axial velocity of the complete simulation. Three meshes Ma, Mb and Mc are tested. They are built in order to discretize the wavelength associated with the upstream acoustic wave at the BPF λ^+_{BPF} by 10, 20 and 30 points respectively. Because of the convected flow, the wavelength associated with the downstream acoustic wave λ^-_{BPF} is longer and is discretized by more points. For Ma, Mb and Mc, this wavelength is discretized by 25, 50 and 75 points respectively. These figures are summarized in Tab. C.1.

The discretization is evaluated by analyzing the pressure fluctuations signal over

Mesh	N_x/λ^+_{BPF}	N_x/λ^-_{BPF}
Ma	10	25
Mb	20	50
Mc	30	75

Table C.1: **Number of points per wavelength for acoustic waves propagating upstream N_x/λ^+_{1BPF} and downstream N_x/λ^-_{1BPF} at the BPF for the three mesh resolutions**

the domain. A wave is said to be correctly propagated if its attenuation over the whole domain does not exceed 12% (equivalent to 0.5 dB approximately). Results for the three mesh resolutions are given in Fig. C.1 where the theoretical signal has also been added for comparison. Note that the test cases are stopped just before the waves reach the outlet to avoid reflections (the study of the reflections on the boundary conditions is done in App. C.2).

For all mesh discretizations, the downstream wave is well propagated (no visible attenuation). Small overestimations of the first peaks (of about 5%) can however be observed on mesh Ma. The upstream wave is subject to important attenuation depending on the mesh because of its lower wavelength. On mesh Ma, the ratio between the amplitude of the second to last peak and the one of the first peak is greater than 70% and the attenuation over the whole domain is estimated to 95% (by accounting for the fact that the wave has travelled over 75% of the domain only). On mesh Mb, it is about 8% and the attenuation over the whole domain becomes 11%. Small overestimations of the first peaks (of about 5%) are also observed. For the mesh Mc, the attenuation is not visible at all.

The errors observed on mesh Mb are considered as acceptable (less than 12%) and it appears that 20 points per wavelength are sufficient to propagate an acoustic wave correctly. The meshes used for the simulations presented in Chap. 2 are therefore built such that they respect this criterion for both upstream and downstream acoustic waves.

C.2 Stretching zones

The test cases presented in App. C.1 have been run longer to study what happens when the wave reaches the outlet boundary condition. The results obtained with the mesh Mc are shown here. Two cases are considered: the first one without stretching zone and the other one with the same stretching zone than the one used in the simulations of the article (expansion ratio of about 1.4 until the cell size reaches half of the value of the acoustic wavelength at the BPF). The downstream propagation of the wave at the BPF is taken as example since it is the most restrictive case (longest wavelength so hardest wave to dissipate in the stretching zone). Fig. C.2 shows the pressure fluctuations when the wave reaches the outlet and when the wave gets back in the physical domain without and with the stretching zone (the stretching zone is

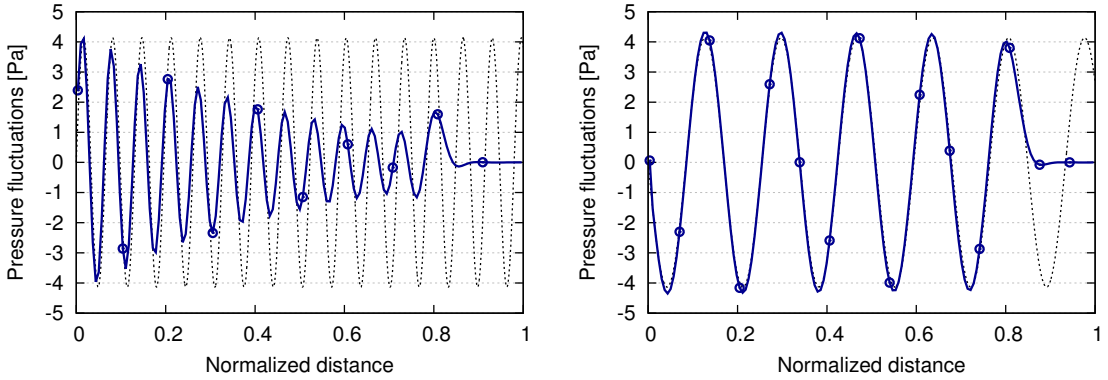

(a) Ma - Upstream wave

(b) Ma - Downstream wave

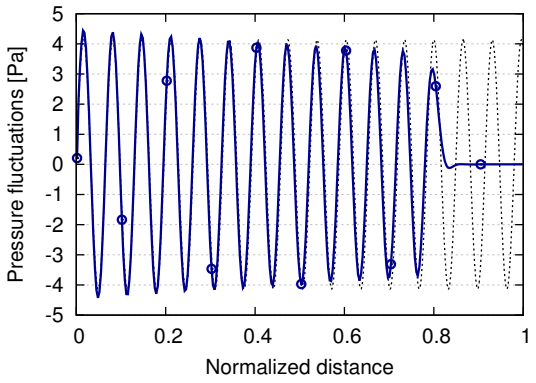

(c) Mb - Upstream wave

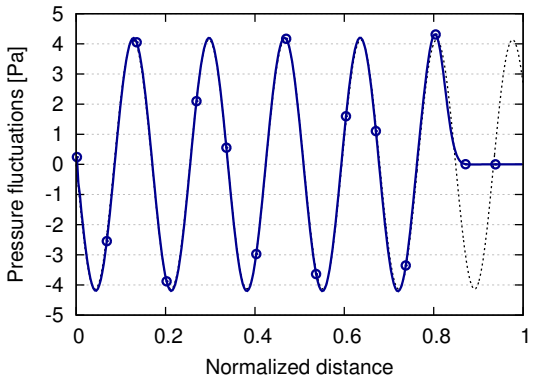

(d) Mb - Downstream wave

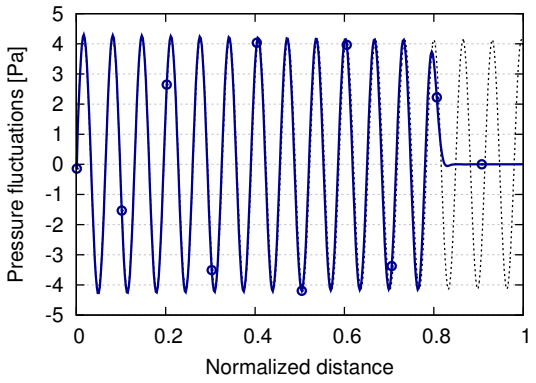

(e) Mc - Upstream wave

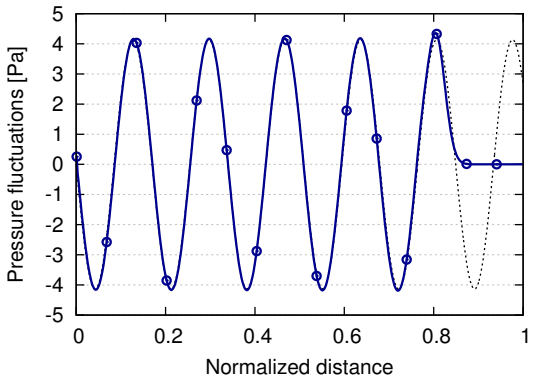

(f) Mc - Downstream wave

Figure C.1: **One-dimensional propagation of an upstream wave and a downstream wave on the different meshes: ..... theoretical pressure fluctuations, —o— numerical pressure fluctuations**

considered outside of the physical domain).

Strong reflections occur when the wave encounters the outlet without the stretching zone and evidence the reflecting character of the outlet. When the stretching zone is added, the fluctuations are well dissipated before reaching the outlet. No

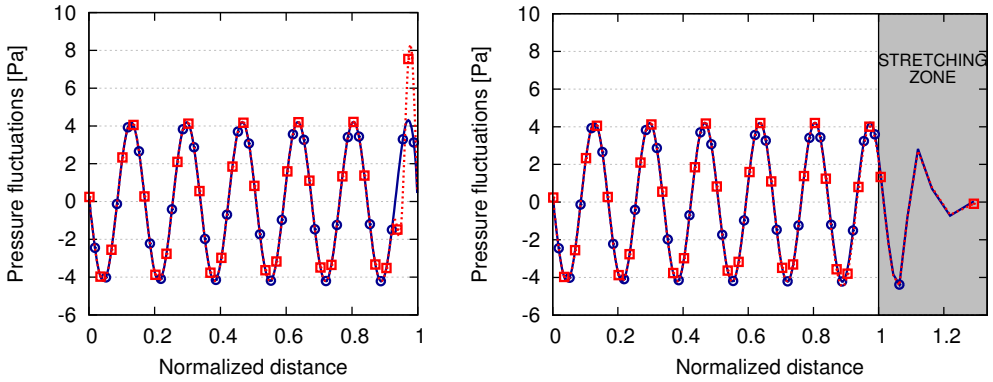

(a) Without stretching zone (b) With stretching zone

Figure C.2: **One-dimensional propagation of a downstream wave encountering the outlet without and with a strectching zone: pressure fluctuations when the wave reaches the outlet, pressure fluctuations when the wave gets back in the physical domain**

spurious reflections are therefore created.

Appendix D

Effects of mesh refinement

The effects of mesh refinement are studied in this appendix by comparing the results obtained with the meshes M1 (70 million points) and M2 (570 million points) described in Sec. 2.3.1. This is done at sideline conditions and with inlet distortion. The temporal discretization is also increased in the simulation of mesh M2 (200 time steps per blade passage instead of 100 for simulations on M1 meshes).

D.1 Effects on aerodynamic patterns

The effects of mesh refinement are shown here on the aerodynamic patterns studied in Chap. 3. The distortion is first analyzed in Fig. D.1 where the azimuthal evolution of the mean normalized axial velocity in planes P2 (upstream of the fan) and P3 (upstream of the OGV) is given. The effects of the mesh refinement are not visible at 25% and 50% of vane height. At 75% and 95% of vane height, very small differences of less than 0.5% are observed and are probably caused by tip-leakage flow that is not perfectly described in the mesh M1. These differences are not expected to have an effect on the distortion-fan interaction noise.

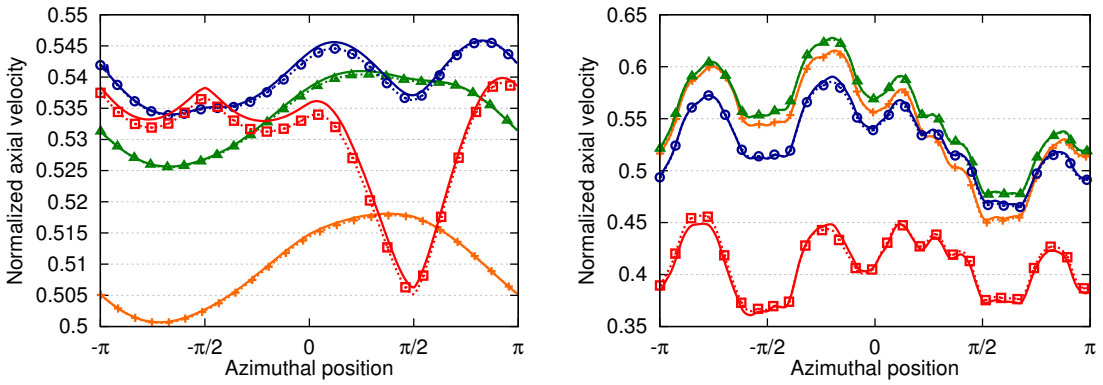

(a) Plane P2

(b) Plane P5

Figure D.1: **Mean normalized axial velocity profiles in planes P2 and P5 at different vane heights: — 25%, — 50%, — 75%, — 95% for mesh M1 and ···+··· 25%, ···△··· 50%, ···○··· 75%, ···□··· 95% for mesh M2**

The effects are now evaluated on the fan-blade wakes. Fig. D.2 shows the evolution of the normalized velocity deficit during the last three blade passage periods. It is represented in plane P5 (right upstream of the OGV) at 25%, 50%, 75% and 95% of vane height for one arbitrary azimuthal position. At all vane heights, the wakes are thicker and the normalized velocity deficits are reduced in the coarse mesh because of the lower resolution. The maximum reduction of the normalized velocity deficit observed at the positions represented here is about 30% when compared with the fine mesh. Consequently, an underestimate of the noise caused by fan-OGV interaction is likely in the mesh M1.

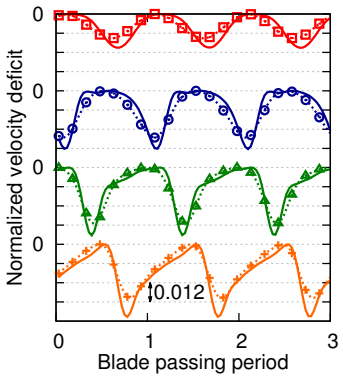

Figure D.2: **Normalized velocity deficit in plane P5 at vane heights: 25%, 50%, 75%, 95% for mesh M1 and 25%, 50%, 75%, 95% for mesh M2**

A comparison of the shocks created on the suction side of the blades is now given. The distribution of instantaneous isentropic Mach number over one fan blade at $h/H = 95\%$ is given for the two meshes in Fig. D.3. The differences in terms of both position and amplitude of the shock are small and the shock noise (at least its generation) is expected to be correctly predicted with the coarse mesh.

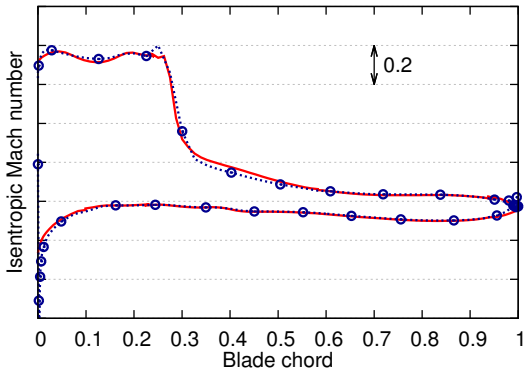

Figure D.3: **Instantaneous isentropic Mach number distribution over one fan blade at $h/H = 95\%$: mesh M1, mesh M2**

D.2 Effects on noise predictions

The effects of mesh refinement on the noise predictions are now evaluated. This is done by comparing the noise levels computed from the simulations using the direct approach detailed in Sec. 4.6. For the downstream noise level, the comparison is done both with and without the filtering based on modal decomposition (P filtering). Results at the BPF are given in Fig. D.4.

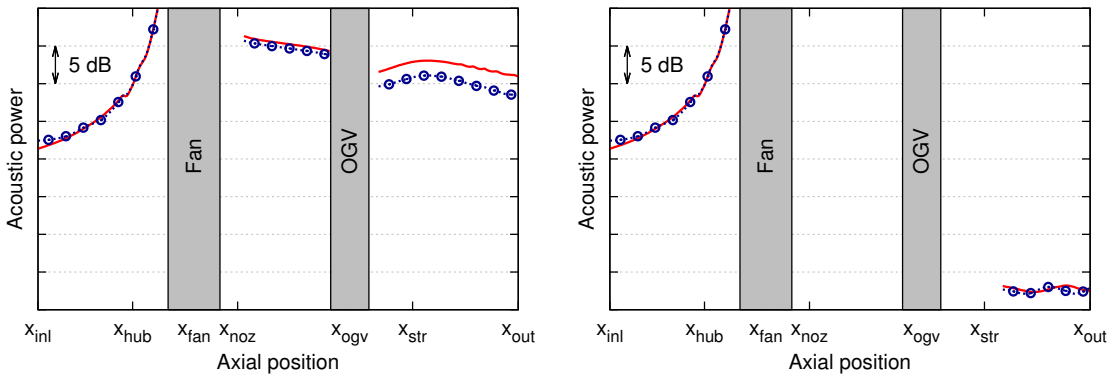

(a) Without filtering

(b) With filtering

Figure D.4: **Axial evolution of acoustic power with and without filtering: ··o·· mesh M1, —— mesh M2**

Upstream of the fan, the noise levels match well in the whole inlet duct, except right at the entrance where a slight difference of about 1 dB is observed because of an increased attenuation with the fine mesh. The origin of this difference still needs to be investigated. When the filtering is not applied, important differences are observed between the downstream levels computed with the two meshes. The downstream fluctuations are dominated by hydrodynamic fluctuations that are subject to dissipation because of their small wavelength. When filtering these fluctuations, the noise level remains approximately constant and the differences are small between the two meshes (always less than 1 dB). This gives credit to the noise predicitions at the BPF realized in this study. However, it may appear surprising given the differences observed in the normalized velocity deficits in Fig. D.2. A deeper analysis should be done to understand exactly these observations (by using Rienstra's theory presented in Sec. 1.6.2 for example).

Bibliography

[1] S. Capoccitti, A. Khare, and U. Mildenberger. Aviation Industry - Mitigating Climate Change Impacts through Technology and Policy. *Journal of Technology Management & Innovation*, 5(2):66–75, 2010.

[2] International Civil Aviation Organization. Annex 16 to the Convention on International Civil Aviation, 2005.

[3] T. Nodé-Langlois. Aeroengine-airframe aeroacoustic integration and installation effects. In *VKI Lecture Series*, 2014.

[4] Advisory Council for Aeronautics Research in Europe. http://www.acare4europe.com/.

[5] P. Fethney. An experimental study of airframe self-noise. In *2nd AIAA Aeroacoustics Conference*, 1975.

[6] N. Peake and A.B. Parry. Modern Challenges Facing Turbomachinery Aeroacoustics. *Annual Review of Fluid Mechanics*, 44(1):227–248, 2012.

[7] M. Lebrun. *Vers une prédiction globale du bruit des soufflantes à partir de l'analogie acoustique et des outils de mécanique des fluides numérique*. PhD thesis, Ecole Centrale de Lyon, 2002.

[8] M.E. Goldstein. *Aeroacoustics*. McGraw-Hill Inc., 1976.

[9] A. McAlpine, P.J.G Schwaller, M.J. Fisher, and B.J. Tester. Buzz-saw noise: Prediction of the rotor-alone pressure field. *Journal of Sound and Vibration*, 331(22):4901–4918, 2012.

[10] J.M. Tyler and T.G. Sofrin. Axial flow compressor noise studies. *Society of Automotive Engineers Transactions*, 70:309–332, 1962.

[11] V. Bonneau. *Prévision du bruit d'interaction tonal et à large bande d'une soufflante de nouvelle génération en régime subsonique*. PhD thesis, Université de Poitiers, 2015.

[12] U.W. Ganz, P.D. Joppa, T.J. Patten, and D.F. Scharpf. Boeing 18-Inch Fan Rig Broadband Noise Test. Technical report, NASA CR-1998-208704, 1998.

[13] J.E. Ffowcs Williams and L.H. Hall. Aerodynamic sound generation by turbulent flow in the vicinity of a scattering half plane. *Journal of Fluid Mechanics*, 40(1970):657–670, 1970.

[14] S. Magne, S. Moreau, and A. Berry. Subharmonic tonal noise from backflow vortices radiated by a low-speed ring fan in uniform inlet flow. *The Journal of the Acoustical Society of America*, 137(1):228–37, 2015.

[15] S. Moreau and M. Sanjosé. Sub-harmonic broadband humps and tip noise in low-speed ring fans. *The Journal of the Acoustical Society of America*, 139(1):118–127, 2016.

[16] T. Léonard, M. Sanjosé, S. Moreau, and F. Duchaine. Large Eddy Simulation of a scale-model turbofan for fan noise source diagnostic. In *22nd AIAA/CEAS Aeroacoustics Conference*, 2016.

[17] J. De Laborderie. *Approches analytiques et numériques pour la prédiction du bruit tonal et large bande de soufflantes de turboréacteurs*. PhD thesis, Université de Sherbrooke, 2013.

[18] K.L. Bekofske, R.E. Sheer, and J.C.F. Wang. Effect of Inlet Disturbances on Fan Inlet Noise During a Static Test. Technical report, NASA CR-135177, 1977.

[19] R.A. Kantola and R.E. Warren. Basic Research in Fan Source Noise -Inlet Distortion and Turbulence Noise. Technical report, NASA CR-159451, 1978.

[20] A. Holewa, C. Weckmüller, and S. Guérin. Impact of Bypass Duct Bifurcations on Fan Noise. In *18th AIAA/CEAS Aeroacoustics Conference*, 2012.

[21] V. Bonneau, C. Polacsek, R. Barrier, S. Lewy, J.-M. Roux, and Y. Gervais. Tonal Noise Prediction of a Turbofan with Heterogeneous Stator and Bifurcations. *AIAA Journal*, 53(11):3354–3369, 2015.

[22] M. Roger and P. Caule. Assessment of the effect of stator inhomogeneity on rotor-stator tonal noise. In *15th International Symposium on Transport Phenomena and Dynamics of Rotating Machinery*, 2014.

[23] T. Oishi, S. Kusuda, H. Kodama, M. Namba, and J. Kazawa. Behaviors of Fan Tone Noise Under the Influence of Circumferentially Non-Uniform Steady Pressure Perturbation. In *19th AIAA/CEAS Aeroacoustics Conference*, 2013.

[24] M. Sturm, M. Sanjosé, S. Moreau, and T. Carolus. Application of Analytical Noise Models Using Numerical and Experimental Fan Data. In *11th European Conference on Turbomachinery, Fluid Dynamics and Thermodynamics*, 2015.

[25] F. Conte, M. Roger, S. Moreau, M. Sanjosé, and P. Caule. Modeling of Installation Effects on the Noise from. In *17th AIAA/CEAS Aeroacoustics Conference*, 2011.

[26] J. Winkler, C.A. Reimann, R.A. Reba, and J. Gilson. Turbofan Inlet Distortion Noise Prediction with a Hybrid CFD-CAA Approach. In *20th AIAA/CEAS Aeroacoustics Conference*, 2014.

[27] M. Doherty and H. Namgoong. Impact of Turbofan Intake Distortion on Fan Noise Propagation and Generation. In *22nd AIAA/CEAS Aeroacoustics Conference*, 2016.

[28] D.J. Acheson. *Elementary Fluid Dynamics*. Clarendon Press, 1990.

[29] M.J. Lighthill. On sound generated aerodynamically. I. General theory. *Proceedings of the Royal Society of London. Series A, Mathematical and Physical Sciences*, 211(1107):564–587, 1952.

[30] S. Moreau. *Aéroacoustique GMC729*. Cours de l'Université de Sherbrooke, 2015.

[31] C. Bailly. Numerical Solution of Acoustic Propagation Problems Using Linearized Euler Equations. *AIAA Journal*, 38(1):22–29, 2000.

[32] B.T. Chu and L.S.G. Kovasnay. Non-linear interactions in a viscous heat-conducting compressible gas. *Journal of Fluid Mechanics*, 3(5):494–514, 1957.

[33] C. L. Rumsey, R. T. Biedron, F. Farassat, and P. L. Spence. Ducted-Fan Engine Acoustic Predictions Using a Navier-Stokes Code. *Journal of Sound and Vibration*, 213(4):643–664, 1998.

[34] A. Wohlbrandt, C. Weckmüller, and S. Guerin. A robust extension to the triple plane pressure mode matching method by filtering convective perturbations. *International Journal of Aeroacoustics*, 15(1-2):41–58, 2016.

[35] S.M. Grace, D.L. Sondak, W. Eversman, and M.J. Cannamela. Hybrid Prediction of Fan Tonal Noise. In *14th AIAA/CEAS Aeroacoustics Conference*, 2008.

[36] C. Polacsek, S. Burguburu, S. Redonnet, and M. Terracol. Numerical Simulations of Fan Interaction Noise using a Hybrid Approach. *AIAA Journal*, 44(6):1188–1196, 2006.

[37] C. Polacsek, G. Desquesnes, and G. Reboul. An equivalent-source model for simulating noise generation in turbofan engines. *Journal of Sound and Vibration*, 323(3-5):697–717, 2009.

[38] H. Posson and N. Peake. The acoustic analogy in an annular duct with swirling mean flow. *Journal of Fluid Mechanics*, 726:439–475, 2013.

[39] S.W. Rienstra and A. Hirschberg. *An Introduction to Acoustics*. Technische Universiteit Eindhoven, 2016.

[40] M. K. Myers. An exact energy corollary for homentropic flow. *Journal of Sound and Vibration*, 109(2):277–284, 1986.

[41] R. H. Cantrell and R. W. Hart. Interaction between Sound and Flow in Acoustic Cavities: Mass, Momentum, and Energy Considerations. *The Journal of the Acoustical Society of America*, 36(4):697–706, 1964.

[42] J.D. Anderson. *Computational Fluid Dynamics - The Basics with Applications*. McGraw-Hill, Inc., 1995.

[43] H. Chen. Volumetric formulation of the lattice Boltzmann method for fluid dynamics: Basic concept. *Physical Review E*, 58(3):3955–3963, 1998.

[44] S. Chen and G.D. Doolen. Lattice Boltzmann Method for Fluid Flows. *Annual Review of Fluid Mechanics*, 30:329–364, 1998.

[45] H. Choi and P. Moin. Grid-point requirements for large eddy simulation: Chapman's estimates revisited. *Physics of Fluids*, 24:011702, 2012.

[46] D.R. Chapman. Computational Aerodynamics Development and Outlook. *AIAA Journal*, 17(12):1293–1313, 1979.

[47] A.P.S. Wheeler, R.D. Sandberg, N.D. Sandham, R. Pichler, V. Michelassi, and G. Laskowski. Direct Numerical Simulations of a High-Pressure Turbine Vane. *Journal of Turbomachinery*, 138(7):071003, 2016.

[48] M. Sanjosé, C. Méon, V. Masson, and S. Moreau. Direct numerical simulation of acoustic reduction using serrated trailing-edge on an isolated airfoil. In *20th AIAA/CEAS Aeroacoustics Conference*, 2014.

[49] J. Winkler, R.D. Sandberg, and S. Moreau. Direct Numerical Simulation of the Self-Noise Radiated by an Airfoil in a Narrow Stream. In *18th AIAA/CEAS Aeroacoustics Conference*, 2012.

[50] J. Smagorinsky. General Circulation Experiments With the Primitive Equations. *Monthly Weather Review*, 91(3):99–164, 1963.

[51] F. Nicoud and F. Ducros. Subgrid-Scale Stress Modelling Based on the Square of the Velocity Gradient Tensor. *Flow, Turbulence and Combustion*, 62(3):183–200, 1999.

[52] N. Gourdain. Prediction of the unsteady turbulent flow in an axial compressor stage. Part 1: Comparison of unsteady RANS and LES with experiments. *Computers and Fluids*, 106:119–129, 2015.

[53] D. Papadogiannis, F. Duchaine, F. Sicot, L. Gicquel, G. Wang, and S. Moreau. Large Eddy Simulation of a High Pressure Turbine Stage: Effects of Sub-Grid Scale Modeling and Mesh Resolution. In *ASME Turbo Expo*, 2014.

[54] J. De Laborderie, L. Gicquel, and F. Duchaine. Analysis of a High-Pressure Multistage Axial Compressor At Off-Design Conditions With Coarse Large Eddy Simulations. In *12th European Conference on Turbomachinery Fluid dynamics & Thermodynamics*, 2017.

[55] N. Odier, F. Duchaine, L. Gicquel, G. Dufour, and N. García Rosa. Comparison of LES and RANS Predictions With Experimental Results of the Fan of a Turbofan. In *12th European Turbomachinery Conference*, 2017.

[56] G. Mouret, N. Gourdain, and L. Castillon. Adaptation of Phase-Lagged Boundary Conditions to Large Eddy Simulation in Turbomachinery Configurations. *Journal of Turbomachinery*, 138(4):041003, dec 2016.

[57] F. Sicot. *Simulation efficace des écoulements instationnaires périodiques en turbomachines*. PhD thesis, Ecole Centrale de Lyon, 2009.

[58] F. Wlassow, N. Gourdain, and M. Montagnac. Numerical simulation of aerodynamic instabilities in a multi-stage compressor. In *12th International Symposium on Unsteady Aerodynamics, Aeroacoustics & Aeroelasticity of Turbomachines*, 2009.

[59] X. Ottavy, N. Courtiade, and N. Gourdain. Experimental and Computational Methods for Flow Investigation in High-Speed Multistage Compressor. *Journal of Propulsion and Power*, 28(6):1141–1155, 2012.

[60] J. Kopitz, E. Bröcker, and W. Polifke. Characteristics-based filter for identification of planar acoustic waves in numerical simulation of turbulent compressible flow. In *12th International Congress on Sound and Vibration*, 2005.

[61] N. Ovenden, S.W. Rienstra, and A. Hirschberg. Mode-matching strategies in slowly varying engine ducts. *AIAA Journal*, 42(9):1832–1840, 2004.

[62] R. K. Amiet. Acoustic radiation from an airfoil in a turbulent stream. *Journal of Sound and Vibration*, 41(4):407–420, 1975.

[63] K. Schwarzschild. Die Beugung und Polarisation des Lichts durch einen Spalt - I. *Mathematische Annalen*, 55:177–247, 1902.

[64] R. W. Paterson and R. K. Amiet. Acoustic Radiation and Surface Pressure Characteristics of an Airfoil due to Incident Turbulence. Technical report, NASA CR-2733, 1976.

[65] Y. Rozenberg. *Modélisation analytique du bruit aérodynamique à large bande des machines tournantes : utilisation de calculs moyennés de mécanique des fluides*. PhD thesis, Ecole Centrale de Lyon, 2007.

[66] J. Christophe. *Application of Hybrid Methods to High Frequency Aeroacoustics*. PhD thesis, Université Libre de Bruxelles, 2011.

[67] S. Moreau, M. Roger, and V. Jurdic. Effect of Angle of Attack and Airfoil Shape on Turbulence-Interaction Noise. In *11th AIAA/CEAS Aeroacoustics Conference*, 2005.

[68] M. R. Myers and E. J. Kerschen. Influence of incidence angle on sound generation by airfoils interacting with high-frequency gusts. *Journal of Fluid Mechanics*, 353:221–259, 1997.

[69] I. Evers and N. Peake. Noise generation by high-frequency gusts interacting with an airfoil in transonic flow. *Journal of Fluid Mechanics*, 411:91–130, 2000.

[70] S. Kaji and T. Okazaki. Propagation of sound waves through a blade row. I. Analysis based on the semi-actuator disk theory. *Journal of Sound and Vibration*, 11(3):339–353, 1970.

[71] S. Kaji and T. Okazaki. Propagation of sound waves through a blade row. II. Analysis based on the acceleration potential method. *Journal of Sound and Vibration*, 11(3):355–375, 1970.

[72] R. Mani and G. Horvay. Sound transmission through blade rows. *Journal of Sound and Vibration*, 12(1):59–83, 1970.

[73] W. Koch. On the transmission of sound waves through a blade row. *Journal of Sound and Vibration*, 18(1):111–128, 1971.

[74] N. Peake. The interaction between a high-frequency gust and a blade row. *Journal of Fluid Mechanics*, 241:261–289, 1992.

[75] S. A. L. Glegg. the Response of a Swept Blade Row To a Three-Dimensional Gust. *Journal of Sound and Vibration*, 227(1):29–64, 1999.

[76] H. Posson, M. Roger, and S. Moreau. On a uniformly valid analytical rectilinear cascade response function. *Journal of Fluid Mechanics*, 663:22–52, 2010.

[77] S. Bouley, B. François, M. Roger, H. Posson, and S. Moreau. On a two-dimensional mode-matching technique for sound generation and transmission in axial-flow outlet guide vanes. *Journal of Sound and Vibration*, 403:190–213, 2017.

[78] M. Roger and B. François. Combined analytical models for sound generation and transmission in cambered axial-flow outlet guide vanes. *European Journal of Mechanics, B/Fluids*, 61:218–225, 2017.

[79] S. Bouley, B. François, and M. Roger. On a mode-matching technique for sound generation and transmission in a three-dimensional annular cascade of outlet guide vanes. In *22nd AIAA/CEAS Aeroacoustics Conference*, 2016.

[80] N. Curle. The Influence of Solid Boundaries upon Aerodynamic Sound. *Proceedings of the Royal Society of London. Series A*, 231(1187):505–514, 1955.

[81] J. E. Ffowcs Williams and D. L. Hawkings. Theory relating to the noise of rotating machinery. *Journal of Sound and Vibration*, 10(1):10–21, 1969.

[82] J. De Laborderie and S. Moreau. Prediction of tonal ducted fan noise. *Journal of Sound and Vibration*, 372:105–132, 2016.

[83] M. Sanjosé, M. Daroukh, J. De Laborderie, S. Moreau, and A. Mann. Tonal noise prediction and validation on the ANCF rotor-stator configuration. *Noise Control Engineering Journal*, 63(6):552–562, 2015.

[84] S. W. Rienstra. Sound transmission in slowly varying circular and annular lined ducts with flow. *Journal of Fluid Mechanics*, 380:279–296, 1999.

[85] S.W. Rienstra and W. Eversman. A numerical comparison between the multiple-scales and finite-element solution for sound propagation in lined flow duets. *Journal of Fluid Mechanics*, 437:367–384, 2001.

[86] A.H. Nayfeh. *Introduction to Perturbation Techniques*. Wiley Classics Library, 1993.

[87] N. C. Ovenden. A uniformly valid multiple scales solution for cut-on cut-off transition of sound in flow ducts. *Journal of Sound and Vibration*, 286:403–416, 2005.

[88] N.C. Ovenden, W. Eversman, and S.W. Rienstra. Cut-on cut-off transition in flow ducts: comparing multiple-scales and finite-element solutions. In *10th AIAA/CEAS Aeroacoustics Conference*, 2004.

[89] J.L. Kerrebrock. Small Disturbances in Turbomachine Annuli with Swirl. *AIAA Journal*, 15(6):794–803, 1977.

[90] V.V. Golubev and H.M. Atassi. Unsteady Swirling Flows in Annular Cascades Part1: Evolution of Incident Disturbances. *AIAA Journal*, 38(7):1142–1149, 2000.

[91] V.V. Golubev and H.M. Atassi. Unsteady Swirling Flows in Annular Cascades, Part 2: Aerodynamic Blade Response. *AIAA Journal*, 38(7):1150–1158, 2000.

[92] A.J. Cooper and N. Peake. Propagation of unsteady disturbances in a slowly varying duct with mean swirling flow. *Journal of Fluid Mechanics*, 445:207–234, 2001.

[93] H. Posson and N. Peake. Swirling mean flow effect on fan-trailing edge broadband noise in a lined annular duct. In *19th AIAA/CEAS Aeroacoustics Conference*, 2013.

[94] V. Masson, H. Posson, M. Sanjosé, S. Moreau, and M. Roger. Fan-OGV interaction broadband noise prediction in a rigid annular duct with swirling and sheared mean flow. In *22nd AIAA/CEAS Aeroacoustics Conference*, 2016.

[95] A. Topol. TFaNS Tone Fan Noise Design/Prediction System. Volume I: System Description, CUP3D Technical Documentation and Manual for Code Developers. Technical report, NASA CR-1999-208882, 1999.

[96] H. Posson and S. Moreau. Effect of Rotor Shielding on Fan-Outlet Guide Vanes Broadband Noise Prediction. *AIAA Journal*, 51(7):1576–1592, 2013.

[97] G.M. Lilley. On the noise from jets. In *AGARD CP-131*, 1974.

[98] S.W. Rienstra. Sound Propagation in Slowly Varying 2D Flow Duct with Shear Flow. In *22nd AIAA/CEAS Aeroacoustics Conference*, 2016.

[99] S.W. Rienstra. Sound propagation in slowly varying lined flow ducts of arbitrary cross-section. *Journal of Fluid Mechanics*, 495:157–173, 2003.

[100] D.B. Hanson. Acoustic reflection and transmission of rotors and stators including mode and frequency scattering. In *3rd AIAA/CEAS Aeroacoustics Conference*, 1997.

[101] E. Envia. Acoustic Power Transmission Loss Through a Ducted Fan. In *22nd AIAA/CEAS Aeroacoustics Conference*, 2016.

[102] L. Cambier, S. Heib, and S. Plot. The Onera elsA CFD software: input from research and feedback from industry. *Mechanics & Industry*, 14(3):159–174, 2013.

[103] D.C. Wilcox. Reassessment of the Scale-Determining Equation for Advanced Turbulence Models. *AIAA Journal*, 26(11):1299–1310, 1988.

[104] X. Zheng, C. Liao, C. Liu, C. H. Sung, and T. T. Huang. Multigrid Computation of Incompressible Flows Using Two-Equation Turbulence Models: Part I - Numerical Method. *Journal of Fluids Engineering*, 119(4):893–899, 1997.

[105] M. Montagnac. Non Coincident Conservative Adjacent Join Boundary Condition. Technical report, CERFACS, 2008.

[106] J. Thisse. *Prévision du bruit d'onde de choc d'un turboréacteur en régime transsonique par des méthodes analytiques et numériques*. PhD thesis, Ecole Nationale Supérieure d'Arts et Métiers, 2015.

[107] W. S. Janna. *Introduction to Fluid Mechanics*. PWS Engineering, 2010.

[108] R. Parker. Relation between blade row spacing and potential flow interaction effects in turbomachines. *Proceedings of the Institution of Mechanical Engineers*, 184(7):1–8, 1969.

[109] M. Sanjosé, S. Moreau, M. Pestana, and M. Roger. Effect of weak Outlet-Guide-Vane heterogeneity on rotor-stator tonal noise. *AIAA Journal*, 2017.

[110] S. Redonnet and Y. Druon. Computational Aeroacoustics of Aft Fan Noises Characterizing a Realistic Coaxial Engine. *AIAA Journal*, 50(5):1029–1046, 2012.

[111] A. Sharma and H. Chen. Prediction of aerodynamic tonal noise from open rotors. *Journal of Sound and Vibration*, 332:3832–3845, 2013.

[112] Antares Development Team. Antares Documentation Release 1.9.0, 2012–2017.

[113] A. Peters, Z.S. Spakovszky, W.K. Lord, and B. Rose. Ultrashort Nacelles for Low Fan Pressure Ratio Propulsors. *Journal of Turbomachinery*, 137(2):021001, 2014.

[114] R.J. Astley, R. Sugimoto, G. Gabard, E. Norde, E.J. Grift, and M. Bocquier. The Effect of Steady Flow Distortion on Noise Propagation in Turbofan Intake. In *20th AIAA/CEAS Aeroacoustics Conference*, number June, 2014.

[115] P.J. Schmid. Dynamic mode decomposition of numerical and experimental data. *Journal of Fluid Mechanics*, 656(July 2010):5–28, 2010.

[116] A. F. Smith, N. C. Ovenden, and R. I. Bowles. Flow and geometry induced scattering of high frequency acoustic duct modes. *Wave Motion*, 49(1):109–124, 2012.

[117] A. Favre. Equations des gaz turbulents compressibles I.- Formes générales. *Journal de Mécanique*, 4:361–390, 1965.

[118] G. Legras. *Analyse des mécanismes d'action des traitements de carter dans les compresseurs axiaux*. PhD thesis, Ecole Centrale de Lyon, 2011.

[119] J. Boussinesq. *Théorie de l'écoulement tourbillonnant et tumultueux des liquides dans les lits rectilignes à grande section*. Gauthier-Villars, 1897.

[120] P.R. Spalart and S.R. Allmaras. A One-Equatlon Turbulence Model for Aerodynamic Flows. In *30th Aerospace Sciences Meeting & Exhibit*, 1992.

[121] B.E. Launder and D.B. Spalding. The numerical computation of turbulent flows. *Computer Methods in Applied Mechanics and Engineering*, 3(2):269–289, 1974.

[122] S. Wallin and A.V. Johansson. An explicit algebraic Reynolds stress model for incompressible and compressible turbulent flows. *Journal of Fluid Mechanics*, 403:89–132, 2000.

[123] K.W. Morton and D.F. Mayers. *Numerical Solution of Partial Differential Equations. An Introduction*. Cambridge University Press, 2005.

[124] H.K Versteeg and W. Malalasekera. *An Introduction to Computational Fluid Dynamics - The Finite Volume Method*. Pearson Education, 2007.

[125] K. Eriksson, D. Estep, P. Hansbo, and C. Johnson. *Computational Differential Equations*. Cambridge University Press, 2009.

[126] A. Jameson, W. Schmidt, and E. Turkel. Numerical Solution of the Euler Equations by Finite Volume Methods Using Runge-Kutta Time-Stepping Schemes. In *14th AIAA Fluid and Plasma Dynamic Conference*, 1981.

[127] P.L. Roe. Approximate Riemann Solvers, Parameter Vectors, and Difference Schemes. *Journal of Computational Physics*, 43:357–372, 1981.

[128] A. Harten. High Resolution Schemes for Hyperbolic Conservation Laws. *Journal of Computational Physics*, 49:357–393, 1983.

[129] B. van Leer. Towards the ultimate conservative difference scheme V: a second order sequel to Godunov' method. *Journal of Computational Physics*, 32:101–136, 1979.

[130] B. Koren. A robust upwind discretization method for advection, diffusion and source terms. *Notes on Numerical Fluid Mechanics*, 45:117–138, 1993.